Shouting Gao
Xiaofan Li

Cloud-Resolving Modeling of Convective Processes

Springer

Cloud-Resolving Modeling of Convective Processes

Shouting Gao · Xiaofan Li

Cloud-Resolving Modeling of Convective Processes

Springer

Shouting Gao
Institute of Atmospheric Physics
Chinese Academy of Sciences
China

Xiaofan Li
NOAA/NESDIS Center for Satellite
Applications and Research
MD, USA

ISBN 978-1-4020-8275-7 e-ISBN 978-1-4020-8276-4

Library of Congress Control Number: 2008923288

Printed on acid-free paper

9 8 7 6 5 4 3 2 1

springer.com

Foreword

Clouds and cloud systems and their interactions with larger scales of motion, radiation, and the Earth's surface are extremely important parts of weather and climate systems. Their treatment in weather forecast and climate models is a significant source of errors and uncertainty. As computer power increases, it is beginning to be possible to explicitly resolve cloud and precipitation processes in these models, presenting opportunities for improving precipitation forecasts and larger-scale phenomena such as tropical cyclones which depend critically on cloud and precipitation physics.

This book by Professor Shouting Gao of the Institute of Atmospheric Physics in Beijing and Dr. Xiaofan Li of NOAA's National Environmental Satellite, Data, and Information Service (NESDIS) presents an update and review of results of high-resolution, mostly two-dimensional models of clouds and precipitation and their interactions with larger scales of motion and the Earth's surface. It provides a thorough description of cloud and precipitation physics, including basic governing equations and related physics, such as phase changes of water, radiation, and mixing. Model results are compared with observations from the 1992–93 Tropical Ocean Global Atmosphere Coupled Ocean Atmosphere Response Experiment (TOGA COARE) experiment. The importance of the ocean to tropical convective systems is clearly shown here in the numerical results of simulations with their air–sea coupled modeling system. While the focus is on tropical convection, the methodology and applicability can be extended to cloud and precipitation processes elsewhere.

The results described in this well-written book form a solid foundation for future high-resolution model weather forecasts and climate simulations that resolve clouds explicitly in three dimensions – a future that I believe has great promise for the understanding and prediction of weather and climate for the great benefit of society.

University Corporation for Atmospheric Research,
June 2007

Richard Anthes
President

Contents

Introduction

The material in this book is based on our recent research work in the last 10 years. This is the first book that focuses on cloud-resolving modeling of convective processes. Clouds play an important role in linking atmospheric and hydrological processes and have profound impacts on regional and global climate. Better description of clouds and associated cloud–radiation interaction is a key for successful simulations of cloud processes, which requires the physical presence of cloud hydrometeors, prognostic cloud equations, and interactive radiative schemes in models. Cloud-resolving models have been developing for four decades towards providing better understanding of cloud-scale processes associated with convective development. With the explosive increase of computational powers, the cloud-resolving models which were once used to develop cloud schemes for general circulation models have been directly applied to a global domain with a high horizontal resolution (grid mesh is less than 5 km), whose preliminary results are promising.

This book starts with basic equations and physical packages used in cloud-resolving models and coupled ocean-cloud-resolving atmosphere model. The cloud-resolving model discussed in this book is the two-dimensional version of the Goddard Cumulus Ensemble Model. The model simulations are evaluated with available observations during Tropical Ocean Global Atmosphere Coupled Ocean-Atmosphere Response Experiment (TOGA COARE). The book covers many research aspects related to convective development, cloud, and precipitation. The material in this book has been used as part of a graduate course at the Graduate School, Chinese Academy of Sciences, Beijing, China. Therefore, this book can be used as a reference and textbook for graduate students and researchers whose research interests are mesoscale, cloud, and precipitation modeling.

This book is comprised of 13 chapters. Chapter 1 presents governing equations, parameterization schemes of radiation, cloud microphysics, and subgrid-scale turbulence. Two model frameworks imposed by different large-scale forcing are intensively discussed. Chapter 2 describes thermal and vapor budgets, surface rainfall equation, energetics equation, and partitioning of convective and stratiform rainfall, which are frequently applied to the analysis of cloud-resolving model simulation

data. The cloud-resolving model simulation data are evaluated with the high-quality observational data from TOGA COARE in terms of thermodynamic states, apparent heat sink and moisture source, surface radiative and latent heat fluxes, and surface rain rate in chapter 3. Since most of the research work is from two-dimensional cloud-resolving modeling, the similarities and differences between two- and three-dimensional cloud-resolving modeling are discussed.

The surface rainfall equation is introduced to examine the contributions of water vapor and cloud hydrometeors in surface rainfall processes in chapter 4. The intensive discussions of surface rainfall processes are conducted in raining stratiform, convective, nonraining stratiform, and clear-sky regions, respectively. In chapter 5, kinematics and propagation of tropical cloud clusters are discussed. Chapter 6 addresses cloud microphysics and radiation. In particular, the depositional growth of snow from cloud ice as an important sink of cloud ice, and precipitation–radiation interaction are interactively examined. The vorticity vectors associated with tropical convection are discussed in chapter 7. The dominant physical processes that are responsible for the diurnal variations of tropical convection including nocturnal and afternoon rainfall peaks and tropical convective and stratiform rainfall are quantitatively identified with analysis of surface rainfall equation in chapter 8. The precipitation efficiencies and statistical equivalence of efficiencies defined with water vapor and cloud-microphysics budgets are addressed in chapter 9. The coupled ocean-cloud-resolving atmosphere model is developed to study the small-scale effects of precipitation in ocean mixing processes in chapter 10. Effects of SST, diurnal variation, and cloud radiation on equilibrium states are discussed in chapter 11. The microwave radiative transfer model with cloud-resolving model simulation data is applied to radiance simulations in chapter 12. Finally, the future perspective of cloud-resolving modeling including simplification of prognostic cloud schemes, application of cloud-resolving modeling to general circulation model and to global domain are discussed in chapter 13.

We would like to thank Dr. Richard A. Anthes, President of the University Corporation for Atmospheric Research, who read the book draft and wrote the preface for this book. Our sincere thanks also go to Dr. Wei-Kuo Tao and Dr. David Adamec at NASA/Goddard Space Flight Center (GSFC), Professor Ming-Dah Chou at National Taiwan University, and Professor Minghua Zhang at the State University of New York, Stony Brook for providing two-dimensional Goddard Cumulus Ensemble (GCE) model, ocean mixed-layer model, radiative transfer code used in GCE model, and TOGA COARE forcing data, respectively. We also thank Dr. Hsiao-Ming Hsu at the National Center for Atmospheric Research for his comments, Drs. Fan Ping, Xiaopeng Cui, Yushu Zhou, and Lingkun Ran at the Institute of Atmospheric Physics, Chinese Academy of Sciences, for efficient and productive research collaborations, and Miss Di Li at the University of Maryland, College Park, for editing this book. Xiaofan Li would like to thank Dr. William K.-M. Lau, Chief of the Laboratory for Atmospheres at NASA/GSFC, and Professor Chung-Hsiung Sui at the National Central University for their support, encouragement, and academic guidance when Xiaofan Li worked at GSFC as a contract research scientist during 1994–2001, Drs. Fuzhong Weng and Quanhua Liu at NOAA/NESDIS/Center

for Satellite Applications and Research for providing microwave radiative transfer model, and Dr. Jian-Jian Wang at the Goddard Center for Earth Science and Technology, University of Maryland, Baltimore County, for research collaboration.

We are also indebted to Dr. Robert Doe and Ms. Nina Bennink at Springer for their editorial efforts. This work was supported by the national Key Basic Research and Development Projects of China under the grants No. 2004CB418301 and G1998040907 and Olympic Meteorological Service Projects under grants No. 2001BA904B09 and KACX1-02.

Beijing, China — Shouting Gao
Camp Springs, Maryland, USA — Xiaofan Li
Fall 2007

Chapter 1
Model and Physics

Cloud-resolving models differ from general circulation and mesoscale models in two ways. First, they cannot simulate large-scale circulations due to small model domains, whereas general circulation and mesoscale models can simulate large-scale circulations. A large-scale forcing is imposed in the cloud-resolving model. Second, cloud-resolving models with fine spatial resolutions use prognostic cloud microphysical parameterization to simulate cloud and precipitation processes. In contrast, general circulation and mesoscale models use diagnostic cumulus parameterization and/or prognostic cloud microphysical parameterization due to coarse spatial resolutions. Many cloud-resolving models have been developed to study convective responses to the large-scale forcing (Table 1.1). In this chapter, the cloud-resolving model and coupled ocean-cloud-resolving atmosphere model will be described in a two-dimensional (2D) framework in terms of governing equations, large-scale forcing, parameterization schemes of cloud microphysics, radiation, subgrid-scale turbulence closure, ocean mixing closure, and boundary conditions.

1.1 Governing Equations

The cloud-resolving model was originally developed by Soong and Ogura (1980) and Soong and Tao (1980). This model was significantly improved by Tao and Simpson (1993) at the National Aeronautics and Space Administration (NASA) Goddard Space Flight Center (GSFC) and was modified by Sui et al. (1994, 1998). The model was named the Goddard cumulus ensemble (GCE) model. The cloud-resolving model used in this book is the 2D-modified version of GCE model. The nonhydrostatic governing equations with an elastic approximation can be exp-ressed by

$$\nabla \cdot \mathbf{V} + \frac{1}{\bar{\rho}} \frac{\partial}{\partial z} \bar{\rho} w = 0, \tag{1.1a}$$

$$\frac{\partial A}{\partial t} = -\nabla \cdot \mathbf{V} A - \frac{1}{\bar{\rho}} \frac{\partial}{\partial z} \bar{\rho} w A + S_A + D_A, \tag{1.1b}$$

$$\frac{\partial B}{\partial t} = -\nabla \cdot \mathbf{V} B - \frac{1}{\bar{\rho}} \frac{\partial}{\partial z} \bar{\rho} (w - w_{TB}) B + S_B + D_B. \tag{1.1c}$$

Table 1.1 A summary of cloud-resolving models

Model	Dynamic core	Cloud scheme	Turbulence closures	Radiation scheme
Clark (1977, 1979), Clark and Hall (1991), Clark et al. (1996)	Anelastic and hydrostatic approximations	Water cloud (Kessler 1969), ice cloud (Koenig and Murray 1976)	Smagorinsky (1963), Lilly (1962)	Kiehl et al. (1994)
Soong and Ogura (1980), Tao and Simpson (1993)	Anelastic approximation and nonhydrostatic form	Water and ice schemes (Lin et al. 1983, Rutledge and Hobbs 1983, 1984; Tao et al. 1989; Krueger et al. 1995)	Klemp and Wilhelmson (1978)	Solar (Chou et al. 1998) and IR infrared (Chou et al. 1991; Chou and Suarez 1994) schemes
Lipps and Hemler (1986, 1988, 1991)	Anelastic and hydrostatic approximations	Water cloud (Kessler 1969)	Klemp and Wilhelmson (1978)	Newtonian damping
Redelsperger and Sommeria (1986)	Deardorff (1972), Sommeria (1976), Redelsperger and Sommeria (1981a, b, 1982)	Water cloud (Kessler 1969)	Subgrid-scale turbulence closure (Redelsperger and Sommeria (1981a, b, 1982)	–
Hu and He (1988), Hu et al. (1998), Zou (1991)	Nonhydrostatic primitive dynamic core (Zou 1991)	Prognostic equations for hydrometeors and number concentrations (Hu and He 1988)	Second-moment turbulence closure	–
Kruegger (1988)	Anelastic and hydrostatic approximations	Three-phase bulk scheme (Lin et al. 1983; Lord et al. 1984; Krueger et al. 1995)	Third-moment turbulence closure (Krueger 1988)	Harshvardhan et al. (1987)
Nakajima and Matsuno (1988)	Yamasaki (1975), Ogura and Philips (1962)	Water cloud (Kessler 1969)	Velocity deformation and static stability dependent	Horizontal homogeneous cooling

Tripoli (1992)	Nonhydrostatic core with enstrophy conservation	Flatau et al. (1989)	A turbulent kinetic closure for eddy diffusion	Chen and Cotton (1983)
Xu (1992), Xu and Huang (1994)	Nonhydrostatic primitive dynamic core	Xu and Duan (1999)	Second-moment turbulence closure	–
Ferrier (1994), Ferrier et al. (1995)	Anelastic approximation and nonhydrostatic form	Double-moment multiple-phase four-class ice scheme (Ferrier 1994)	Klemp and Wilhelmson (1978)	Chou (1984, 1986), Chou and Kouvaris (1991)
Tompkins and Craig (1998)	Anelastic quasi-Boussineq approximation	Three-phase ice scheme (Swann 1994; Brown and Swann 1997); the water vapor and cloud water are combined into the total-water mixing ratio	First-order subgrid-scale turbulence closure (Shutts and Gray 1994)	Two-stream plane-parallel approximation (Edwards and Slingo 1996; Petch 1998)
Satoh et al. (2005)	Nonhydrostatic formulations in the icosahedral grids covering the global domain	Grabowski (1998)	Mellor and Yamada (1974) level-2 closure	Nakajima et al. (2000)

Here, $\mathbf{V}$ and w are horizontal wind vector and vertical wind, respectively; $\bar{\rho}$ is a mean density, which is a function of height only; $A = (\theta, q_v, \mathbf{V}, w)$; $B = (q_c, q_r, q_i, q_s, q_g)$; θ and q_v are potential temperature and specific humidity, respectively; q_c, q_r, q_i, q_s, q_g are the mixing ratios of cloud water (small cloud droplets), raindrops, cloud ice (small ice crystals), snow (density $0.1\,\mathrm{g\,cm^{-3}}$), and graupel (density $0.4\,\mathrm{g\,cm^{-3}}$), respectively; w_{TB} is a terminal velocity that is zero for cloud water and ice; S_A is a source and sink in momentum, temperature, and moisture equations such as pressure gradient force, buoyancy force, condensational heating, and radiative heating. The radiation parameterization schemes will be addressed in section 1.3; S_B is a cloud source and sink that is determined by microphysical processes, which will be discussed in section 1.2; D_A and D_B are dissipation terms related to subgrid-scale turbulence closure, which will be elucidated in section 1.4.

For model calculations by Li et al. (1999), it is convenient to partition $(A,\ \mathbf{V})$ into area means $(\bar{A},\ \bar{\mathbf{V}})$ and deviations $(A',\ \mathbf{V}')$, i.e.,

$$A = \bar{A} + A', \tag{1.2a}$$

$$\mathbf{V} = \bar{\mathbf{V}} + \mathbf{V}'. \tag{1.2b}$$

Applying (1.2) to (1.1b) leads to

$$\begin{aligned}\frac{\partial A}{\partial t} = &-\nabla\cdot(\mathbf{V}'A' + \mathbf{V}'\bar{A} + \bar{\mathbf{V}}A') - \frac{1}{\bar{\rho}}\frac{\partial}{\partial z}\bar{\rho}(w'A' + w'\bar{A} + \bar{w}A') \\ &+ S_A + D_A - \bar{\mathbf{V}}\cdot\nabla\bar{A} - \bar{w}\frac{\partial}{\partial z}\bar{A}.\end{aligned} \tag{1.3}$$

Here, the area mean continuity equation (1.1a) is used in the derivation of (1.3).

Taking an area mean over (1.3), we get the equation for $\bar{A}$,

$$\frac{\partial \bar{A}}{\partial t} = -\nabla\cdot\overline{\mathbf{V}'A'} - \frac{1}{\bar{\rho}}\frac{\partial}{\partial z}\bar{\rho}\overline{w'A'} + \bar{S}_A + \bar{D}_A - \bar{\mathbf{V}}\cdot\nabla\bar{A} - \bar{w}\frac{\partial}{\partial z}\bar{A}. \tag{1.4a}$$

Perturbation equation for A' is obtained by subtracting (1.4a) from (1.3):

$$\begin{aligned}\frac{\partial A'}{\partial t} = &-\nabla\cdot(\mathbf{V}'\bar{A} + \bar{\mathbf{V}}A') - \frac{1}{\bar{\rho}}\frac{\partial}{\partial z}\bar{\rho}(w'\bar{A} + \bar{w}A') - \nabla\cdot(\mathbf{V}'A' - \overline{\mathbf{V}'A'}) \\ &- \frac{1}{\bar{\rho}}\frac{\partial}{\partial z}\bar{\rho}(w'A' - \overline{w'A'}) + S_A - \bar{S}_A + D_A - \bar{D}_A.\end{aligned} \tag{1.4b}$$

Environment has an important impact on convective development. When convection develops, associated momentum, heat, and moisture transport upward through convective activity, which in turn modify environment significantly. Environment and convection interact in a nonlinear way (e.g., Chao 1962). Due to a small domain in the cloud-resolving model (e.g., 768 km in a 2D framework), the large-scale circulation cannot be simulated. Thus, the large-scale forcing needs to be imposed in the cloud-resolving model. Soong and Ogura (1980) were the first to develop ways to impose the observed large-scale variables into the cloud-resolving model

to examine the convective response to the imposed large-scale forcing. The major forcing is vertical velocity and associated vertical advections. Thus, there are two ways to impose the large-scale forcing into the cloud model. The horizontally uniform and vertically varying vertical velocity can be imposed, as first introduced by Soong and Ogura (1980), or the horizontally uniform total advection of the heat and moisture can be imposed (e.g., Wu et al. 1998). Li et al. (1999) discussed the two model setups intensively.

For the model with the imposed vertical velocity ($\bar{w}^o$), horizontal wind ($\bar{\mathbf{V}}^o$) and horizontal advection ($-\bar{\mathbf{V}}^o \cdot \nabla \bar{A}^o$) are also imposed. These forcing data denoted by superscript "^{o}" are calculated from the observational data [e.g., Tropical Ocean Global Atmosphere Coupled Ocean-Atmosphere Response Experiment (TOGA COARE) in Li et al. (1999) and Global Atmosphere Research Program (GARP) Atlantic Tropical Experiment (GATE) in Grabowski et al. (1996)]. With the assumption that $-\mathbf{V}' \cdot \nabla \bar{A}^o = 0$, the model equations for potential temperature and specific humidity can be expressed by

$$\begin{aligned}\frac{\partial A}{\partial t} = &-\nabla \cdot \mathbf{V}' A' - \bar{\mathbf{V}}^o \cdot \nabla A' - \frac{1}{\bar{\rho}} \frac{\partial}{\partial z} \bar{\rho} w' A' - \bar{w}^o \frac{\partial}{\partial z} A' - w' \frac{\partial}{\partial z} \bar{A} \\ &+ S_A + D_A - \bar{\mathbf{V}}^o \cdot \nabla \bar{A}^o - \bar{w}^o \frac{\partial}{\partial z} \bar{A}.\end{aligned} \tag{1.5}$$

The model consists of (1.1a) and (1.1c), perturbation momentum equation (1.4b), and equations for potential temperature and specific humidity (1.5).

For the model with imposed horizontally uniform total advection of heat and moisture, horizontal wind is also imposed. With the assumption that $-\nabla \cdot \bar{\mathbf{V}}^o\, A' - \partial \bar{\rho} A' \bar{w}^o / \bar{\rho} \partial z = 0$, the model equations for potential temperature and specific humidity can be written by

$$\frac{\partial A}{\partial t} = -\nabla \cdot \mathbf{V}' A - \frac{1}{\bar{\rho}} \frac{\partial}{\partial z} \bar{\rho} w' A + S_A + D_A - \bar{\mathbf{V}}^o \cdot \nabla \bar{A}^o - \bar{w}^o \frac{\partial}{\partial z} \bar{A}^o \tag{1.6}$$

This model is comprised of (1.1a) and (1.1c), perturbation momentum equation (1.4b), and equations for potential temperature and specific humidity (1.6). Li et al. (1999) found that the terms omitted in (1.5) and (1.6) do not have any impact on the model simulations. The comparison between simulations by the two model setups will be discussed with the TOGA COARE data in chapter 3.

The governing equations in the 2D cloud-resolving model can be expressed as follows:

$$\frac{\partial u'}{\partial x} + \frac{1}{\bar{\rho}} \frac{\partial (\bar{\rho} w')}{\partial z} = 0, \tag{1.7a}$$

$$\begin{aligned}\frac{\partial u'}{\partial t} = &-\frac{\partial}{\partial x}(2u'\bar{u}^o + u'u') - \frac{1}{\bar{\rho}} \frac{\partial}{\partial z} \bar{\rho} (w'\bar{u}^o + \bar{w}^o u' + w'u' - \overline{w'u'}) \\ &- c_p \frac{\partial (\bar{\theta} \pi')}{\partial x} + D_u - \bar{D}_u\end{aligned}, \tag{1.7b}$$

$$\frac{\partial w'}{\partial t} = -\frac{\partial}{\partial x}(u'\bar{w}^o + \bar{u}^o w' + u'w') - \frac{1}{\bar{\rho}}\frac{\partial}{\partial z}\bar{\rho}(2w'\bar{w}^o + w'w' - \overline{w'w'}) - c_p\frac{\partial(\bar{\theta}\pi')}{\partial z} + g\left(\frac{\theta'}{\theta_o} + 0.61q_v{}' - q_l{}'\right) + D_w - \bar{D}_w, \tag{1.7c}$$

$$\frac{\partial \theta}{\partial t} = -\frac{\partial(u'\theta')}{\partial x} - \bar{u}^o\frac{\partial\theta'}{\partial x} - \frac{1}{\bar{\rho}}\frac{\partial}{\partial z}(\bar{\rho}w'\theta') - \bar{w}^o\frac{\partial\theta'}{\partial z} - w'\frac{\partial\bar{\theta}}{\partial z} + \frac{Q_{cn}}{\pi c_p} + \frac{Q_R}{\pi c_p} - \bar{u}^o\frac{\partial\bar{\theta}^o}{\partial x} - \bar{w}^o\frac{\partial\bar{\theta}}{\partial z} + D_\theta, \tag{1.7d}$$

$$\frac{\partial q_v}{\partial t} = -\frac{\partial(u'q_v{}')}{\partial x} - \bar{u}^o\frac{\partial q_v{}'}{\partial x} - \bar{w}^o\frac{\partial q_v{}'}{\partial z} - w'\frac{\partial\bar{q}_v}{\partial z} - \frac{1}{\bar{\rho}}\frac{\partial}{\partial z}\bar{\rho}w'q_v{}' - S_{qv} - \bar{u}^o\frac{\partial\bar{q}_v^o}{\partial x} - \bar{w}^o\frac{\partial\bar{q}_v}{\partial z} + D_{qv}, \tag{1.7e}$$

$$\frac{\partial q_c}{\partial t} = -\frac{\partial(uq_c)}{\partial x} - \frac{1}{\bar{\rho}}\frac{\partial(\bar{\rho}wq_c)}{\partial z} + S_{qc} + D_{qc}, \tag{1.7f}$$

$$\frac{\partial q_r}{\partial t} = -\frac{\partial(uq_r)}{\partial x} - \frac{1}{\bar{\rho}}\frac{\partial}{\partial z}\bar{\rho}(w - w_{Tr})q_r + S_{qr} + D_{qr}, \tag{1.7g}$$

$$\frac{\partial q_i}{\partial t} = -\frac{\partial(uq_i)}{\partial x} - \frac{1}{\bar{\rho}}\frac{\partial(\bar{\rho}wq_i)}{\partial z} + S_{qi} + D_{qi}, \tag{1.7h}$$

$$\frac{\partial q_s}{\partial t} = -\frac{\partial(uq_s)}{\partial x} - \frac{1}{\bar{\rho}}\frac{\partial}{\partial z}\bar{\rho}(w - w_{Ts})q_s + S_{qs} + D_{qs}, \tag{1.7i}$$

$$\frac{\partial q_g}{\partial t} = -\frac{\partial(uq_g)}{\partial x} - \frac{1}{\bar{\rho}}\frac{\partial}{\partial z}\bar{\rho}(w - w_{Tg})q_g + S_{qg} + D_{qg}, \tag{1.7j}$$

where

$$\begin{aligned} Q_{cn} = {} & L_v(P_{CND} - P_{REVP}) + L_s\{P_{DEP} + (1-\delta_1)P_{SDEP}(T < T_o) \\ & + (1-\delta_1)P_{GDEP}(T < T_o) - P_{MLTS}(T > T_o) \\ & - P_{MLTG}(T > T_o)\} \\ & + L_f\{P_{SACW}(T < T_o) + P_{SFW}(T < T_o) + P_{GACW}(T < T_o) \\ & + P_{IACR}(T < T_o) + P_{GACR}(T < T_o) + P_{SACR}(T < T_o) \\ & + P_{GFR}(T < T_o) - P_{RACS}(T > T_o) - P_{SMLT}(T > T_o) \\ & - P_{GMLT}(T > T_o) + P_{IHOM}(T < T_{oo}) \\ & - P_{IMLT}(T > T_o) + P_{IDW}(T_{oo} < T < T_o)\}, \end{aligned} \tag{1.8a}$$

$$\begin{aligned} S_{qv} = {} & P_{CND} - P_{REVP} + P_{DEP} + (1-\delta_1)P_{SDEP}(T < T_o) \\ & + (1-\delta_1)P_{GDEP}(T < T_o) - P_{MLTS}(T > T_o) - P_{MLTG}(T > T_o), \end{aligned} \tag{1.8b}$$

$$\begin{aligned} S_{qc} = {} & -P_{SACW} - P_{RAUT} - P_{RACW} - P_{SFW}(T < T_o) - P_{GACW} \\ & + P_{CND} - P_{IHOM}(T < T_{oo}) + P_{IMLT}(T > T_o) - P_{IDW}(T_{oo} < T < T_o), \end{aligned} \tag{1.8c}$$

$$\begin{aligned} S_{qr} =& P_{SACW}(T > T_o) + P_{RAUT} + P_{RACW} + P_{GACW}(T > T_o) \\ & - P_{REVP} + P_{RACS}(T > T_o) - P_{IACR}(T < T_o) - P_{GACR}(T < T_o) \\ & - P_{SACR}(T < T_o) - P_{GFR}(T < T_o) + P_{SMLT}(T > T_o) + P_{GMLT}(T > T_o), \end{aligned} \tag{1.8d}$$

$$\begin{aligned} S_{qi} =& - P_{SAUT}(T < T_o) - P_{SACI}(T < T_o) - P_{RACI}(T < T_o) \\ & - P_{SFI}(T < T_o) - P_{GACI}(T < T_o) + P_{IHOM}(T < T_{oo}) \\ & - P_{IMLT}(T > T_o) + P_{IDW}(T_{oo} < T < T_o) + P_{DEP}, \end{aligned} \tag{1.8e}$$

$$\begin{aligned} S_{qs} =& P_{SAUT}(T < T_o) + P_{SACI}(T < T_o) + \delta_4 P_{SACW}(T < T_o) \\ & + P_{SFW}(T < T_o) + P_{SFI}(T < T_o) + \delta_3 P_{RACI}(T < T_o) \\ & - P_{RACS}(T > T_o) - P_{GACS} - P_{SMLT}(T > T_o) \\ & - (1 - \delta_2) P_{RACS}(T < T_o) + \delta_2 P_{SACR}(T < T_o) \\ & + (1 - \delta_1) P_{SDEP}(T < T_o) - P_{MLTS}(T > T_o) \\ & + \delta_3 P_{IACR}(T < T_o) - (1 - \delta_4) P_{WACS}(T < T_o), \end{aligned} \tag{1.8f}$$

$$\begin{aligned} S_{qg} =& + (1 - \delta_3) P_{RACI}(T < T_o) + P_{GACI}(T < T_o) \\ & + P_{GACW}(T < T_o) + (1 - \delta_4) P_{SACW}(T < T_o) + P_{GACS} \\ & + (1 - \delta_3) P_{IACR}(T < T_o) + P_{GACR}(T < T_o) \\ & + (1 - \delta_2) P_{RACS}(T < T_o) + P_{GFR}(T < T_o) \\ & + (1 - \delta_4) P_{WACS}(T < T_o) - P_{GMLT}(T > T_o) \\ & + (1 - \delta_1) P_{GDEP}(T < T_o) - P_{MLTG}(T > T_o) \\ & + (1 - \delta_2) P_{SACR}(T < T_o), \end{aligned} \tag{1.8g}$$

and

$$\delta_1 = 1, \text{ only if } q_c + q_i > 10^{-8} g g^{-1}, T < T_o, \tag{1.8h}$$

$$\delta_2 = 1, \text{ only if } q_s + q_r < 10^{-4} g g^{-1}, T < T_o, \tag{1.8i}$$

$$\delta_3 = 1, \text{ only if } q_r > 10^{-4} g g^{-1}, T < T_o, \tag{1.8j}$$

$$\delta_4 = 1, \text{ only if } q_s \le 10^{-4} g g^{-1}, q_c > 5 \times 10^{-4} g g^{-1}, T < T_o. \tag{1.8k}$$

Here, $\pi = (p/p_o)^{\kappa}$, $\kappa = R/c_p$; R is the gas constant; c_p is the specific heat of dry air at constant pressure p, and $p_o = 1{,}000\,\text{mb}$; T is air temperature, and $T_o = 0^{\circ}\text{C}$, $T_{oo} = -35^{\circ}\text{C}$. L_v, L_s, and L_f are latent heat of vaporization, sublimation, and fusion at 0°C, respectively, and $L_s = L_v + L_f$. Q_R is the radiative heating rate due to convergence of the net flux of solar and infrared (IR) radiative fluxes, which will be discussed in section 1.3. The cloud microphysical terms in (1.8b–g) are defined in Table 1.2, which will be discussed in section 1.2. The cloud microphysical processes are also summarized in Fig. 1.1.

When the model is integrated over the ocean, a time-invariant or temporally varied horizontally uniform sea surface temperature (SST) is imposed in both model setups. Li et al. (2000) developed a coupled ocean-cloud-resolving atmosphere model to study the impacts of precipitation and associated salinity stratification in

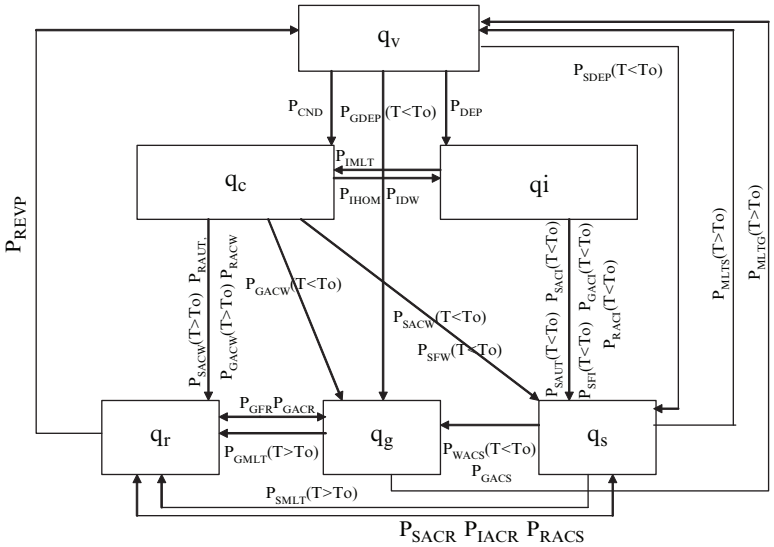

Fig. 1.1 A flowchart of the cloud microphysical schemes

ocean mixed-layer temperature and salinity at small spatial scales. An embedded mixed-layer ocean circulation model was originally developed by Adamec et al. (1981). The mixed-layer equations in the 2D framework are

$$\frac{\partial h_m}{\partial t} = -\frac{\partial u_m h_m}{\partial x} + W_e, \tag{1.9a}$$

$$\frac{\partial u_m}{\partial t} = -\frac{W_e}{h_m}\mathrm{H}(W_e)(u_m - u_e) - \frac{\tau_o}{\rho_r h_m}, \tag{1.9b}$$

$$\frac{\partial T_m}{\partial t} = -\frac{W_e}{h_m}\mathrm{H}(W_e)(T_m - T_e) - \frac{Q_o + I(0) - I(h_m)}{\rho_r c_w h_m}, \tag{1.9c}$$

$$\frac{\partial S_m}{\partial t} = -\frac{W_e}{h_m}\mathrm{H}(W_e)(S_m - S_e) - \frac{S_m(P_s - E_s)}{\rho_r c_w h_m}. \tag{1.9d}$$

Here, T_m, S_m, u_m, and h_m are ocean mixed-layer temperature, salinity, zonal current, and depth respectively; T_e and S_e are temperature and salinity of the level just beneath the mixed layer, respectively; H is the Heavyside step function in which $H = 1$ as $W_e > 0$, while $H = 0$ as $W_e < 0$; ρ_r is a constant reference seawater density; c_w is the heat capacity of water; $I = I_o[re^{-\gamma_1 z} + (1-r)e^{-\gamma_2 z}]$, I_o is solar radiation at the ocean surface; γ_1, γ_2 are attenuation parameters for solar radiation penetration, and z is positive downward with $z = 0$ being the ocean surface; Q_o is the sum of longwave radiation, sensible and latent heat at the ocean surface; P_s and E_s denote the rates of precipitation and evaporation at the ocean surface, respectively; W_e is the entrainment velocity at the mixed-layer base, which can be obtained by calculating Kraus–Turner's equation that was originally derived by Niiler and Kraus (1977), modified by Sui et al. (1997), and is similar to Garper (1988),

$$\begin{aligned} W_e H(W_e) h_m g[\alpha(T_m - T_e) - \beta(S_m - S_e)] \\ = 2m_s {u_*}^3 - \frac{h_m}{2}[(1+m_b)B_o + (1-m_b)|B_o|] \end{aligned} \tag{1.10}$$

$$\begin{aligned} B_o = \frac{g\alpha}{\rho_r c_w}\left\{ Q_o + \left[1 + re^{-\gamma_1 h_m} + (1-r)e^{-\gamma_2 h_m} - \frac{2r}{\gamma_1 h_m}(1 - e^{-\gamma_1 h_m}) \right.\right. \\ \left.\left. - \frac{2(1-r)}{\gamma_2 h_m}(1 - e^{-\gamma_2 h_m}) \right] I_o \right\} + \frac{g}{\rho_r}\beta S_m (P_s - E_s), \end{aligned} \tag{1.10a}$$

where u_* is a surface friction velocity; α and β describe the logarithmic expansion of ocean water density ρ_r as a function of temperature and salinity, respectively; g is the gravitational acceleration; m_s and m_b are turbulent mixing factors due to wind stirring and convection, respectively.

The 2D model equation for ocean circulations on the equator can be written as

$$\frac{\partial u_1}{\partial t} = -\frac{\partial u_1 u_1}{\partial x} - \frac{\partial w_1 u_1}{\partial z} + A_M \frac{\partial^2 u_1}{\partial x^2} + K_M \frac{\partial^2 u_1}{\partial z^2}, \tag{1.11a}$$

$$\frac{\partial T_1}{\partial t} = -\frac{\partial u_1 T_1}{\partial x} - \frac{\partial w_1 T_1}{\partial z} + A_T \frac{\partial^2 T_1}{\partial x^2} + K_T \frac{\partial^2 T_1}{\partial z^2} - \frac{1}{\rho_r c_w}\frac{\partial I}{\partial z}, \tag{1.11b}$$

$$\frac{\partial S_1}{\partial t} = -\frac{\partial u_1 S_1}{\partial x} - \frac{\partial w_1 S_1}{\partial z} + A_S \frac{\partial^2 S_1}{\partial x^2} + K_S \frac{\partial^2 S_1}{\partial z^2}, \tag{1.11c}$$

$$\frac{\partial u_1}{\partial x} + \frac{\partial w_1}{\partial z} = 0, \tag{1.11d}$$

$$\frac{\partial p_1}{\partial z} = -\rho_1 g, \tag{1.11e}$$

$$\rho_1 = \rho_r[1 - \alpha(T_1 - T_r) - \beta(S_1 - S_r)], \tag{1.11f}$$

where u_1 and w_1 are zonal and vertical components of ocean current, respectively; T_1 and S_1 are ocean temperature and salinity, respectively; A_M, A_T, and A_S are horizontal momentum, heat and salinity diffusivity coefficients, respectively; K_M, K_T, and K_S are vertical momentum, heat and salinity diffusivity coefficients, respectively; T_r and S_r are the reference temperature and salinity, respectively. The mixed-layer model and the ocean circulation model communicate with each other through the embedding technique proposed by Adamec et al. (1981). The model also includes a convective adjustment scheme that ensures the static stability of the upper ocean.

1.2 Cloud Microphysical Parameterization Schemes

The formulations of cloud microphysical parameterization schemes are documented in this section. Table 1.2 shows the list of microphysical processes and their parameterization schemes. The schemes are by Rutledge and Hobbs (1983, 1984), Lin et al. (1983), Tao et al. (1989), and Krueger et al. (1995).

Table 1.2 List of microphysical processes and their parameterization schemes. The schemes are Rutledge and Hobbs (1983, 1984; RH83, RH84), Lin et al. (1983, LFO), Tao et al. (1989, TSM), and Krueger et al. (1995, KFLC)

Notation	Description	Scheme
P_{MLTG}	Growth of vapor by evaporation of liquid from graupel surface	RH84
P_{MLTS}	Growth of vapor by evaporation of melting snow	RH83
P_{REVP}	Growth of vapor by evaporation of raindrops	RH83
P_{IMLT}	Growth of cloud water by melting of cloud ice	RH83
P_{CND}	Growth of cloud water by condensation of supersaturated vapor	TSM
P_{GMLT}	Growth of raindrops by melting of graupel	RH84
P_{SMLT}	Growth of raindrops by melting of snow	RH83
P_{RACI}	Growth of raindrops by the accretion of cloud ice	RH84
P_{RACW}	Growth of raindrops by the collection of cloud water	RH83
P_{RACS}	Growth of raindrops by the accretion of snow	RH84
P_{RAUT}	Growth of raindrops by the autoconversion of cloud water	LFO
P_{IDW}	Growth of cloud ice by the deposition of cloud water	KFLC
P_{IACR}	Growth of cloud ice by the accretion of rain	RH84
P_{IHOM}	Growth of cloud ice by the homogeneous freezing of cloud water	
P_{DEP}	Growth of cloud ice by the deposition of supersaturated vapor	TSM
P_{SAUT}	Growth of snow by the conversion of cloud ice	RH83
P_{SACI}	Growth of snow by the collection of cloud ice	RH83
P_{SACW}	Growth of snow by the accretion of cloud water	RH83
P_{SFW}	Growth of snow by the deposition of cloud water	KFLC
P_{SFI}	Depositional growth of snow from cloud ice	KFLC
P_{SACR}	Growth of snow by the accretion of raindrops	LFO
P_{SDEP}	Growth of snow by the deposition of vapor	RH83
P_{GACI}	Growth of graupel by the collection of cloud ice	RH84
P_{GACR}	Growth of graupel by the accretion of raindrops	RH84
P_{GACS}	Growth of graupel by the accretion of snow	RH84
P_{GACW}	Growth of graupel by the accretion of cloud water	RH84
P_{WACS}	Growth of graupel by the riming of snow	RH84
P_{GDEP}	Growth of graupel by the deposition of vapor	RH84
P_{GFR}	Growth of graupel by the freezing of raindrops	LFO

$$P_{MLTG} = \frac{2\pi N_{oG}(S-1)}{\rho(A'+B')}\left[\frac{0.78}{{\lambda_G}^2} + 0.31\left(\frac{\bar{a}\rho}{\mu}\right)^{\frac{1}{2}}\left(\frac{\rho_o}{\rho}\right)^{\frac{1}{4}}\frac{\Gamma\left(\frac{\bar{b}+5}{2}\right)}{{\lambda_G}^{\frac{\bar{b}+5}{2}}}\right], \tag{1.12}$$

where $N_{0G}(=4\times10^6\,\mathrm{m}^{-4})$ is the intercept value in graupel size distribution; $S(=q_w/q_{ws})$, where q_{ws} is the saturated mixing ratio with respect to water; $\bar{a}(=19.3\,\mathrm{m}^{1-\bar{b}}\mathrm{s}^{-1})$ is the constant in fall-speed relation for graupel; $\bar{b}(=0.37)$ is the fall-speed exponent for graupel; $A' = L_v/K_aT\ (L_vM_w/RT-1)$; $B' = RT/\chi M_w e_{ws}$ (Pruppacher and Klett (1978); $K_a(=2.43\times10^{-2}\,\mathrm{J\,m^{-1}\ s^{-1}\ K^{-1}})$ is the thermal conductivity coefficient of air; $M_w(=18.016)$ is the molecular weight of water; $\chi(=2.26\times10^{-5}\,\mathrm{m^2s^{-1}})$ is the diffusivity coefficient of water vapor in air; $R(=8.314\times10^3\,\mathrm{J\,kmol^{-1}\ K^{-1}})$ is the universal gas constant; e_{ws} is the saturation vapor pressure for water; $\lambda_G\left[=(\pi\rho_G N_{0G}/\rho q_g)^{\frac{1}{4}}\right]$ is the slope of graupel size distri-

bution; ρ_G ($=400\,\mathrm{kg\ m^{-3}}$) is the density of graupel; $\mu(=1.718\times10^{-5}\,\mathrm{kg\ m^{-1}\ s^{-1}})$ is the dynamic viscosity of air; Γ is the Gamma function.

$$P_{MLTS}=\frac{4N_{0S}(S-1)}{\rho(A'+B')}\left[\frac{0.65}{{\lambda_S}^2}+0.44\left(\frac{a''\rho}{\mu}\right)^2\left(\frac{\rho_o}{\rho}\right)^{\frac{1}{4}}\frac{\Gamma\left(\frac{b+5}{2}\right)}{{\lambda_S}^{\frac{b+5}{2}}}\right], \tag{1.13}$$

where $N_{0S}(=4\times10^6\,\mathrm{m^{-4}})$ is the intercept value in snowflake size distribution; $a''(=1.139\,\mathrm{m^{1-b}\ s^{-1}})$ is the constant in fall-speed relation for snow; $b(=0.11)$ is the fall-speed exponent for snow; $\lambda_S[=(\pi\rho_S N_{0S}/\rho q_s)^{\frac{1}{4}}]$ is the slope of snowflake size distribution; $\rho_S(=100\,\mathrm{kg\ m^{-3}})$ is the density of snow.

$$P_{REVP}=\frac{2\pi N_{0R}(S-1)}{\rho(A'+B')}\left[\frac{0.78}{{\lambda_R}^2}+0.31\left(\frac{a'\rho}{\mu}\right)^{\frac{1}{2}}\left(\frac{\rho_o}{\rho}\right)^{\frac{1}{4}}\frac{\Gamma(3)}{{\lambda_R}^3}\right], \tag{1.14}$$

where $N_{0R}(=8\times10^6\,\mathrm{m^{-4}})$ is the intercept value in raindrop size distribution; $a'(=3\times10^3\,\mathrm{s^{-1}})$ is the constant in linear fall-speed relation for raindrops; $\lambda_R[=(\pi\rho_L N_{0R}/\rho q_r)^{\frac{1}{4}}]$ is the slope of raindrop size distribution; $\rho_L(=10^3\,\mathrm{kg\ m^{-3}})$ is the density of raindrops.

$$P_{IMLT}=\frac{q_i}{\Delta t}, \tag{1.15}$$

where Δt is the time step.

$$P_{CND}=\frac{1}{\Delta t}\frac{T-T_{oo}}{T_o-T_{oo}}\frac{q_v-(q_{qws}+q_{is})}{1+\left(\frac{A_1q_cq_{ws}+A_2q_iq_{is}}{q_c+q_i}\right)\left(\frac{L_v(T-T_{oo})+L_s(T_o-T)}{c_p(T_o-T_{oo})}\right)}, \tag{1.16}$$

where q_{is} is the saturation mixing ratio with respect to ice; $A_1=237.3B_1/(T-35.86)^2$; $A_2=265.5B_2/(T-7.66)^2$; $B_1=17.2693882$; $B_2=21.8745584$.

$$P_{GMLT}=-\frac{2\pi}{\rho L_f}K_a(T-T_o)N_{0G}\left[\frac{0.78}{{\lambda_G}^2}+0.31\left(\frac{\bar{a}\rho}{\mu}\right)^{\frac{1}{2}}\left(\frac{\rho_o}{\rho}\right)^{\frac{1}{4}}\frac{\Gamma\left(\frac{\bar{b}+5}{2}\right)}{{\lambda_G}^{\frac{\bar{b}+5}{2}}}\right], \tag{1.17}$$

$$P_{SMLT}=-\frac{2\pi}{\rho L_f}K_a(T-T_o)N_{0S}\left[\frac{0.65}{{\lambda_S}^2}+0.44\left(\frac{a''\rho}{\mu}\right)^{\frac{1}{2}}\left(\frac{\rho_o}{\rho}\right)^{\frac{1}{4}}\frac{\Gamma\left(\frac{b+5}{2}\right)}{{\lambda_S}^{\frac{b+5}{2}}}\right], \tag{1.18}$$

$$P_{RACI}=\frac{\pi}{4}q_iE_{RI}N_{0R}\left(\frac{\rho_o}{\rho}\right)^{\frac{1}{2}}\left[\frac{a_o\Gamma(3)}{{\lambda_R}^3}+\frac{a_1\Gamma(4)}{{\lambda_R}^4}+\frac{a_2\Gamma(5)}{{\lambda_R}^5}+\frac{a_3\Gamma(6)}{{\lambda_R}^6}\right], \tag{1.19}$$

where $E_{RI}(=1)$ is the rain/cloud ice collection efficiency coefficient; $a_0=0.267\,\mathrm{m\ s^{-1}}$, $a_1=5.15\times10^3\,\mathrm{s^{-1}}$, $a_2=-1.0225\times10^6\,\mathrm{m^{-1}\ s^{-1}}$, $a_3=7.55\times10^7\,\mathrm{m^{-2}\,s^{-1}}$, which are the coefficients in polynomial fall-speed relation for raindrops.

$$P_{RACIW} = \frac{\pi}{4} q_c E_{RC} N_{0R} \left(\frac{\rho_o}{\rho}\right)^{\frac{1}{2}} \left[\frac{a_o \Gamma(3)}{{\lambda_R}^3} + \frac{a_1 \Gamma(4)}{{\lambda_R}^4} + \frac{a_2 \Gamma(5)}{{\lambda_R}^5} + \frac{a_3 \Gamma(6)}{{\lambda_R}^6}\right], \quad (1.20)$$

where $E_{RC}(=1)$ is the rain/cloud water collection efficiency coefficient.

$$P_{RACS} = E_{SR} \pi^2 \frac{\rho_s}{\rho} |\bar{V}_R - \bar{V}_S| N_{0R} N_{0S} \left(\frac{\rho_o}{\rho}\right)^{\frac{1}{2}} \left[\frac{5}{{\lambda_S}^6 \lambda_R} + \frac{2}{{\lambda_S}^5 {\lambda_R}^2} + \frac{1}{2{\lambda_S}^4 {\lambda_R}^3}\right], \quad (1.21)$$

where $E_{SR}(=1)$ is the snow/rain collection efficiency coefficient;

$$\bar{V}_R = \left(-0.267 + \frac{206}{\lambda_R} - \frac{2.045 \times 10^3}{{\lambda_R}^2} + \frac{9.06 \times 10^3}{{\lambda_R}^3}\right) \left(\frac{\rho_o}{\rho}\right)^{\frac{1}{2}}, \quad (1.21a)$$

$$\bar{V}_S = a'' \frac{\Gamma(4+b)}{6{\lambda_S}^b} \left(\frac{\rho_o}{\rho}\right)^{\frac{1}{2}}, \quad (1.21b)$$

where $\bar{V}_R$ and $\bar{V}_S$ are the mass-weighted fall-speed for rain and snow, respectively.

$$P_{RAUT} = \alpha (q_c - q_o), \quad (1.22)$$

where $\alpha(=10^{-3}\,\mathrm{s}^{-1})$ is the rate coefficient for auto-conversion; $q_o(=1.25 \times 10^{-3}\,\mathrm{g\,g}^{-1})$ is the mixing ratio threshold.

$$P_{IDW} = \frac{n_0 e^{\frac{1}{2}|T-T_o|}}{10^3 \rho} b_1 \left(\frac{\rho q_i}{n_0 e^{\frac{1}{2}|T-T_o|}}\right)^{b_2}, \quad (1.23)$$

where $n_0 = 10^{-8}\,\mathrm{m}^{-3}$; b_1 and b_2 are the positive temperature-dependent coefficients tabulated by Koenig (1971).

$$P_{IACR} = n_{ci} E_{RI} \frac{\pi^2}{24} \frac{\rho_L}{\rho} N_{0R} \left(\frac{\rho_o}{\rho}\right)^{\frac{1}{2}} \left[\frac{a_o \Gamma(6)}{{\lambda_R}^6} + \frac{a_1 \Gamma(7)}{{\lambda_R}^7} + \frac{a_2 \Gamma(8)}{{\lambda_R}^8} + \frac{a_3 \Gamma(9)}{{\lambda_R}^9}\right], \quad (1.24)$$

where $n_{ci}(=\rho q_i / \bar{M}_i)$ is the number concentration of cloud ice crystals; $\bar{M}_i(=6 \times 10^{-12}\,\mathrm{kg})$ is the average mass of a cloud ice particle.

$$P_{IHOM} = \frac{q_c}{\Delta t}, \quad (1.25)$$

$$P_{DEP} = \frac{1}{\Delta t} \frac{T_o - T}{T_o - T_{oo}} \frac{q_v - (q_{qws} + q_{is})}{1 + \left(\frac{A_1 q_c q_{ws} + A_2 q_i q_{is}}{q_c + q_i}\right) \left(\frac{L_v (T - T_{oo}) + L_s (T_o - T)}{c_p (T_o - T_{oo})}\right)}, \quad (1.26)$$

$$P_{SAUT} = \frac{\rho q_i - M_{\max} n_0 e^{0.6(T-T_o)}}{\rho \Delta t}, \quad (1.27)$$

where $M_{\max}(=9.4\times10^{-10}\,\mathrm{kg})$ is the maximum allowed crystal mass.

$$P_{SACI}=\frac{\pi a'' q_i E_{SI} N_{0S}}{4}\left(\frac{\rho_o}{\rho}\right)^{\frac{1}{2}}\frac{\Gamma(b+3)}{{\lambda_S}^{b+3}}, \tag{1.28}$$

where $E_{SI}(=0.1)$ is the snow/cloud ice collection efficiency coefficient.

$$P_{SACW}=\frac{\pi a'' q_c E_{SC} N_{0S}}{4}\left(\frac{\rho_o}{\rho}\right)^{\frac{1}{2}}\frac{\Gamma(b+3)}{{\lambda_S}^{b+3}}, \tag{1.29}$$

where $E_{SC}(=1)$ is the snow/cloud water collection efficiency coefficient.

$$P_{SFW}=\frac{q_i\Delta t}{m_{ir}\Delta t_1}(b_1{m_{ir}}^{b_2}+\pi\rho q_c r^2 U_{ir}), \tag{1.30}$$

where $\Delta t_1[=({m_{ir}}^{1-b_2}-{m_{iro}}^{1-b_2})/b_1(1-b_2)]$ is the timescale needed for a crystal to grow from radius r_o to radius r; $m_{ir}(=3.84\times10^{-9}\,\mathrm{kg})$ and $U_{ir}(1\,\mathrm{m\,s^{-1}})$ are the mass and terminal velocity of an ice crystal $r(=10^2\,\mu\mathrm{m})$; $m_{ir}(=2.46\times10^{-10}\,\mathrm{kg})$ is the mass of an ice crystal $r_o(=40\,\mu\mathrm{m})$.

$$P_{SFI}=\frac{q_i}{\Delta t_1}, \tag{1.31}$$

$$P_{SACR}=E_{SR}\pi^2\frac{\rho_L}{\rho}|\bar{V}_S-\bar{V}_R|N_{0R}N_{0S}\left(\frac{\rho_o}{\rho}\right)^{\frac{1}{2}}\left[\frac{5}{{\lambda_R}^6\lambda_S}+\frac{2}{{\lambda_R}^5{\lambda_S}^2}+\frac{1}{2{\lambda_R}^4{\lambda_S}^3}\right], \tag{1.32}$$

$$P_{SDEP}=\frac{4N_{0S}(S_i-1)}{\rho(A''+B'')}\left[\frac{0.65}{{\lambda_S}^2}+0.44\left(\frac{a''\rho}{\mu}\right)^{\frac{1}{2}}\left(\frac{\rho_o}{\rho}\right)^{\frac{1}{4}}\frac{\Gamma\left(\frac{b+5}{2}\right)}{{\lambda_S}^{\frac{b+5}{2}}}\right], \tag{1.33}$$

where $S_i(=q_v/q_{is})$; $A''=L_v/K_aT(L_sM_w/RT-1)$; $B''=RT/\chi M_w e_{is}$; e_{is} is the saturation vapor pressure for ice.

$$P_{GACI}=\frac{\pi\bar{a}q_i E_{GI} N_{0G}}{4}\left(\frac{\rho_o}{\rho}\right)^{\frac{1}{2}}\frac{\Gamma(\bar{b}+3)}{{\lambda_S}^{\bar{b}+3}}, \tag{1.34}$$

where $E_{GI}(=0.1)$ is the graupel/cloud ice collection efficiency coefficient.

$$P_{GACR}=E_{GR}\pi^2\frac{\rho_L}{\rho}|\bar{V}_G-\bar{V}_R|N_{0R}N_{0G}\left(\frac{\rho_o}{\rho}\right)^{\frac{1}{2}}\left[\frac{5}{{\lambda_R}^6\lambda_G}+\frac{2}{{\lambda_R}^5{\lambda_G}^2}+\frac{1}{2{\lambda_R}^4{\lambda_G}^3}\right], \tag{1.35}$$

where $E_{GR}(=1)$ is the graupel/rain collection efficiency coefficient;

$$\bar{V}_G=\bar{a}\frac{\Gamma(4+\bar{b})}{6{\lambda_G}^{\bar{b}}}\left(\frac{\rho_o}{\rho}\right)^{\frac{1}{2}}, \tag{1.35a}$$

where $\bar{V}_G$ is the mass-weighted fall-speed for graupel.

$$P_{GACS} = E_{GS}\pi^2 \frac{\rho_s}{\rho} |\bar{V}_G - \bar{V}_S| N_{0S} N_{0G} \left(\frac{\rho_o}{\rho}\right)^{\frac{1}{2}} \left[\frac{5}{{\lambda_S}^6 \lambda_G} + \frac{2}{{\lambda_S}^5 {\lambda_G}^2} + \frac{1}{2{\lambda_S}^4 {\lambda_G}^3}\right], \tag{1.36}$$

where $E_{GS}(=0.1)$ is the graupel/snow collection efficiency coefficient.

$$P_{GACW} = \frac{\pi \bar{a} q_c E_{GC} N_{0G}}{4} \left(\frac{\rho_o}{\rho}\right)^{\frac{1}{2}} \frac{\Gamma(\bar{b}+3)}{{\lambda_S}^{\bar{b}+3}}, \tag{1.37}$$

where $E_{GC}(=1)$ is the graupel/cloud water collection efficiency coefficient.

$$P_{WACS} = \bar{n}_c E_{SC} a'' \frac{\pi^2}{24} \frac{\rho_s}{\rho} \left(\frac{\rho_o}{\rho}\right)^{\frac{1}{2}} \frac{\Gamma(b+6)}{{\lambda_S}^{b+6}}, \tag{1.38}$$

where $\bar{n}_c(=\rho q_c/\bar{M}_c)$ is the number concentration of cloud water droplets; $\bar{M}_c(=4\times10^{-12})$ is the average mass of cloud water droplets.

$$P_{GDEP} = \frac{2\pi N_{0G}(\bar{S}_i - 1)}{\rho(A'' + B'')} \left[\frac{0.78}{{\lambda_S}^2} + 0.31 \left(\frac{\bar{a}\rho}{\mu}\right)^{\frac{1}{2}} \left(\frac{\rho_o}{\rho}\right)^{\frac{1}{4}} \frac{\Gamma\left(\frac{\bar{b}+5}{2}\right)}{{\lambda_S}^{\frac{\bar{b}+5}{2}}}\right], \tag{1.39}$$

$$P_{GFR} = 20\pi^2 B_3 N_{0R} \frac{\rho_L}{\rho} \frac{e^{A_3(T_o - T)} - 1}{{\lambda_R}^7}, \tag{1.40}$$

where $A_3(=0.66\,\mathrm{K}^{-1})$ is the constant in Bigg freezing; $B_3(=10^2\,\mathrm{m}^{-3}\,\mathrm{s}^{-1})$ is the constant in the raindrop freezing equation.

1.3 Radiation Parameterization Schemes

The parameterization of solar and IR radiation is based on the model developed by Chou (1992), Chou et al. (1991), and Chou and Suarez (1994). The effective radii (μm) for cloud water (r_{ec}), raindrops (r_{er}), cloud ice and snow (r_{eis}), and graupel (r_{eg}) can be calculated by

$$r_{ec} = 15, \tag{1.41a}$$

$$r_{er} = \frac{3}{\lambda_R}, \tag{1.41b}$$

$$r_{eis} = 125 + 5 \times (T - 243.16) \text{ for } 243.16 \le T \le 223.16, \tag{1.41c}$$

$$r_{eg} = \frac{3}{\lambda_G}. \tag{1.41d}$$

The optical thicknesses for cloud water (τ_c), raindrops (τ_r), cloud ice and snow (τ_{isVIS} in the visible region and τ_{isIR} in the IR window), and graupel (τ_g) can be expressed as

$$\tau_c = \frac{\rho q_c \Delta z}{r_{ec}}, \tag{1.42a}$$

$$\tau_r = \frac{\rho q_r \Delta z}{r_{er}}, \tag{1.42b}$$

$$\tau_{isVIS} = \rho(q_i + q_s)\Delta z \left(-0.006656 + \frac{3.686}{r_{eis}}\right), \tag{1.42c}$$

$$\tau_{isIR} = \rho(q_i + q_s)\Delta z \left(-0.0115 + \frac{4.11}{r_{eis}} + \frac{17.3}{r_{eis}^2}\right), \tag{1.42d}$$

$$\tau_g = \frac{\rho q_g \Delta z}{r_{eg}}. \tag{1.42e}$$

Here, Δz is the thickness of a vertical layer.

The optical thicknesses for the calculations of solar (τ_{SW}) and IR (τ_{IR}) radiation parameterization schemes are

$$\tau_{SW} = \frac{3}{2}(\tau_c + \tau_r) + \tau_{isVIS} + \tau_g, \tag{1.43a}$$

$$\tau_{IR} = \frac{3}{4}(\tau_c + \tau_r) + \tau_{isIR} + \tau_g. \tag{1.43b}$$

Chou and Suarez (1994) broke down the spectrum into eight bands to compute IR fluxes due to water vapor, carbon dioxide, and ozone (see their Table 1). Water vapor line absorption covers the entire IR spectrum (0–3,000 cm^{-1}), whereas water vapor continuum absorption is included in the spectral region of 540–1,380 cm^{-1}. The absorptions due to carbon dioxide and ozone are included in the spectral ranges of 540–800 and 980–1,100 cm^{-1}, respectively. All calculations of IR fluxes are based on k-distribution method with linear pressure scaling, table lookup with temperature and pressure scaling, and one-parameter temperature scaling.

Chou et al. (1998) divided the solar spectrum into an ultraviolet (UV) and visible region (wavelengths are smaller than 0.7 μm) and an IR region (wavelengths are between 0.7 and 10 μm) in the calculations of the solar radiation parameterization. The absorptions due to ozone and aerosols and scattering due to gases, clouds, and aerosols are included in the UV and visible region. The UV and visible region is further divided into eight spectral intervals. Thus, the fluxes in the photosynthetically active radiation (wavelengths are between 0.4 and 0.7 μm), UV-A (wavelengths are between 0.328 and 0.4 μm), UV-B (wavelengths are between 0.28 and 0.328 μm), and UV-C (wavelengths are between 0.18 and 0.28 μm) can be separately computed. The absorptions due to water vapor, oxygen, carbon dioxide, clouds, and aerosols are included in the IR region. The schemes developed by Chou and Lee (1996) were used to calculate the absorptions due to water vapor and ozone, whereas those developed by Chou (1990) were used to compute the absorptions due to oxygen and

carbon dioxide. Chou et al. (1988) calculated the solar radiation fluxes using varied cloud single-scattering properties including the extinction coefficient, single scattering albedo, and asymmetric factor.

1.4 Subgrid-Scale Turbulence Closure

The subgrid-scale turbulence closure developed by Klemp and Wilhelmson (1978) is used in the cloud-resolving model.

$$D_\eta = \frac{\partial}{\partial x}\left(K_m \frac{\partial \eta}{\partial x}\right) + \frac{\partial}{\partial z}\left(K_m \frac{\partial \eta}{\partial z}\right), \tag{1.44a}$$

$$D_\chi = \frac{\partial}{\partial x}\left(K_h \frac{\partial \chi}{\partial x}\right) + \frac{\partial}{\partial z}\left(K_h \frac{\partial \chi}{\partial z}\right), \tag{1.44b}$$

where $\eta = u, w$; $\chi = \theta,\ q_v,\ q_c,\ q_r,\ q_i,\ q_s,\ q_g$; K_m is the momentum eddy mixing coefficient, which can be determined by

$$K_m = c_m E^{\frac{1}{2}} l. \tag{1.45}$$

Here $c_m = 0.2$; $l = \Delta x \Delta z$, Δx and Δz are the zonal and vertical grid intervals, l is the appropriate length scale (Lilly 1967); E is the subgrid-scale kinetic energy, which can be calculated using the following prognostic equation

$$\begin{aligned}\frac{\mathrm{d}E}{\mathrm{d}t} = {} & \overline{\overline{gw''\left(\frac{\theta''}{\bar{\theta}} + 0.61 q_v'' - q_l''\right)}} - \overline{\overline{u''u''}}\frac{\partial u}{\partial x} - \overline{\overline{u''w''}}\left(\frac{\partial u}{\partial z} + \frac{\partial w}{\partial x}\right) \\ & - \overline{\overline{w''w''}}\frac{\partial w}{\partial z} + \frac{\partial}{\partial x}\left(K_m \frac{\partial E}{\partial x}\right) + \frac{\partial}{\partial z}\left(K_m \frac{\partial E}{\partial z}\right) - \left(\frac{c_e}{l}\right) E^{\frac{3}{2}}\end{aligned} \tag{1.46}$$

where the double overbar denotes an average over each grid point in the cloud model and the double-primed variables are the deviation from the grid values; $c_e = 0.7$; and

$$\overline{\overline{u''u''}} = -2K_m \frac{\partial u}{\partial x} + \frac{2}{3}E, \tag{1.46a}$$

$$\overline{\overline{u''w''}} = -K_m\left(\frac{\partial u}{\partial z} + \frac{\partial w}{\partial x}\right), \tag{1.46b}$$

$$\overline{\overline{w''w''}} = -2K_m \frac{\partial w}{\partial z} + \frac{2}{3}E. \tag{1.46c}$$

(1.46) is similar to the equation used by Deardorff (1975), Mellor and Yamada (1974), and Schemm and Lipps (1976).

In a saturated area,

$$\overline{\overline{w''\left(\frac{\theta''}{\bar{\theta}}+0.61q_v''-q_l''\right)}}=K_h\left(-\frac{1}{\bar{\theta}}\frac{1+\frac{1.61\varepsilon Lq_v}{R_dT}}{\frac{\varepsilon L^2q_v}{c_pR_dT^2}}\frac{\partial\theta_e}{\partial z}+\frac{\partial q_l}{\partial z}\right) \tag{1.47a}$$

and $\varepsilon = 0.622$.

In an unsaturated area,

$$\overline{\overline{w''\left(\frac{\theta''}{\bar{\theta}}+0.61q_v''-q_l''\right)}}=-K_h\left(-\frac{1}{\bar{\theta}}\frac{\partial\theta}{\partial z}+0.61\frac{\partial q_v}{\partial z}\right). \tag{1.47b}$$

Here, $K_h = 3K_m$ (Deardorff 1975).

1.5 Boundary Conditions and Basic Parameters

Lateral boundaries are cyclic. A free-slip condition is applied to the upper boundary, which allows no advection or diffusion of any quantity. The sensible heat flux from ocean surface is expressed by

$$(\overline{\overline{w''\theta''}})_{z=0}=-\frac{C_Du_s(T_m-T_s)}{\pi}. \tag{1.48}$$

Here u_s and T_s are atmospheric zonal wind and temperature at ocean surface; C_D is the drag coefficient, which is given by Roll (1965) as

$$C_D=(1.1+0.04u_s)\times10^{-3}, \tag{1.48a}$$

where u_s is larger than 4 m s^{-1}. The moisture flux from ocean surface is written as

$$(\overline{\overline{w''q_v''}})_{z=0}=-C_Du_s(q_{ms}-q_s), \tag{1.49}$$

where q_{ms} is the saturation mixing ratio at *SST* or mixed-layer temperature; q_s is the atmospheric mixing ratio at ocean surface.

A Rayleigh relaxation (RL) term is imposed above 15 km with the form

$$\mathrm{RL}=\frac{z-15}{1000}. \tag{1.50}$$

Here z is in units of kilometers.

Following Anthes (1970) and Wilhelmson and Chen (1982), a stretched grid is used in vertical coordinate. The grid is obtained by mapping the physical coordinate (z) onto the map coordinate (z'):

$$z=(c_1+c_2z')z', \tag{1.51}$$

where c_1 and c_2 are 10 and 0.01 cm^{-1}. A constant grid interval $\Delta z'$ (34 cm) is used in $z'_I = I\Delta z'$, I is the number of vertical level. The mapping factor M is defined by

$$M \equiv \frac{\partial z'}{\partial z} = \frac{1}{c_1 + 2c_2 z'}. \tag{1.52}$$

The vertical derivative of any function F in z coordinate $(\partial F/\partial z)$ can be transformed into z' coordinate by

$$\frac{\partial F}{\partial z} = M\frac{\partial F}{\partial z'}. \tag{1.53}$$

The vertical grid resolution ranges from about 200 m near the surface to about 1 km near 100 mb. The top model level is 42 mb. The time step is 12 s. The typical horizontal domain is 768 km with a horizontal grid resolution of 1.5 km.

References

Adamec D, Elsberry RL, Garwood RW, Haney RL (1981) An embedded mixed-layer-ocean circulation model. Dyn Atmos Oceans 6(2):69–96

Anthes RA (1970) Numerical experiments with a two-dimensional horizontal variable grid. Mon Wea Rev 98:810–822

Brown P, Swann H (1997) Evaluation of key microphysical parameters in three-dimensional cloud model simulations using aircraft and multiparameter radar data. Quart J Roy Meteor Soc 123:2245–2275

Chen C, Cotton WR (1983) A one-dimensional simulation of the stratocumulus-capped mixed layer. Bound Layer Meteor 25:289–321

Chao J (1962) On the nonlinear impacts of stratification and wind on development of small-scale disturbances. Acta Meteor Sinica 32:164–176

Chou MD (1984) Broadband water vapor transmission functions for atmospheric IR flux computation. J Atmos Sci 41:1775–1778

Chou MD (1986) Atmospheric solar heating rate in the water vapor bands. J Climate Appl Meteor 25:1532–1542

Chou MD (1990) Parameterization for the absorption of solar radiation by O_2 and CO_2 with application to climate studies. J Climate 3:209–217

Chou MD (1992) A solar radiation model for use in climate studies. J Atmos Sci 49:762–772

Chou MD, Kouvaris L (1991) Calculations of transmission functions in the IR CO_2 and O_3 Band. J Geophys Res 96:9003–9012

Chou MD, Suarez MJ (1994) An efficient thermal infrared radiation parameterization for use in General Circulation Model. NASA Technical Memorandum 104606, 3

Chou MD, Lee KT (1996) Parameterization for the absorption of solar radiation by water vapor and ozone. J Atmos Sci 53:1203–1208

Chou MD, Kratz DP, Ridgway W (1991) IR radiation parameterization in numerical climate studies. J Climate 4:424–437

Chou MD, Suarez MJ, Ho CH, Yan MMH, Lee KT (1998) Parameterizations for cloud overlapping and shortwave single-scattering properties for use in General Circulation and Cloud Ensemble Models. J Climate 11:202–214

Clark TL (1977) A small-scale dynamic model using a terrain following coordinate transformation. J Comput Phys 24:186–215

Clark TL (1979) Numerical simulations with a three-dimension cloud model: Lateral boundary condition experiments and multicellular severe storm simulations. J Atmos Sci 36:2191–2215

Clark TL, Hall WD (1991) Multi-domain simulations of the time dependent Navier-Stokes equations: Benchmark error analysis of some nesting procedures. J Comput Phys 92:456–481

Clark TL, Hall WD, Coen JL (1996) Source code documentation for the Clark-Hall cloud-scale model: Code version G3CH01. NCAR Tech. Note NCAR/TN-426 + STR, 137pp. [Available from NCAR Information Service, P. O. Box 3000, Boulder, CO 80307.]

Deardorff JW (1972) Numerical investigation of neutral and unstable planetary boundary layers. J Atmos Sci 29:91–115

Deardorff JW (1975) The development of boundary-layer turbulence models for use in studying the severe storm environment. Proceedings of the SESAME Opening Meeting, Boulder, NOAA-ERL, 251–264

Edwards JM, Slingo A (1996) Studies with a flexible new radiation code. I: Choosing a configuration for a large-scale model. Quart J Roy Meteor Soc 122:689–719

Ferrier BS (1994) A double-moment multiple-phase four-class bulk ice scheme. Part I: Description. J Atmos Sci 51:249–280

Ferrier BS, Tao WK, Simpson J (1995) A double-moment multiple-phase four-class bulk ice scheme. Part II: Simulations of convective storms in different large-scale environments and comparisons with other bulk parameterizations. J Atmos Sci 52:1001–1033

Flatau P, Tripoli GJ, Verlinde J, Cotton WR (1989) The CSU RAMS cloud microphysics module: General theory and code documentation, Technical Report 451, Colorado State University, Fort Collins, CO, USA

Garper Ph (1988) Modeling the seasonal cycle of the upper ocean. J Phys Oceanogr 18:161–180

Grabowski WW (1998) Toward cloud resolving modeling of large-scale tropical circulations: A simple cloud microphysics parameterization. J Atmos Sci 55:3283–3298

Grabowski WW, Wu X, Moncrieff MW (1996) Cloud-resolving model of tropical cloud systems during Phase III of GATE. Part I: Two-dimensional experiments. J Atmos Sci 53:3684–3709

Harshvardhan, Davies R, Randall DA, Corsetti TG (1987) A fast radiation parameterization for general circulation models. J Geophys Res 92:1009–1016

Hu Z, He G (1988) Numerical simulation of microphysical processes in cumulonimbus. Part I: Microphysical model. Acta Meteor Sinica 2:471–488

Hu Z, Lou X, Bao S, Wang X (1998) A simplified explicit scheme of mixed phase cloud and precipitation. Quart J Appl Meteor 9:257–264

Kessler E (1969) On the distribution and continuity of water substance in atmospheric circulations. Meteor Monogr 32, Amer Meteor Soc, Boston, MA

Kiehl JT, Hack JJ, Briegleb BP (1994) The simulated Earth radiation budget of the National Center for Atmospheric Research community climate model CCM2 and comparisons with the Earth Radiation Budget Experiment (ERBE). J Geophys Res 99:20815–20827

Klemp JB, Wilhelmson RB (1978) The simulation of three-dimensional convective storm dynamics. J Atmos Sci 35:1070–1093

Koenig LR, Murray FW (1976) Ice-bearing cumulus cloud evolution: Numerical simulation and general comparison against observations. J Appl Meteor 15:747–762

Krueger SK (1988) Numerical simulation of tropical cumulus clouds and their interaction with the subcloud layer. J Atmos Sci 45:2221–2250

Krueger SK, Fu Q, Liou KN, Chin HNS (1995) Improvement of an ice-phase microphysics parameterization for use in numerical simulations of tropical convection. J Appl Meteor 34:281–287

Li X, Sui CH, Lau KM, Chou MD (1999) Large-scale forcing and cloud-radiation interaction in the tropical deep convective regime. J Atmos Sci 56:3028–3042

Li X, Sui CH, Lau KM, Adamec D (2000) Effects of precipitation on ocean mixed-layer temperature and salinity as simulated in a 2-D coupled ocean-cloud resolving atmosphere model. J Meteor Soc Japan 78:647–659

Lilly DK (1962) On the numerical simulation of buoyant convection. Tellus 14:148–172

Lilly DK (1967) The representation of small-scale turbulence in numerical simulation experiment. Proc IBM Sci Comput Symp Environmental Sciences, White Plains, NY

Lin YL, Farley RD, Orville HD (1983) Bulk parameterization of the snow field in a cloud model. J Climate Appl Meteor 22:1065–1092

Lipps FB, Hemler RS (1986) Numerical simulation of deep tropical convection associated with large-scale convergence. J Atmos Sci 43:1796–1816
Lipps FB, Hemler RS (1988) Numerical modeling of a line of towering cumulus on day 226 of GATE. J Atmos Sci 45:2428–2444
Lipps FB, Hemler RS (1991) Numerical modeling of a midlatitude squall line: Features of the convection and vertical momentum fluxes. J Atmos Sci 48:1909–1929
Lord SJ, Willoughby HE, Piotrowicz JM (1984) Role of a parameterized ice phase microphysics in an axisymmetric, nonhydrostatic tropical cyclone model. J Atmos Sci 41:2836–2848
Mellor GL, Yamada T (1974) A hierarchy of turbulence closure models for planetary boundary layers. J Atmos Sci 31:1791–1806
Nakajima K, Matsuno T (1988) Numerical experiments concerning the origin of cloud clusters in the tropical atmosphere. J Meteor Soc Japan 66:309–329
Nakajima T, Tsukamoto M, Tsushima Y, Numaguti A, Kimura T (2000) Modeling of the radiative process in an atmospheric general circulation model. Appl Opt 39:4869–4878
Niiler PP, Kraus EB (1977) One-dimensional models. In: Kraus EB (ed) Modeling and Prediction of the Upper Layers of the Ocean. Pergamon, New York
Ogura Y, Philips NA (1962) Scale analysis of deep and shallow convection in the atmosphere. J Atmos Sci 19:173–179
Petch JC (1998) Improved radiative transfer calculations from information provided by bulk microphysical schemes. J Atmos Sci 55:1846–1858
Pruppacher HR, Klett JO (1978) Microphysics of Clouds and Precipitation. Reidel, Dordrecht, The Netherlands
Redelsperger JL, Sommeria G (1981a) Methode de representation de la turbulence d'echelle inferieure a la maille pour un medele tri-dimensional de convection nuageuse. Bound Layer Meteor 21:509–530
Redelsperger JL, Sommeria G (1981b) Three-dimensional simulations of a convective storm: Sensitivity studies on subgrid parameterization and spatial resolution. J Atmos Sci 43:2619–2635
Redelsperger JL, Sommeria G (1982) Methode de representation de la turbulence associee aux precipitations dans un modele tri-dimensional de convection nuageuse. Bound Layer Meteor 24:231–252
Redelsperger JL, Sommeria G (1986) Three-dimensional simulation of a convective strom: Sensitivity studies on subgrid parameterization and spatial resolution. J Atmos Sci 43:2619–2635
Roll HU (1965) Physics of the Marine Atmosphere. Academic Press, New York
Rutledge SA, Hobbs RV (1983) The mesoscale and microscale structure and organization of clouds and precipitation in midlatitude cyclones. Part VIII: A model for the "seeder-feeder" process in warm-frontal rainbands. J Atmos Sci 40:1185–1206
Rutledge SA, Hobbs RV (1984) The mesoscale and microscale structure and organization of clouds and precipitation in midlatitude cyclones. Part XII: A diagnostic modeling study of precipitation development in narrow cold-frontal rainbands. J Atmos Sci 41:2949–2972
Satoh M, Tomita H, Miura H, Iga S, Nasumo T (2005) Development of a global resolving model – a multi-scale structure of tropical convections. J Earth Sim 3:1–9
Schemm CE, Lipps FB (1976) Some results from a simplified three-dimensional numerical model of atmospheric turbulence. J Atmos Sci 33:1021–1041
Shutts GJ, Gray MEB (1994) A numerical modeling study of the geostrophic adjustment following deep convection. Quart J Roy Meteor Soc 120:1145–1178
Smagorinsky J (1963) General circulation experiments with the primitive equations: I. The basic experiment. Mon Wea Rev 91:99–164
Sommeria G (1976) Three-dimensional simulation of turbulent process in an undisturbed trade wind boundary layer. J Atmos Sci 33:216–241
Soong ST, Ogura Y (1980) Response of tradewind cumuli to large-scale processes. J Atmos Sci 37:2035–2050
Soong ST, Tao WK (1980) Response of deep tropical cumulus clouds to mesoscale processes. J Atmos Sci 37:2016–2034

Sui CH, Lau KM, Tao WK, Simpson J (1994) The tropical water and energy cycles in a cumulus ensemble model. Part I: Equilibrium climate. J Atmos Sci 51:711–728

Sui CH, Li X, Lau KM, Adamec D (1997) Multi-scale air-sea interactions during TOGA COARE. Mon Wea Rev 125:448–462

Sui CH, Li X, Lau KM (1998) Radiative-convective processes in simulated diurnal variations of tropical oceanic convection. J Atmos Sci 55:2345–2359

Swann H (1994) Cloud microphysical processes – a description of the parameterization used in the Large Eddy Model. UK Meteorological Office, JCMM Internal Report 10, Bracknell

Tao WK, Simpson J (1993) The Goddard Cumulus Ensemble model. Part I: Model description. Terr Atmos Oceanic Sci 4:35–72

Tao WK, Simpson J, McCumber M (1989) An ice-water saturation adjustment. Mon Wea Rev 117:231–235

Tompkins AM, Craig GC (1998) Radiative-convective equilibrium in a three-dimensional cloud-ensemble model. Quart J Roy Meteor Soc 124:2073–2097

Tripoli GJ (1992) A nonhydrostatic mesoscale model designed to simulate scale interaction. Mon Wea Rev 120:1342–1359

Wilhelmson RB, Chen CS (1982) A simulation of the development of successive cells along a cold outflow boundary. J Atmos Sci 39:1466–1483

Wu X, Grabowski WW, Moncrieff MW (1998) Long-term evolution of cloud systems in TOGA COARE and their interactions with radiative and surface processes. Part I: Two-dimensional cloud-resolving model. J Atmos Sci 55:2693–2714

Xu H (1992) A meso-β modeling study. Comput Phys 9:731–734

Xu H, Duan Y (1999) Some issues associated with growth of cloud concentration numbers. Acta Meteor Sinica 57:450–460

Xu H, Huang S (1994) A three-dimensional meso-β modeling study: A numerical simulation of mesoscale structures associated with frontogenesis over the warm sector of a cyclone. Acta Meteor Sinica 52:165–171

Yamasaki M (1975) A numerical experiment of the interaction between cumulus convection and large-scale motion. Papers Meteor Geophys 26:63–91

Zou G (1991) Three-dimensional convective cloud model. Chinese Academy of Meteorological Sciences, Beijing, China

Chapter 2
Analysis Methodology

To examine dominant physical processes associated with the development of convective systems, the simulation data can be analyzed in terms of heat, vapor, and cloud budgets, surface rainfall budget, and energy budget. These budgets in the 2D framework are summarized in this chapter. Convective and stratiform clouds could have different thermodynamic, microphysical, radiative, and rainfall properties. Convective–stratiform cloud partitioning analysis is an important part of the modeling study towards better understanding of clouds and associated microphysics and thermodynamics and their impacts on tropical hydrological and energy cycles, which is discussed in this chapter.

2.1 Heat and Vapor Budgets

Li et al. (1999) derived zonal-mean heat and vapor budgets and zonal- and mass-weighted mean heat budget, and zonal-mean precipitable water (PW) budget. For a zonal-mean heat budget, multiplying (1.7d) by π and averaging the resulting equation zonally yields

$$\frac{\partial \bar{T}}{\partial t} = \frac{\bar{Q}_{cn}}{c_p} + \frac{\bar{Q}_R}{c_p} - \frac{\pi}{\bar{\rho}} \frac{\partial (\bar{\rho} \overline{w'\theta'})}{\partial z} - \pi \bar{w}^o \frac{\partial \bar{\theta}}{\partial z} - \bar{u}^o \frac{\partial \bar{T}^o}{\partial x}. \tag{2.1a}$$

Thus, the local change of zonal-mean temperature is contributed to by condensational heating, radiative heating, convergence of vertical heat flux, vertical temperature advection, and imposed horizontal temperature advection. A zonal-mean mass-weighted heat budget can be derived by multiplying (2.1a) by $\bar{\rho}$ and integrating the resulting equation vertically, and dividing it by the mass of the air column,

$$\frac{\partial \langle \bar{T} \rangle}{\partial t} = \frac{\langle \bar{Q}_{cn} \rangle}{c_p} + \frac{\langle \bar{Q}_R \rangle}{c_p} + \bar{H}_s - \left\langle \pi \bar{w}^o \frac{\partial \bar{\theta}}{\partial z} \right\rangle - \left\langle \bar{u}^o \frac{\partial \bar{T}^o}{\partial x} \right\rangle. \tag{2.1b}$$

Here, $\langle \mathrm{F} \rangle = \int_0^{z_t} \bar{\rho}\ F \mathrm{d}z / \int_0^{z_t} \bar{\rho}\, \mathrm{d}z$, F is a variable, and z_t is the model top; $\bar{H}_s$ is the surface sensible heat flux. In the zonal-mean mass-weighted heat budget, the local temperature change is determined by condensational heating, radiative heating, surface sensible heat flux, vertical temperature advection, and imposed horizontal temperature advection.

For a zonal-mean vapor budget, averaging (1.7e) zonally leads to

$$\frac{\partial \bar{q}_v}{\partial t} = -\bar{S}_{qv} - \frac{1}{\bar{\rho}} \frac{\partial (\bar{\rho} \overline{w' q_v'})}{\partial z} - \bar{w}^o \frac{\partial \bar{q}_v}{\partial z} - \bar{u}^o \frac{\partial \bar{q}_v^o}{\partial x}. \tag{2.2a}$$

Thus, the local change of zonal-mean water vapor is contributed to by net condensation, convergence of vertical moisture flux, vertical moisture advection, and imposed horizontal moisture advection. A zonal-mean *PW* budget is derived by multiplying (2.2a) by $\bar{\rho}$ and integrating the resulting equation vertically,

$$\frac{\partial [\bar{q}_v]}{\partial t} = -[\bar{S}_{qv}] - \bar{E}_s - \left[\bar{w}^o \frac{\partial \bar{q}_v}{\partial z} \right] - \left[\bar{u}^o \frac{\partial \bar{q}_v^o}{\partial x} \right]. \tag{2.2b}$$

Here, [F] $(= \int_0^{z_t} \bar{\rho} F\, dz)$ is a mass integration; $\bar{E}_s$ is the surface evaporation flux, and $[\bar{q}_v]$ is PW. In the zonal-mean *PW* budget, the local *PW* change is determined by net condensation, surface evaporation flux, vertical moisture advection, and imposed horizontal moisture advection.

2.2 Surface Rainfall Equation

Gao et al. (2005) derived the surface rainfall equation to study the role of water vapor and cloud source/sink in the surface rainfall processes. The equations of cloud hydrometeors (1.7f–j) are added to yield

$$\frac{\partial q_l}{\partial t} = -\frac{\partial (u q_l)}{\partial x} - \frac{1}{\bar{\rho}} \frac{\partial}{\partial z} \bar{\rho} w q_l + \frac{1}{\bar{\rho}} \frac{\partial}{\partial z} \bar{\rho} (w_{Tr} q_r + w_{Ts} q_s + w_{Tg} q_g) - S_{qv}, \tag{2.3}$$

where $q_l = q_c + q_r + q_i + q_s + q_g$. The equation of cloud hydrometeors (2.3) and the equation of water vapor (1.7e) are added to eliminate S_{qv} and then are mass-integrated to derive a surface rainfall equation (P_s),

$$P_s = Q_{WV} + Q_{CM}, \tag{2.4}$$

where

$$P_s = \bar{\rho} (w_{Tr} q_r + w_{Ts} q_s + w_{Tg} q_g), \tag{2.4a}$$

$$Q_{WV} = Q_{WVT} + Q_{WVF} + Q_{WVE}, \tag{2.4b}$$

$$Q_{WVT} = -\frac{\partial [q_v]}{\partial t}, \tag{2.4c}$$

$$Q_{WVF} = -\left[\bar{u}^o \frac{\partial \bar{q}_v^o}{\partial x}\right] - \left[\bar{w}^o \frac{\partial \bar{q}_v}{\partial z}\right] - \left[\frac{\partial (u' q_v')}{\partial x}\right] - \left[\bar{u}^o \frac{\partial q_v{}'}{\partial x}\right] - \left[\bar{w}^o \frac{\partial q_v{}'}{\partial z}\right] - \left[w' \frac{\partial \bar{q}_v}{\partial z}\right], \tag{2.4d}$$

$$Q_{WVE} = E_s, \tag{2.4e}$$

$$Q_{CM} = -\frac{\partial [q_l]}{\partial t} - \left[u \frac{\partial q_l}{\partial x}\right] - \left[w \frac{\partial\, q_l}{\partial\, z}\right]. \tag{2.4f}$$

In tropics, $P_s = \bar{\rho}(w_{Tr} q_r)$. Equation (2.4) indicates that the surface rain rate can be calculated if the wind, specific humidity, and cloud mixing ratios are known. Surface rain rate is contributed to by the local vapor change (Q_{WVT}), vapor convergence (Q_{WVF}), surface evaporation (Q_{WVE}), and cloud source/sink (Q_{CM}). Positive values of Q_{WVT}, Q_{WVF}, and Q_{CM} denote local vapor loss (atmospheric drying), vapor convergence, and local hydrometeor loss/hydrometeor convergence, respectively, whereas negative Q_{WVT}, Q_{WVF}, and Q_{CM} denote local vapor gain (atmospheric moistening), vapor divergence, and local hydrometeor gain/hydrometeor divergence, respectively.

In zonal-mean surface rainfall equation,

$$\bar{P}_s = \bar{Q}_{WVT} + \bar{Q}_{WVF} + \bar{Q}_{WVE} + \bar{Q}_{CM}, \tag{2.5}$$

$$\bar{Q}_{WVT} = -\frac{\partial [\bar{q}_v]}{\partial t}, \tag{2.5a}$$

$$\bar{Q}_{WVF} = -\left[\bar{u}^o \frac{\partial \bar{q}_v{}^o}{\partial x}\right] - \left[\bar{w}^o \frac{\partial \bar{q}_v}{\partial z}\right], \tag{2.5b}$$

$$\bar{Q}_{WVE} = \bar{E}_s, \tag{2.5c}$$

$$\bar{Q}_{CM} = -\frac{\partial [\bar{q}_l]}{\partial t}. \tag{2.5d}$$

Note that in (2.5d) the convergence of cloud hydrometeors is zero due to cyclic lateral boundary conditions. Thus, positive value of zonal-mean $\bar{Q}_{CM}$ denotes local hydrometeor loss, whereas negative value is local hydrometeor gain.

2.3 Energetics Equations in Moist Atmosphere and Convective Available Potential Energy

Lorenz (1955) first introduced the concept of available potential energy for a dry atmosphere that represents the portion of the potential energy that can be transferred into kinetic energy. He defined the available potential energy for a dry atmosphere

as the difference between the actual total enthalpy and the minimum total enthalpy that could be achieved by rearranging the mass under an adiabatic flow. The dry enthalpy per unit mass is defined as the product of the temperature and the specific heat at constant pressure. In the absence of energy sources and sinks, the total kinetic energy and total enthalpy are conserved during adiabatic expansion. In a moist atmosphere, latent heat energy should be included in the energy conservation. The latent heat energy per unit mass is defined as the product of the specific humidity and the latent heat of vaporization at 0°C. In the absence of energy sources and sinks, the total kinetic energy, enthalpy, and latent heat energy are conserved during dry and subsequent saturated adiabatic expansion. Therefore, the moist available potential energy is defined as the difference between the actual moist potential energy (sum of the enthalpy and latent heat energy) and the minimum moist potential energy that could be achieved by rearranging the mass under moist adiabatic processes. Li et al. (2002a) derived a set of equations for conversions between the moist available potential energy and kinetic energy in a Eulerian framework.

Zonal-mean and perturbation moist available potential energy ($\bar{P}$, P') and perturbation kinetic energy (K') are, respectively, defined by

$$\bar{P} = \left[\frac{\Lambda}{2c_p}(\bar{h}^2 - {h_b}^2)\right], \tag{2.6a}$$

$$P' = \left[\frac{\Lambda}{2c_p}\overline{(h')^2}\right], \tag{2.6b}$$

$$K' = \left[\frac{\overline{(u')^2 + (w')^2}}{2}\right], \tag{2.6c}$$

where

$$h = c_p T + L_v q_v, \tag{2.6d}$$

$$\Lambda = -\frac{R\theta}{c_p p T}\frac{1}{\dfrac{\partial \theta_b}{\partial p} + \dfrac{L_v}{c_p \pi}\dfrac{\partial q_{vb}}{\partial p}}, \tag{2.6e}$$

h_b is a constant reference state, and is calculated from the initial observed sounding.

The equation of h is derived by multiplying (1.7d) by $c_p\pi$ and (1.7e) by L_v and adding the resulting equations,

$$\begin{aligned}\frac{\partial h}{\partial t} = &-\frac{\partial (u'h')}{\partial x} - \bar{u}^o\frac{\partial h'}{\partial x} - \frac{c_p\pi}{\bar{\rho}}\frac{\partial}{\partial z}\bar{\rho}w'\theta' - c_p\pi\bar{w}^o\frac{\partial \theta'}{\partial z} - c_p\pi w'\frac{\partial \bar{\theta}}{\partial z}\\ &-\frac{L_v}{\bar{\rho}}\frac{\partial}{\partial z}\bar{\rho}w'{q_v}' - L_v\bar{w}^o\frac{\partial {q_v}'}{\partial z} - L_v w'\frac{\partial \bar{q}_v}{\partial z} + L_f P_{18} + Q_R - \bar{u}^o\frac{\partial \bar{h}^o}{\partial x},\\ &-c_p\pi\bar{w}^o\frac{\partial \bar{\theta}}{\partial z} - L_v\bar{w}^o\frac{\partial \bar{q}_v}{\partial z}\end{aligned} \tag{2.7}$$

where

$$\begin{aligned} P_{18} = & P_{DEP} + (1-\delta_1)P_{SDEP}(T<T_o) + (1-\delta_1)P_{GDEP}(T<T_o) \\ & - P_{MLTS}(T>T_o) - P_{MLTG}(T>T_o) + P_{SACW}(T<T_o) \\ & + P_{SFW}(T<T_o) + P_{GACW}(T<T_o) + P_{IACR}(T<T_o) \\ & + P_{GACR}(T<T_o) + P_{SACR}(T<T_o) + P_{GFR}(T<T_o) \\ & - P_{RACS}(T>T_o) - P_{SMLT}(T>T_o) - P_{GMLT}(T>T_o) \\ & + P_{IHOM}(T<T_{oo}) - P_{IMLT}(T>T_o) \\ & + P_{IDW}(T_{oo}<T<T_o). \end{aligned} \tag{2.7a}$$

The equations for $\bar{P}$ and P' can be derived by multiplying (2.7) by $\Lambda(\bar{h}-h_b)/c_p$ and $\Lambda h'/c_p$, and applying the zonal mean and vertical integration on the resulting equations.

$$\frac{\partial \bar{P}}{\partial t} = C(P',\bar{P}) + G_R(\bar{P}) + G_{cn}(\bar{P}) + C_h(\bar{K},\bar{P}) + C_v(\bar{K},\bar{P}), \tag{2.8}$$

where

$$C(P',\bar{P}) = -\left[\frac{\Lambda}{c_p}(\bar{h}-h_b)\left(\frac{c_p\pi}{\bar{\rho}}\frac{\partial}{\partial z}\bar{\rho}\overline{w'\theta'} + \frac{L_v}{\bar{\rho}}\frac{\partial}{\partial z}\bar{\rho}\overline{w'q_v'}\right)\right], \tag{2.8a}$$

$$G_R(\bar{P}) = \left[\frac{\Lambda}{c_p}\bar{Q}_R(\bar{h}-h_b)\right], \tag{2.8b}$$

$$G_{cn}(\bar{P}) = \left[\frac{\Lambda L_f}{c_p}\bar{P}_{18}(\bar{h}-h_b)\right], \tag{2.8c}$$

$$C_h(\bar{K},\bar{P}) = -\left[\frac{\Lambda}{c_p}(\bar{h}-h_b)\bar{u}^o\left(c_p\pi\frac{\partial\bar{\theta}^o}{\partial x} + L_v\frac{\partial\bar{q}_v^o}{\partial x}\right)\right], \tag{2.8d}$$

$$C_h(\bar{K},\bar{P}) = -\left[\frac{\Lambda}{c_p}(\bar{h}-h_b)\bar{w}^o\left(c_p\pi\frac{\partial\bar{\theta}}{\partial z} + L_v\frac{\partial\bar{q}_v}{\partial z}\right)\right]. \tag{2.8e}$$

Here, $C(P',\bar{P})$ is the conversion between P' and $\bar{P}$ through covariance between $\bar{h}-h_b$ and convergence of vertical flux of potential temperature and moisture. $G_R(\bar{P})$ and $G_{cn}(\bar{P})$ are the generation terms of $\bar{P}$ through covariances between $\bar{h}-h_b$ and horizontal-mean radiative heating, and between $\bar{h}-h_b$ and horizontal-mean heating due to phase change of the cloud contents, respectively. $C_h(\bar{K},\bar{P})$ and $C_v(\bar{K},\bar{P})$ are the conversion between $\bar{K}$ and $\bar{P}$ through covariances between $\bar{h}-h_b$ and imposed horizontal temperature and moisture advections, and between $\bar{h}-h_b$ and the horizontal-mean vertical temperature and moisture advections by imposed vertical velocity, respectively.

$$\frac{\partial P'}{\partial t} = -C(P',\bar{P}) - C(P',K') + G_R(P') + G_{cn}(P') + G(P'), \tag{2.9}$$

where

$$C(P',K') = \left[g\frac{\overline{w'T'}}{T_b} \right], \tag{2.9a}$$

$$G_R(P') = \left[\frac{\Lambda}{c_p}\overline{Q_R h'} \right], \tag{2.9b}$$

$$G_{cn}(P') = \left[\frac{\Lambda}{c_p}\overline{P_{18} h'} \right], \tag{2.9c}$$

$$\begin{aligned} G(P') = &- \left[\frac{gL_v}{c_p T_b}\overline{w'q_v'} \right] - \left[\frac{\Lambda}{c_p\bar{\rho}}\frac{\partial}{\partial z}(\bar{h}-h_b)\bar{\rho}\overline{h'w'} \right] - \left[\frac{g\Lambda}{c_p T_b}\left(\frac{\bar{T}}{T_b} - 1 \right)\overline{h'w'} \right] \\ &- \left[\frac{g\Lambda}{c_p T_b}(\bar{h}-h_b)\overline{w'T'} \right] - \left[\frac{\Lambda}{2c_p\bar{\rho}}\frac{\partial}{\partial z}\bar{\rho}\overline{(h')^2(\bar{w}^o + w')} \right] \\ &- \left[\frac{g\Lambda}{c_p T_b}\overline{h'T'(\bar{w}^o + w')} \right]. \end{aligned} \tag{2.9d}$$

Here, $C(P',K')$ is the conversion between P' and K' through covariance between perturbation vertical velocity and temperature. $G_R(P')$ and $G_{cn}(P')$ are the generation terms of P' through covariances between h' and perturbation radiative heating, and between h' and perturbation heating due to phase changes of the cloud contents, respectively. $G(P')$ is the generation term of P'. Note that $C(\bar{P},P') + C(K',P') + G(P')$ causes changes of P' due to the vertical advection processes.

$$\frac{\partial K'}{\partial t} = C(\bar{K},K') + C(P',K') + G_{qv}(K') + G_{ql}(P'), \tag{2.10}$$

where

$$C(\bar{K},K') = -\left[\overline{u'w'}\frac{\partial \bar{u}^o}{\partial z} \right] - \left[\overline{w'w'}\frac{\partial \bar{w}^o}{\partial z} \right], \tag{2.10a}$$

$$G_{qv}(K') = [0.61g\overline{w'q_v'}], \tag{2.10b}$$

$$G_{ql}(K') = -[g\overline{w'q_l'}]. \tag{2.10c}$$

Here, $C(\bar{K},K')$ is the conversion between $\bar{K}$ and K' through covariance between perturbation zonal wind and vertical velocity under vertical shear of imposed horizontal-mean zonal wind, and between perturbation vertical velocities under vertical shear of imposed horizontal-mean vertical velocity. $G_{qv}(K')$ and $G_{ql}(K')$ are the generation terms of K' through covariance between perturbation vertical velocity and specific humidity, and between perturbation vertical velocity and cloud mixing ratio, respectively.

Li et al. (2002a) calculated the convective available potential energy (CAPE) using

$$CAPE = g\int_{LFC}^{z_c} \frac{\theta_{pcl}(z) - \theta_{env}(z)}{\theta_{env}(z)} \mathrm{d}z. \tag{2.11}$$

Here, θ_{pcl} is the potential temperature of an air parcel lifted from the bottom of the atmosphere to the top of the atmosphere while not mixing with its environment (θ_{env}). The air parcel is lifted dry adiabatically until it becomes saturated and then is lifted moist adiabatically thereafter. The level of free convection (LFC) is the height where $\theta_{pcl} > \theta_{env}$, z_c is the level where $\theta_{pcl} = \theta_{env}$.

The CAPE can be calculated for a pseudo-adiabatic process and a reversible moist adiabatic process, respectively. In the pseudo-adiabatic process, an air parcel is lifted adiabatically while all condensed water drops out from the parcel. In the reversible moist adiabatic process, an air parcel is lifted adiabatically while all condensed water is kept in the parcel. Following Xu and Emanuel (1989), the virtual temperatures (T_{vpa}) for the pseudo-adiabatic process and (T_{vre}) for the reversible moist adiabatic process are respectively expressed by

$$T_{vpa} = T_p \frac{1 + \dfrac{q_{vs}(T_p)}{0.622}}{1 + q_v} \tag{2.12a}$$

and

$$T_{vre} = T_p \frac{1 + \dfrac{q_{vs}(T_p)}{0.622}}{1 + q_{vs}(T_p)}, \tag{2.12b}$$

where T_p is the temperature of a pseudo-adiabatically displaced air parcel; q_{vs} is the saturation specific humidity. The CAPE for the pseudo-adiabatic process $(CAPE_{pa})$ and for the reversible moist adiabatic process $(CAPE_{re})$ is calculated by using (2.12a and b), respectively. Li et al. (2002a) showed that both $CAPE_{pa}$ and $CAPE_{re}$ have the same evolution but different magnitudes.

2.4 Ocean Mixed-Layer Thermal and Saline Budgets

The Zonal-mean ocean mixed-layer thermal and saline budgets can be respectively expressed as

$$\frac{\partial \bar{T}_m}{\partial t} = -\overline{u_m \frac{\partial T_m}{\partial x}} - \overline{\frac{W_e}{h_m} \mathrm{H}(W_e)(T_m - T_e)} + \overline{\frac{Q_o + I(0) - I(h_m)}{\rho_r c_w h_m}}, \tag{2.13}$$

$$\frac{\partial \bar{S}_m}{\partial t} = -\overline{u_m \frac{\partial S_m}{\partial x}} - \overline{\frac{W_e}{h_m} \mathrm{H}(W_e)(S_m - S_e)} + \overline{\frac{S_m(P_s - E_s)}{\rho_r c_w h_m}}. \tag{2.14}$$

Equation (2.13) shows that local tendency of ocean mixed-layer temperature is determined by horizontal thermal advection, thermal entrainment, and thermal forcing.

Equation (2.14) states that local tendency of ocean mixed-layer salinity is determined by horizontal saline advection, saline entrainment, and saline forcing.

2.5 Partition of Convective and Stratiform Clouds

Convective precipitation is associated with high rain rate, strong horizontal reflectivity gradients, and large vertical velocity. Stratiform precipitation that usually falls from the anvil clouds is associated with light to moderate rain rates, weak horizontal reflectivity gradients, the "bright band" near the melting level in radar echo, and weak vertical velocity. The primary microphysical process responsible for the growth of convective clouds and precipitation is a collection of cloud water by rain particles in the strong updraft cores, whereas the primary microphysical process responsible for the growth of stratiform clouds and precipitation is vapor deposition on ice particles (Houghton 1968).

Convective–stratiform rainfall partition has been applied to radar data in most of the observational studies. Based on the assumption that convective cells have peak rainfall rates at least twice as high as the surrounding background rainfall rate, Churchill and Houze (1984) used a similar technique developed by Houze (1973) to classify the convective and stratiform precipitation. In their scheme, the cores of convective cells are first assigned to those data points in the radar reflectivity field that have rain rates twice as high as the average taken over the surrounding $400\,\mathrm{km}^2$. These convective cores and the surrounding $150\,\mathrm{km}^2$ of area are identified as convective precipitation. In addition, any radar echo 40 dBZ or more in intensity is considered convective precipitation. Stratiform precipitation is identified as any precipitation not designated as convective by either of the above criteria. Steiner and Houze (1993) developed a similar partition method, and Steiner et al. (1995) further refined this technique. They categorized the peaks of rain rate as convective when the peaks satisfy specified criteria regarding background rain rate. The remainder of the precipitation is categorized as stratiform after all the peaks and surrounding areas have been located and identified as convective. Steiner et al. (1995) argued that their method is fundamentally different from the method employed by Rosenfeld et al. (1995), which uses the bright band to separate the precipitation. Yuter and Houze (1997) employed an algorithm first developed for application to $4 \times 4\,\mathrm{km}$ grids (Churchill and Houze 1984) and later refined for application to $2 \times 2\,\mathrm{km}$ grids (Steiner et al. 1995) to study raindrop size distribution associated with convective and stratiform rainfall over the Pacific warm pool during TOGA COARE.

Adler and Negri (1988) developed a convective–stratiform technique for analysis of satellite infrared data that locates all local minima in the brightness temperature field. After an empirical screening to eliminate cirrus, these points are assumed to be convective centers. They used a brightness temperature threshold based on the mode temperature of thunderstorm anvils to determine the stratiform rain.

Convective–stratiform cloud partitioning analysis has been applied to the modeling studies. Tao and Simpson (1989) and Tao et al. (2000) developed a partition

method that is similar to the method of Churchill and Houze (1984) and added more criteria in which the point is made convective if the cloud water and ice or the updraft exceeds certain threshold values. Xu (1995) developed a partition method using information of vertical motion. In addition, liquid water path is used to identify the stratiform rainfall, and cloud water path and rain water path are used for shallow convection. Lang et al. (2003) developed a new partition method based on the premise that the fall speed of precipitation particles is large relative to the vertical velocity in regions of stratiform precipitation. In this method, the model point is considered stratiform if the ratio of fall velocity to vertical velocity exceeds a threshold value (3.16 in their paper). Lang et al. (2003) compared six different partition methods including Churchill and Houze (1984), Tao and Simpson (1989), Caniaux et al. (1994), Xu (1995), Steiner et al. (1995), and Lang et al. (2003) in terms of surface rain rate, mass fluxes, apparent heating and moistening, hydrometeor contents, reflectivity and vertical velocity contoured frequency with altitude diagram (CFAD), microphysics, and latent heat retrieval. They showed that the method based on surface rain rate was consistently the most stratiform, whereas the method based on radar information below the melting level and the new method of Lang et al. (2003) were consistently the most convective.

Tao et al. (1990, 1991, 1993) developed the convective–stratiform cloud partitioning method based on Churchill and Houze (1984) and Adler and Negri (1988), and Sui et al. (1994) modified this partitioning scheme. In Sui et al. (1994), each vertical column containing clouds is partitioned into convective or stratiform based on the following criterion. Model grid points in the surface rain field that have a rain rate twice as large as the average taken over the surrounding four grid points (two on the left and two on the right in the 2D framework) are identified as the cores of convective cells. For each core grid point, the one on either side (in the 2D framework) is also considered as convective. In addition, any grid point with a rain rate of $20\,\mathrm{mm\ h^{-1}}$ or more is designated as convective regardless of the above criterion. All nonconvective cloudy points are regarded as stratiform. Since the above separation criterion is strictly based on surface precipitation, the stratiform region may actually include areas with tilted convective updrafts aloft. It may also include light- or nonprecipitating convective cells that are initiated ahead of the organized convective system. Therefore, grid points in the stratiform regions are further checked and classified as convective if (i) in the precipitating stratiform regions, cloud water below the melting level is greater than $0.5\,\mathrm{g\ kg^{-1}}$ or the maximum updraft above 600 mb exceeds $5\,\mathrm{m\ s^{-1}}$; or (ii) in the nonprecipitating stratiform regions, cloud water exists at a level greater than $0.025\,\mathrm{g\ kg^{-1}}$; or the maximum updraft exceeds $5\,\mathrm{m\ s^{-1}}$ below the melting level. The main difference between Sui's method and Churchill and Houze's method is that in the former the average is taken over four grids (6 km here) and only three grids surrounding rainfall peaks are considered as convective, whereas in the latter the average is taken over $400\,\mathrm{km^2}$ (equivalent to 20 km in 2D or 13 grids), and $150\,\mathrm{km^2}$ (equivalent to 12 km in 2D or eight grids) surrounding rainfall peaks are considered as convective. The fractional cover of convective precipitation (Fig. 10b in Li et al. 2002b) and convective fraction of rain volume (Li et al. 1999) calculated using Sui's method are in the ranges of calculations using the

methods of Churchill and Houze (1984) and Steiner et al. (1995). The convective–stratiform cloud partitioning method developed by Tao et al. (1993) and modified by Sui et al. (1994) will be used in the following analysis throughout the book.

References

Adler RF, Negri AJ (1988) A satellite infrared technique to estimate tropical convective and stratiform rainfall. J Appl Meteor 27:30–51

Caniaux G, Redelsperger JL, Lafore JP (1994) A numerical study of the stratiform region of a fast-moving squall line. Part I: General description and water and heat budgets. J Atmos Sci 51:2046–2074

Churchill DD, Houze RA Jr (1984) Development and structure of winter monsoon cloud clusters on 10 December 1978. J Atmos Sci 41:933–960

Gao S, Cui X, Zhou Y, Li X (2005) Surface rainfall processes as simulated in a cloud resolving model. J Geophys Res, doi:10.1029/2004JD005467

Houghton HG (1968) On precipitation mechanisms and their artificial modification. J Appl Meteor 7:851–859

Houze RA Jr (1973) A climatological study of vertical transports by cumulus-scale convection. J Atmos Sci 30:1112–1123

Lang S, Tao WK, Simpson J, Ferrier B (2003) Modeling of convective-stratiform precipitation processes: Sensitivity to partition methods. J Appl Meteor 42:505–527

Li X, Sui CH, Lau KM, Chou MD (1999) Large-scale forcing and cloud-radiation interaction in the tropical deep convective regime. J Atmos Sci 56:3028–3042

Li X, Sui CH, Lau KM (2002a) Interactions between tropical convection and its environment: An energetics analysis of a 2-D cloud resolving simulation. J Atmos Sci 59:1712–1722

Li X, Sui CH, Lau KM (2002b) Dominant cloud microphysical processes in a tropical oceanic convective system: A 2-D cloud resolving modeling study. Mon Wea Rev 130:2481–2491

Lorenz EN (1955) Available potential energy and the maintenance of the general circulation. Tellus 7:157–167

Rosenfeld D, Amitai E, Wolff DB (1995) Classification of rain regimes by the three-dimensional properties of reflectivity fields. J Appl Meteor 34:198–211

Steiner M, Houze RA Jr (1993) Three-dimensional validation at TRMM ground truth sites: Some early results from Darwin, Australia. 26th International Conference on Radar Meteorology, Norman, OK

Steiner M, Houze RA Jr, Yuter SE (1995) Climatological characterization of three-dimensional storm structure from operational radar and rain gauge data. J Appl Meteor 34:1978–2007

Sui CH, Lau KM, Tao WK, Simpson J (1994) The tropical water and energy cycles in a cumulus ensemble model. Part I: Equilibrium climate. J Atmos Sci 51:711–728

Tao WK, Simpson J (1989) Modeling study of a tropical squall-type convective line. J Atmos Sci 46:177–202

Tao WK, Simpson J, Lang S, McCumber M, Adler R, Penc R (1990) An algorithm to estimate the heating budget from vertical hydrometeor profiles. J Appl Meteor 29:1232–1244

Tao WK, Simpson J, Soong ST (1991) Numerical simulation of a subtropical squall line over Taiwan Strait. Mon Wea Rev 119:2699–2723

Tao WK, Simpson J, Sui CH, Ferrier B, Lang S, Scala J, Chou MD, Pickering K (1993) Heating, moisture, and water budgets of tropical and midlatitude squall lines: Comparisons and sensitivity to longwave radiation. J Atmos Sci 50:673–690

Tao WK, Lang S, Simpson J, Olson WS, Johnson D, Ferrier B, Kummerow C, Adler R (2000) Vertical profiles of latent heat release and their retrieval for TOGA COARE convective systems using a cloud resolving model, SSM/I, and ship-borne radar data. J Meteor Soc Japan 78: 333–355

Xu KM (1995) Partitioning mass, heat, and moisture budgets of explicit simulated cumulus ensembles into convective and stratiform components. J Atmos Sci 52:1–23

Xu KM, Emanuel KA (1989) Is the tropical atmosphere conditionally unstable? Mon Wea Rev 117:1471–1479

Yuter SE, Houze RA Jr (1997) Measurements of raindrop size distribution over the Pacific warm pool and implications for Z-R relations. J Appl Meteor 36:847–867

Chapter 3
Comparison Between Simulations and Observations

The validation of cloud-resolving model simulations with observations highlights how well the models reproduce observed vertical structures of temperature and moisture, surface fluxes, and precipitation. The evaluation of simulations with observations lays down the foundation for further process studies with cloud-resolving models, aiming towards understanding dynamic, thermodynamic, cloud microphysical processes associated with the development of convection. In this chapter, the could-resolving model simulation and coupled ocean-cloud-resolving atmosphere model simulation are intensively compared with available observations based on Li et al. (1999, 2000).

The cloud-resolving model simulations are sensitive to initial conditions. The uncertainties of initial conditions could affect the simulations of clouds and precipitation. The sensitivity of cloud and precipitation simulations to initial water vapor conditions and associated physical processes are discussed in this chapter based on Li et al. (2006).

Due to limitations in computational power, the cloud-resolving model simulations have been mainly carried out in the 2D (x–z) framework while the three-dimensional (3D) simulations have been conducted in small horizontal domains. Thus, the comparison between the 2D and 3D model simulations is discussed in this chapter.

3.1 Comparison Between Simulations and Observations

Grabowski et al. (1996) integrated the 2D cloud model with the forcing of heat and vapor sources and sinks from Phase III of GATE for 7 days, conducted a comparison study between simulations and observations, and found that the differences of temperature could be as large as 2–3°C, whereas the differences of specific humidity could be $1.5\,\mathrm{g\,kg^{-1}}$. The simulated mid and upper troposphere is moister than what is observed, which may result from the lack of forcing data in upper-tropospheric ice and cyclic lateral boundary conditions. Xu and Randall (1996) conducted an 18-day

2D cloud model with the forcing of large-scale vertical velocity from Phase III of GATE, and showed that the temperature differences between simulations and observations are as large as 3°C and the differences in water vapor mixing ratio are as large as 2–3 g kg^{-1}. Wu et al. (1998) carried out a 39-day integration of cloud model with the forcing of heat and vapor sources and sinks from TOGA COARE and found that simulations agree well with observations when the forcing is strong, whereas simulations show notable differences with observations (6°C in temperature difference and 4 g kg^{-1} in specific humidity difference) when the forcing is weak. The further sensitivity test shows that the big difference is from the vapor difference. Moncrieff et al. (1997) conducted intercomparison study for the simulations of four cloud-resolving models in terms of temperature at 500 mb, PW, upwelling IR flux at the top of atmosphere, cloud ice water path (*IWP*), and cloud mass flux at 500 mb, and found notable differences between model simulations such as a cold bias of 2°C at 500 mb.

Li et al. (1999) carried out the two experiments with different model setups to examine convective responses to the large-scale forcing data during TOGA COARE, and conducted a comparison study between simulations and observations. Figure 3.1 shows the imposed large-scale vertical velocity in pressure coordinate and total temperature and water vapor advections (the sums of horizontal and vertical advections) for a selected 6-day period during the TOGA COARE Intensive Observation Period (IOP), as calculated by Sui et al. (1997). Strong upward motion centers occur on 20, 23, and 25 December, signaling quasi-2-day oscillation (Takayabu et al. 1996) embedded in the active phase of intraseasonal oscillation during COARE. Two moderate ascending motion centers appear on 19 and 21 December, forming diurnal variations with nocturnal rainfall peaks (Sui et al. 1997). Large-scale advective cooling and moistening are largely associated with these ascending motion centers. Two model setups are used. The model in experiment COARE1 uses vertical velocity, zonal wind, horizontal thermal and vapor advection, and SST as the forcing data. The large-scale vertical velocity is the major forcing during the integration in COARE1. The model in experiment COARE2 uses total temperature and vapor advections, zonal wind, and SST. The total advections are the major forcing during the integration in COARE2.

The simulated temperatures in COARE1 are 1–2°C colder than the observed temperatures (Fig. 3.2a), whereas the simulated temperatures in COARE2 are 2–4°C colder than the observed temperatures (Fig. 3.2b), indicating that the model with imposed total advections produces a larger cooling bias than the model with imposed vertical velocity does. The differences in specific humidity between COARE1 and observations and between COARE 2 and observations are similar (Fig. 3.2c, d), but the latter is slightly larger than the former.

The quantitative analysis of the differences between simulations and observations can be done with the calculations of root-mean-square (RMS) differences and linear correlation coefficients between simulations and observations. The vertical distributions of the RMS differences and correlation coefficients are shown in Fig. 3.3. The RMS difference in temperature between COARE1 and observations reaches the minimum at surface, which is smaller than 1°C (Fig. 3.3a). The maximum RMS

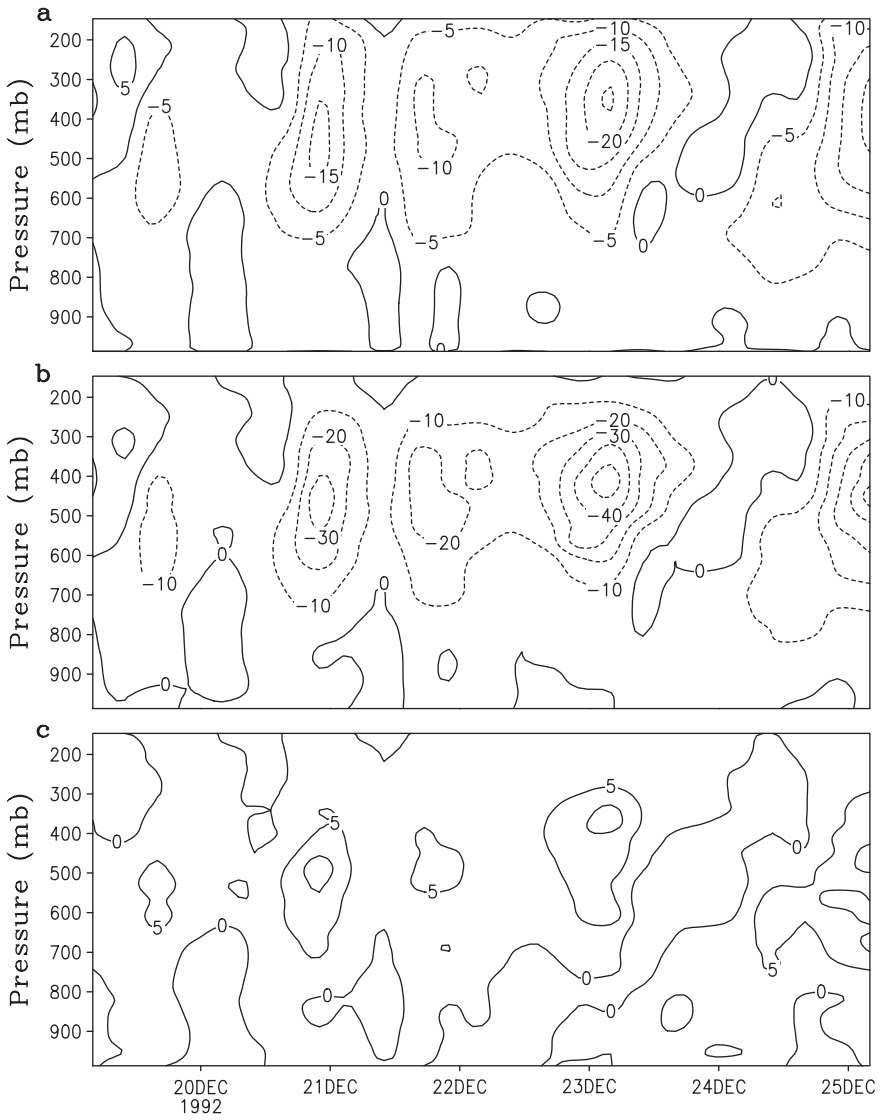

Fig. 3.1 Temporal and vertical distributions of vertical velocity in pressure coordinate (mb h^{-1}) in **a** and total advection of potential temperature (°C day^{-1}) in **b**, and water vapor (g kg^{-1} day^{-1}) in **c** calculated from the TOGA COARE data for a selected 6-day period (After Li et al. 1999)

differences of 1.5°C occur around 650, 400, and 200 mb. The RMS differences in temperature between COARE2 have the maxima of 1.5°C at surface and 550 mb, whereas the RMS maximum reaches 3.5°C above 200 mb. The RMS differences in temperature between COARE1 and observations are 0.5–2°C smaller than that between COARE2 and observations. The linear correlation coefficients between

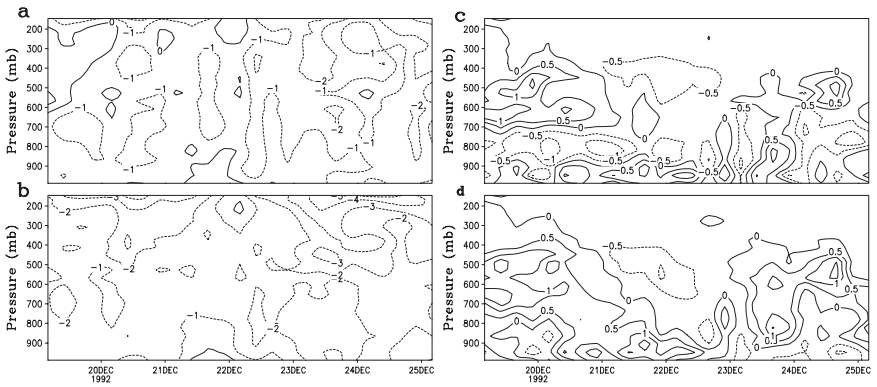

Fig. 3.2 Temporal and vertical distributions of temperature differences (°C) of **a** simulation in COARE1 minus observation and **b** simulation in COARE2 minus observation and specific humidity differences (g kg^{-1}) of **c** simulation in COARE1 minus observation, and **d** simulation in COARE2 minus observation (After Li et al. 1999)

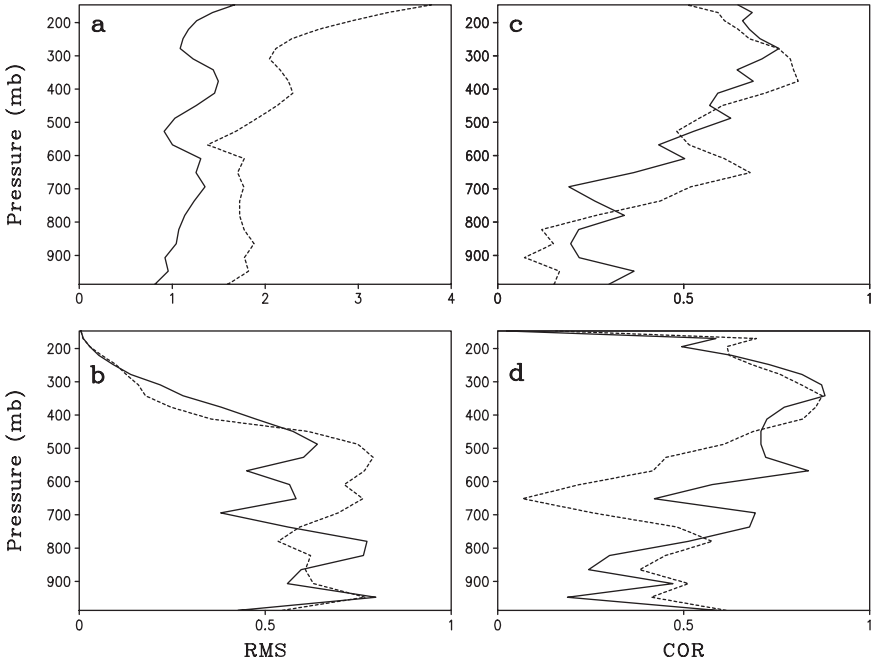

Fig. 3.3 Vertical distributions of root-mean-square (RMS) differences of **a** temperatures (°C) and **b** specific humidity (g kg^{-1}) and linear correlation coefficients (COR) of **c** temperatures and **d** specific humidity between simulations and observations. Solid and dashed lines denote COARE1 and COARE2, respectively

COARE2 and observations are larger than those between COARE1 and observations in 300–800 mb (Fig. 3.3c). A student's t-test on the significance of the correlation coefficients is further conducted and the critical correlation coefficient at the 5% confidence level is 0.41. Thus, the correlation in mid and upper troposphere passes the significance tests, whereas it fails the significance tests in the lower troposphere. The RMS differences in specific humidity between simulations and observations are 0.5–0.7 g kg^{-1} (Fig. 3.3b). The RMS differences between COARE1 and observations are smaller than that between COARE2 and observations in mid troposphere (500–700 mb). The linear correlation coefficient of specific humidity between COARE1 and observations is much larger than that between COARE2 and observations around 400–800 mb although the former is slightly smaller than the latter in the lower troposphere (below 800 mb) (Fig. 3.3d).

Following Yanai et al. (1973), apparent heat source (Q_1) and apparent vapor source (Q_2) are calculated in Fig. 3.4. Simulated Q_1 and Q_2 basically follow observed Q_1 and Q_2, which is due to the imposed large-scale vertical velocity in COARE1 and large-scale advective cooling and moistening in COARE2. The differences of magnitudes between simulations and observations could be 5–10°C day^{-1}. More positive centers of Q_1 occur in COARE1 than in COARE2 and observations, as a result of high-frequency convective response (Li et al. 1999).

Although the simulated solar fluxes follow the observed flux, the simulated solar fluxes (e.g., time-mean in COARE1 is 205 W m^{-2}) are much larger than the observed flux (time-mean is 148 W m^{-2}) (Fig. 3.5). The possible causes for the differences include that parameterized cloud–radiation interaction processes in the model may produce more convective cells and less stratiform cells (Sui et al. 1998) and

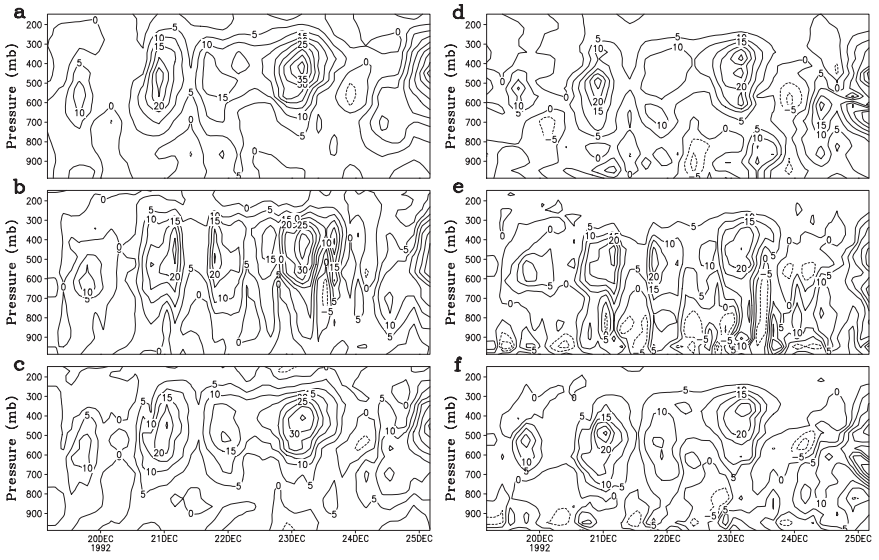

Fig. 3.4 Temporal and vertical distributions of Q_1 for **a** observation, **b** COARE1, and **c** COARE2, and Q_2 for **d** observation, **e** COARE1, and **f** COARE2. Unit is °C day^{-1} (After Li et al. 1999)

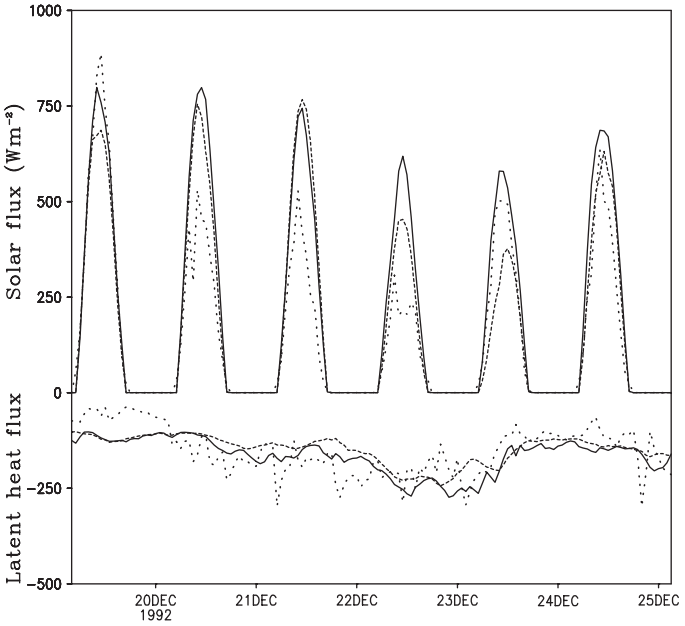

Fig. 3.5 Time series of surface solar radiative fluxes and latent heat fluxes simulated in COARE1 (solid) and COARE2 (dashed). Dotted lines denote observed fluxes. Unit is W m^{-2} (After Li et al. 1999)

that observational data quality is problematic as indicated by unclosed budgets. The simulated latent heat fluxes (e.g., time-mean in COARE1 is 164 W m^{-2}) are also larger than the observed flux (time-mean is 145 W m^{-2}), which may be caused by the treatment of surface gusty winds associated with strong convective events. The simulated surface rain rates have larger fluctuations than the observed rain rate does although the former basically follow the latter (Fig. 3.6). Since the surface rain rate is largely determined by the imposed large-scale forcing (Gao et al. 2005), the mismatch between vapor budget and surface rain rate in observations may yield the difference. For example, a strong ascending motion and associated advective cooling and moistening occur in the late evening of 22 December and early morning of 23 December 1992 (Fig. 3.1), whereas the observed surface rain rate is small (Fig. 3.6). Li et al. (1999) also compared convective and stratiform rainfalls between COARE1 and COARE2 and found that COARE1 produces more convective rainfall (67%) than COARE2 does (57%).

Li et al. (2000) conducted a 2D coupled ocean-cloud-resolving atmosphere simulation with the forcing from TOGA COARE and showed remarkable similarity of surface fluxes between simulations and observations in both phase and amplitude (Fig. 3.7). However, the model simulations differ from the observations in three ways. First, simulated surface wind stresses are much smaller than observed wind stresses on 21–23 December 1992. Second, simulated surface net heat fluxes are larger than observed net heat fluxes on 20–22 December. The smaller magnitudes of

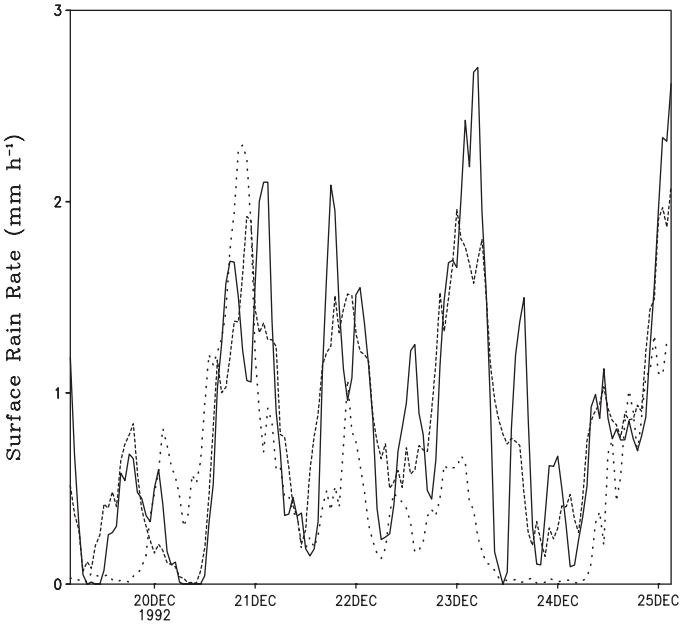

Fig. 3.6 Time series of surface rain rates simulated in COARE1 (solid) and COARE2 (dashed). Dotted lines denote observed rain rate. Unit is mm h^{-1} (After Li et al. 1999)

observed surface net heat fluxes are caused by the smaller magnitudes of observed surface solar radiative fluxes. The larger magnitudes of solar radiative fluxes in the model simulation may be due to the fact that the model produces more convective cells and less stratiform cells. Third, simulated fresh water fluxes are much larger than observed fresh water fluxes on 21–23 December. The larger amplitudes of simulated fresh water fluxes are accounted for by the larger simulated surface rain rate associated with stronger ascending motion imposed in the cloud-resolving model. The observed surface rain rate is not consistent with observed ascending motion imposed in the model. The differences include the small simulated zonal wind stresses, large simulated surface heat fluxes, and large simulated fresh water fluxes. The coupled model produces mixed-layer temperature and salinity reasonably well (Fig. 3.8), although the simulated diurnal temperature amplitudes are larger than the observed diurnal amplitudes. The RMS differences in mixed-layer temperature and 3-m salinity between simulations and observations are 0.28°C and 0.09PSU, respectively.

3.2 Model Responses to Initial Moisture Perturbations

Accurate precipitation forecast may rely on accurate initial conditions. Initial conditions include temperature, moisture, and cloud hydrometeors. As a unique source for condensation, deposition, and surface rainfall, water vapor plays a crucial role

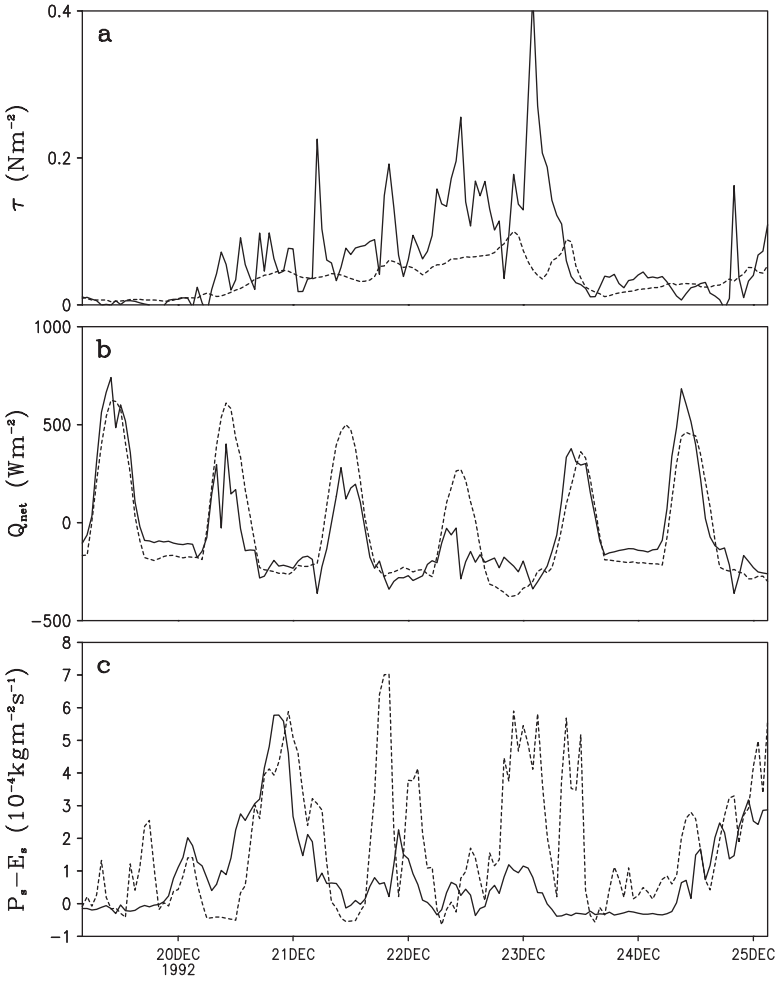

Fig. 3.7 Time series of **a** zonal-mean zonal wind stress ($\mathrm{N\,m^{-2}}$), **b** net surface heat fluxes ($\mathrm{W\,m^{-2}}$), and **c** fresh water flux ($10^{-4}\,\mathrm{kg\,m^{-2}\,s^{-1}}$) observed during TOGA COARE (solid) and simulated in the 2D coupled ocean-cloud-resolving atmosphere model (dashed) with the forcing from TOGA COARE (see Fig. 3.1a) (After Li et al. 2000)

in determining tropical convective development. The comparison between National Oceanic and Atmospheric Administration (NOAA)/National Environmental Satellite, Data, and Information Service (NESDIS)/Microwave Surface and Precipitation Products System (MSPPS) data and National Centers for Environmental Prediction (NCEP)/Global Data Assimilation System (GDAS) data showed that the RMS difference in *IWP* is 0.12 mm, which is larger than the standard deviation of *IWP* for GDAS (0.06 mm). The RMS difference in *PW* over cloudy regions is 4.5 mm, which is smaller than the standard deviation of *PW* for GDAS (6 mm). The area mean *IWP* and *PW* for GDAS are 0.04 mm and 52.1 mm, respectively. Thus, the

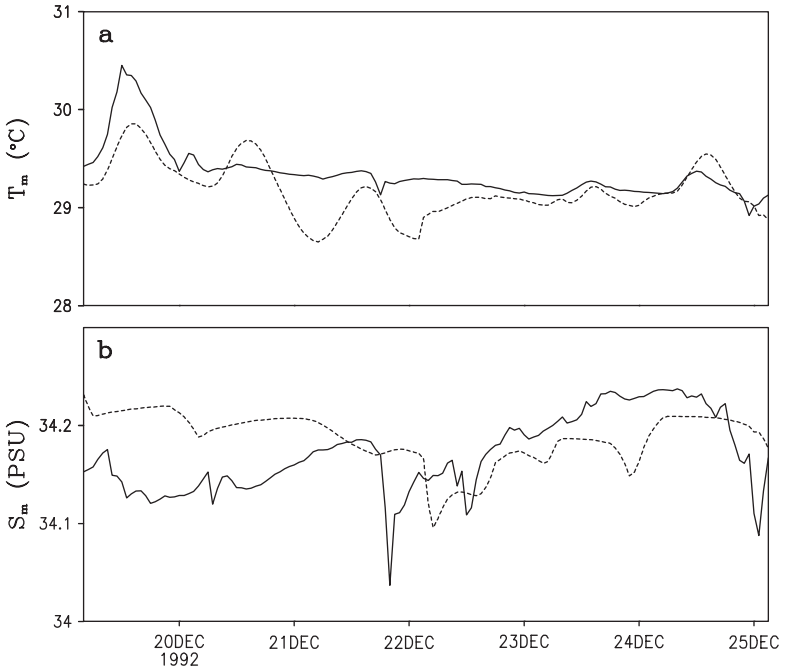

Fig. 3.8 Time series of **a** zonal-mean ocean mixed-layer temperature (°C) and 3-m salinity (PSU) simulated in a coupled ocean-cloud-resolving atmosphere model with the forcing from TOGA COARE (see Fig. 3.1a). Solid lines denote observed SST in **a** and 3-m salinity in **b** (After Li et al. 1999)

statistical error that is defined as the ratio of the RMS difference to the area mean is 300% for *IWP* while it only is 8.6% for *PW*. Does a small initial *PW* error lead to a large *IWP* error? Li et al. (2006) used 2D cloud-resolving model with imposed forcing (zonally uniform vertical velocity, zonal wind, along with thermal and moisture advection) based on 6-hourly NCEP/GDAS data over tropical area (averaged over 150–160°E, EQ) to study model responses to initial moisture perturbations. Daily mean SST data retrieved from NASA/Tropical Rainfall Measuring Mission (TRMM) Microwave Imager (TMI) radiometer with a 10.7 GHz channel (Wentz et al. 2000) are also imposed in the model. Figure 3.9 shows temporal and vertical distribution of the large-scale vertical velocity and zonal wind from 1100 Local Standard Time (LST) 18 April to 1700 LST 26 April 2003 (8.25 days total), which are imposed in the model during the integrations. The ascending motion with maximum of $-4\,\mathrm{mb\,h^{-1}}$ occurs around 300 mb on 18 April 2003. Moderate upward motions of $-2\,\mathrm{mm\,h^{-1}}$ appear daily in mid and lower troposphere from 20 to 22 April when westerly winds are confined in the lower troposphere while easterly winds weaken gradually. Two strong ascending motion centers dominate the troposphere on 24 and 25 April when the westerly winds switch into the intensified easterly winds. Three experiments are designed. The control experiment C is considered

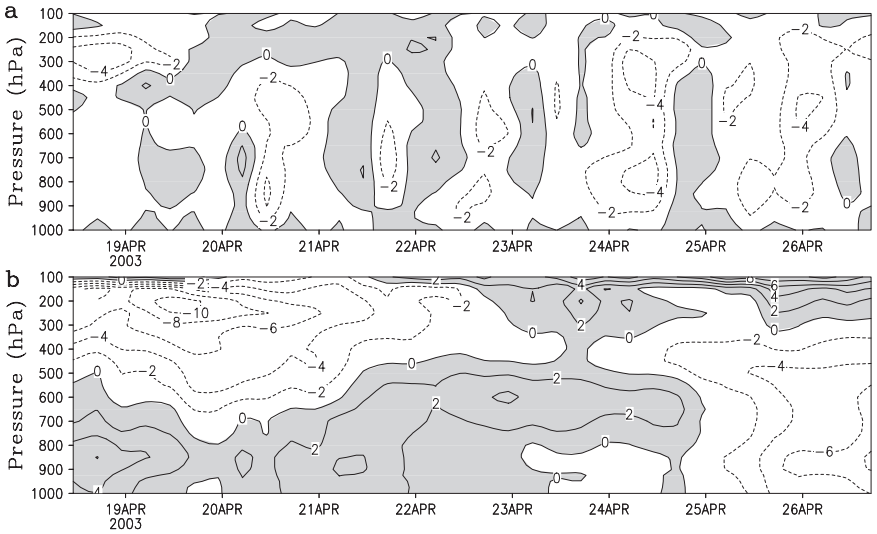

Fig. 3.9 Time-pressure cross sections of **a** vertical motion $(\mathrm{mb\,h^{-1}})$, and **b** zonal wind $(\mathrm{m\,s^{-1}})$ obtained from GDAS during the selected 8-day period. Downward motion in **a** and westerly wind in **b** are shaded (After Li et al. 2006)

as a true experiment. Experiments CP and CM are identical to experiment C except that 10% of *PW* is added and reduced in initial conditions in CP and CM, respectively, while the vertical structures of initial specific humidity are kept.

The scatter plotting of CP versus C and CM versus C for *PW, IWP*, and liquid water path (*LWP*) is shown in Fig. 3.10. The *PW* simulated in CP and C is along the diagonal line of the diagram, indicating a small RMS difference (1.1 mm), although the initial difference in *PW* is 5.1 mm. The *PW* simulated in CM and C is below the diagonal line of the diagram, suggesting a large RMS difference (3.3 mm). The RMS difference between CP and C is much smaller than the standard deviation of CP (3.3 mm), whereas that between CM and C is marginally smaller than the standard deviation of CM (3.8 mm).

Cloud hydrometeors (*LWP* and *IWP*) simulated in CP and CM versus those simulated in C show large scattering patterns that are away from the diagonal lines (Fig. 3.10c–f). The RMS difference in *IWP* between CP and C is 0.104 mm, whereas that between CM and C is 0.107 mm. Both are larger than the standard deviations of CP (0.094 mm) and CM (0.093 mm). The small initial difference in *PW* produces the large difference in *IWP*. This demonstrates that the large RMS difference in *IWP* between MSPPS and GDAS data may be caused by the small RMS difference in *PW*. The large scattering in *IWP* between CP/CM and C associated with the small scattering in *PW* implies uncertainties in cloud microphysical parameterization schemes that are nonlinear functions of temperature and water vapor. The RMS difference in *LWP* between CP and C is 0.085 mm, whereas that between CM and C is 0.096 mm. Both are smaller than the standard deviations of CP (0.098 mm) and CM (0.103 mm).

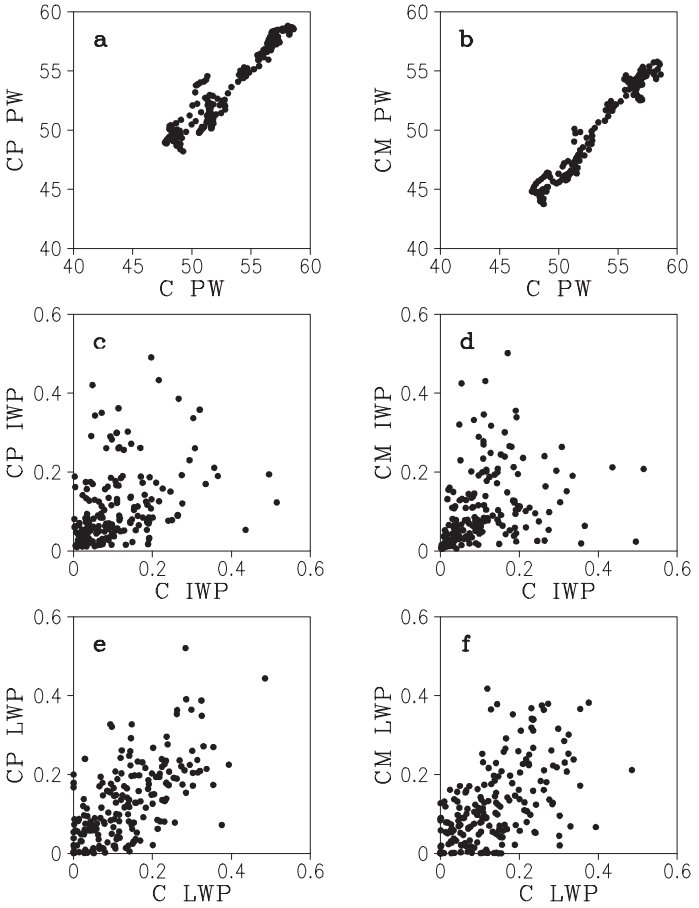

Fig. 3.10 Scatter plots of CP versus C for zonally averaged **a** *PW*, **c** *IWP*, **e** *LWP*; and of CM versus C for **b** *PW*, **d** *IWP*, **f** *LWP*. Unit is mm (After Li et al. 2006)

Surface rain rates simulated in CP and CM versus those simulated in C also show large scattering patterns (Fig. 3.11a, b). The RMS difference in P_s between CP and C is 0.28 mm h^{-1}, whereas that between CM and C is 0.33 mm h^{-1}. Both are similar to the standard deviations of CP (0.29 mm) and CM (0.32 mm). Although the imposed large-scale ascending motion is identical in three experiments, the small differences in *PW* still produce the large differences in the surface rain rate.

Q_{WVT} and Q_{CM} display large scattering patterns between CP/CM and C, whereas Q_{WVF} and Q_{WVE} show good relationships between CP and C, and CM and C (Fig. 3.11). The RMS differences in Q_{WVF} (~ 0.01 mm h^{-1}) and Q_{WVE} (~ 0.02 mm h^{-1}) are significantly smaller than the standard deviations of CP (0.24 mm h^{-1}) and CM (0.04 mm h^{-1}), respectively. The small RMS difference in Q_{WVF} reflects the dominance of imposed vertical velocity during the integrations. The RMS differences in Q_{WVT} between CP and C (0.37 mm h^{-1}) and CM and C

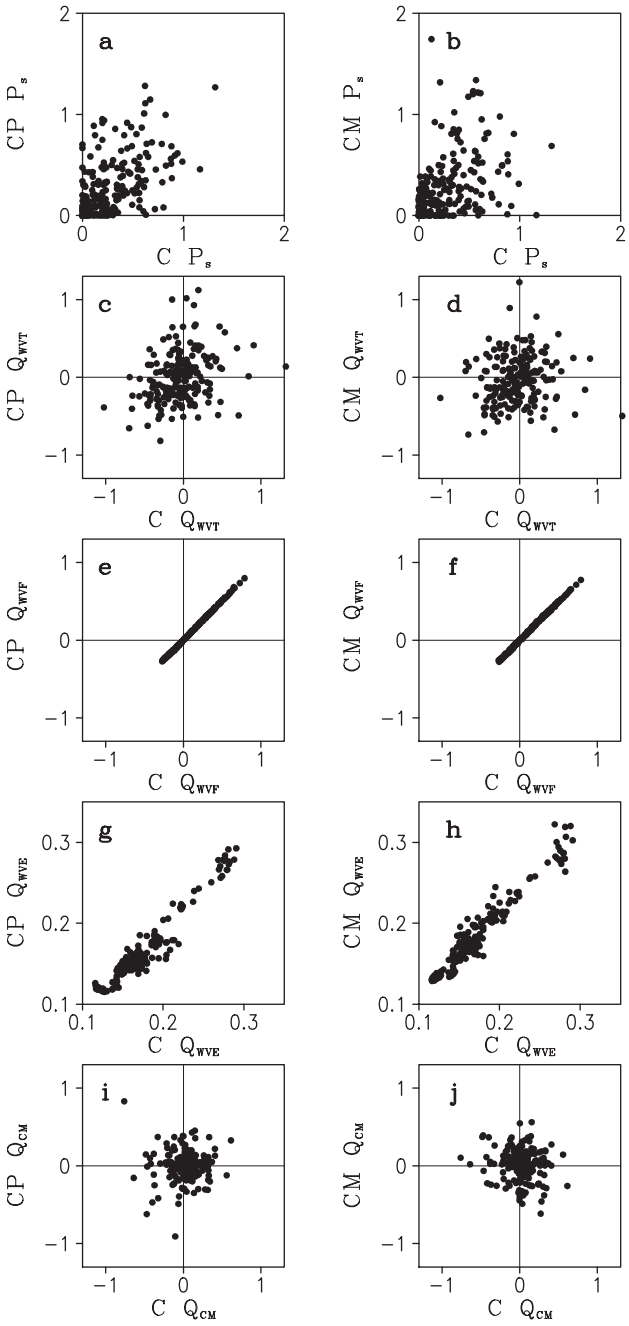

Fig. 3.11 Scatter plots of CP versus C for **a** P_s, **c** Q_{WVT}, **e** Q_{WVF}, **g** Q_{WVE}, **i** Q_{CM}; and of CM versus C for **b** P_s, **d** Q_{WVT}, **f** Q_{WVF}, **h** Q_{WVE}, **j** Q_{CM}. Unit is mm h^{-1} (After Li et al. 2006)

($0.4\,\mathrm{mm\,h^{-1}}$) are larger than the standard deviations of CP ($0.32\,\mathrm{mm\,h^{-1}}$) and CM ($0.3\,\mathrm{mm\,h^{-1}}$), respectively, whereas the RMS differences in Q_{CM} between CP and C ($0.27\,\mathrm{mm\,h^{-1}}$) and CM and C ($0.29\,\mathrm{mm\,h^{-1}}$) are larger than the standard deviations of CP ($0.19\,\mathrm{mm\,h^{-1}}$) and CM ($0.19\,\mathrm{mm\,h^{-1}}$), respectively. This indicates that the RMS differences in Q_{WVT} and Q_{CM} largely contribute to the RMS differences in P_s.

To explain the large RMS differences in Q_{WVT} and Q_{CM}, the PW and total cloud budgets will be separately analyzed. The PW budget (2.2b) can be expressed as

$$Q_{WVT} + Q_{WVF} + Q_{WVE} = P_{CND} + P_{DEP} + P_{SDEP} + P_{GDEP} - P_{REVP} - P_{MLTS} - P_{MLTG}, \tag{3.1a}$$

and the cloud budget (2.3) is mass-integrated and zonally averaged to yield

$$Q_{CM} = P_s - P_{CND} - P_{DEP} - P_{SDEP} - P_{GDEP} + P_{REVP} + P_{MLTS} + P_{MLTG}. \tag{3.1b}$$

Figure 3.12 shows scatter diagrams of CP versus C and CM versus C for $[P_{CND}]$, $[P_{DEP}]$, $[P_{SDEP}]$, $[P_{GDEP}]$, $[P_{REVP}]$, $[P_{MLTS}]$, and $[P_{MLTG}]$. The standard deviations of $[P_{CND}]$ ($\sim 0.36\,\mathrm{mm\,h^{-1}}$) are much larger than those of $[P_{DEP}]$, $[P_{SDEP}]$, $[P_{GDEP}]$, $[P_{REVP}]$, $[P_{MLTS}]$, and $[P_{MLTG}]$ (~ 0.06–$0.12\,\mathrm{mm\,h^{-1}}$), indicating a large fluctuation of vapor condensation rate. The RMS differences in $[P_{CND}]$ between CP and C ($0.38\,\mathrm{mm\,h^{-1}}$) and CM and C ($0.41\,\mathrm{mm\,h^{-1}}$) are larger than the standard deviations. Thus, vapor condensational process is responsible for the large RMS differences in Q_{WVT}, Q_{CM}, as well as P_s.

The results show that $[P_{CND}]$ accounts for large RMS differences in Q_{WVT}, Q_{CM}, and P_s between CP/CM and C. The scheme of $[P_{CND}]$ used in the cloud-resolving model is from Tao et al. (1989), which can be written as

$$P_{CND} = P_{CND1} + P_{CND2}, \tag{3.2}$$

$$P_{CND1} = Cq_v, \tag{3.2a}$$

$$P_{CND2} = -C(q_{qws} + q_{is}), \tag{3.2b}$$

$$C = \frac{1}{\Delta t}\frac{T - T_{oo}}{T_o - T_{oo}}\frac{1}{1 + \left(\frac{A_1 q_c q_{ws} + A_2 q_i q_{is}}{q_c + q_i}\right)\left(\frac{L_v(T - T_{oo}) + L_s(T_0 - T)}{c_p(T_0 - T_{oo})}\right)}. \tag{3.2c}$$

Equation (3.2) reveals that the vapor condensation rate is primarily determined by the difference between air specific humidity and saturated specific humidity that is the nonlinear function of air temperature. This suggests that the air temperature may play an important role in producing large RMS difference in $[P_{CND}]$. The RMS difference in mass-weighted mean temperatures between CP and C (0.63°C) is twice larger than that between CM and C (0.32°C) (see Fig. 3.13a), although both are smaller than the standard deviations (0.79–1.01°C).

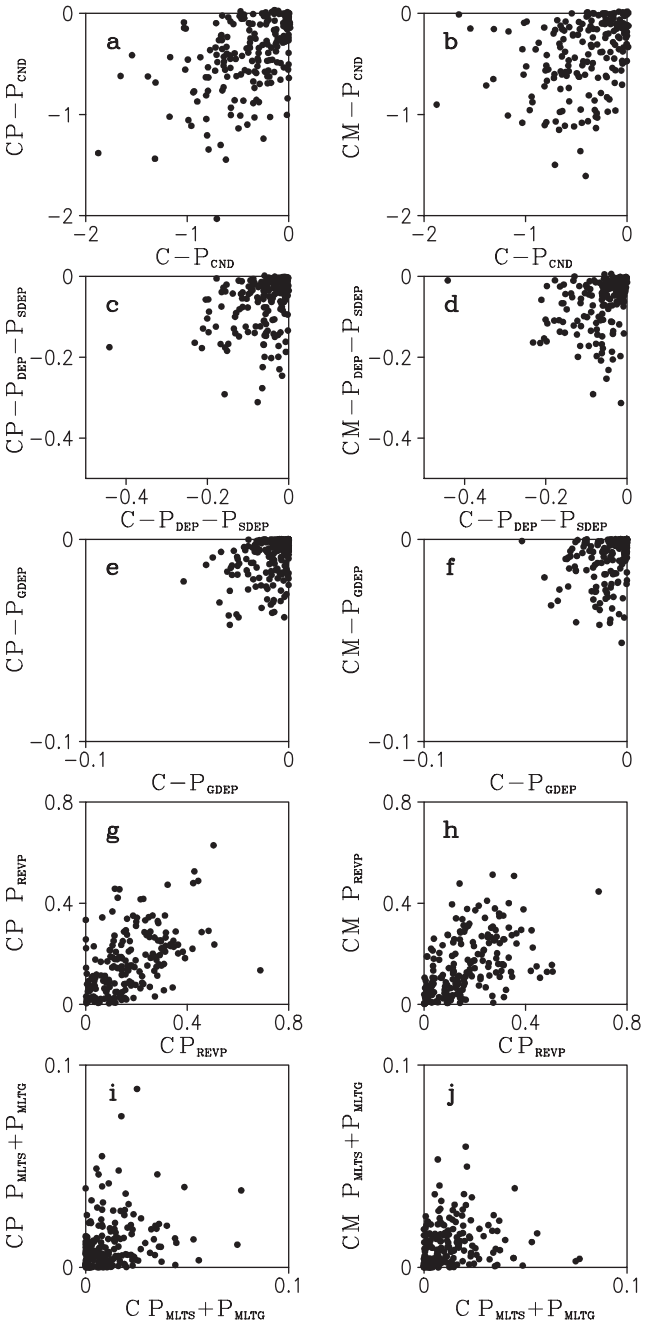

Fig. 3.12 Scatter plots of CP versus C for **a** $-[P_{CND}]$, **c** $-[P_{DEP}]-[P_{SDEP}]$, **e** $-[P_{GDEP}]$, **g** $[P_{REVP}]$, **i** $[P_{MLTS}]+[P_{MLTG}]$; and of CM versus C for **b** $-[P_{CND}]$, **d** $-[P_{DEP}]-[P_{SDEP}]$, **f** $-[P_{GDEP}]$, **h** $[P_{REVP}]$, **j** $[P_{MLTS}]+[P_{MLTG}]$. Unit is mm h^{-1} (After Li et al. 2006)

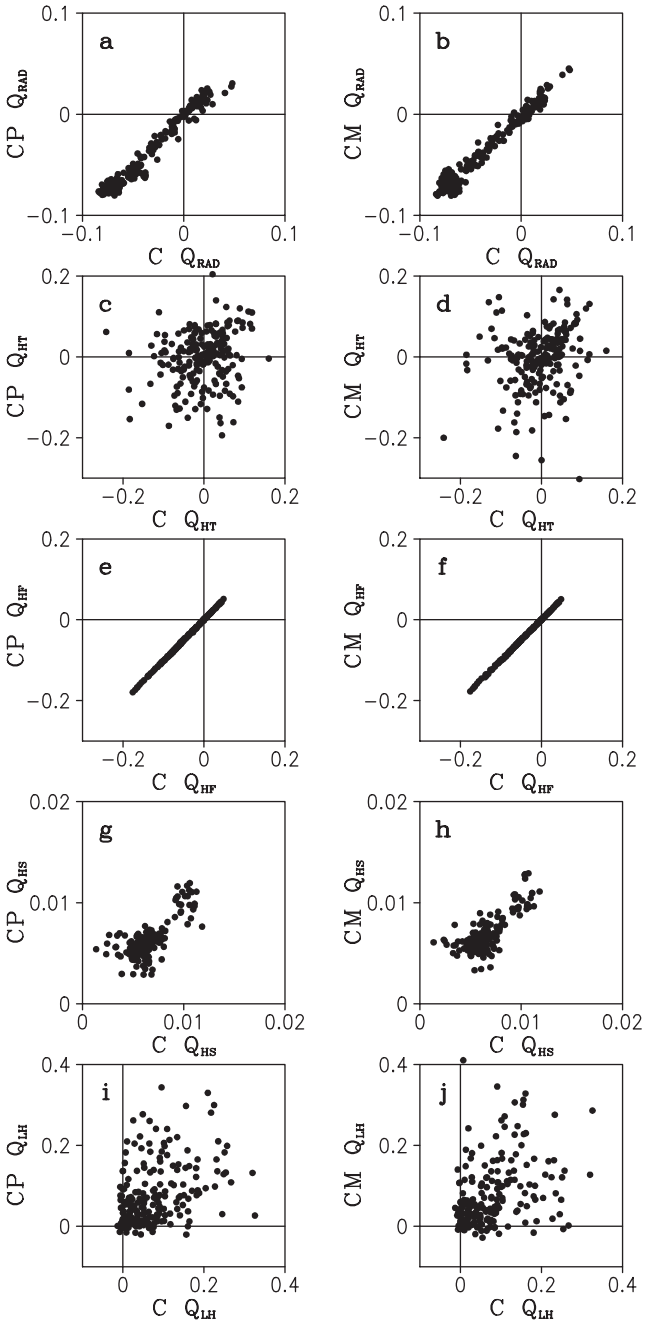

Fig. 3.13 Scatter plots of CP versus C for **a** Q_{RAD}, **c** Q_{HT}, **e** Q_{HF}, **g** Q_{HS}, **i** Q_{LH}; and of CM versus C for **b** Q_{RAD}, **d** Q_{HT}, **f** Q_{HF}, **h** Q_{HS}, **j** Q_{LH}. Unit is °C h^{-1} (After Li et al. 2006)

To explain the RMS differences in air temperature, the heat budgets are analyzed for three experiments. Zonal-mean mass-weighted mean thermal budget (2.1b) can be expressed by

$$Q_{HT} + Q_{HF} + Q_{HS} + Q_{LH} + Q_{RAD} = 0, \tag{3.3}$$

where

$$Q_{HT} = -\frac{\partial < T >}{\partial t}, \tag{3.3a}$$

$$Q_{HF} = -\left\langle \bar{u}^o \frac{\partial \bar{T}^o}{\partial x} \right\rangle - \left\langle \pi \bar{w}^o \frac{\partial \bar{\theta}}{\partial z} \right\rangle, \tag{3.3b}$$

$$Q_{HS} = H_s, \tag{3.3c}$$

$$Q_{LH} = \frac{1}{c_p} < Q_{cn} >, \tag{3.3d}$$

$$Q_{RAD} = \frac{1}{c_p} < Q_R > . \tag{3.3e}$$

In (3.3), Q_{HT} is local thermal change; Q_{HF} is thermal convergence, which is mainly contributed by vertical advective cooling/warming since imposed horizontal thermal advection is much smaller than the vertical advection; H_s is surface-sensible heat flux; Q_{LH} denotes the net latent heat release through phase changes among different cloud species; and Q_{RAD} is the radiative heating rate due to convergence of net flux of solar and infrared radiative fluxes. The RMS differences (also see Fig. 3.13) are $0.01\,^{\circ}\mathrm{C}$ for Q_{RAD}, $0.09\,^{\circ}\mathrm{C}$ for Q_{HT}, $0.001\,^{\circ}\mathrm{C}$ for Q_{FT}, $0.01\,^{\circ}\mathrm{C}$ for Q_{HS}, and $0.09\,^{\circ}\mathrm{C}$ for Q_{LH}, indicating that the RMS differences in condensational heating account for those in local thermal changes. The RMS differences in Q_{HT} and Q_{LH} are larger than the standard deviations ($0.07\,^{\circ}\mathrm{C}$ for Q_{HT} and $0.08\,^{\circ}\mathrm{C}$ for Q_{LH}).

$[P_{CND}]$ can be broken down into $[P_{CND1}]$ and $[P_{CND2}]$ as indicated by (3.2). The variation of $[P_{CND1}]$ is determined by specific humidity, whereas the variation of $[P_{CND2}]$ is determined by saturated specific humidity that is a function of temperature. $[P_{CND1}]$ and $[P_{CND2}]$ are negatively correlated with similar magnitudes of about $3 \times 10^3\,\mathrm{mm\,h^{-1}}$ (not shown), whereas $[P_{CND}]$ has the magnitudes of about $2\,\mathrm{mm\,h^{-1}}$ (see Fig. 3.12). Thus, vapor condensation rate is the small residual between the two large terms related to specific humidity and temperature-dependent saturated specific humidity. Furthermore, the variance in $[P_{CND}]$ between CP and C can be calculated by

$$\begin{aligned} Var(P_{CND,CP}, P_{CND,C}) = {} & Var(P_{CND1,CP}, P_{CND1,C}) + 2CoVar(P_{CND1,CP} - P_{CND1,C}, \\ & P_{CND2,CP} - P_{CND2,C}), + Var(P_{CND2,CP}, P_{CND2,C}) \end{aligned} \tag{3.4}$$

$$Var(P_{F,CP}, P_{F,C}) = \frac{1}{N} \sum_{I=1}^{N} [P_{F,CP}(I) - P_{F,C}(I)]^2, \tag{3.4a}$$

$$CoVar(P_{CND1,CP} - P_{CND1,C}, P_{CND2,CP} - P_{CND2,C}) = \frac{1}{N}\sum_{I=1}^{N}[P_{CND1,CP}(I) - P_{CND1,C}(I)][P_{CND2,CP}(I) - P_{CND2,C}(I)], \quad (3.4b)$$

where $N = 198$, $F = CND, CND1, CND2$. Equation (3.4) can be also applied to calculate the variance in P_{CND} between CM and C. $Var(P_{CND,CP},\ P_{CND,C})$, $Var(P_{CND1,CP},\ P_{CND1,C})$, $CoVar(P_{CND1,CP} - P_{CND1,C},\ P_{CND2,CP} - P_{CND2,C})$, and $Var(P_{CND2,CP},\ P_{CND2,C})$ are 0.142, 3,151.803, −6,304.007, and 3,152.346 $\mathrm{mm^2\ h^{-2}}$, respectively. $Var(P_{CND,CM},\ P_{CND,C})$, $Var(P_{CD1,CM},\ P_{CND1,C})$, $CoVar(P_{CND1,CM} - P_{CND1,C},\ P_{CND2,CM} - P_{CND2,C})$, and $Var(P_{CND2,CM},\ P_{CND2,C})$ are 0.167, 26,395.184, −52,792.895, and 26,397.871 $\mathrm{mm^2\ h^{-2}}$, respectively. The variances in $[P_{CND}]$ between CP/CM and C is four to five orders of magnitudes smaller than variances in $[P_{CND1}]$ and $[P_{CND2}]$ as well as covariances between CP/CM and C, implying that small perturbations in specific humidity and saturated specific humidity could cause large differences in $[P_{CND}]$.

The above analysis suggests that the improvement of cloud simulations may rely on the reduced error in initial conditions or improvement of accuracy of calculation of vapor condensation rate. Experiment CP shows that the small difference in PW during the integration can produce a large difference in cloud simulation. Thus, the improvement of calculation of vapor condensation rate may be the only way to produce accurate cloud simulations.

3.3 Comparison Between 2D and 3D Simulations

Due to limitations in computational power, 3D cloud-resolving simulations have been carried out less frequently than 2D simulations. With increasing computer power in recent decades, 3D cloud-resolving simulations have been conducted to study deep convection (e.g., Wilhelmson 1974; Miller and Pearce 1974; Pastushkov 1975; Klemp and Wilhelmson 1978; Cotton and Tripoli 1978; Clark 1979; Tao and Soong 1986; Redelsperger and Sommeria 1986; Redelsperger and Lafore 1988; Grabowski et al. 1998; Tompkins and Craig 1998).

It should be noted that some cloud structures and mass circulations may not be well represented by a 2D model. For example, Moncrieff and Miller (1976) showed that the 3D crossover flow pattern associated with propagating tropical squall lines can only be simulated in the 3D framework. In contrast, Rotunno et al. (1988) found that the 2D framework captures well the basic dynamics associated with long-lived squall lines in strong low-level shear. Tao and Soong (1986) and Tao et al. (1987) conducted a comparison study between 2D and 3D cloud-resolving model simulations in terms of the collective thermodynamic feedback effects and vertical transports of mass, sensible heat, and moisture and found profound similarities since both 2D and 3D models simulate the convective line structures well. Grabowski et al. (1998) compared 2D and 3D cloud-resolving model simulations with the GATE forcing in terms of their thermodynamic fields, surface heat fluxes, and surface

precipitation and showed similarity. Sui et al. (2005) showed the statistical equivalence between large-scale precipitation efficiency and cloud-microphysics precipitation efficiency in the calculations with grid data from both 2D cloud-resolving model simulation of tropical squall lines with the TOGA COARE forcing and 3D cloud-resolving model simulation of typhoons without imposed forcing. Wang et al. (2007) combined a 2D cloud-resolving model simulation with dual-Doppler and polarimetric radar analysis to study the evolution, dynamic structure, cloud microphysics, and rainfall process of a monsoon convection observed during South China Sea (SCS) summer monsoon onset, and found a good agreement between the model simulations and the radar observations. Therefore, we will use a 2D cloud-resolving model with the large-scale forcing of vertical velocity from the TOGA COARE in the following discussions unless otherwise clearly indicated.

References

Clark TL (1979) Numerical simulations with a three-dimension cloud model: lateral boundary condition experiments and multicellular severe storm simulations. J Atmos Sci 36:2191–2215

Cotton WR, Tripoli GJ (1978) Cumulus convection in shear flow: Three-dimensional numerical experiments. J Atmos Sci 35:1503–1521

Gao S, Cui X, Zhou Y, Li X (2005) Surface rainfall processes as simulated in a cloud resolving model. J Geophys Res, doi:10.1029/2004JD005467

Grabowski WW, Wu X, Moncrieff MW (1996) Cloud-resolving model of tropical cloud systems during Phase III of GATE. Part I: Two-dimensional experiments. J Atmos Sci 53:3684–3709

Grabowski WW, Wu X, Moncrieff MW, Hall WD (1998) Cloud-resolving model of tropical cloud systems during Phase III of GATE. Part II: Effects of resolution and the third spatial dimension. J Atmos Sci 55:3264–3282

Klemp JB, Wilhelmson RB (1978) The simulation of three-dimensional convective storm dynamics. J Atmos Sci 35:1070–1093

Li X, Sui CH, Lau KM, Chou MD (1999) Large-scale forcing and cloud-radiation interaction in the tropical deep convective regime. J Atmos Sci 56:3028–3042

Li X, Sui CH, Lau KM, Adamec D (2000) Effects of precipitation on ocean mixed-layer temperature and salinity as simulated in a 2-D coupled ocean-cloud resolving atmosphere model. J Meteor Soc Japan 78:647–659

Li X, Zhang S, Zhang DL (2006) Thermodynamic, cloud microphysics and rainfall responses to initial moisture perturbations in the tropical deep convective regime. J Geophys Res, doi:10.1029/2005JD006968

Miller MJ, Pearce RP (1974) A three-dimensional primitive equation model of cumulonimbus convection. Quart J Roy Meteor Soc 100:133–154

Moncrieff MW, Miller MJ (1976) The dynamics and simulation of tropical cumulonimbus and squall line. Quart J Roy Meteor Soc 102:373–394

Moncrieff MW, Krueger SK, Gregory D, Redelsperger JL, Tao WK (1997) GEWEX cloud system study (GCSS) working group 4: Precipitating convective cloud systems. Bull Am Meteor Soc 78:831–845

Pastushkov RS (1975) The effects of vertical wind shear on the evolution of convective clouds. Quart J Roy Meteor Soc 101:281–291

Redelsperger JL, Sommeria G (1986) Three-dimensional simulation of a convective strom: Sensitivity studies on subgrid parameterization and spatial resolution. J Atmos Sci 43:2619–2635

Redelsperger JL, Lafore JP (1988) A three-dimensional simulation of a tropical squall line: Convective organization and thermodynamic vertical transport. J Atmos Sci 45:1334–1356

Rotunno R, Klemp JB, Weisman ML (1988) A theory for strong, long-lived squall lines. J Atmos Sci 45:463–485

Sui CH, Lau KM, Takayabu Y, Short D (1997) Diurnal variations in tropical oceanic cumulus ensemble during TOGA COARE. J Atmos Sci 54:639–655

Sui CH, Li X, Lau KM (1998) Radiative-convective processes in simulated diurnal variations of tropical oceanic convection. J Atmos Sci 55:2345–2359

Sui CH, Li X, Yang MJ, Huang HL (2005) Estimation of oceanic precipitation efficiency in cloud models. J Atmos Sci 62:4358–4370

Takayabu YN, Lau KM, Sui CH (1996) Observation of a quasi-2-day wave during TOGA COARE. Mon Wea Rev 124:1892–1913

Tao WK, Soong ST (1986) The study of the response of deep tropical clouds to mesoscale processes: Three-dimensional numerical experiments. J Atmos Sci 43:2653–2676

Tao WK, Simpson J, Soong ST (1987) Statistical properties of a cloud ensemble: A numerical study. J Atmos Sci 44:3175–3187

Tao WK, Simpson J, McCumber M (1989) An ice-water saturation adjustment. Mon Wea Rev 117:231–235

Tompkins AM, Craig GC (1998) Radiative-convective equilibrium in a three-dimensional cloud-ensemble model. Quart J Roy Meteor Soc 124:2073–2097

Wang JJ, Li X, Carey L (2007) Evolution, structure, cloud microphysical and surface rainfall processes of a monsoon convection during the South China Sea Monsoon Experiment. J Atmos Sci 64:360–379

Wentz FJ, Gentemann C, Smith D, Chelton D (2000) Satellite measurements of sea surface temperature through clouds. Science 288:847–850

Wilhelmson RB (1974) The life cycle of a thunderstorm in three dimensions. J Atmos Sci 31: 1629–1651

Wu X, Grabowski WW, Moncrieff MW (1998) Long-term evolution of cloud systems in TOGA COARE and their interactions with radiative and surface processes. Part I: Two-dimensional cloud-resolving model. J Atmos Sci 55:2693–2714

Xu KM, Randall DA (1996) Explicit simulation of cumulus ensembles with the GATE Phase III data: Comparison with observations. J Atmos Sci 53:3710–3736

Yanai M, Esbensen S, Chu JH (1973) Determination of Bulk properties of tropical cloud clusters from large-scale heat and moisture budgets. J Atmos Sci 30:611–627

Chapter 4
Surface Rainfall Processes

Surface rain rate is one of the most important parameters in meteorology and hydrology, and its accurate measurement and quantitative estimate and forecast have significant economic and social impacts in rainfall-rich countries. However, it is very difficult to accurately measure and predict the surface rain rate since surface rainfall processes are associated with multiscale dynamic, thermodynamic, cloud microphysical and radiative processes and their interactions. The roles of clouds in moist air mass conservation have been given attention in the meteorological research community, in which cloud source/sink is included in the governing equation of water vapor with prognostic variables for cloud hydrometeors (e.g., Ooyama 1990, 2001; Bannon 2002). Following the derivation in section 2.2, the surface rain rate can be expressed by

$$P_s = Q_{WV} + Q_{CM}. \tag{4.1}$$

Kuo (1965, 1974) calculated the surface rain rate and local vapor increase by the large (∼95%) and small (∼5%) parts of the vapor sink (vapor convergence plus surface evaporation) in his cumulus parameterization scheme, respectively:

$$P_s = 0.95(Q_{WVF} + Q_{WVE}), \tag{4.2a}$$

$$-Q_{WVT} = 0.05(Q_{WVF} + Q_{WVE}). \tag{4.2b}$$

The addition of (4.2a and b) leads to

$$P_s = Q_{WVT} + Q_{WVF} + Q_{WVE} = Q_{WV}. \tag{4.3}$$

Thus, the comparison between (4.1) and (4.3) indicates that Q_{CM} is not included in the calculation of precipitation in Kuo's scheme. The impacts of clouds on surface rainfall processes as an important link between environment and precipitation are missing in Kuo's scheme. What roles do water vapor and cloud hydrometeors play in surface rainfall processes? How different are the surface rainfall processes in convective and stratiform clouds, and in different stages of convective development? These questions will be addressed in this chapter based on Gao et al. (2005), Cui and Li (2006), and Zhou et al. (2006).

4.1 Time Series of Zonal-Mean Surface Rain Rate

The experiment COARE uses the model with the imposed vertical velocity, zonal wind, horizontal thermal and vapor advection, and sea surface temperature. Figure 4.1 shows the time evolution of vertical distribution of the large-scale atmospheric vertical velocity, zonal wind, and *SST* during 19 December 1992–8 January 1993 that is imposed during the 21-day integration in experiment COARE. During this period, a westerly wind burst occurred along with a strong upward motion causing significant cooling over the ocean surface, which was associated with the intraseasonal variability (Webster and Lukas 1992; Sui et al. 1997b). From 19 to 25 December 1992, the upward motion was dominant, indicating strong convection. From 26 December 1992 to 3 January 1993, the downward motion became dominant, along with occasional upward motion, suggesting a dry phase. In the last few days, the moderate upward motion occurred. Diurnal and 2-day signals are also detected in Fig. 4.1a as indicated by Sui et al. (1997a) and Takayabu et al. (1996), respectively. The large-scale westerly winds increase significantly in the lower and mid troposphere and reach their maximum of 20 m s^{-1} at 600 mb around

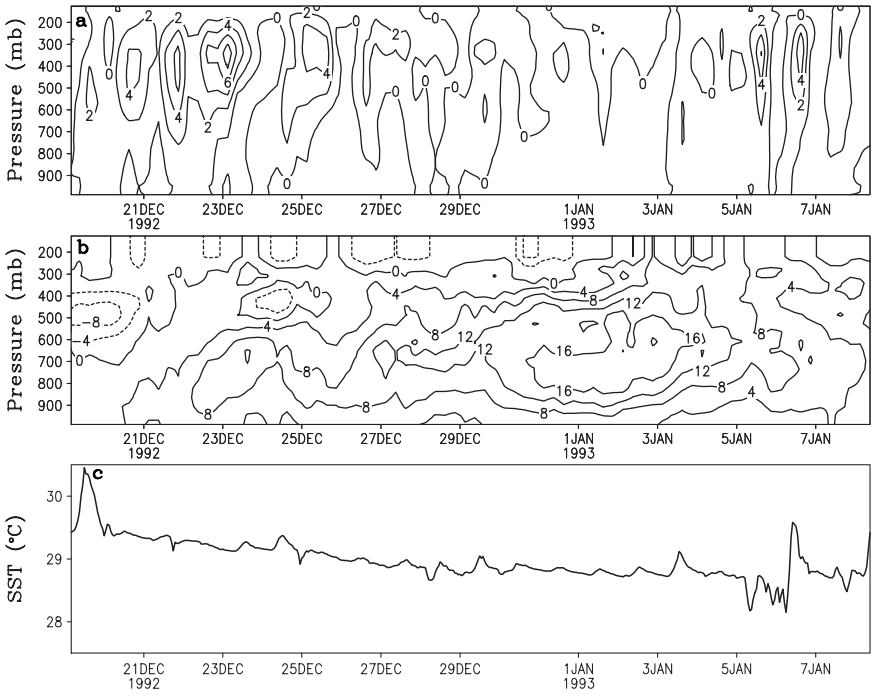

Fig. 4.1 Temporal and vertical distributions of **a** vertical velocity (cm s^{-1}), **b** zonal wind (m s^{-1}), and **c** time series of sea surface temperature (°C) observed and derived during a selected 21-day TOGA COARE period, which are imposed in the model as the forcing in experiment COARE (After Gao et al. 2005)

3 January 1993 (Fig. 4.1b). Except for the first and last 4 days, the *SST* had only a weak diurnal variation with a slowly decreasing trend (Fig. 4.1c). COARE also includes the imposed horizontal temperature and moisture advections derived by Sui et al. (1997a) (not shown), which have much smaller amplitudes than the vertical advections, respectively.

Figure 4.2 shows time series of zonal-mean P_s, Q_{WVT}, Q_{WVF}, Q_{WVE}, and Q_{CM}. The variation of the surface rain rate basically follows the variation of vapor convergence associated with the imposed vertical velocity. Its high-frequency fluctuation is associated with the local vapor and hydrometeor changes. The calculations of variances that measure the fluctuations indicate that the variance of rain rate ($0.18\,\mathrm{mm^2\,h^{-2}}$) is dominated by those of the local vapor change ($0.11\,\mathrm{mm^2\,h^{-2}}$) and vapor convergence ($0.12\,\mathrm{mm^2\,h^{-2}}$) as well as the local condensate change ($0.03\,\mathrm{mm^2\,h^{-2}}$), whereas the magnitudes of other variances and covariances are relatively small ($<0.01\,\mathrm{mm^2\,h^{-2}}$). The linear correlation coefficients between P_s and Q_{WVT}, P_s and Q_{WVF}, P_s and Q_{WVE}, and P_s and Q_{CM} are 0.54, 0.62, 0.01, and 0.16, respectively. There are 486 samples and the critical correlation coefficient at the 1% significance level in the student t-test is 0.12. Thus, the variation of the surface rain rate can be largely explained by the local vapor change and vapor convergence. The results suggest that Kuo's cumulus parameterization scheme cannot predict the variation of the surface rain rate because Q_{WVT} and $Q_{WVF} + Q_{WVE}$ have similar variances but their linear correlation coefficient is only -0.16, which is marginally statistically significant.

Q_{WV} and P_s are closely correlated with the coefficient of 0.92. Their RMS difference is $0.17\,\mathrm{mm\,h^{-1}}$, which is much smaller than the standard deviation of P_s ($0.43\,\mathrm{mm\,h^{-1}}$). Thus, the variation of vapor sink (Q_{WV}) largely explains the variation of surface rain rate (P_s). The approximate balance between the surface rain rate and vapor sink guarantees reasonable simulations of the zonal-mean surface rain rate in the cloud-resolving model if the zonally uniform horizontal and vertical moisture advections imposed in the model are derived from moisture budgets.

The magnitudes of Q_{CM} are generally smaller than those of Q_{WV}, but they have similar magnitudes on 3 January 1993 when the negative Q_{CM} with the maximum negative value of up to $-1\,\mathrm{mm\,h^{-1}}$ compensates for the overestimation of P_s with Q_{WV} significantly. Q_{WV} and Q_{CM} are negatively correlated, but their linear correlation coefficient is small (-0.33). The negative correlation in which a negative Q_{CM} associated with a positive Q_{WV} suggests that the increase of cloud hydrometeors is a result of vapor loss. In particular, Q_{WV} and Q_{CM} have the same magnitudes but they have the opposite signs on 26 and 31 December 1992, indicating that the entire vapor sink supports the growth of cloud hydrometeors during the genesis of tropical convection.

Accuracy of the calculations of the surface rain rate with the vapor sink (in Kuo's scheme) can be evaluated with magnitudes of the cloud source/sink (Q_{CM}). Figure 4.3 shows zonal-mean Q_{CM} ($= P_s - Q_{WV}$) versus zonal-mean P_s. A positive Q_{CM} measures the underestimation of P_s with Q_{WV}, whereas a negative Q_{CM} denotes the overestimation of P_s. Maximum positive ($1.2\,\mathrm{mm\,h^{-1}}$) and negative ($-0.8\,\mathrm{mm\,h^{-1}}$) Q_{CM} occur around $1\,\mathrm{mm\,h^{-1}}$ of P_s. When P_s is small

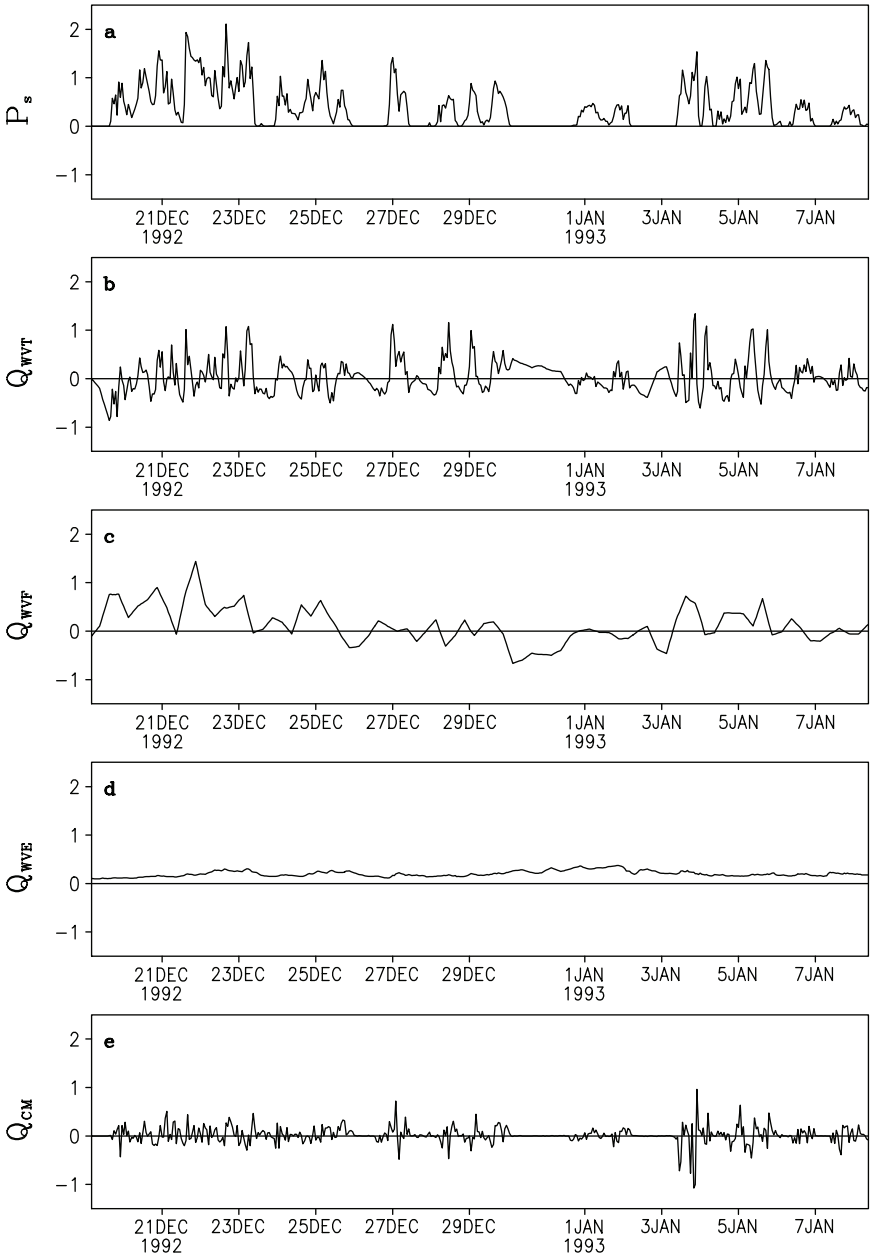

Fig. 4.2 Time series of zonal-mean P_s in **a** Q_{WVT} in **b**, Q_{WVF} in **c**, Q_{WVE} in **d**, and Q_{CM} in **e** during the 21-day integration in COARE (mm h^{-1})

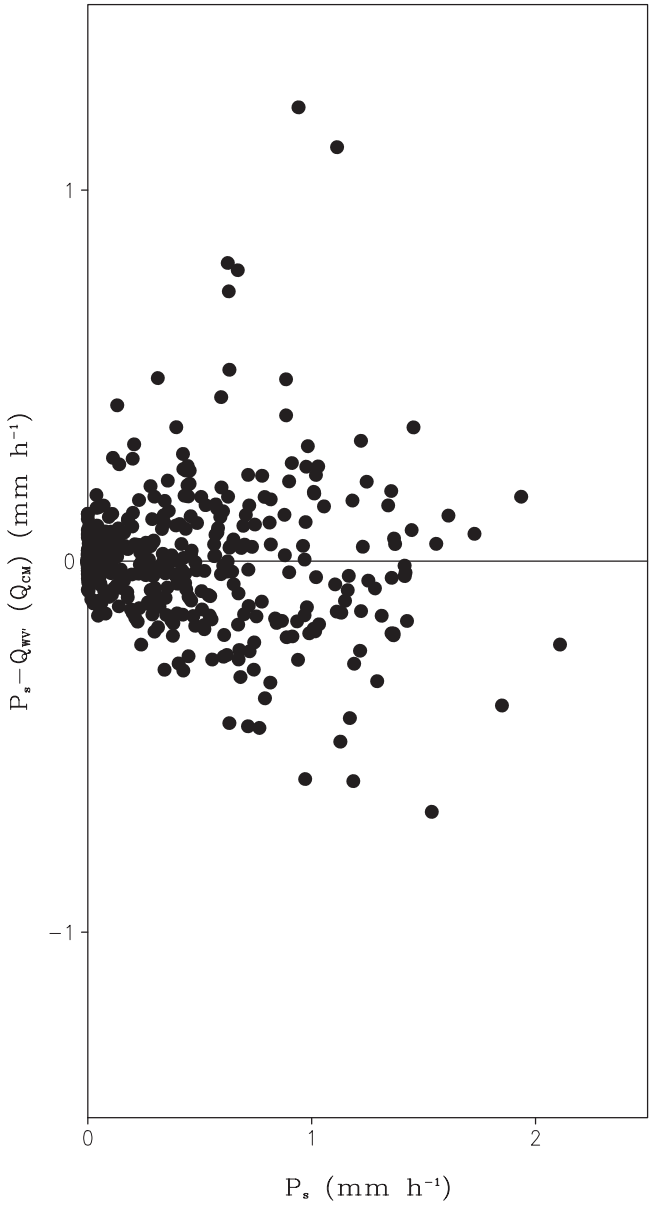

Fig. 4.3 Zonal-mean Q_{CM} $(P_s - Q_{WV})$ versus zonal-mean P_s in COARE (mm h^{-1}) (After Gao et al. 2005)

(0–0.2 mm h^{-1}), the amplitudes of Q_{CM} could be larger than P_s. The results show a significant contribution from the cloud source/sink in the calculations of surface rain rates, and particularly in the estimation of small surface rain rates.

Since clouds consist of water and ice clouds, the cloud source/sink (Q_{CM}) can be further broken into water cloud $(Q_{CMW} = -\partial[q_2]/\partial t,\ q_2 = q_c + q_r)$ and ice

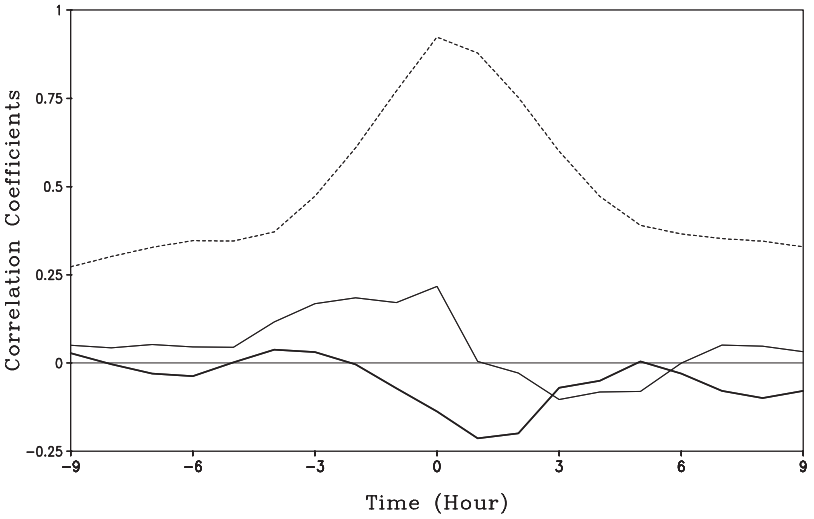

Fig. 4.4 Lag correlation coefficients between P_s and Q_{CMI} (dark solid), between P_s and Q_{CMW} (light solid), and between P_s and Q_{WV} (dashed) calculated with the zonal-mean data from COARE (After Gao et al. 2005)

cloud ($Q_{CMI} = -\partial[q_3]/\partial t,\ q_3 = q_i + q_s + q_g$) sources/sinks. The linear correlation coefficient between Q_{CMI} and Q_{CM} (0.61) is larger than that between Q_{CMW} and Q_{CM} (0.4). The RMS difference between Q_{CMI} and Q_{CM} ($0.15\,\mathrm{mm\,h^{-1}}$) is smaller than that between Q_{CMW} and Q_{CM} ($0.166\,\mathrm{mm\,h^{-1}}$). This suggests that the variation of ice hydrometeors may contribute to the variation of cloud source/sink more than the variation of water hydrometeors does.

To detect the precursor for development of surface rainfall, the phase differences between P_s and its contributors ($Q_{WV}/Q_{CMW}/Q_{CMI}$) are analyzed by calculating lag correlation coefficients (Fig. 4.4). Lag correlation coefficients between P_s and Q_{WV} and between P_s and Q_{CMW} have maximum values of 0.92 and 0.21 at lag hour 0, respectively, indicating that the surface rain rate is in-phase with the vapor sink and water cloud sink in tropical deep convective regime. The lag correlation coefficient between P_s and Q_{CMI} has the maximum negative value (-0.23) at lag hours 1–2. The discussion of statistical significance for this phase lag can be found in Gao et al. (2005). A positive lag time means that Q_{CMI} leads P_s by 1–2 h, while the negative correlation coefficient indicates that P_s and Q_{CMI} are out of phase. Since a negative Q_{CMI} denotes local ice hydrometeor gain, the ice clouds develop 1–2 h ahead of subsequent gain in the surface rainfall.

4.2 Time-Mean Surface Rainfall Processes

The time and zonal means of P_s, Q_{WVT}, Q_{WVF}, Q_{WVE}, and Q_{CM} are 0.37, 0.03, 0.12, 0.2, and $0.02\,\mathrm{mm\,h^{-1}}$, respectively. This indicates that 8.1%, 32.4%, 54.1%, and 5.4% of P_s come from Q_{WVT}, Q_{WVF}, Q_{WVE}, and Q_{CM}, respectively. Thus,

Table 4.1 Time means of fractional cloud coverage, *IWP*, *LWP*, P_s, Q_{WVT}, Q_{WVF}, Q_{WVE}, and Q_{CM} over clear-sky regions, raining stratiform regions, convective regions, and nonraining stratiform regions and their sums (zonal means) in COARE (After Cui and Li 2006)

	Clear-sky regions	Raining stratiform regions	Convective regions	Nonraining stratiform regions	Zonal mean
Fractional coverage (%)	47.1	9.9	4.3	38.7	100.0
IWP (mm)	0.000	0.080	0.027	0.038	0.145
LWP (mm)	0.000	0.083	0.077	0.011	0.171
P_s (mm h^{-1})	0.000	0.151	0.217	0.000	0.368
Q_{WVT} (mm h^{-1})	−0.064	0.197	−0.116	0.012	0.029
Q_{WVF} (mm h^{-1})	−0.029	−0.165	0.410	−0.097	0.120
Q_{WVE} (mm h^{-1})	0.090	0.024	0.014	0.075	0.203
Q_{CM} (mm h^{-1})	0.003	0.096	−0.091	0.009	0.017

the surface evaporation rate and vapor convergence associated with the imposed vertical velocity mainly contribute to the time- and zonal-mean surface rain rate. Since zonal-mean data include information from convective, raining stratiform, nonraining stratiform clouds as well as clear sky regions, Cui and Li (2006) applied the partitioning method to each grid point to determine the type (clear sky, raining stratiform, convective, or nonraining stratiform) and took the summations of grid points, and other quantities (e.g., *IWP, LWP*, and the others) and divided them by the total zonal gird points (512) and the length of hourly data (486). They used the time-mean data to study the processes from different regions that contribute to zonal-mean rainfall.

In COARE, convective clouds (4.3%) occupy smaller areas than raining stratiform clouds (9.9%) do (Table 4.1). In clear-sky regions, Q_{WVE} (0.090 mm h^{-1}) is balanced by Q_{WVT} (−0.064 mm h^{-1}) and Q_{WVF} (−0.029 mm h^{-1}), indicating that the surface evaporation is the only vapor source. One third of the mean evaporation rate is used to offset the vapor divergence associated with subsidence, whereas two thirds is used to moisten the atmosphere.

Over raining stratiform regions, *IWP* (0.080 mm) and *LWP* (0.083 mm) are similar. P_s (0.151 mm h^{-1}), Q_{WVT} (0.197 mm h^{-1}), Q_{WVF} (−0.165 mm h^{-1}), and Q_{CM} (0.092 mm h^{-1}) have similar magnitudes, while Q_{WVE} (0.024 mm h^{-1}) is relatively small. Thus, about a half of magnitudes of the sum of local vapor loss and local hydrometeor loss/hydrometeor convergence loss is cancelled out by the vapor divergence, whereas the other half feeds the stratiform rainfall.

Over convective regions, *IWP* (0.027 mm) is smaller than *LWP* (0.077 mm), suggesting that the water hydrometeors are more common than the ice hydrometeors. Q_{WVF} (0.410 mm h^{-1}) supports convective rainfall ($P_s = 0.217$ mm h^{-1}), local atmospheric moistening ($Q_{WVT} = -0.116$ mm h^{-1}), and local cloud growth ($Q_{CM} = -0.091$ mm h^{-1}). Q_{WVE} (0.014 mm h^{-1}) is negligibly small. The small surface evaporation in convective and raining stratiform regions is also demonstrated

by the analysis of moisture budget by Gao et al. (2006) in their 2D coupled ocean-cloud-resolving atmosphere model experiment.

Over nonraining stratiform regions, *IWP* (0.038 mm) is significantly larger than *LWP* (0.011 mm), indicating the dominance of ice hydrometeors. Q_{WVE} (0.075 mm h^{-1}) compensates vapor divergence ($Q_{WVF} = -0.097$ mm h^{-1}), local atmospheric drying ($Q_{WVT} = 0.012$ mm h^{-1}), and local hydrometeor loss ($Q_{CM} = 0.009$ mm h^{-1}). The vapor divergence associated with the subsidence has a larger magnitude than does the surface evaporation that leads to local atmospheric drying ($Q_{WVT} = 0.012$ mm h^{-1}).

Thus, the zonal-mean surface evaporation flux comes mainly from the nonraining regions (clear sky and nonraining stratiform regions), whereas zonal-mean vapor convergence is mainly from the convective regions. Therefore, in addition to rainfall forced by the imposed upward motion, surface evaporation pumps water vapor into rainfall-free regions, and the water vapor is transported from rainfall-free regions into rainfall regions, which feeds rainfall.

4.3 Surface Rainfall Processes Associated with Individual Cloud

Since the surface rain rate at model grid is much larger than the zonal-mean value, the grid data (in the box in Fig. 4.5) are analyzed by Zhou et al. (2006). The box along the propagation of the major rainband in a life cycle of tropical convection has a zonal length of 18 km and a temporal length of 15 h. Hours 6–11, 12–18,

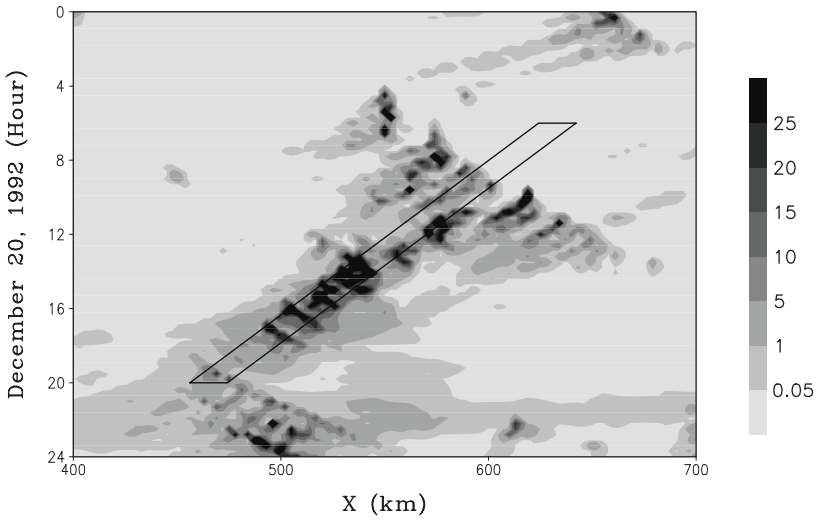

Fig. 4.5 Time evolution and horizontal distribution of surface rain rate (mm h^{-1}) within 400–700 km on 20 December 1992 simulated in COARE. The box between hours 6 and 20 (0600–2000 LST) is used to analyze the surface rainfall processes during the life cycle of convection (After Li et al. 2002)

Table 4.2 Contributions of Q_{WV} and Q_{CM} to P_s in case A (hours 6–11), case B (hours 12–18), and case C (hours 19–20) on 19–20 December 1992 in the box shown in Fig. 4.5 (After Zhou et al. 2006)

Case	P_s (mm h^{-1})	Q_{WV} (mm h^{-1})	Q_{CM} (mm h^{-1})
A	3.3	4.54	−1.24
B	15.9	19.6	−3.7
C	1.9	2.6	−0.7

Table 4.3 Contribution of Q_{WV} and Q_{CM} to P_s in case BL (the left half of the box in hours 13–15 in Fig. 4.5) and case BR (the right half) (mm h^{-1}) (After Zhou et al. 2006)

Case	P_s	Q_{WV}	Q_{CM}
BL	41.7	31.1	10.6
BR	19.5	35.8	−16.3

and 19–20 represent the genesis, development, and decay of tropical convection, respectively, which are denoted by cases A, B, and C. The time- and zonal-mean surface rain rates are 3.3 mm h^{-1} in case A, 15.9 mm h^{-1} in case B, and 1.9 mm h^{-1} in case C. Table 4.2 shows contributions of Q_{WV} and Q_{CM} to P_s in cases A, B, and C, respectively. In all three cases, Q_{WV} is positive whereas Q_{CM} is negative. Calculations with the water vapor overestimate P_s by 38% in case A, 23% in case B, and 37% in case C, respectively.

The analysis is further carried out in the left half (case BL) and the right half (case BR) of the box in hours 13–15 for mature convection. Maximum upward motion appears between 500 and 750 mb with the surface rain rate of 41.7 mm h^{-1} in case BL, whereas maximum upward motion occurs around 400 mb with the surface rain rate of 19.5 mm h^{-1} in case BR [see Fig. 6 in Li et al. (2002)]. Deep convective clouds are dominant in case BL, whereas anvil clouds are dominant in case BR. In case BL, P_s (41.7 mm h^{-1}) is contributed to by both Q_{WV} (31.1 mm h^{-1}) and Q_{CM} (10.6 mm h^{-1}) (Table 4.3). This suggests that the calculation with water vapor underestimates P_s by 25% in deep convective clouds during the development of the convective system. It is interesting to note that in both BL and BR, calculations of surface rain rates with water vapor (Q_{WV}) are similar; the difference of surface rain rate (P_s) depends on the effects of cloud condensate (Q_{CM}).

The linear correlation coefficient between Q_{WV} and Q_{CM} using all grid data is −0.85, which exceeds the 1% confidence level. This indicates that Q_{WV} and Q_{CM} are negatively correlated much more highly in the grid data than in the zonal-mean data (Gao et al. 2005). The regression equation can be expressed by

$$Q_{CM} = 2.6 - 0.7 Q_{WV}. \tag{4.4}$$

This statistical relation reveals that the overestimate of P_s with water vapor is associated with the growth of clouds. When Q_{WV} becomes negative, Q_{CM} will be positive. The cloud condensate plays an active role in surface rainfall processes and assures a positive value for surface rain rate.

Q_{CM} is further broken into Q_{CMW} and Q_{CMI} for water and ice clouds, respectively. The variation of Q_{CM} is largely contributed by that of Q_{CMW}. Their regression equation can be expressed by

$$Q_{CM} = -0.17 + 1.02 Q_{CMW} \cong Q_{CMW}. \tag{4.5}$$

The linear correlation coefficient is 0.91, which is much larger than the linear correlation coefficient calculated with the zonal-mean data (0.4) (Gao et al. 2005). Gao et al. (2005) showed that the linear correlation coefficient between Q_{CM} and Q_{CMI} (0.61) is larger than that between Q_{CM} and Q_{CMW} (0.4) in the calculations with the zonal-mean data, whereas Zhou et al. (2006) displayed that the results are opposite in the calculations with the grid data. This may be due to the fact that the vertical structures of vertical velocity for water and ice clouds can be separated in the grid data [e.g., Fig. 6 in Li et al. (2002)] and the large surface rain rate is associated with a large Q_{CM} as a result of a large Q_{CMW} (e.g., in case BL), whereas the zonal-mean data show that the maximum zonal-mean upward motions appear in 350–450 mb and the surface rain rate, ice-cloud and water-cloud sources/sinks are positively correlated. Thus, contribution of cloud hydrometeors to surface rain rate comes mainly from the variation of water hydrometeors in tropical convection in the analysis of grid data.

References

Bannon PR (2002) Theoretical foundations for models of moist convection. J Atmos Sci 59: 1967–1982

Cui X, Li X (2006) Role of surface evaporation in surface rainfall processes. J Geophys Res, doi:10.1029/2005JD006876

Gao S, Cui X, Zhou Y, Li X (2005) Surface rainfall processes as simulated in a cloud resolving model. J Geophys Res, doi:10.1029/2004JD005467

Gao S, Ping F, Cui X, Li X (2006) Short timescale air-sea coupling in the tropical deep convective regime. Meteor Atmos Phys 93:37–44

Kuo HL (1965) On formation and intensification of tropical cyclones through latent heat release by cumulus convection. J Atmos Sci 22:40–63

Kuo HL (1974) Further studies of the parameterization of the influence of cumulus convection on large-scale flow. J Atmos Sci 31:1232–1240

Li X, Sui CH, Lau KM (2002) Dominant cloud microphysical processes in a tropical oceanic convective system: A 2-D cloud resolving modeling study. Mon Wea Rev 130:2481–2491

Ooyama KV (1990) A thermodynamic foundation for modeling the moist atmosphere. J Atmos Sci 47:2580–2593

Ooyama KV (2001) A dynamic and thermodynamic foundation for modeling the moist atmosphere with parameterized microphysics. J Atmos Sci 58:2073–2102

Sui CH, Lau KM, Takayabu Y, Short D (1997a) Diurnal variations in tropical oceanic cumulus ensemble during TOGA COARE. J Atmos Sci 54:639–655

Sui CH, Li X, Lau KM, Adamec D (1997b) Multi-scale air-sea interactions during TOGA COARE. Mon Wea Rev 125:448–462

Takayabu YN, Lau KM, Sui CH (1996) Observation of a quasi-2-day wave during TOGA COARE. Mon Wea Rev 124:1892–1913

Webster PJ, Lukas R (1992) TOGA COARE: The Coupled Ocean-Atmosphere Response Experiment. Bull Am Meteor Soc 73:1377–1416

Zhou Y, Cui X, Li X (2006) Contribution of cloud condensate to Surface rain rate. Prog Nat Sci 16:967–973

Chapter 5
Tropical Cloud Clusters

Observational studies using satellite measurements have revealed that cloud cluster groups (super cloud clusters) and individual cloud clusters embedded within them propagate in different directions and have different evolution and spatial distributions (e.g., Nakazawa 1988; Lau et al. 1991; Sui and Lau 1992). These hierarchical cloud structures and behaviors can be simulated with a 2D cloud-resolving model (e.g., Peng et al. 2001; Ping et al. 2007). The kinetics and spatial structures of cloud clusters are discussed in this chapter based on Ping et al. (2007). The cloud clusters with different propagations also can merge, and merging processes can affect intensity and spatial structures of merged cloud clusters. The composite analyses of vertical structure of temperature and water vapor anomalies, cloud hydrometeors, and surface rainfall processes before and after merging are compared in this chapter. The surface rainfall processes associated with the development of cloud clusters by Wang et al. (2007) are also discussed.

5.1 Introduction

Lau et al. (1991) analyzed IR radiance measurements at cloud top from the Japanese geostationary meteorological satellite (GMS) and showed the observed cloud clusters with a hierarchy of collective motions at timescales of 1 day, 2–3 days, and 10–15 days. The 1–15-day timescale is closely related to the intraseasonal oscillation, and the super cloud clusters propagate eastward along the equator from the Indian Ocean to the western Pacific all around the global tropics. The cloud clusters embedded in the super cloud clusters have the 2–3-day timescale, and propagate in the opposite direction of the super cloud clusters. The diurnal timescale is significant in the cloud clusters, in which the signals are more pronounced over the continent than over the open ocean. Sui and Lau (1992) analyzed the First GARP Global Experiment IIIb circulation data along with the Japanese GMS-1 IR data to study the atmospheric multiscale variabilities over the tropical western Pacific during the 1979 northern hemisphere. Two intraseasonal oscillations propagate eastward from

the Indian Ocean to the western Pacific. Over the western Pacific warm pool, the intraseasonal oscillations develop and move barely with the enhanced rotational circulations. The intraseasonal oscillations interact with regional and synoptic-scale systems such as monsoon circulations. The intraseasonal oscillations also excite 2–4-day disturbances. Sui and Lau also found that the diurnal signal becomes strong when the intraseasonal oscillation loses the intensity, whereas the opposite is true.

The hierarchical cloud structures and behaviors have been given much attention in the meteorological research community for recent decades. Various numerical models have been employed to search the physical processes controlling their formation, development, and propagation (e.g., Lau et al. 1989; Numaguti and Hayashi 1991; Chao and Lin 1994; Yano et al. 1995). Chao and Lin (1994) simulated hierarchical cloud patterns with a 2D hydrostatic model and found that the simulations of hierarchical cloud clusters are sensitive to spatial-mean flows and cumulus parameterization schemes. The spatial-mean flows are critical in organizing patterns for cloud clusters and the cumulus parameterization schemes are crucial to their formation. Peng et al. (2001) conducted a 2D cloud-resolving experiment over a large domain, in which there is a warm pool surrounded by cold pools that mimics the equatorial western Pacific, to examine the genesis and evolution of hierarchical cloud clusters. The model used an open lateral boundary. The simulated cloud clusters have the typical horizontal scale of a few hundred kilometers. The new cloud clusters are generated at the leading edge of a propagating cold-air pool. The largest cloud cluster has a horizontal scale of 3,000 km that consists of four cloud clusters having a life cycle of 12–36 h. The condensational heating associated with the constituent cloud clusters initiates an overall tropospheric-deep gravity wave. The cumulative cluster-induced wave effects lead to the development of new cloud clusters.

5.2 Kinetics and Spatial Structures of Cloud Clusters

Ping et al. (2007) analyzed kinematics and spatial structures of tropical cloud clusters using the 2D simulation data in COARE. There are four eastward-propagating rainbands as shown in Fig. 5.1 (cloud clusters A–D; CCA, CCB, CCC, CCD hereafter), a westward-propagating rainband (cloud clusters F; CCF hereafter), and a newly formed rainband (cloud clusters E; CCE hereafter). CCD shows that the individual cloud propagates westward while the cloud clusters move eastward. CCF exhibits that the individual cloud moves eastward while the cloud clusters propagate westward. This is consistent with the observations reported by Nakazawa (1988) and model simulations reported by Peng et al. (2001). CCA and CCB merge into CCF. CCC weakens and dissipates while it moves eastward, whereas CCD undergoes genesis, development, and weakening during its eastward-propagating course. CCE forms between the weakening CCD and CCF.

At 1600 LST, CCF and CCA extend to upper and mid troposphere, respectively (Fig. 5.2a). Both share a negative vorticity circulation centered at 550 mb

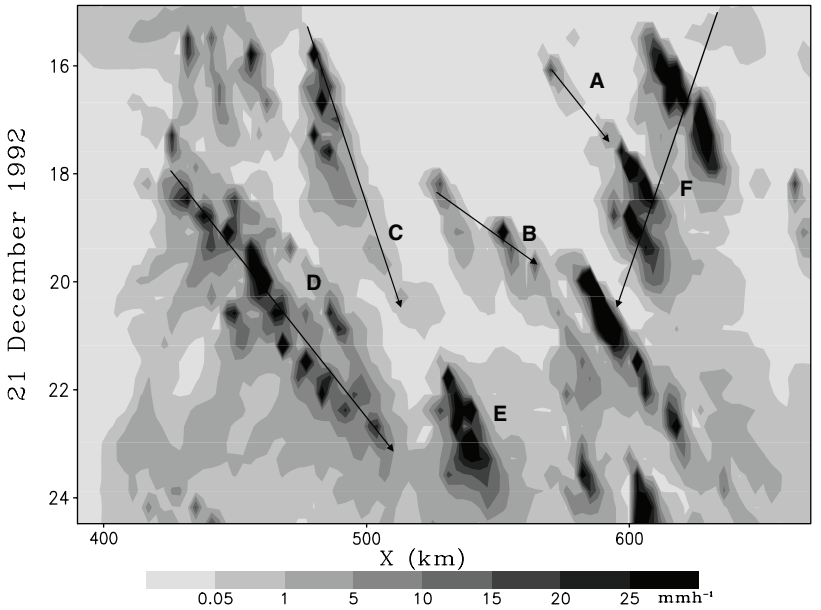

Fig. 5.1 Temporal evolution and zonal distribution of surface rain rate $(\mathrm{mm\,h^{-1}})$ simulated in COARE on 21 December 1992. Arrows indicate propagation directions of cloud clusters A–F (After Ping et al. 2007)

and 590 km. CCF is supported by an upward motion in the eastern part of the circulation, whereas CCA is suppressed by a weak downward motion in the western part. The two clusters move closer as the circulation associated with the clusters weakens and propagates upward at 1700 LST (Fig. 5.2b). At 1800 LST, CCA merges with CCF around 600 km, west of the previous CCF and east of the previous CCA (Fig. 5.2c). The merging CCF extends to 100 mb. Meanwhile, CCB forms and is 70–80 km away from CCF. A circulation linking CCF and CCB is developing above 500 mb. At 1900 LST, with the weakening of circulation, the clouds extend upward to form ice clouds while moving eastward (Fig. 5.2d). At 2000 LST, CCB merges with CCF around 580 km while the circulation associated with the cells disappears (Fig. 5.2e). The downward circulation develops around CCF at 2100 LST (Fig. 5.2f), which leads to its dissipation at 2200 LST (Fig. 5.2g).

5.3 Cloud Merger

Cloud merger has been observed and studied for decades (e.g., Malkus 1954; Simpson and Woodley 1971; Leavy and Houze 1979). Simpson (1980) showed the important roles of cumulus downdrafts and associated cold outflows in the cloud merging process. Tao and Simpson (1984) conducted 48 experiments with a 2D

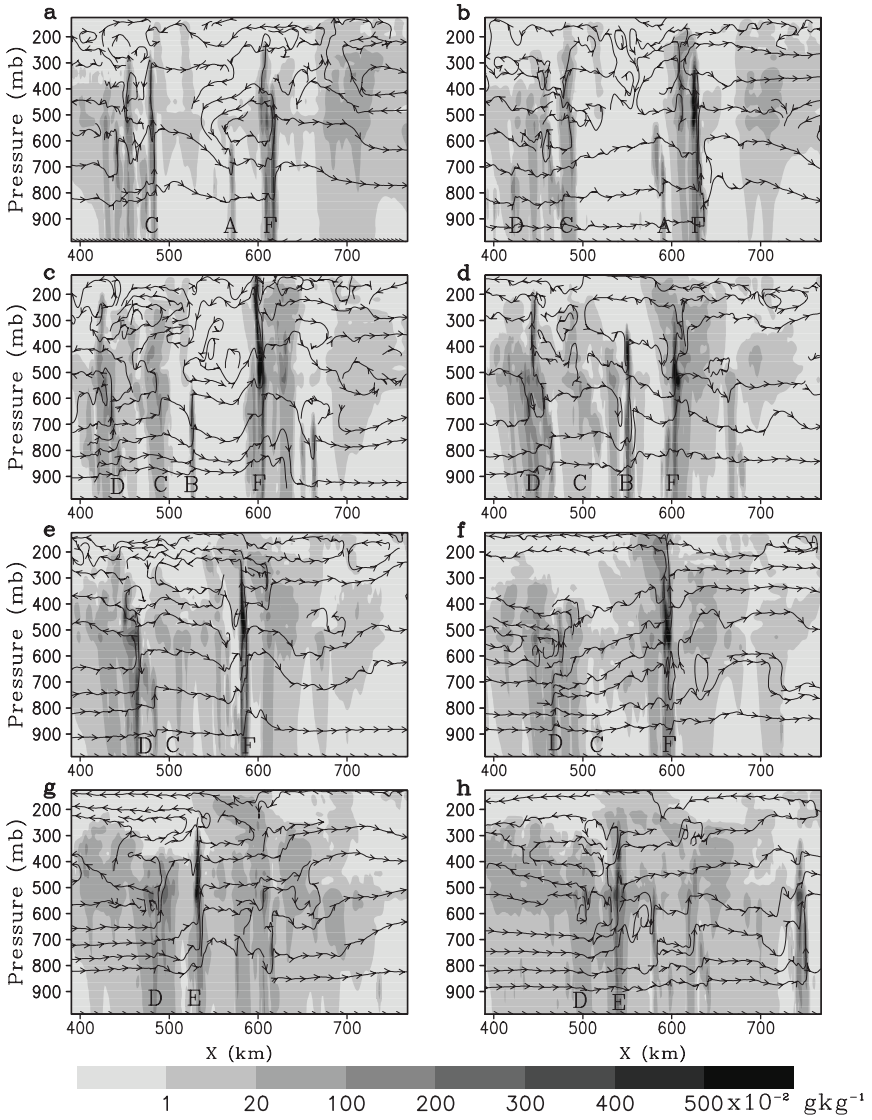

Fig. 5.2 Zonal-vertical cross sections of streamlines and total hydrometeor mixing ratio (background shading) for cloud clusters A–F simulated in COARE in 1-h interval from 1600 to 2300 LST 21 December 1992 (After Ping et al. 2007)

multicell model and found a total of 14 cloud merging cases. One of the 14 cloud merging cases (the case with a merger of two cells in different cycle stages) is very similar to cloud clusters A and B here, except that the weak cell has a significant eastward propagation in this study whereas it barely moves in their study. Tao and Simpson showed that the downdraft and cold outflow associated with the strong cell

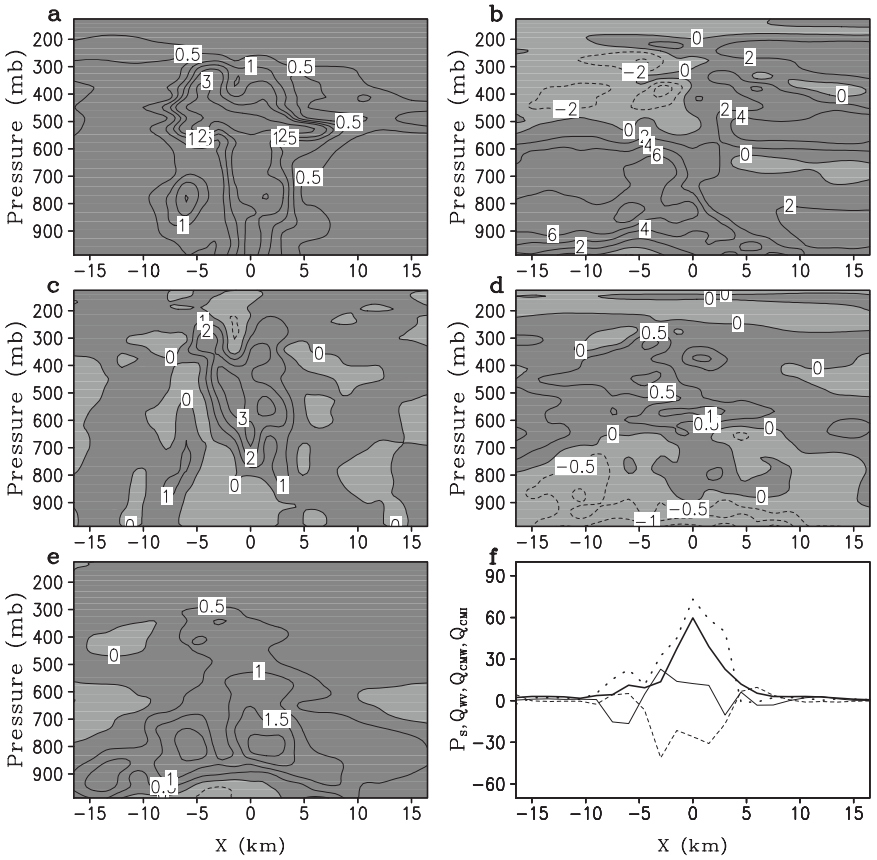

Fig. 5.3 Composites of zonal and vertical distributions of (a) total hydrometeor mixing ratio $(\mathrm{g\ kg^{-1}})$; (b) zonal wind $(\mathrm{m\ s^{-1}})$; (c) vertical velocity $(\mathrm{m\ s^{-1}})$; (d) temperature perturbation (°C); (e) specific humidity perturbation $(\mathrm{g\ kg^{-1}})$; and (f) P_s (dark solid), Q_{WV} (dot), Q_{CMW} (light solid), Q_{CMI} (dashed) $(\mathrm{mm\ h^{-1}})$ for cloud cluster F1 simulated in COARE (After Ping et al. 2007)

induce the formation of a new cell between the two old cells. The weak old cell eventually merges with the new cell while the strong old cell dissipates into an anvil cloud. In contrast, CCF and CCA/CCB move together, causing the merger.

To examine the impacts of merging processes in CCF, composites of CCF before merging (CCF1) and after merging (CCF2) are calculated using the data of 1700 and 1900 LST and of 1800 and 2000 LST, respectively (Figs. 5.3 and 5.4). For the composite calculations, the maximum surface rain rate is defined as the center point $(x = 0)$ and the area of interest extends 16.5 km to the west and east of this point for each hour of the cluster's existence. The composite is temporally averaged over this period. Both clusters are limited to the zonal size of 15 km. CCF2 $(4\,\mathrm{g\ kg^{-1}})$ has a larger total hydrometeor mixing ratio (q_1) than CCF1 $(2.5\,\mathrm{g\ kg^{-1}})$ does. CCF2 displays smaller zonal scales of perturbations than does CCF1 in the

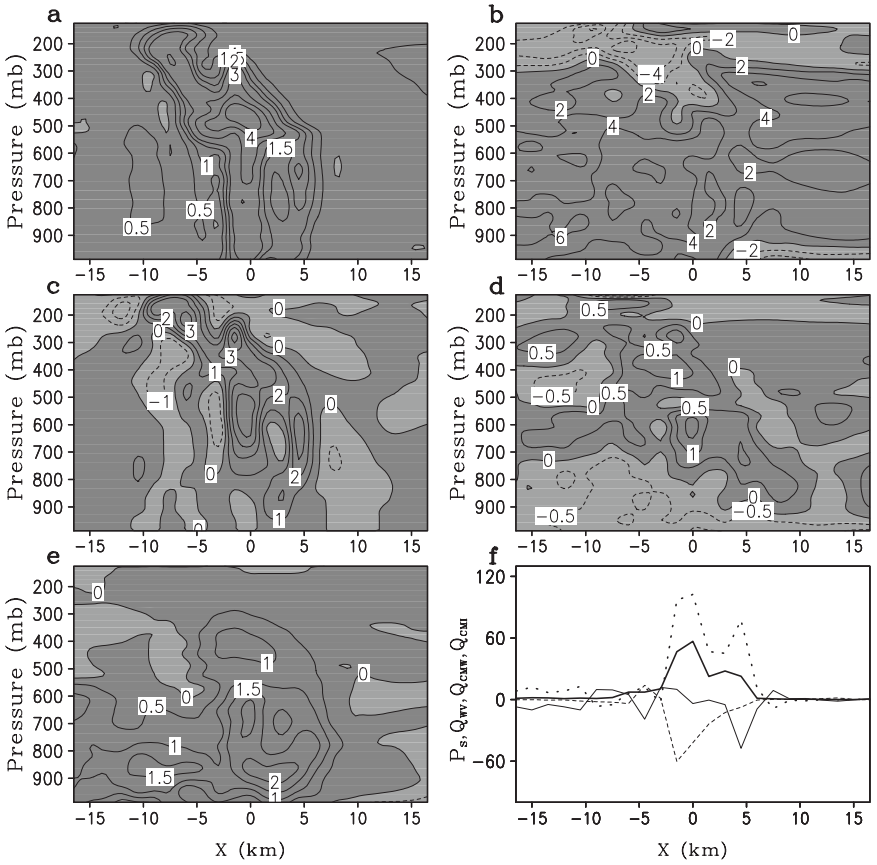

Fig. 5.4 As in Fig. 5.3 except for cloud cluster F2 (After Ping et al. 2007)

total hydrometeor mixing ratio, updrafts and downdrafts, and temperature and specific humidity perturbations. The weak westerly winds advect the maximum total hydrometeor mixing ratio to the east while CCF moves westward, suggesting that westerly winds may be accountable for eastward propagation but may not be responsible for the propagation of cloud clusters. While maximum negative Q_{CMI} occurs at −3 km in CCF1 and −1.5 km in CCF2 (Figs. 5.3f and 5.4f), maximum negative Q_{CMW} appears at −6 km in CCF1 and 4.5 km in CCF2. The positive Q_{WV} mainly balances the maximum negative Q_{CMW} while the surface rain rate is small in CCF1 (Fig. 5.3f). This suggests that the maximum negative Q_{CMW} at −6 km in CCF1 is the growth of a new water cloud. The positive Q_{WV} mainly balances P_s and maximum negative Q_{CMW} in CCF2 (Fig. 5.4f). This indicates that the maximum negative Q_{CMW} at 4.5 km in CCF2 is the growth of the existing cloud after merging. Thus, the development of the new cloud at the west of the cloud cluster in CCF1 may explain the westward movement of cloud cluster group, whereas the advection of the maximum total hydrometeor mixing ratio by the westerly winds may account for

the eastward propagation of individual cloud clusters inside CCF2. An organized downdraft associated with CCF1 in the lower troposphere causes negative specific humidity perturbations near surface. The positive specific humidity perturbations associated with CCF2 near the surface indicate that the environment has a more favorable water vapor condition for the development of clouds after merging, which leads to larger Q_{WV} in CCF2 than in CCF1 (see Figs. 5.3f and 5.4f).

5.4 Surface Rainfall Processes Associated with Cloud Clusters

To examine surface rainfall processes associated with the development of cloud clusters, the results by Wang et al. (2007) are discussed here. Wang et al. (2007) conducted a 2D cloud-resolving model simulation with the forcing of meridionally uniform vertical velocity, meridional wind, along with thermal and moisture advection calculated over the area of 116–117°E, 16–23°N during South China Sea Monsoon Experiment (SCSMEX). The model simulations show many similarities to the radar observations. The rainband associated with the convection remains at a very stable position throughout its life cycle in the northern SCS region. The reflectivity pattern exhibits a straight upward structure with a little tilt. The positions of the convective, transition, and stratiform regions produced by the model are consistent with observations. The major difference from the observations is that the model tends to overestimate the magnitude of updraft. As a result, the maximum reflectivity generated by the model appears at an elevated altitude.

Figure 5.5a shows that a major rainband initiates around 670 km after hour 5, barely moves and intensifies quickly, reaching up to 21.9 mm h^{-1} at hour 7 (also see Table 5.1). The rainband weakens quickly after hour 8 and it maintains light rain until hour 13. Meanwhile, new rainbands form around 660, 653, 647, and 640 km at hour 7, 8, 9, and 10, respectively. Thus, rainbands propagate southward while the individual rainband barely moves. The surface rain rate is contributed by the local vapor change, vapor convergence, and the local cloud change/hydrometeor convergence, whereas the surface evaporation flux is much smaller than the other rainfall processes and negligible (Fig. 5.5b–e). The surface rainfall is always located to the north of large amounts of the *CAPE* and the *CAPE* becomes small after the passage of rainbands (Fig. 5.5f), indicating the release of unstable energy for the development of convection. As an example, the rainband around 670 km from hour 5 to hour 9 will be analyzed.

The averaged surface rainfall budget during its preformation stage at 0500 LST (Table 5.1) shows that local atmospheric moistening ($Q_{WVT} = -2.6$ mm h^{-1}) and vapor convergence ($Q_{WVF} = 2.4$ mm h^{-1}) nearly cancel each other out. This indicates that the vapor convergence moistens the atmosphere so that surface rainfall as well as clouds does not occur. During its formation stage at 0600 LST, the rain rate ($P_s = 6.7$ mm h^{-1}) is mainly determined by vapor convergence ($Q_{WVF} = 16.0$ mm h^{-1}) and hydrometeor convergence ($Q_{CM} = -7.2$ mm h^{-1}). Thus, the vapor convergence enhances both surface rainfall and cloud hydrometeors.

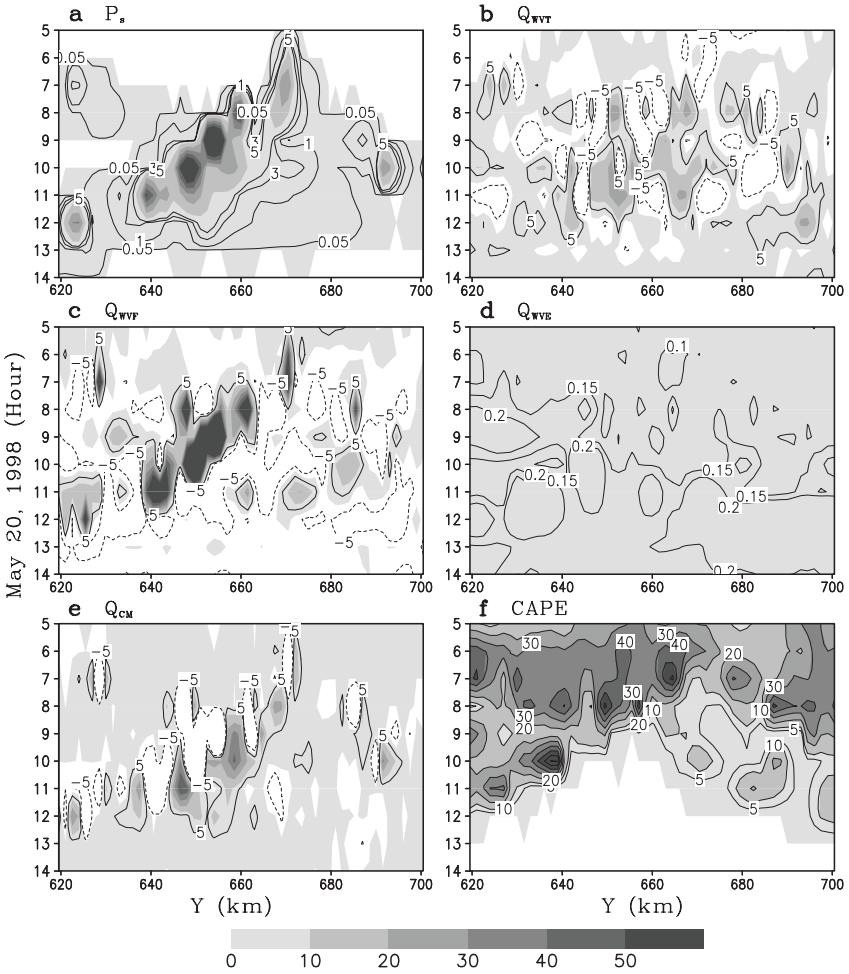

Fig. 5.5 Temporal and horizontal distribution of **a** P_s, **b** Q_{WVT}, **c** Q_{WVF}, **d** Q_{WVE}, **e** Q_{CM}, and **f** *CAPE* on 20 May 1998. Contour intervals are 0.05, 1, 3, 5 mm h^{-1} for P_s; −5, 5 mm h^{-1} for Q_{WVT}, Q_{WVF}, and Q_{CM}; 0.05, 0.1, 0.15, 0.2 mm h^{-1} for Q_{WVE}; and 5, 10, 20, 30, 40, 50, 60 × 10 J kg^{-1} for *CAPE* (After Wang et al. 2007)

Table 5.1 P_s, Q_{WVT}, Q_{WVF}, Q_{WVE}, and Q_{CM} (mm h^{-1}) along a life span of convection averaged in 669–672 km from 0500 LST to 0900 LST 19 May 1998 (After Wang et al. 2007)

Stage	LST	P_s	Q_{WVT}	Q_{WVF}	Q_{WVE}	Q_{CM}
Preformation	0500	0	−2.6	2.4	0.2	0
Formation	0600	6.7	−2.3	16.0	0.2	−7.2
Mature	0700	21.9	−7.2	30.8	0.2	−1.9
Weakening	0800	12.1	11.7	−11.8	0.2	12.0
Dissipating	0900	0.2	2.8	−4.5	0.2	1.7

During its mature phase at 0700 LST, the rain rate ($P_s = 21.9\,\mathrm{mm\,h^{-1}}$) is mainly determined by vapor convergence ($Q_{WVF} = 30.8\,\mathrm{mm\,h^{-1}}$) and local atmospheric moistening ($Q_{WVT} = -7.2\,\mathrm{mm\,h^{-1}}$). Thus, the vapor convergence is the only source that is responsible for the surface rainfall. During its weakening stage at 0800 LST, the rain rate ($P_s = 12.1\,\mathrm{mm\,h^{-1}}$) is determined by local vapor change ($Q_{WVT} = 11.7\,\mathrm{mm\,h^{-1}}$), vapor convergence ($Q_{WVF} = -11.8\,\mathrm{mm\,h^{-1}}$), and hydrometeor convergence ($Q_{CM} = 12\,\mathrm{mm\,h^{-1}}$). Thus, the local vapor and hydrometeor loss overcome the vapor divergence to support the surface rainfall. During its dissipating stage at 0900 LST, the rain rate ($P_s = 0.2\,\mathrm{mm\,h^{-1}}$) is small because of a large cancellation among local vapor change ($Q_{WVT} = 2.8\,\mathrm{mm\,h^{-1}}$), vapor convergence ($Q_{WVF} = -4.5\,\mathrm{mm\,h^{-1}}$), and hydrometeor convergence ($Q_{CM} = 1.7\,\mathrm{mm\,h^{-1}}$).

References

Chao WC, Lin SJ (1994) Tropical intraseasonal oscillation, super cloud clusters, and cumulus convection schemes. J Atmos Sci 51:1282–1297

Lau KM, Peng L, Sui CH, Nakazawa T (1989) Super cloud clusters, westerly wind bursts, 30–60 day oscillations, and ENSO: A unified view. J Meteor Soc Japan 67:205–219

Lau KM, Nakazawa T, Sui CH (1991) Observations of cloud cluster hierarchy over the tropical western Pacific. J Geophys Res 96:3197–3208

Leavy CA, Houze RA Jr (1979) The structure and evolution of convection in a tropical cloud cluster. J Atmos Sci 36:437–457

Malkus JS (1954) Some results of a trade cumulus cloud investigation. J Meteor 11:220–237

Nakazawa T (1988) Tropical super clusters within intraseasonal variations over the western Pacific. J Meteor Soc Japan 66:823–839

Numaguti A, Hayashi YY (1991) Behavior of cumulus activity and the structures of circulations in an "aqua planet" model. Part I. The structure of the super cloud clusters. J Meteor Soc Japan 69:541–561

Peng L, Sui CH, Lau KM, Tao WK (2001) Genesis and evolution of hierarchical cloud clusters in a two-dimensional cumulus-resolving model. J Atmos Sci 58:877–895

Ping F, Luo Z, Li X (2007) Kinematics, cloud microphysics, and spatial structures of tropical cloud clusters: A two-dimensional cloud-resolving modeling study. Atmos Res (in press), doi:10.1016/j.atmosres.2007.11.002

Simpson J (1980) Downdrafts as linkages in dynamic cumulus seeding effects. J Appl Meteor 19:477–487

Simpson J, Woodley WL (1971) Seeding cumulus in Florida: New 1970 results. Science 172: 117–126

Sui CH, Lau KM (1992) Multi-scale phenomena in the tropical atmosphere over the western Pacific. Mon Wea Rev 120:407–430

Tao WK, Simpson J (1984) Cloud interactions and merging: Numerical simulations. J Atmos Sci 41:2901–2917

Wang JJ, Li X, Carey L (2007) Evolution, structure, cloud microphysical and surface rainfall processes of a monsoon convection during the South China Sea Monsoon Experiment. J Atmos Sci 64:360–379

Yano JI, McWilliams JC, Moncrieff MW, Emanuel RA (1995) Hierarchical tropical cloud systems in an analog shallow-water model. J Atmos Sci 52:1723–1742

Chapter 6
Cloud Radiative and Microphysical Processes

Convective systems affect vertical heat and water vapor distributions through radiative and cloud microphysical processes. Due to fine spatial resolution, cloud-resolving models resolve individual cloud and simulate cloud radiative and microphysical processes through solar and IR radiative parameterization and prognostic cloud microphysics parameterization. Cloud microphysical processes include vapor condensation and deposition, autoconversion, evaporation, collection, accretion, riming, and melting. Cloud–radiation interaction processes can be simulated by solar and IR radiative parameterization coupling with cloud single scattering albedo and asymmetry factor associated with cloud hydrometeor mixing ratios. In this chapter, radiative and cloud microphysical processes associated with the development of tropical convection are intensively discussed based on Li et al. (1999, 2002a,b, 2005), Sui and Li (2005), Li (2006), Gao et al. (2006a,b), and Cui et al. (2007).

6.1 Radiative Processes

Cloud–radiation interaction can be examined by a comparison between two experiments during selective 7-day period of TOGA COARE. In one, cloud single scattering albedo and asymmetry factor varied with clouds and environmental thermodynamic conditions; in the other, they were fixed at 0.99 and 0.843, respectively (Li et al. 1999). A comparison of solar radiation calculations between the two experiments showed that the experiment with the varying single scattering albedo and asymmetry factor had stronger solar radiation absorption by ice clouds in the upper troposphere than did the experiment with the constant single scattering albedo and asymmetry factor. The difference in temperatures between the two experiments further showed that the temperature was 2°C warmer around 200 mb in the experiment with variable single scattering albedo and asymmetry factor than in the experiment with values that were kept constant.

A statistical analysis of the clouds and surface rain rates revealed that stratiform (convective) clouds contributed to 33% (67) of the total rain in the experiment with the variable cloud optical properties and 40% (60) in the experiment with the constant cloud optical properties. The fractional cover by stratiform clouds increased from 64% in the experiment with the variations to 70% in the experiment with the constants. These sensitivity tests showed the cloud–radiation interaction process for stabilizing the atmosphere in which the change in the vertical heating gradient by solar radiation due to variations of cloud optical properties stabilizes the middle and upper troposphere and contributes to the reduction of stratiform clouds that further stabilizes the cloud system by reducing infrared cloud top cooling and cloud base warming.

Li et al. (2005) examined the effects of precipitating cloud–radiation interactions on thermodynamic states by conducting two experiments (COAREN and COARE). Both experiments are conducted by the same TOGA COARE forcing and integrated for 10 days. The difference between COAREN and COARE is that COAREN excludes the precipitation–radiation interaction by simply setting mixing ratios of precipitation water (raindrops) and ice (snow and graupel) to zero in the calculation of radiation.

Within the first 3 days of integration, the temperature differences for COAREN–COARE are mostly positive except on late 21 December 1992 when negative temperature differences occur (Fig. 6.1a in left panel). From late 22 December 1992 on, the temperature differences below 200 mb become persistently negative, with minimum values ranging from -1.5°C to -2°C. This indicates that the exclusion of precipitation–radiation interaction causes a cold bias in the troposphere. The differences in specific humidity for COAREN and COARE are persistently negative below 500 mb during the integrations, with minimum around -1 to $-1.5\,\mathrm{g\,kg^{-1}}$ (Fig. 6.1a in left panel). The significant atmospheric drying begins on 23 December 1992.

To examine the physical processes responsible for the temperature and water vapor differences, each term of (2.1) is integrated with time for COAREN and COARE separately and then the difference for COAREN and COARE is measured to obtain the corresponding temperature differences due to condensational heating, radiative heating, convergence of vertical heat flux, vertical temperature advection (Fig. 6.1b–e in left panel), and water vapor differences due to condensation, convergence of vertical moisture flux, and vertical moisture advection (Fig. 6.1b–d in right panel), respectively. The same horizontal temperature and moisture advections are imposed in both experiments that do not contribute to the temperature and moisture differences.

The temperature differences due to radiation are negative below 500 mb and positive above, with the maximum and minimum values reaching 6°C around 325 mb and -6°C around 575 mb, respectively, at the end of the integrations (Fig. 6.1c in left panel). The radiation-induced differences in thermal stratification cause a more stable layer above 500 mb in COAREN than in COARE. This corresponds to less ice hydrometeors in COAREN than in COARE (also see Fig. 6.1b in right panel), which lead to less latent heating above 500 mb in COAREN from 23 December 1992 on

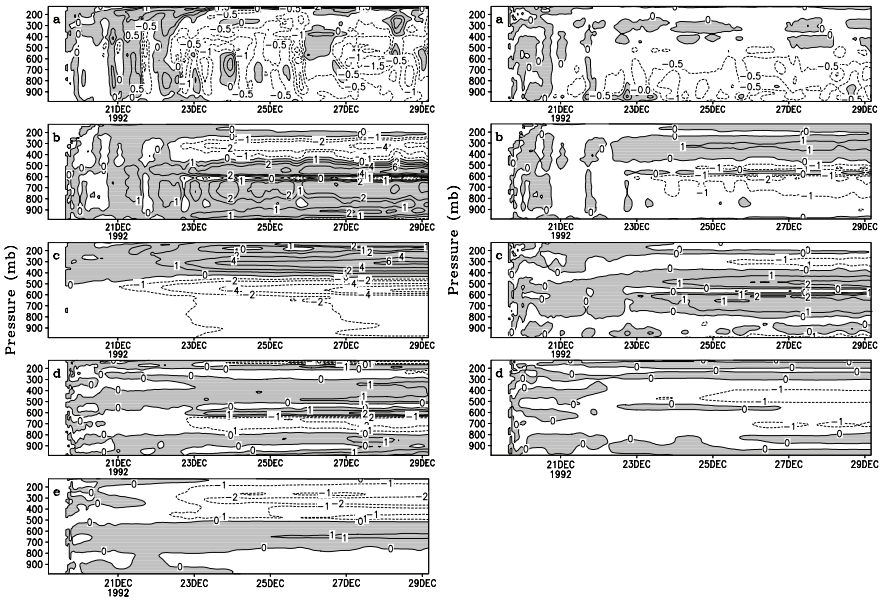

Fig. 6.1 Temporal and vertical distribution of **a** zonal-mean temperature differences (°C) between COAREN and COARE (COAREN-COARE), and differences due to **b** condensational heating, **c** radiative heating, **d** convergence of vertical heat flux, and **e** vertical temperature advection in left panel, and **a** differences in zonal-mean specific humidity $(\mathrm{g\ kg^{-1}})$ for COAREN-COARE, and the differences due to **b** condensation, **c** convergence of vertical moisture flux, and **d** vertical moisture advection in right panel. Positive differences are shaded (After Li et al. 2005)

(Fig. 6.1b in left panel). The temperature differences due to the convergence of vertical heat flux (Fig. 6.1d in left panel) show a banded structure with negative zones around 650–800 mb and 550 mb and mostly positive values elsewhere. The temperature differences due to vertical advection as shown in Fig. 6.1e are all negative except the 500–800 mb layer where positive values exist. Considering the contribution to the temperature differences for COAREN and COARE by all terms, the negative temperature differences above 500 mb level are mainly contributed to by less cloud heating as a result of more stability in COAREN, whereas more radiative cooling in COAREN is directly responsible for the negative temperature differences below 500 mb level.

The exclusion of precipitation–radiation interaction in COAREN causes the lower troposphere to become more unstable, which leads to less evaporation of raindrops associated with subsidence that results in more drying, compared to COARE (Fig. 6.1b in right panel). The contributions to vertical distributions of moisture differences by the other two terms, the convergence of vertical moisture flux and vertical moisture advection, largely cancel each other out due to an out-of-phase relation (Fig. 6.1c, d in right panel). Thus, the lesser rain evaporation associated with large-scale subsidence as a result of more instability in the lower troposphere increases water vapor more slowly, which leads to negative vapor differences. In summary, the

comparison between COAREN and COARE indicates that exclusion of the interaction of precipitation with radiation in the simulations causes a significant cooling and drying bias in the troposphere.

6.2 Cloud Microphysical Processes

Cloud microphysical properties in deep convective regions significantly differ from those in stratiform regions. Along with the westward propagation and during the development of tropical convection, the area-mean vertical velocity profiles exhibit the major ascending motion below 500 mb in the left half of the cloud and the maximum ascending motion between 300 and 500 mb in the right half (Li et al. 2002b), indicating that the left half of the cloud undergoes the deep convective development, whereas the anvil cloud grows in the right half (see the box in Fig. 4.5). The surface rainfall is much larger in the left half than in the right half (Fig. 6.2). *LWP* (9 mm) is much larger than *IWP* (4.8 mm) in the left half, whereas *LWP* (6.1 mm) and *IWP* (6.4 mm) have similar amounts in the right half. The analysis of raindrops budget reveals the collection of cloud water by raindrops (P_{RACW}) is a major process that is responsible for the surface rainfall, and thus the water hydrometeor processes are dominant in the deep convective clouds in the left half. Both the collection of cloud water by raindrops and the melting of precipitation ice into raindrops (P_{GMLT}) are responsible for the surface rainfall in the anvil clouds in the right half.

The P_{SFI} is one of the main processes to consume cloud ice in the growth of snow, particularly in the deep convective clouds (e.g., Fig. 6.2). Hsie et al. (1980) modified the work of Orville and Kopp (1977) that was based on the equation of the rate of growth of ice crystals by deposition proposed by Koenig (1971), and formulated P_{SFI} by dividing the mixing ratio by the timescale that is needed for an ice crystal to grow from radius 40 μm to 50 μm. Based on the aircraft observations, Krueger et al. (1995) suggested that the timescale in P_{SFI} should be for a crystal to grow from radius 40 μm to 100 μm, which increases mixing ratio of cloud ice as indicated in Li et al. (1999). The modified formulation of P_{SFI} by Krueger et al. (1995) is used by Li et al. (2005). Krueger et al. (1995) referred to P_{SFI} as the snow formation associated with the Bergeron process (snow production from cloud ice via the growth of Bergeron-process embryos). However, the Bergeron (Bergeron-Findeisen) process is the diffusional growth of ice crystals in the presence of supercooled water droplets. Therefore, P_{SFI} is defined as the depositional growth of snow from cloud ice.

Li et al. (2005) first examined the differences between experiments COARE and C14. The two experiments are identical except that C14 excludes 14 cloud microphysical processes including P_{SFI} based on Zhao and Carr (1997). Figure 6.3 shows the time series of P_s, $[q_c]$, and $[q_i]$. The surface rain rates in the two experiments have similar temporal evolution because of the same imposed vertical velocity. However, $[q_c]$ and $[q_i]$ are much larger in C14 than in COARE, and particularly, $[q_i]$ in C14 is more than one order of magnitude larger than in COARE.

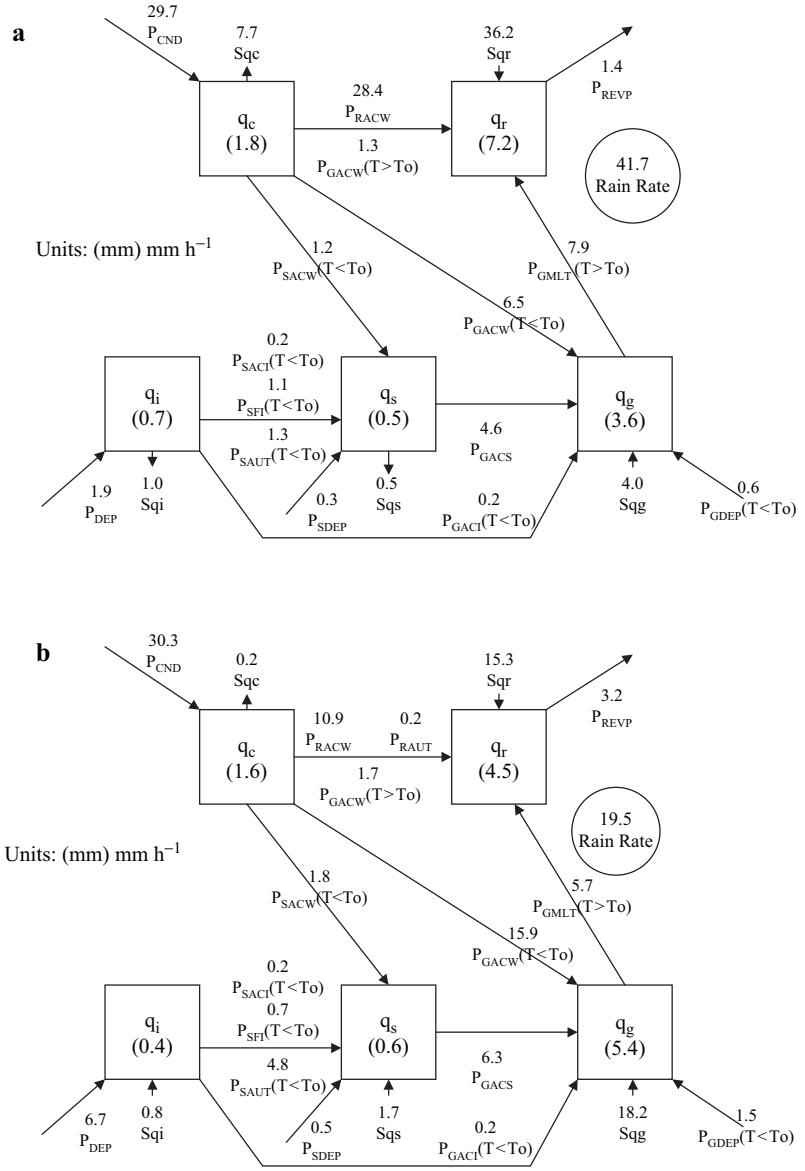

Fig. 6.2 Cloud microphysical budgets averaged within hours 13–15 in **a** the left half and **b** the right half of the box in Fig. 4.5. Units for cloud hydrometeor and conversions are mm and mm h^{-1}, respectively (After Li et al. 2002b)

The anomalous $[q_i]$ causes a large cooling above the ice clouds due to the reflection of the solar radiation and a large warming below due to the energy trapping of the longwave radiation, and positive difference of water vapor fields between C14 and COARE. The 10-day mean fractional covers of convective, raining stratiform,

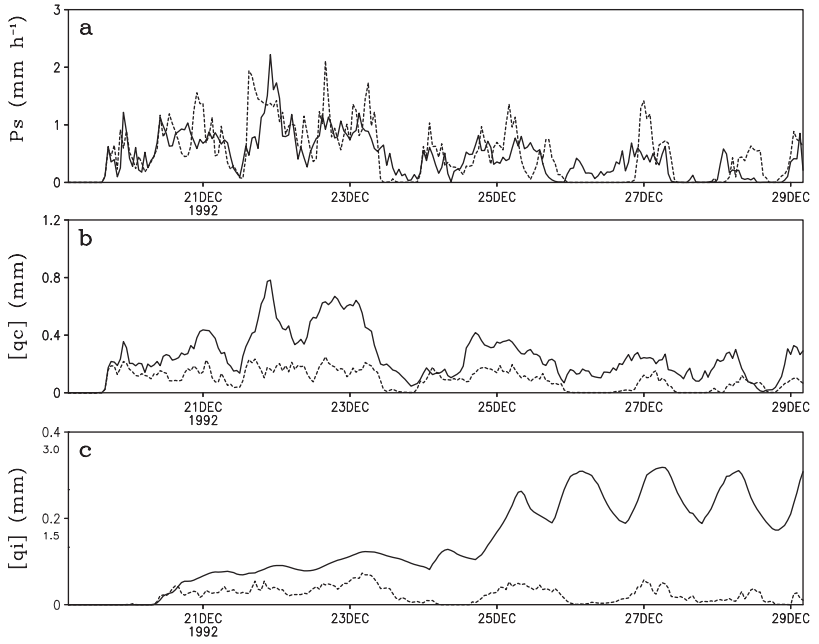

Fig. 6.3 Time series of **a** zonal-mean surface rain rate (P_s), and mass-integrated mixing ratios of **b** cloud water ($[q_c]$) and **c** cloud ice ($[q_i]$) simulated in COARE (dashed) and C14 (solid). The plotting scales for $[q_i]$ are 0–0.4 mm for COARE and 0–3 mm for C14, respectively. Units are mm h^{-1} for P_s and mm for $[q_c]$ and $[q_i]$ (After Li et al. 2005)

and nonraining stratiform clouds in C14 are 7.1%, 15.6%, and 65.6%, respectively, whereas those in COARE are 4.8%, 12.8%, and 52.4%, respectively. The result indicates a respective increase of 48%, 22%, and 25% in the fractional coverage of convective, raining stratiform, and nonraining stratiform clouds from COARE to C14. C14 confirms unrealistic simulation of cloud ice. The budgets of $[q_i]$ in COARE and C14 are then analyzed to identify the cause of the unrealistic $[q_i]$ simulation in C14.

The time series of vertically integrated budgets of $[q_i]$ (1.8e) in COARE and C14 are shown, respectively, in Fig. 6.4a and b. In COARE, $[P_{DEP}]$ is nearly balanced by $[P_{SAUT}]$ and $[P_{SFI}]$ (Fig. 6.4a). Thus, $[S_{qi}]$ is very small. $[P_{SFI}]$ is smaller than $[P_{SAUT}]$, but it is an important sink of cloud ice. In the first 5 days of the integration of C14, $[P_{DEP}]$ and $[P_{SAUT}]$ cancel each other out in large part, but there is a considerable magnitude of $[S_{qi}]$ contributed by $[P_{IHOM}]$, which leads to the initial anomalous growth of cloud ice (Fig. 6.4b). The rapid decrease of the magnitude of $[P_{SAUT}]$ cannot offset $[P_{DEP}]$ so that a large $[S_{qi}]$ is responsible for the rapid increase of $[q_i]$ in late evening of 24 December and early morning of 25 December. In the second 5 days of the integration, $[P_{IHOM}]$ and $[P_{SACI}]$ become as important as $[P_{DEP}]$ and $[P_{SAUT}]$ in the budget of $[q_i]$. A comparison of budgets of $[q_i]$ between COARE and C14 indicates that $[P_{SFI}]$ is the important sink of cloud ice in COARE,

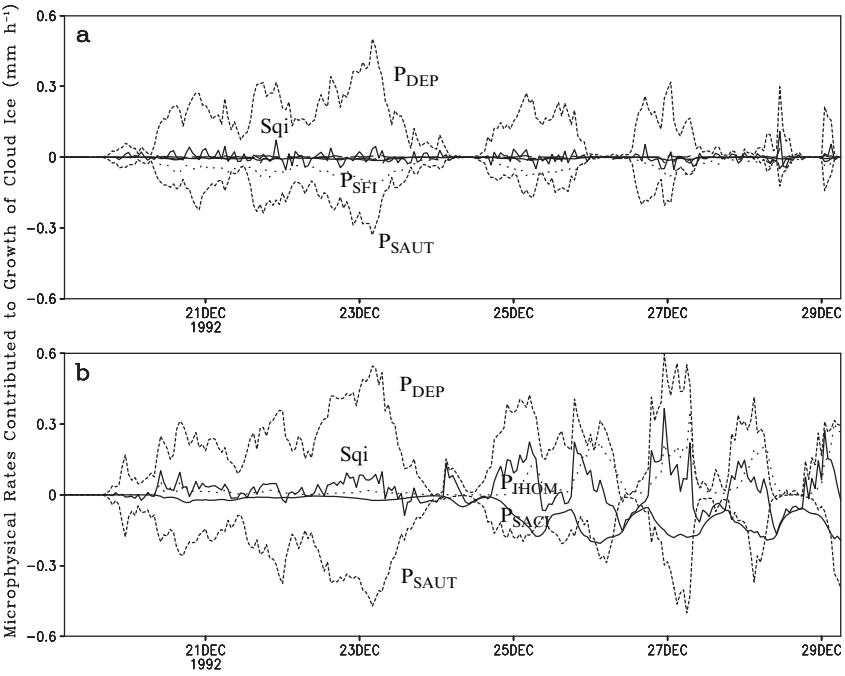

Fig. 6.4 Time series of zonal-mean cloud ice budgets simulated in **a** COARE and **b** C14, respectively. All terms are mass-integrated. Unit is mm h^{-1} (After Li et al. 2005)

but it is excluded in C14, which may cause anomalous growth of cloud ice in C14. Thus, P_{SFI} is included in the additional experiment CSFI that is conducted to further examine the cause of the difference between C14 and COARE.

The temperature differences in the upper troposphere are significantly reduced in CSFI–COARE compared to those in C14–COARE. Also notice that the positive and negative temperature differences appear alternately. The differences of water vapor exhibit a slightly positive trend with most of the positive differences at less than 1 g kg^{-1}. The fractional cloud covers in CSFI also display significant reduction from C14 and their 10-day mean values in CSFI become similar to those in COARE. Thus, CSFI confirms the crucial role of P_{SFI} as the sink of $[q_i]$ in the balance of cloud ice. The results suggest that the budget of cloud ice should be carefully treated to avoid unrealistic cloud calculations.

6.3 Impacts of Ice Microphysics in Development of Tropical Convection

Ice hydrometeors play an important role in the development of tropical convective systems. Inclusion of ice microphysical parameterization schemes in the numerical simulations has led to the improvements in cloud-resolving simulations

of squall lines (e.g., Yoshizaki 1986; Nicholls 1987; Fovell and Ogura 1988; Tao and Simpson 1989; McCumber et al. 1991; Tao et al. 1991), in cloud-resolving and mesoscale simulations of tropical cyclones (e.g., Willoughby et al. 1984; Lord et al. 1984; Liu et al. 1997), and in simulations of general circulation models (e.g., Ramanathan et al. 1983; Slingo 1987; Heymsfield and Donner 1990; Fowler et al. 1996). The major conclusion of previous short-term cloud-resolving modeling (less than 1 day) studies on ice effects is that the ice phase is crucial for better simulation of stratiform development, such as the light precipitation associated with stratiform clouds over the trailing region of convective systems. The main results from recent long-term cloud-resolving modeling (more than 1 week) studies reveal that (1) the effects of cloud microphysics on temperature and water vapor profiles are statistically significant and the temperature in the upper troposphere is modified by microphysical processes associated with anvil clouds (Grabowski et al. 1999); (2) the simulations of cloud radiative properties have been improved due to the modified ice microphysical parameterization schemes, and the radiative flux, cloud radiative forcing, and albedo are sensitive to the effective radius of ice particles (Wu et al. 1999); (3) the convective systems simulated without ice microphysics have a reduced stratiform component, a larger propagation speed, and a shorter life cycle than do those simulated with ice microphysics (Grabowski and Moncrieff 2001; Grabowski 2003); (4) the models both with and without ice microphysics simulated similar propagation speeds and life cycles of convective systems (Tao and Simpson 1989); (5) the model without ice microphysics simulated a much weaker and less organized convective system than does the model with ice microphysics in a weak unstable environment, whereas ice microphysics has important effects on the system-scale structures in a strong unstable environment, indicating that the environmental thermodynamics is a major factor in regulating ice effects on tropical convection (Liu and Moncrieff 1997).

Gao et al. (2006b) conducted an experiment (COAREW) that excludes ice microphysics and compared COAREW with COARE that includes ice microphysics. The *LWP* is larger in COAREW than in COARE. This indicates that exclusion of ice microphysics in the simulation enhances water hydrometeors. To explain the difference in *LWP* between the two experiments, 21-day mean cloud microphysics budgets in both experiments are calculated and shown in Fig. 6.5. $[q_c]$ is much larger in COAREW (0.173 mm) than in COARE (0.066 mm), whereas $[q_r]$ is slightly smaller in COAREW (0.091 mm) than in COARE (0.107 mm). Thus, a larger *LWP* in COAREW is mainly caused by a larger amount of cloud water. In COARE, $[P_{CND}]$ $(0.48\,\mathrm{mm\,h^{-1}})$ is nearly balanced by $[P_{RACW}]$ $(0.33\,\mathrm{mm\,h^{-1}})$ and $[P_{GACW}(T < T_O)]$ $(0.09\,\mathrm{mm\,h^{-1}})$. In COAREW, the accretion rate of cloud water by precipitation ice is excluded. Only $[P_{RACW}]$ $(0.39\,\mathrm{mm\,h^{-1}})$ and $[P_{RAUT}]$ $(0.02\,\mathrm{mm\,h^{-1}})$ consume cloud water, which leads to the growth of cloud water $([S_{qc}] = 0.03\,\mathrm{mm\,h^{-1}})$.

Surface rain rate is smaller in COAREW $(0.29\,\mathrm{mm\,h^{-1}})$ than in COARE $(0.36\,\mathrm{mm\,h^{-1}})$. In COAREW, the vapor condensation rate $([P_{CND}] = 0.44\,\mathrm{mm\,h^{-1}})$ supports the surface rain rate and the evaporation rate of rain $([P_{REVP}] = 0.12\,\mathrm{mm\,h^{-1}})$ through the collection rate of cloud water by raindrops $([P_{RACW}] =$

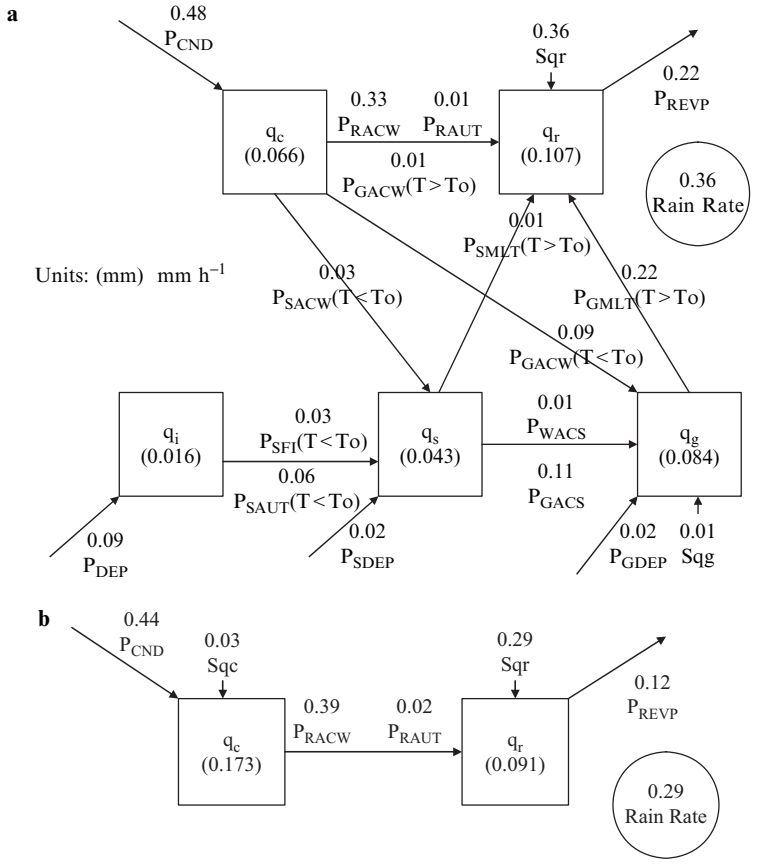

Fig. 6.5 21-day and zonal-mean cloud microphysics budgets in **a** COARE and **b** COAREW. Units for cloud hydrometeors and conversions are mm and mm h^{-1}, respectively (After Gao et al. 2006b)

$0.39\,\mathrm{mm\,h^{-1}}$) and the autoconversion rate from cloud water to raindrops ($[P_{RAUT}] = 0.02\,\mathrm{mm\,h^{-1}}$), while it enhances cloud water persistently with a rate of $0.03\,\mathrm{mm\,h^{-1}}$ ($[S_{qc}]$). In COARE, the vapor condensation rate ($[P_{CND}] = 0.48\,\mathrm{mm\,h^{-1}}$) supports the surface rain rate and the evaporation rate of rain ($[P_{REVP}] = 0.22\,\mathrm{mm\,h^{-1}}$) directly through the collection rate of cloud water by raindrops ($[P_{RACW}] = 0.33\,\mathrm{mm\,h^{-1}}$) and the autoconversion rate from cloud water to raindrops ($[P_{RAUT}] = 0.01\,\mathrm{mm\,h^{-1}}$). Meanwhile, vapor deposition rates ($[P_{DEP}] + [P_{SDEP}] + [P_{GDEP}] = 0.13\,\mathrm{mm\,h^{-1}}$) and accretion rates of cloud water by precipitation ice ($[P_{SACW}] + [P_{GACW}(T < T_O)] = 0.03 + 0.09\,\mathrm{mm\,h^{-1}}$) support the surface rain rate and the evaporation rate of rain through melting rates of precipitation ice to rain ($[P_{SMLT}] + [P_{GMLT}] = 0.01 + 0.22\,\mathrm{mm\,h^{-1}}$). Thus, the larger surface rain rate and larger evaporation rate of rain in COARE stem from vapor deposition processes and conversion from precipitation ice to rain.

The zonal-mean surface rain rates in both experiments show similar evolution (Fig. 6.6). The vapor convergence (Q_{WVF}) in both experiments exhibits the same

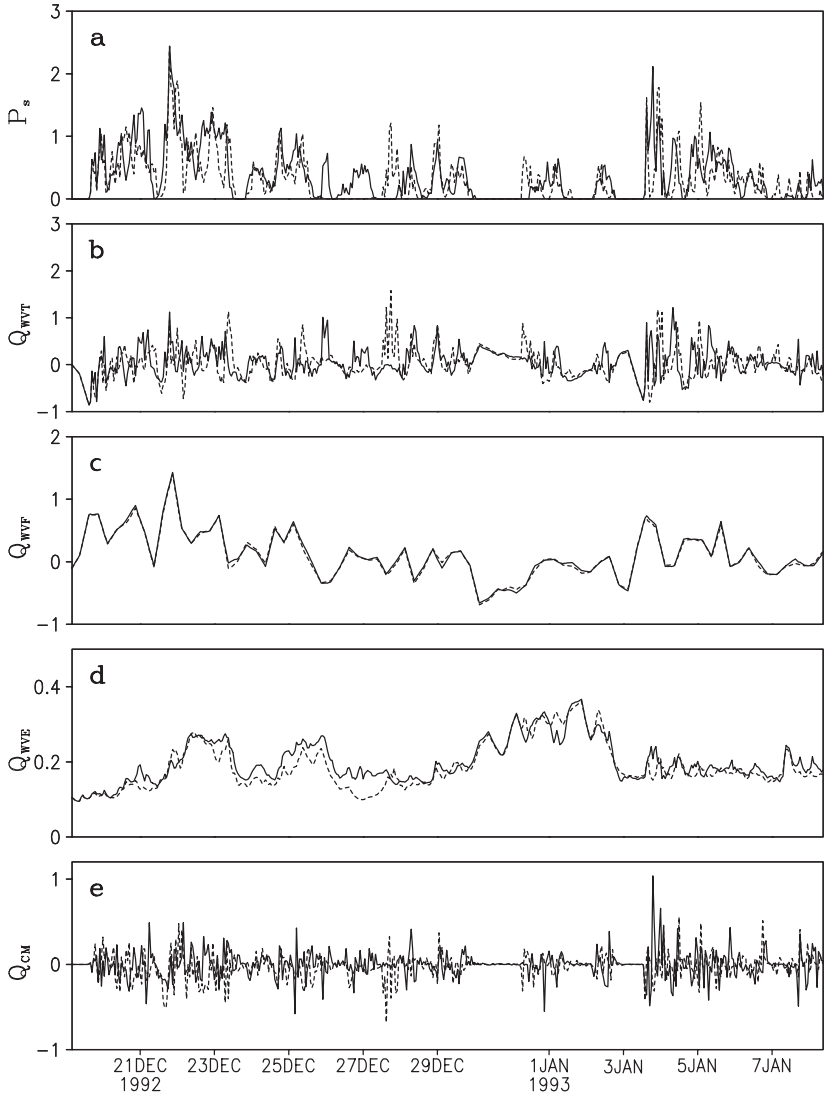

Fig. 6.6 Time series of zonal-mean **a** P_s, **b** Q_{WVT}, **c** Q_{WVF}, **d** Q_{WVE}, and **e** Q_{CM} during the 21-day integrations. Solid and dashed lines denote COARE and COAREW, respectively. Unit is mm h^{-1} (After Gao et al. 2006b)

magnitudes and evolution due to similar effects of the mean ascent on the moisture profiles (Fig. 6.6c). The surface evaporation fluxes (Q_{WVE}) in both experiments are small (Fig. 6.6d). Thus, the differences in local vapor (Q_{WVT}) and hydrometeor (Q_{CM}) changes (Fig. 6.6b and e) are responsible for the differences in magnitudes. In COARE, the 21-day means of P_s, Q_{WVT}, Q_{WVF}, Q_{WVE}, and Q_{CM} are 0.36, 0.04, 0.12, 0.20, and 0.0 mm h^{-1}, respectively. In COAREW, the 21-day means of

P_s, Q_{WVT}, Q_{WVF}, Q_{WVE}, and Q_{CM} are 0.29, 0.02, 0.11, 0.19, and $-0.03\,\mathrm{mm\,h^{-1}}$, respectively. The difference in time-mean $P_s(-0.07\,\mathrm{mm\,h^{-1}})$ for COAREW–COARE is contributed to by the differences in vapor sink $(-0.04\,\mathrm{mm\,h^{-1}})$ and cloud sink $(-0.03\,\mathrm{mm\,h^{-1}})$, partially because a smaller amount of water vapor source from the atmospheric environment is available for rainfall in COAREW than in COARE, and partially because existing cloud hydrometeors contribute to rainfall in COAREW, whereas they do not contribute to rainfall processes in COARE.

The mass-weighted mean temperature is colder in COAREW than in COARE, whereas the amount of *PW* is larger in COAREW than in COARE. This indicates that the exclusion of ice microphysics causes colder and moister atmospheres than does its inclusion. The negative difference in mass-weighted mean temperatures for COAREW–COARE is mainly contributed to by the negative difference of temperature in 100–400 mb (Fig. 6.7a in left panel). The differences in heat budgets (Fig. 6.7b–e in left panel) reveal that the negative temperature difference in the upper troposphere is mainly due to the negative difference in condensational heating since ice cloud heating is excluded in COAREW. The difference in convergence of vertical heat flux is largely cancelled out by the difference in vertical temperature advection in the upper troposphere, whereas the difference in radiative heating is relatively small compared to the differences in the other thermal processes.

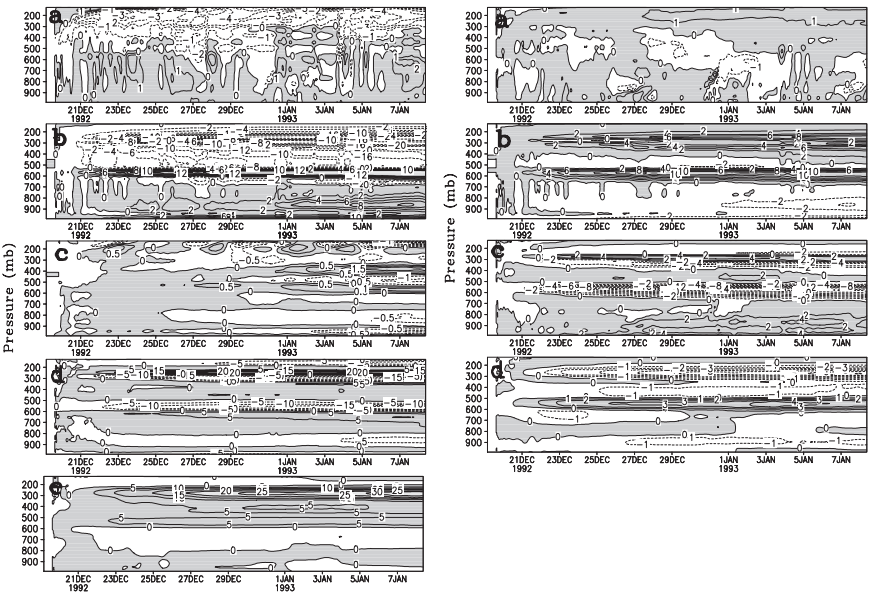

Fig. 6.7 Temporal and vertical distribution of **a** zonal-mean temperature differences (°C) for COAREW-COARE, and differences due to **b** condensational heating, **c** radiative heating, **d** convergence of vertical heat flux, and **e** vertical temperature advection in left panel, and **a** differences of zonal-mean specific humidity $(\mathrm{g\,kg^{-1}})$ for COAREW-COARE, and the differences due to **b** condensation, **c** convergence of vertical vapor flux, and **d** vertical vapor advection in right panel. Positive differences are shaded (After Gao et al. 2006b)

The positive difference in *PW* for COAREW–COARE is mainly contributed to by the positive difference in specific humidity in 100–300 mb (Fig. 6.7a in right panel). The differences in water vapor budgets (Fig. 6.7b–d in right panel) show that the positive difference in specific humidity in the upper troposphere is mainly due to the positive difference in condensation in the upper troposphere, which has a larger magnitude than the negative differences in vertical vapor advection, as well as in convergence of vertical vapor flux do.

Note that the imposed vertical velocity that is derived from observational data during TOGA COARE includes effects of ice clouds. To examine the sensitivity of effects of ice clouds to imposed vertical velocity, the zero vertical velocity is imposed in the experiments with (SST29) and without (SST29NIM) ice clouds. The two experiments are integrated to quasi equilibrium states by Ping et al. (2007) (see section 11.4 for detailed discussions of experiments). The similarities include the fact that the exclusion of ice microphysics yields a cold temperature bias and enhances cloud water amount. The difference is that the exclusion of ice microphysics in the simulation with the zero vertical velocity produces a dry bias, whereas the exclusion of ice microphysics in the simulation with the nonzero vertical velocity generates a weak moist bias.

6.4 Interaction Between Water and Ice Clouds

To study the interaction between water and ice clouds, Sui and Li (2005) defined a cloud ratio (*CR*) as the ratio of the *IWP* to *LWP*, which measures the importance of ice and water hydrometeors in precipitating clouds. Figure 6.8 displays x–z cross sections of the total hydrometeor mixing ratio and vertical profiles of zonal-mean total hydrometeor mixing ratio and vertical velocity at 0800 LST 20 December, 0000 LST 21 December, and 0600 LST 24 December 1992, respectively. The zonal-mean *CR* is 0.2 when several cloud clusters only extend to 400 mb and the water clouds dominate at 0800 LST 20 December 1992, representing the development of convective clouds. The vertical velocities in the upper and lower troposphere have similar magnitudes. When clouds extend to 100 mb at 0000 21 December 1992 and the zonal-mean *CR* is 0.8, both ice and water clouds develop. There exists a strong upward motion above 600 mb which supports ice clouds. The zonal-mean *CR* is 2.8 at 0600 LST 24 December 1992 when anvil ice clouds exist and the ice hydrometeor mixing ratio is larger than water hydrometeor mixing ratio, denoting the development of stratiform clouds. A strong mean upward motion occurs in the upper troposphere, whereas a downward motion appears in the lower troposphere.

Cui et al. (2007) calculated the 21-day mean cloud hydrometeors and associated microphysical budgets in raining stratiform, convective, and nonraining stratiform regions in COARE (Fig. 6.9). In raining stratiform regions, the *IWP* (0.89 mm) is slightly smaller than the *LWP* (0.98 mm), and *CR* is 0.91. The magnitude of cloud ice (0.09 mm) only is about one third of the magnitude of cloud water (0.28 mm), whereas the magnitude of precipitation ice ($[q_s] + [q_g] = 0.8$ mm) is slightly larger than that of precipitation water (0.7 mm). In convective regions, the *IWP* (0.6 mm) is

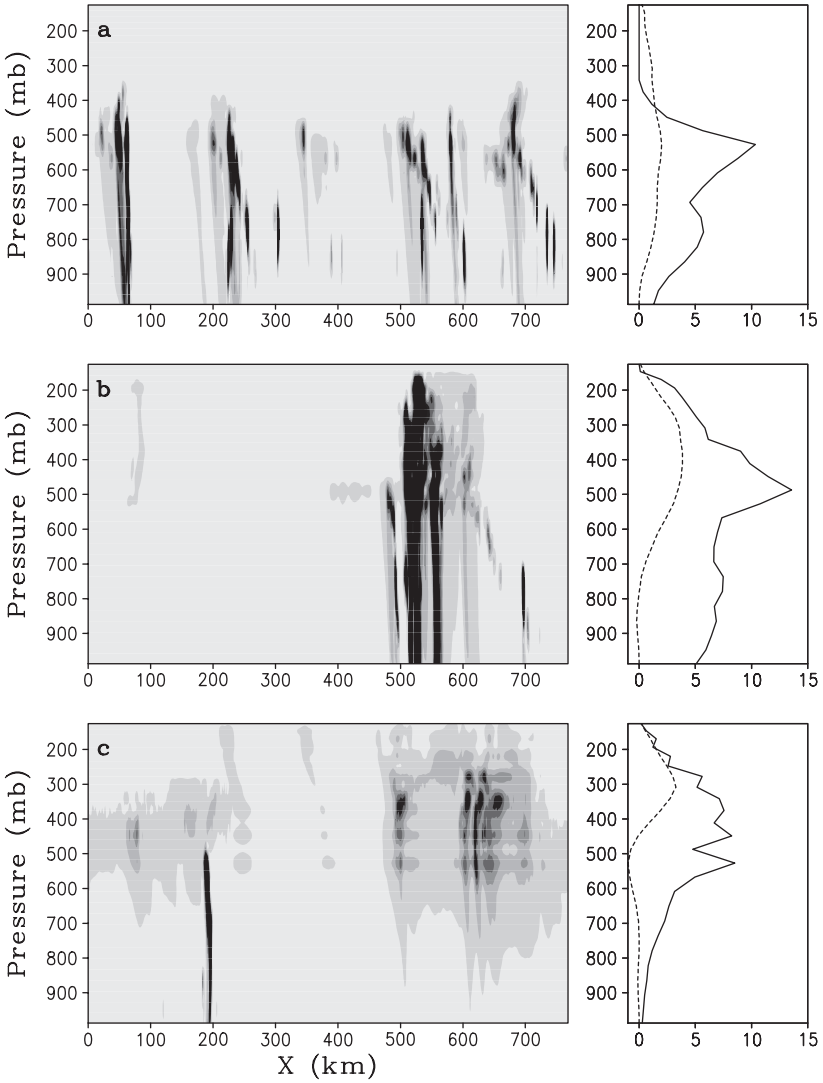

Fig. 6.8 Horizontal and vertical distributions of total hydrometeor mixing ratio (left panels) and vertical profiles of zonally averaged total hydrometeor mixing ratio (solid) and vertical velocity (dashed) (right panels) simulated in COARE at **a** 0800 LST 20 December, **b** 0000 LST 21 December, and **c** 0600 LST 24 December 1992. Units are 10^{-2} g kg^{-1} for total hydrometeor mixing ratio and cm s^{-1} for vertical velocity, respectively (After Sui and Li 2005)

much smaller than the *LWP* (1.72 mm), and *CR* is 0.35. The cloud ice (0.05 mm) is one order of magnitude smaller than the magnitude of cloud water (0.78 mm) and the magnitude of precipitation ice (0.55 mm) is smaller than that of precipitation water (0.94 mm). In nonraining stratiform regions, the *IWP* (0.12 mm) is much larger than the *LWP* (0.043 mm), and *CR* is 2.79. The cloud ice (0.018 mm) and cloud

water (0.017 mm) have similar magnitudes, whereas the magnitude of precipitation ice (0.102 mm) is much larger than that of precipitation water (0.026 mm). Thus, both water and ice clouds are important in raining stratiform regions, whereas water and ice clouds are dominant in convective and nonraining stratiform regions, respectively.

In raining stratiform regions (Fig. 6.9a), the vapor deposition rate ($[P_{DEP}] + [P_{SDEP}] + [P_{GDEP}] = 0.71\,\mathrm{mm\,h^{-1}}$) is less than half of the vapor condensation rate ($[P_{CND}] = 1.64\,\mathrm{mm\,h^{-1}}$), and the ratio of the deposition rate to condensation rate is 0.43. In convective regions (Fig. 6.9b), the vapor deposition rate ($0.62\,\mathrm{mm\,h^{-1}}$) is one order of magnitude smaller than the vapor condensation rate ($7.24\,\mathrm{mm\,h^{-1}}$), and the ratio of the deposition rate to condensation rate is 0.09. In nonraining stratiform regions (Fig. 6.9c), the vapor deposition rate ($0.078\,\mathrm{mm\,h^{-1}}$) is much higher than the vapor condensation rate ($0.029\,\mathrm{mm\,h^{-1}}$), and the ratio of the deposition rate to condensation rate is 2.7. These results indicate that a large *LWP* is associated with a large vapor condensation rate in convective regions, whereas a relatively large *IWP* is due to a large vapor deposition rate in nonraining stratiform regions.

The cloud water is converted into precipitation water mainly through the collection of cloud water by rain ($[P_{RACW}]$) and precipitation ice mainly through the accretion of cloud water by snow ($[P_{SACW}(T < T_o)]$) and graupel ($[P_{GACW}(T < T_o)]$). In raining stratiform regions (Fig. 6.9a), the conversion rate from cloud water to precipitation ice ($[P_{GACW}(T < T_o)] + [P_{SACW}(T < T_o)] = 0.79\,\mathrm{mm\,h^{-1}}$) is lower than the conversion rate from cloud water to precipitation water

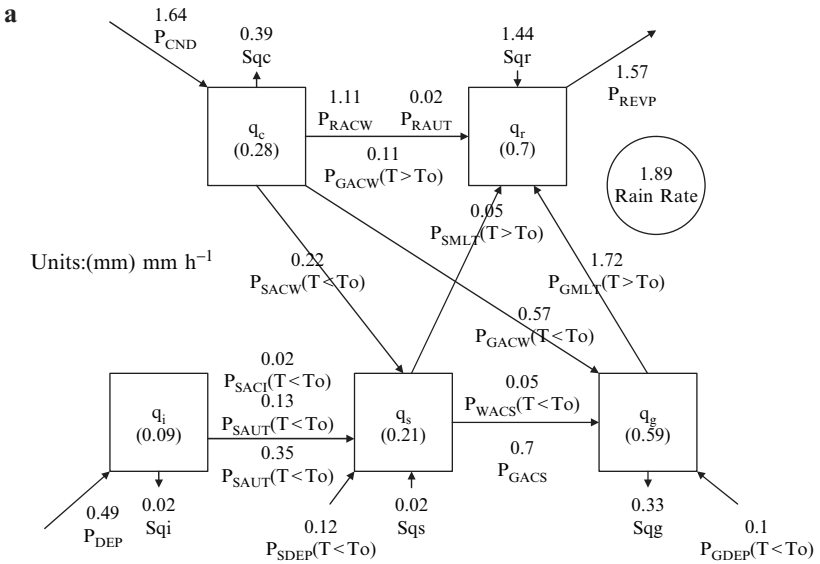

Fig. 6.9 21-day mean cloud microphysics budgets in **a** raining stratiform regions, **b** convective regions, and **c** nonraining stratiform regions simulated in COARE. Units for cloud hydrometeors and conversions are mm and mm $\mathrm{h^{-1}}$, respectively (After Cui et al. 2007)

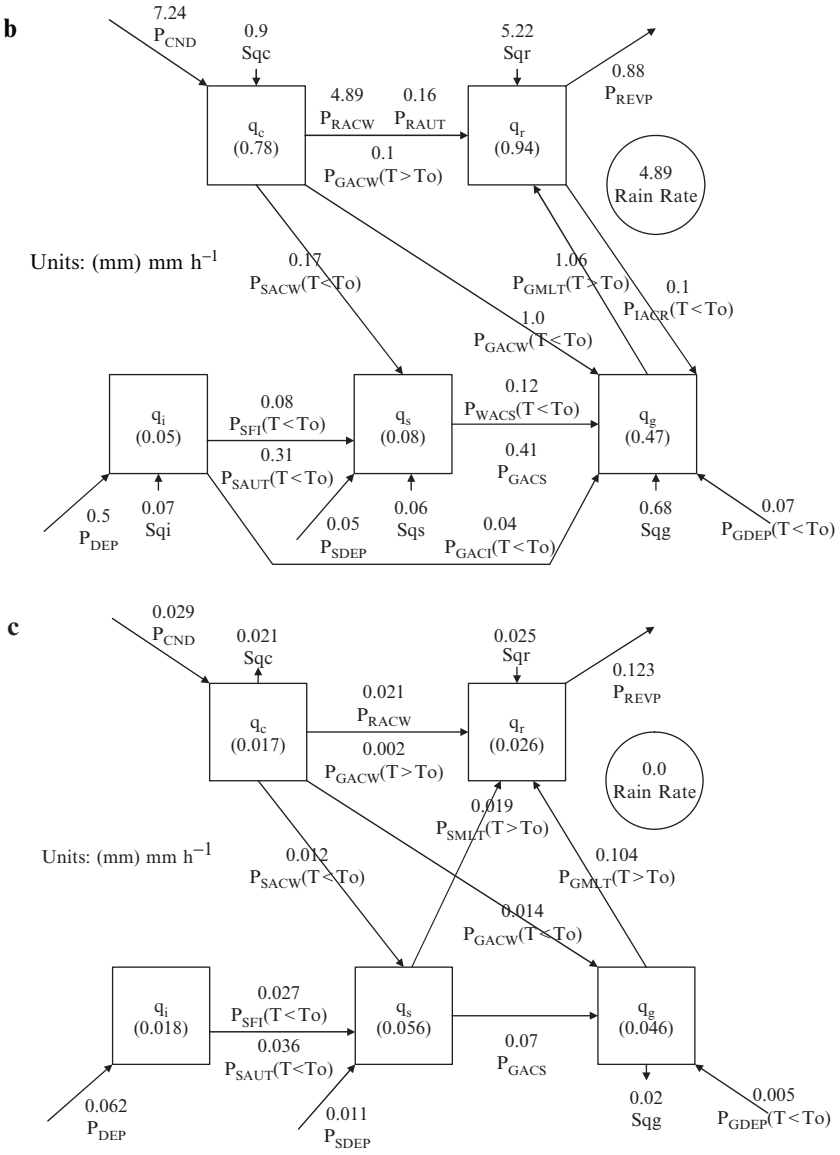

Fig. 6.9 Continued

$([P_{RACW}] + [P_{RAUT}] + [P_{GACW}(T > T_o)] = 1.24\,\mathrm{mm\,h^{-1}})$. About two thirds of cloud water becomes raindrops whereas about one third of cloud water is converted to precipitation ice. The vapor condensation rate is smaller than the conversion rates to precipitation water and ice, which leads to a reduction in cloud water at a rate of $0.39\,\mathrm{mm\,h^{-1}}$ (S_{qc}). In convective regions (Fig. 6.9b), the conversion rate from cloud water to precipitation ice $(1.17\,\mathrm{mm\,h^{-1}})$ is lower than the conversion rate

from cloud water to precipitation water ($5.15\,\mathrm{mm\,h^{-1}}$). About four fifths of cloud water becomes raindrops whereas about one fifths is converted to precipitation ice. The vapor condensation rate is larger than the conversion rates to precipitation water and ice, which enhances the cloud water at a rate of $0.9\,\mathrm{mm\,h^{-1}}$. In nonraining stratiform regions (Fig. 6.9c), the conversion rate from cloud water to precipitation ice ($0.026\,\mathrm{mm\,h^{-1}}$) is slightly higher than the conversion rate from cloud water to precipitation water by $0.023\,\mathrm{mm\,h^{-1}}$. The vapor condensation rate is lower than the conversion rates from cloud water to precipitation water and ice, suppressing the cloud water at a rate of $0.021\,\mathrm{mm\,h^{-1}}$.

In the budgets of raindrops, the important sources for raindrops and surface rainfall are from the collection of cloud water by raindrops ($[P_{RACW}]$) as well as the melting of graupel into raindrops ($[P_{GMLT}(T > T_o)]$). In raining stratiform regions (Fig. 6.9a), the conversion rate from precipitation ice to raindrops ($[P_{GMLT}(T > T_o)] + [P_{SMLT}(T > T_o)]$) is $1.77\,\mathrm{mm\,h^{-1}}$, which is larger than the conversion rate from cloud water to raindrops ($1.24\,\mathrm{mm\,h^{-1}}$). In convective regions (Fig. 6.9b), the conversion rate from precipitation ice to raindrops ($0.96\,\mathrm{mm\,h^{-1}}$) is much lower than the conversion rate from cloud water to raindrops ($5.15\,\mathrm{mm\,h^{-1}}$). In nonraining stratiform regions (Fig. 6.9c), the conversion rate from precipitation ice to raindrops ($0.123\,\mathrm{mm\,h^{-1}}$) is much higher than the conversion rate from cloud water to raindrops ($0.023\,\mathrm{mm\,h^{-1}}$). Thus, the source for raindrops is mainly from the conversion of cloud water (84.3%) in convective regions, whereas it is mainly from the conversion of precipitation ice (84.2%) in nonraining stratiform regions.

The source/sink of raindrops (S_{qr}) can be different from the surface rain rate due to the local raindrop change and exchange of raindrops between regions. S_{qr} ($1.44\,\mathrm{mm\,h^{-1}}$) is lower than the surface rain rate ($1.89\,\mathrm{mm\,h^{-1}}$) in raining stratiform regions (Fig. 6.9a), whereas it is higher ($5.22\,\mathrm{mm\,h^{-1}}$) than the rain rate ($4.89\,\mathrm{mm\,h^{-1}}$) in convective regions (Fig. 6.9b). In nonraining stratiform regions (Fig. 6.9c), S_{qr} is $0.025\,\mathrm{mm\,h^{-1}}$ even though there is no surface rainfall. Since the sum of S_{qr} should be the sum of the surface rain rates in three regions, the differences between S_{qr} and the surface rain rate in raining regions are mainly due to the exchange between raining stratiform regions and convective regions. In addition to the surface rainfall, the evaporation of raindrops ($[P_{REVP}]$) is another sink for the raindrops. The rain evaporation rate in raining stratiform regions ($1.57\,\mathrm{mm\,h^{-1}}$) is higher than in convective regions ($0.88\,\mathrm{mm\,h^{-1}}$) and in nonraining stratiform regions ($0.123\,\mathrm{mm\,h^{-1}}$).

The conversion between the *IWP* and *LWP* is mainly determined by the melting of precipitation ice ($[P_{GMLT}(T > T_o)] + [P_{SMLT}(T > T_o)]$) and the accretion of cloud water by precipitation ice ($[P_{GACW}(T < T_o)] + [P_{SACW}(T < T_o)]$) (Fig. 6.9). The conversion rates from the *IWP* to *LWP* are $0.98\,\mathrm{mm\,h^{-1}}$ in raining stratiform regions, $0.097\,\mathrm{mm\,h^{-1}}$ in nonraining stratiform regions, and $0.21\,\mathrm{mm\,h^{-1}}$ in convective regions. This suggests that over the tropical deep convective regime, the exchange between the water and ice clouds enhances the *LWP*. Over raining stratiform regions, S_{qg} is $-0.33\,\mathrm{mm\,h^{-1}}$. This suggests that cloud microphysical processes suppress the graupel in raining stratiform regions. Over convective regions, S_{qg} is

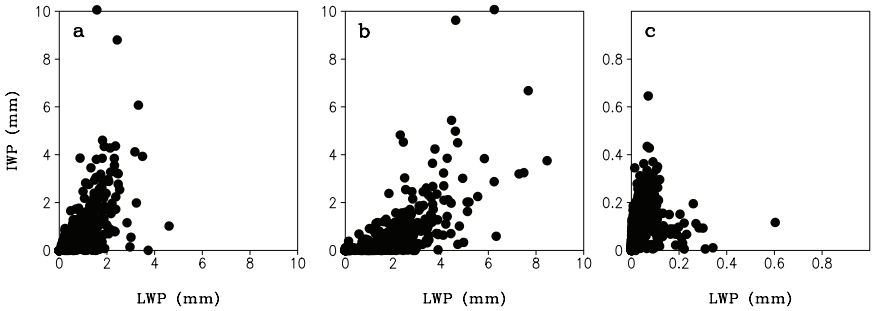

Fig. 6.10 *IWP* versus *LWP* in **a** raining stratiform regions, **b** convective regions, and **c** nonraining stratiform regions simulated in COARE (After Cui et al. 2007)

$0.68\,\mathrm{mm\,h^{-1}}$. This indicates that cloud microphysical processes enhance the graupel in convective regions. In nonraining stratiform regions, S_{qg} $(0.02\,\mathrm{mm\,h^{-1}})$ is small.

CR is different over different regions as indicated in Fig. 6.10. Thus, the linear regression between *IWP* and *LWP* is calculated over three regions. The linear regression equations are $IWP = 0.88LWP - 0.01$ in raining stratiform regions, $IWP = 0.49LWP - 0.21$ in raining convective regions, and $IWP = 1.15LWP + 0.06$ in nonraining stratiform regions. Thus, the ratios of *IWP* to *LWP* (slopes of the regression equations) are 0.88 in raining stratiform regions, 0.49 in raining convective regions, and 1.15 in nonraining stratiform regions. The linear correlation coefficients are 0.61 in raining stratiform regions, 0.68 in raining convective regions, and 0.3 in nonraining stratiform regions. Thus, the linear relations over three regions are statistically significant. To statistically determine an upper limit in the ratio of the *IWP* to *LWP* over convective and raining stratiform clouds, the ratio of $(IWP_M + IWP_{SD})$ to $(LWP_M + LWP_{SD})$, where subscripts *M* and *SD* are time mean and standard deviation, respectively, is defined as the critical value for the upper limit, which is 0.54 for convective clouds and 1.15 for raining stratiform clouds. Thus, the areas where $CR < 0.54$, $0.54 < CR < 1.15$, and $CR > 1.15$ are defined as the convective, raining stratiform, and nonraining stratiform regions, respectively.

The increase of *CR* shows development of ice clouds whereas the decrease of *CR* indicates the development of water clouds. Thus, Sui and Li (2005) further derived a tendency equation for *CR* by adding (1.7f and g) and (1.7h–j), respectively, and vertically integrate the resulting equations:

$$\frac{\partial LWP}{\partial t} = CONV_{LWP} - P_{qr} + [P_{CND}] + C(IWP, LWP) - [P_{REVP}], \tag{6.1}$$

$$\begin{aligned}\frac{\partial IWP}{\partial t} &= CONV_{IWP} + [P_{DEP}] + [P_{SDEP}] + [P_{GDEP}] - C(IWP, LWP) \\ &\quad - P_{MLTS}(T > T_o) - P_{MLTG}(T > T_o) - P_{qs} - P_{qg},\end{aligned} \tag{6.2}$$

where

$$CONV_{LWP} = -\left[\frac{\partial}{\partial x}u(q_c + q_r)\right], \tag{6.3a}$$

$$CONV_{IWP} = -\left[\frac{\partial}{\partial x}u(q_i + q_s + q_g)\right], \tag{6.3b}$$

$$P_{qr} = \bar{\rho} w_{Tr} q_r|_{z=0}, \tag{6.3c}$$

$$P_{qs} = \bar{\rho} w_{Ts} q_s|_{z=0}, \tag{6.3d}$$

$$P_{qg} = \bar{\rho} w_{Tg} q_g|_{z=0}, \tag{6.3e}$$

$$\begin{aligned} C(IWP,LWP) = &-[P_{SACW}(T<T_o)] - [P_{SFW}(T<T_o)] \\ &- [P_{GACW}(T<T_o)] - [P_{IHOM}(T<T_{oo})] \\ &+ [P_{IMLT}(T>T_o)] - [P_{IDW}(T_{oo}<T<T_o)] \\ &+ [P_{RACS}(T<T_o)] - [P_{IACR}(T<T_o)] \\ &- [P_{GACR}(T<T_o)] - [P_{SACR}(T<T_o)] \\ &- [P_{GFR}(T<T_o)] + [P_{SMLT}(T>T_o)] \\ &+ [P_{GMLT}(T>T_o)]. \end{aligned} \tag{6.3f}$$

C(*IWP, LWP*) is simplified as $[P_{GMLT}] - [P_{SACW}] - [P_{GACW}]$ for tropical convective systems (Li et al. 2002b). Precipitation due to snow and graupel (P_{qs} and P_{qg}) is negligible, and P_{qr} accounts for surface rain rate (P_s) in tropical case, here $[P_{DEP}] + [P_{SDEP}] + [P_{GDEP}] = [\Sigma P_{DEP}]$. Therefore, (6.1) and (6.2) can be simplified as

$$\frac{\partial LWP}{\partial t} = CONV_{LWP} - P_s + [P_{CND}] + C(IWP,LWP) - [P_{REVP}] \tag{6.4a}$$

$$\frac{\partial IWP}{\partial t} = CONV_{IWP} + [\Sigma P_{DEP}] - C(IWP,LWP). \tag{6.4b}$$

Taking zonal mean on (6.4) leads to

$$\frac{\partial LWP}{\partial t} = -P_s + [P_{CND}] + C(IWP,LWP) - [P_{REVP}], \tag{6.5a}$$

$$\frac{\partial IWP}{\partial t} = [\Sigma P_{DEP}] - C(IWP,LWP). \tag{6.5b}$$

Take the time derivative of zonal-mean *CR* and use (6.5); the tendency equation of zonal-mean *CR* can be expressed by

$$\frac{\partial \ln CR}{\partial t} = CR_{CLI} + CR_{CNDDEP} + CR_{PSREVP}, \tag{6.6}$$

$$CR_{CLI} = C(LWP,IWP)\left(\frac{LWP + IWP}{LWP \times IWP}\right), \tag{6.6a}$$

$$CR_{CNDDEP} = \frac{[\Sigma P_{DEP}]}{IWP} - \frac{[P_{CND}]}{LWP}, \tag{6.6b}$$

$$CR_{PSREVP} = \frac{P_{sfc}}{LWP} + \frac{[P_{REVP}]}{LWP}. \tag{6.6c}$$

The relation $C(IWP,\ LWP) = -C(LWP,\ IWP)$ is used in the derivation of ((6.6)). Equation ((6.6)) shows that the tendency of the zonal-mean *CR* is determined by the conversion between *LWP* and *IWP* through the melting of graupel and the accretion of cloud water by precipitation ice (CR_{CLI}), vapor condensation and deposition (CR_{CNDDEP}), rainfall, and evaporation of rain (CR_{PSREVP}). The accretion of cloud water by precipitation ice and vapor deposition enhances the development of ice clouds, and the rainfall and evaporation of rain suppress the development of water clouds increasing the cloud ratio, whereas the melting of graupel and vapor condensation enhance the development of water clouds decreasing the cloud ratio.

Dominant responsible processes for the *CR* tendency may be different in different stages of cloud development, which can be identified by surface rain rates (Fig. 6.11). Two stages are categorized based on the hourly zonal-mean data. Since the time-mean surface rain rate during the integration is $0.37\,\mathrm{mm\,h^{-1}}$, we choose $P_s < 0.3\,\mathrm{mm\,h^{-1}}$ as the genesis/dissipating stages and $P_s > 0.3\,\mathrm{mm\,h^{-1}}$ as the mature stage of tropical convection. In the genesis/dissipating stages of tropical convection, the linear correlation coefficients and RMS differences between ln *CR* tendency and its components are 0.13 and $2.31\,\mathrm{h^{-1}}$ for CR_{CLI}, 0.66 and $1.5\,\mathrm{h^{-1}}$ for CR_{CNDDEP}, and 0.14 and $3.33\,\mathrm{h^{-1}}$ for CR_{PSREVP}, respectively. Thus, the ln *CR* tendency is mainly determined by CR_{CNDDEP} (Fig. 6.11b in left panel). The ln *CR* tendency increases with increasing CR_{CNDDEP}, indicating that the vapor condensation and deposition rates associated with the upward motion determine the *CR* tendency and the variations of convective and stratiform clouds. The vapor deposition causes positive *CR* tendency and development of ice clouds, whereas the vapor condensation leads to negative *CR* tendency and growth of water clouds. In the mature stage of tropical convection, the linear correlation coefficients and RMS differences between the ln *CR* tendency and its components are 0.78 and $1.76\,\mathrm{h^{-1}}$ for CR_{CLI}, 0.01 and $2.81\,\mathrm{h^{-1}}$ for CR_{CNDDEP}, and 0.27 and $3.55\,\mathrm{h^{-1}}$ for CR_{PSREVP}, respectively. Thus, the ln *CR* tendency is mainly contributed to by CR_{CLI} (Fig. 6.11a in right panel). The ln *CR* tendency increases with increasing $([P_{SACW}] + [P_{GACW}] - [P_{GMLT}])$. The *CR* decreases (increases) and clouds are more convective (stratiform) when the melting rate of graupel is larger (smaller) than the accretion rate of cloud water by precipitation ice in the mature stages of clouds.

As discussed in section 2.5, the existing partition methods for convective and stratiform clouds have some disadvantages. The separation between convective and stratiform clouds needs information from the neighboring grids (e.g., Churchill and Houze 1984) or some unconventional information such as vertical motion (e.g., Xu 1995) and fall speed of precipitation particles (e.g., Lang et al. 2003). Sui et al. (2007) proposed a new convective–stratiform rainfall partitioning method with *IWP* and *LWP* information. The rainfall is designated convective when *CR* is smaller than 0.2 or *IWP* is larger than the sum of its mean and standard deviation.

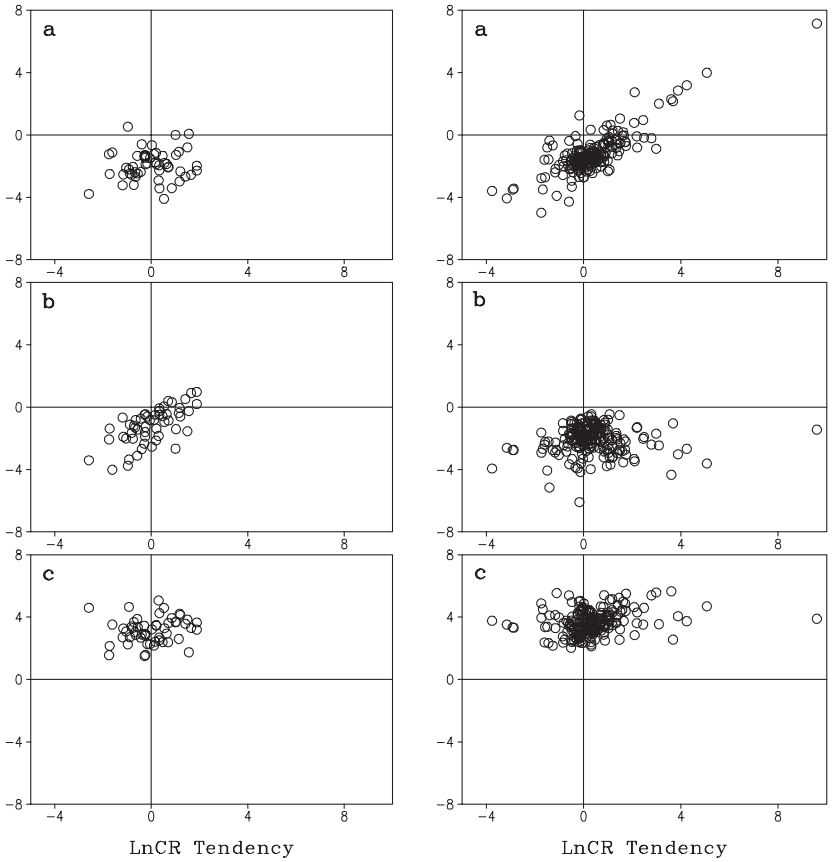

Fig. 6.11 ln *CR* tendency versus the contributions from **a** CR_{CLI}, **b** CR_{CNDDEP}, and **c** CR_{PSREVP} simulated in COARE when the zonal-mean surface rain rates are smaller than 0.3 mm h^{-1} in left panel and larger than 0.3 mm h^{-1} in right panel. Unit is h^{-1} (After Sui and Li 2005)

The vertical profiles of time-mean vertical velocity and CFAD of vertical velocity in the convective and stratiform regions show that this new partition method performs as well as the partition method developed by Tao et al. (1993) and modified by Sui et al. (1994).

6.5 Condensation, Associated Heating, and Large-Scale Forcing

Gao et al. (2006a) analyzed the mass-weighted mean heat budget and *PW* budget using hourly zonal-mean data simulated in COARE. The linear regression equations between $\partial\langle\bar{T}\rangle/\partial t$ and $\langle\bar{Q}_{cn}\rangle/c_p - \langle\pi\bar{w}^o\partial\bar{\theta}/\partial z\rangle$ in the heat budget (Fig. 6.12a in left panel), and between $\partial[\bar{q}_v]/\partial t$ and $-\bar{P}_s - [\bar{w}^o\partial\bar{q}_v/\partial z]$ (here $[\bar{S}_{qv}] \cong \bar{P}_s$) in the *PW* budget (Fig. 6.12b in left panel) can be respectively expressed by

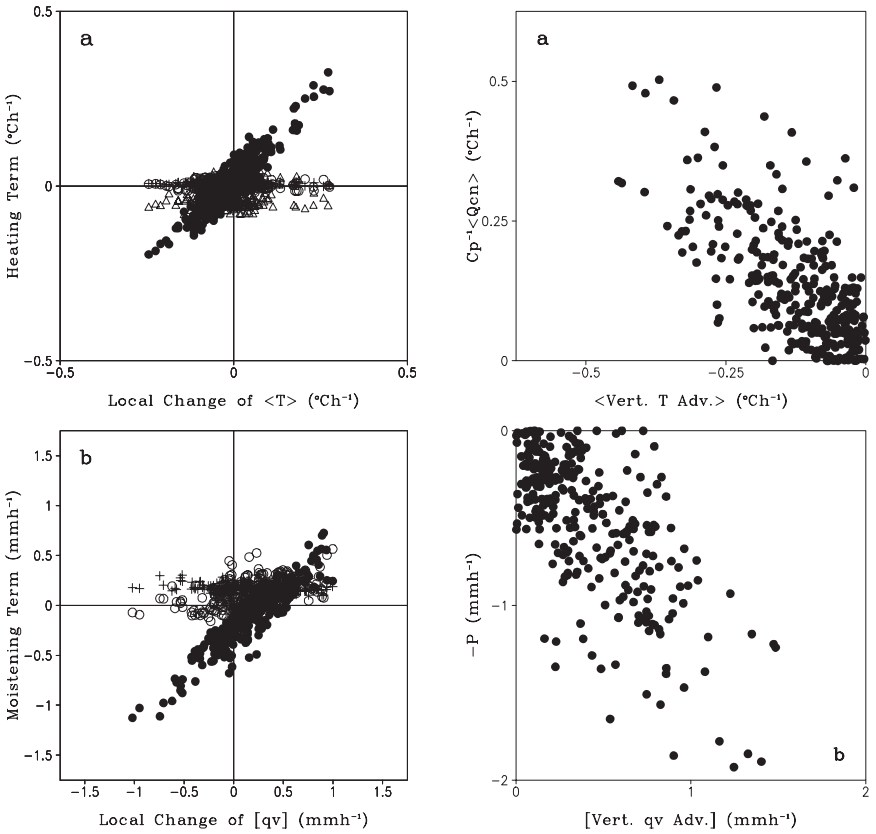

Fig. 6.12 Left panel: **a** components of zonal- and mass-weighted mean heat budget versus local change of mass-weighted mean temperature (°C h^{-1}), and **b** components of zonal-mean *PW* budget versus local *PW* change (mm h^{-1}) in rainy conditions simulated in COARE. Closed dots denote $<\bar{Q}_{cn}>/c_p - <\pi\bar{w}^o\partial\bar{\theta}/\partial z>$ in **a** and $-\bar{P}_s - [\bar{w}^o\partial\bar{q}_v/\partial z]$ in **b**. Open dots represent $-<\bar{u}^o\partial\bar{T}^o/\partial x>$ in (a) and $-[\bar{u}^o\partial\bar{q}_v^o/\partial x]$ in (b). Symbols "x" are $\bar{H}_s$ in (a) and $\bar{E}$ in (b). Symbols delta denote $<\bar{Q}_R>/c_p$ in (a). Right panel: **a** $<\bar{Q}_{cn}>/c_p$ versus $-<\pi\bar{w}^o\partial\bar{\theta}/\partial z>$ (°C h^{-1}), and **b** $-\bar{P}_s$ versus $-[\bar{w}^o\partial\bar{q}_v/\partial z]$ (mm h^{-1}) simulated in COARE (After Gao et al. 2006a)

$$\frac{\partial\langle\bar{T}\rangle}{\partial t} = -0.02 + 0.9\left(\frac{\langle\bar{Q}_{cn}\rangle}{c_p} - \left\langle\pi\bar{w}^o\frac{\partial\bar{\theta}}{\partial z}\right\rangle\right), \tag{6.7a}$$

$$\frac{\partial[\bar{q}_v]}{\partial t} = 0.27 + \left(-\bar{P} - \left[\bar{w}^o\frac{\partial\bar{q}_v}{\partial z}\right]\right). \tag{6.7b}$$

The linear correlation coefficients for both equations are 0.9, which is statistically significant. Thus, the local heat change is largely determined by the sum of condensational heating and vertical thermal advection, whereas the local moisture change is mainly controlled by the sum of precipitation and vertical moisture advection.

Further analysis of the relations between $\langle \bar{Q}_{cn} \rangle / c_p$ and $-\langle \pi \bar{w}^o \partial \bar{\theta} / \partial z \rangle$, and between $-\bar{P}_s$ and $-[\bar{w}^o \partial \bar{q}_v / \partial z]$, respectively, shows that the latent heat of condensation and vertical potential temperature advection in the mass-weighted mean heat budget (Fig. 6.12a in right panel) and the precipitation and vertical moisture advection in the *PW* budget (Fig. 6.12b in right panel) have the same orders of magnitudes, although they have opposite signs. This indicates that in the first-order approximation $\langle \bar{Q}_{cn} \rangle / c_p - \langle \pi \bar{w}^o \partial \bar{\theta} / \partial z \rangle \approx 0$ and $-\bar{P}_s - [\bar{w}^o \partial \bar{q}_v / \partial z] \approx 0$.

To explain the balances between the latent heat of condensation and vertical potential temperature advection in the heat budget and between the precipitation and vertical moisture advection in the *PW* budget in the lowest order approximation and smaller variations of local temperature and *PW* in raining conditions, $\langle \bar{Q}_{cn} \rangle / c_p - \langle \pi \bar{w}^o \partial \bar{\theta} / \partial z \rangle$ versus $\langle \bar{Q}_{cn} \rangle / c_p$ and $-\bar{P}_s - [\bar{w}^o \partial \bar{q}_v / \partial z]$ versus $\bar{P}_s$ are plotted in Fig. 6.13. $\langle \bar{Q}_{cn} \rangle / c_p - \langle \pi \bar{w}^o \partial \bar{\theta} / \partial z \rangle$ is negative (positive) whereas $-\bar{P}_s - [\bar{w}^o \partial \bar{q}_v / \partial z]$ is positive (negative) for the weak (strong) convection with small (large) values of $\langle \bar{Q}_{cn} \rangle / c_p$ and $\bar{P}_s$. Thus, vertically advective moistening and cooling have larger (smaller) magnitudes than the condensation and associated latent heat so that the local vapor gains (losses) and local heat losses (gains) for the weak (strong) convection.

Li (2006) studied the cloud microphysical responses to the COARE-derived large-scale forcing by analyzing the 50-day coupled ocean-cloud-resolving atmosphere model simulation. Figure 6.14 displays upward and downward motions with similar amplitudes imposed in the model with large amplitudes in the upper troposphere and strong easterly winds with strong vertical shears in the upper troposphere and with 4-day oscillations in the lower troposphere during the selected 10-day weak-forcing period. From 15 to 17 November 1992, the sum of zonal-mean *IWP* and *LWP* is smaller than 0.2 mm (Fig. 6.15). $[q_c]$ and $[q_r]$ have similar magnitudes that are smaller than 0.1 mm. $[q_g]$ is occasionally large around late 16 and 17 November 1992 whereas $[q_i]$ and $[q_s]$ are negligibly small. Thus, water clouds are dominant during this period. From 18 November 1992 on, *IWP*+*LWP* increases its magnitudes to 0.4 mm. $[q_r]$ has significant enhancements and becomes twice as large as $[q_c]$ is. $[q_g]$ has large increases with the amplitudes of larger than 0.15 mm. A large increase in $[q_g]$ is associated with a large upward motion with the maximum magnitudes around 200 mb. $[q_i]$ and $[q_s]$ also show increases and they are as large as $[q_g]$ around 19 November 1992.

To examine the enhancement of raindrops around 18 November 1992, the budgets of raindrops are analyzed based on the daily mean data on 15 and 18 November, respectively. On 15 November, $[P_{GMLT}(T > T_o)]$ $(0.0053\,\mathrm{mm\,h^{-1}})$ is more than one order of magnitude smaller than P_s $(0.101\,\mathrm{mm\,h^{-1}})$ and $[P_{RACW}]$ $(0.1081\,\mathrm{mm\,h^{-1}})$ because $[q_g]$ (0.0016 mm) is more than one order of magnitude smaller than $[q_r]$ (0.0204 mm) and $[q_c]$ (0.0266 mm). $[P_{RACW}]$ is nearly balanced by P_s, and $-[P_{REVP}]$ $(-0.0273\,\mathrm{mm\,h^{-1}})$ contributes to $\partial [q_r]/\partial t$ $(-0.0084\,\mathrm{mm\,h^{-1}})$, which suppresses raindrops. On 18 November, $[P_{GMLT}(T > T_o)]$ $(0.0936\,\mathrm{mm\,h^{-1}})$ becomes as large as P_s $(0.156\,\mathrm{mm\,h^{-1}})$ and $[P_{RACW}]$ $(0.1554\,\mathrm{mm\,h^{-1}})$ are because $[q_g]$ (0.0406 mm) grows to the magnitude of $[q_r]$ (0.0403 mm). $[P_{RACW}]$ is nearly balanced by P_s and $[P_{GMLT}(T > T_o)]$ overcomes $-[P_{REVP}]$ $(-0.0763\,\mathrm{mm\,h^{-1}})$,

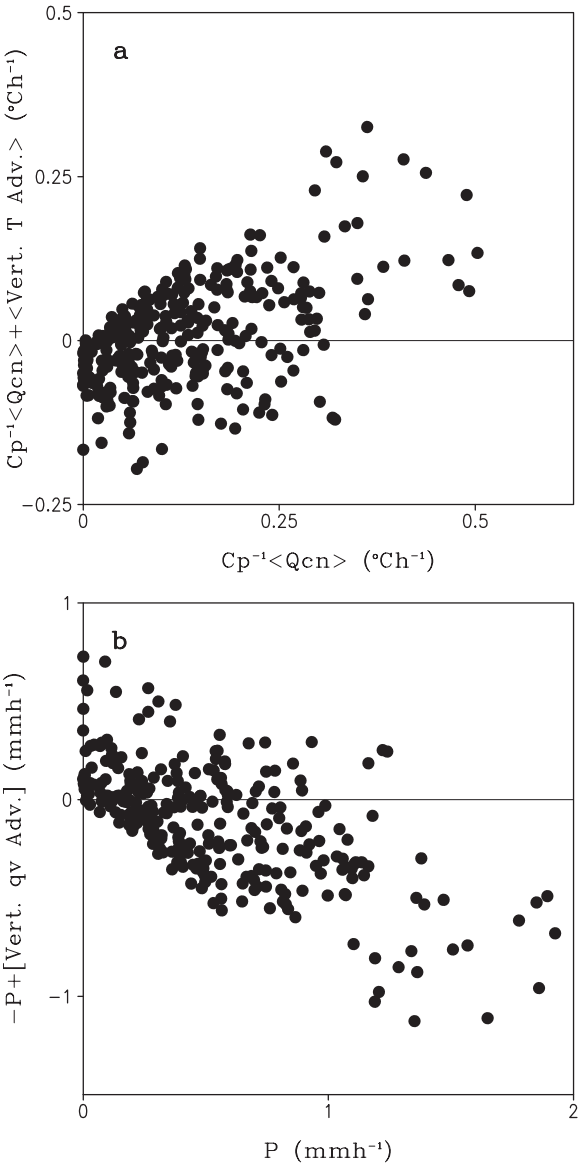

Fig. 6.13 **a** $\langle \bar{Q}_{cn} \rangle / c_p - \langle \pi \bar{w}^o \partial \bar{\theta} / \partial z \rangle$ versus $\langle \bar{Q}_{cn} \rangle / c_p$ (°C h^{-1}), and **b** $-\bar{P}_s - [\bar{w}^o \partial \bar{q}_v / \partial z]$ versus $\bar{P}_s$ (mm h^{-1}) simulated in COARE (After Gao et al. 2006a)

producing a positive $\partial [q_r] / \partial t$ (0.025 mm h^{-1}). Thus, the graupel enhances raindrops through its melting in the tropical convection. The enhancement of raindrops results from the growth of graupel on 18 November. The analysis of the budget of $[q_g]$ (1.7j and 1.8g) shows that the local growth of $[q_g]$ is mainly supported by $[P_{GACW}(T < T_o)]$ (0.0688 mm h^{-1}). $[P_{GACS}]$ (0.0244 mm h^{-1}) plays a second role.

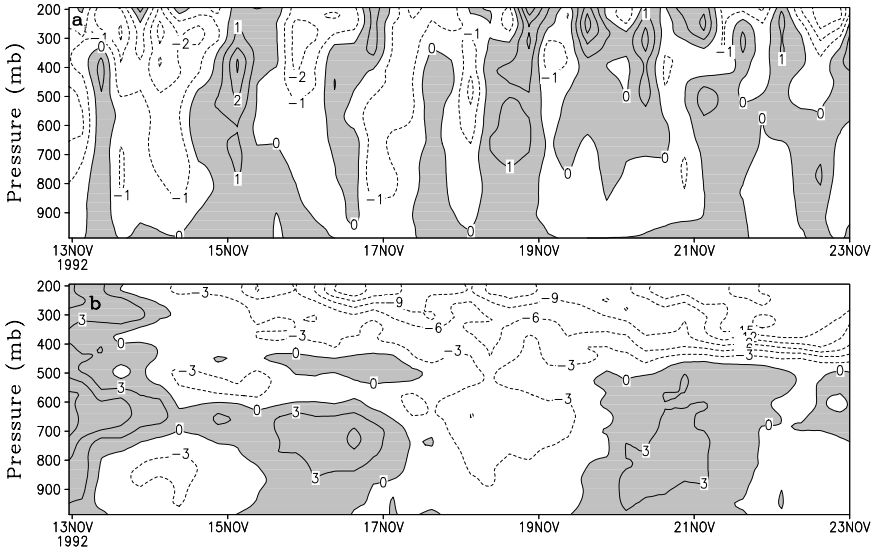

Fig. 6.14 Temporal and vertical distribution of **a** vertical velocity $(\mathrm{cm\,s^{-1}})$ and **b** zonal wind $(\mathrm{m\,s^{-1}})$ from 13 to 22 November 1992. Upward motion in (a) and westerly winds in **b** are shaded (After Li 2006)

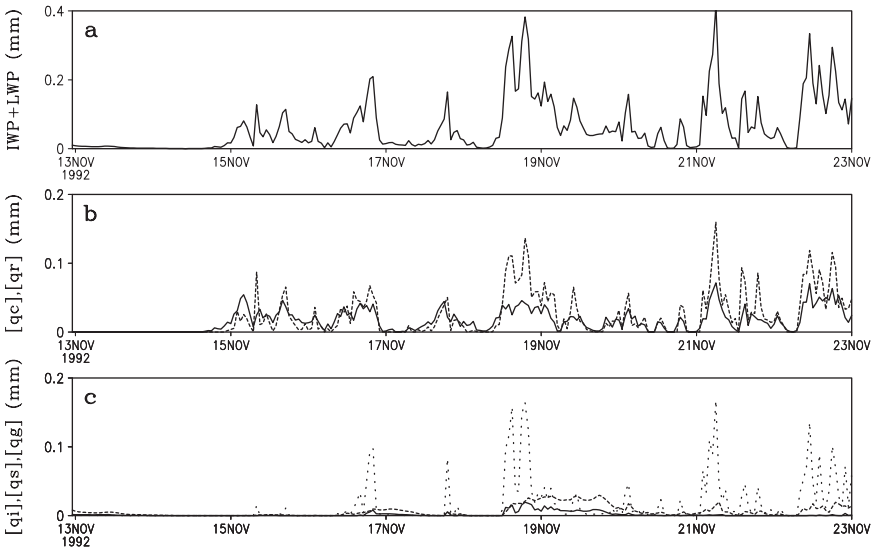

Fig. 6.15 Time series of $IWP + LWP$ in **a**, $[q_c]$ (solid) and $[q_r]$ (dashed) in **b** and $[q_i]$ (solid), $[q_s]$ (dashed), and $[q_g]$ (dot) in **c** simulated in coupled experiment from 13 to 22 November 1992. Unit is mm (After Li 2006)

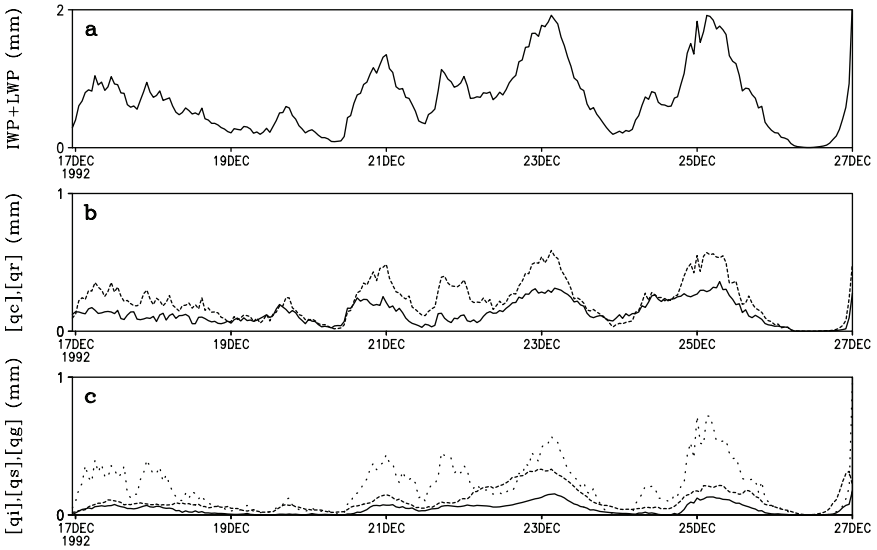

Fig. 6.16 Same as in Fig. 6.15 except from 17 to 26 December 1992 (After Li 2006)

Convective responses to the strong forcing are studied by analyzing the simulation data from 17 to 27 December 1992 (see vertical velocity and zonal wind in Fig. 4.1). The maxima of *IWP+LWP* correspond to the maxima of upward motions (Fig. 6.16a). Although the upward motion ($14\,\mathrm{cm\ s^{-1}}$) around the early morning of 23 December is stronger than that ($10\,\mathrm{cm\ s^{-1}}$) around the early morning of 25 December, the vertical extent of the former (e.g., contour of $2\,\mathrm{cm\ s^{-1}}$) is smaller than that of the latter. Thus, their magnitudes of *IWP+LWP* are about the same ($\sim 2\,\mathrm{mm}$). *IWP+LWP* is largely contributed to by the precipitation water and ice. The amplitudes of $[q_r]$ are larger than those of $[q_c]$ (Fig. 6.16b), whereas the magnitudes of $[q_g]$ are larger than those of $[q_i]$ and $[q_s]$ (Fig. 6.16c). It is interesting to notice that $[q_s]$ increases significantly around late night of 22 December and early morning of 23 December 1992.

To examine the enhancement of snow around late night of 22 December 1992, the daily mean budget of snow on 22 December is compared with the budget on 21 December. $\partial[q_s]/\partial t$ switches to a positive value on 22 December ($0.0058\,\mathrm{mm\ h^{-1}}$) from a negative value on 21 December ($-0.0275\,\mathrm{mm\ h^{-1}}$). The positive $\partial[q_s]/\partial t$ is mainly contributed to by a significant increase of $[P_{SAUT}]$ from $0.1428\,\mathrm{mm\ h^{-1}}$ on 21 December to $0.2273\,\mathrm{mm\ h^{-1}}$ on 22 December and an increase of $[P_{SFW}]$ from $0.0808\,\mathrm{mm\ h^{-1}}$ on 21 December to $0.1241\,\mathrm{mm\ h^{-1}}$ on 22 December, which are in turn due to the increase of $[P_{DEP}]$ from $0.2546\,\mathrm{mm\ h^{-1}}$ on 21 December to $0.3621\,\mathrm{mm\ h^{-1}}$ on 22 December. The increased deposition rate of vapor corresponds to the intensified vertical velocity center in the upper troposphere. The local growth of $[q_s]$ also causes the local enhancement of $[q_g]$ on 22 December, in which $[P_{GACS}]$ ($0.4412\,\mathrm{mm\ h^{-1}}$) plays a primary role and $[P_{GACW}(T < T_o)]$ ($0.2377\,\mathrm{mm\ h^{-1}}$) is a second factor.

6.6 Phase Relation Between Unstable Energy and Surface Rainfall

Tropical convection occurs as a result of instability in the environment. The large-scale environment provides favorable thermal and moisture conditions for the occurrence and development of convection. In return, it is affected by the vertical redistribution of temperature, moisture, and momentum as a result of the convection. Such an interaction allows us to use environmental conditions to estimate properties of the convection such as the precipitation. Since the environmental timescales (a few days and longer) are much longer than the convective timescales (a few hours or less), the rate of production of available potential energy by the large-scale processes is nearly balanced by the rate of consumption of the available potential energy by the convection (Manabe and Strickler 1964). This quasi-equilibrium concept is the basic premise of the cumulus parameterization scheme proposed by Arakawa and Schubert (1974). A decrease in the *CAPE*, which measures the thermal and moisture conditions of the environment, often coincides with the development of convection so that the *CAPE* and rain rate are negatively correlated (e.g., Thompson et al. 1979; Cheng and Yanni 1989; Wang and Randall 1994; Xu and Randall 1998). The phase relation between the *CAPE* and rainfall is due to the coupling between the environmental dynamic and thermodynamic fields (Cheng and Yanni 1989).

The phases of *CAPE* and rainfall could be different because it takes time for clouds to develop. This phase difference can be included by relaxing the quasi-equilibrium assumption in cumulus parameterization (e.g., Betts and Miller 1986; Randall and Pan 1993). The minimum *CAPE* typically occurs a few hours after the maximum rainfall. Such a phase lag was also demonstrated by Xu and Randall (1998) in their 2D cloud-resolving model simulations. Xu and Randall (1998) interpreted the maximum phase lag as the adjustment timescale from disequilibrium to equilibrium states in the presence of time-varying large-scale forcing. Since the *CAPE* is calculated in a Lagrangian framework and the relevant equations cannot be derived in that framework, the physical processes responsible for the phase difference between the *CAPE* and the surface rain rate cannot be examined. Potential and kinetic energy in the Eulerian framework represent the *CAPE* and surface rain rate, respectively, in the Lagrangian framework. Li et al. (2002a) derived a set of equations for conversions between the moist available potential energy and kinetic energy in the Eulerian framework (see section 2.3). Their equations were demonstrated to be the same as those derived by Lorenz (1955) in the absence of moisture.

The analysis of lag correlation between the *CAPE* and surface rain rate shows that maximum *CAPE* leads maximum surface rain rate by 3 h, whereas minimum *CAPE* lags maximum surface rain rate by 2 h. The calculations of lag correlation coefficients between zonal-mean moist available potential energy ($\bar{P}$) and layer-mean vertical velocity as well as between perturbation kinetic energy (K') and layer-mean vertical velocity display that minimum $\bar{P}$ lags maximum upward motion by 6 h, whereas maximum K' lags maximum upward motion by 1–2 h. Thus, the phase

relation between $\bar{P}$ and K' is similar to that between the *CAPE* and surface rain rate, which lays down the foundation to use the moist energetics framework to explain the physical processes associated with the phase difference between the *CAPE* and surface rain rate.

The further calculations between $\partial\bar{P}/\partial t$ and layer-mean vertical velocity and between $\partial K'/\partial t$ and layer-mean vertical velocity reveal that minimum $\partial\bar{P}/\partial t$ lags maximum ascending motion by 3 h, whereas maximum $\partial K'/\partial t$ leads maximum ascending motion by 1–2 h. To elucidate dominant physical processes that are responsible for the phase differences, lag correlation coefficients between each term of $\partial\bar{P}/\partial t$ (2.8) and $\partial P'/\partial t$, $\partial\bar{P}/\partial t$ and each term of $\partial P'/\partial t$ (2.9), each term of $\partial P'/\partial t$ and $\partial K'/\partial t$ (2.10), and $\partial P'/\partial t$ and each term of $\partial K'/\partial t$ are calculated. The term $C_v(\bar{K},\bar{P})$ of $\partial\bar{P}/\partial t$ associated with the vertical thermal and vapor advections and the term $G_R(P')$ of $\partial P'/\partial t$ associated with covariance between the radiation and h' are major players in the determination of phase relation between $\partial\bar{P}/\partial t$ and $\partial P'/\partial t$. The term $C_{cn}(P')$ of $\partial P'/\partial t$ associated with the covariance between the depositional heating and h' and the term $C(P',K')$ of $\partial K'/\partial t$ associated with the covariance between perturbation vertical velocity and temperature are major contributors to the phase relation between $\partial P'/\partial t$ and $\partial K'/\partial t$.

The phase relations between the convection and its environment are summarized in the following way. The imposed large-scale downward motion yields a growth of $\bar{P}$ by the associated vertical advective warming $[C_v(\bar{K},\bar{P}) > 0]$, building the favorable environment for occurrence of convection. The near simultaneous occurrence of maximum $\partial K'/\partial t$, K', and imposed large-scale upward motion implies that convection is phase-locked with the large-scale forcing. The life cycle of the simulated convective events (about 9 h) is much shorter than the timescales of imposed large-scale forcing (longer than the diurnal cycle). In the convective events, maximum $\partial K'/\partial t$ leads maximum $\partial P'/\partial t$ by about 3 h through perturbation cloud heating $[C_{cn}(P')]$ and the vertical heat transport by perturbation circulations $[C(P',K')]$. Maximum $\partial K'/\partial t$ also leads maximum K' by about 3 h, indicating that 3 h is the time required by convection to reach the maximum strength. Minimum $\partial P'/\partial t$ leads minimum $\partial\bar{P}/\partial t$ by about 1 h through perturbation radiative processes $[G_R(P')]$ and the large-scale vertical advective cooling $[C_v(\bar{K},\bar{P})]$. Consequently, maximum $\partial K'/\partial t$ leads minimum $\partial\bar{P}/\partial t$ by 4–5 h, which is about half of the convective life span.

References

Arakawa A, Schubert WH (1974) Interaction of a cumulus cloud ensemble with the large-scale environment. Part I. J Atmos Sci 31:674–701

Betts AK, Miller MJ (1986) A new convective adjustment scheme. Part II: Single column tests using GATE wave, BOMEX, ATEX and arctic airmass data sets. Quart J Roy Meteor Soc 112:692–709

Cheng MD, Yanni M (1989) Effects of downdrafts and mesoscale convective organization on the heat and moisture budgets of tropical cloud cluster. Part III: Effects of mesoscale convective organization. J Atmos Sci 56:3028–3042

Churchill DD, Houze RA Jr (1984) Development and structure of winter monsoon cloud clusters on 10 December 1978. J Atmos Sci 41:933–960
Cui X, Zhou Y, Li X (2007) Cloud microphysical properties in tropical convective and stratiform regions. Meteor Atmos Phys 98:1–11
Fovell RG, Ogura Y (1988) Numerical simulation of a midlatitude squall line in two dimensions. J Atmos Sci 45:3846–3879
Fowler LD, Randall DA, Rutledge DA (1996) Liquid and ice cloud microphysics in the CSU general circulation model. Part I: Model description and simulated microphysical processes. J Climate 9:489–529
Gao S, Ping F, Li X (2006a) Tropical heat/water vapor quasi-equilibrium and cycle as simulated in a 2D cloud resolving model. Atmos Res 79:15–29
Gao S, Ran L, Li X (2006b) Impacts of ice microphysics on rainfall and thermodynamic processes in the tropical deep convective regime: A 2D cloud-resolving modeling study. Mon Wea Rev 134:3015–3024
Grabowski WW (2003) Impact of ice microphysics on multiscale organization of tropical convection in two-dimensional cloud-resolving simulations. Quart J Roy Meteor Soc 129:67–81
Grabowski WW, Moncrieff MW (2001) Large-scale organization of tropical convection in two-dimensional explicit numerical simulations. Quart J Roy Meteor Soc 127:445–468
Grabowski WW, Wu X, Moncrieff MW (1999) Cloud-resolving model of tropical cloud systems during Phase III of GATE. Part III: Effects of cloud microphysics. J Atmos Sci 56:2384–2402
Heymsfield AJ, Donner LJ (1990) A scheme for parameterization ice-cloud water content in general circulation models. J Atmos Sci 47:1865–1877
Hsie EY, Farley RD, Orville HD (1980) Numerical simulation of ice phase convective cloud seeding. J Appl Meteor 19:950–977
Koenig LR (1971) Numerical modeling of ice deposition. J Atmos Sci 28:226–237
Krueger SK, Fu Q, Liou KN, Chin HNS (1995) Improvement of an ice-phase microphysics parameterization for use in numerical simulations of tropical convection. J Appl Meteor 34:281–287
Lang S, Tao WK, Simpson J, Ferrier B (2003) Modeling of convective-stratiform precipitation processes: Sensitivity to partition methods. J Appl Meteor 42:505–527
Li X (2006) Cloud microphysical and precipitation responses to a large-scale forcing in the tropical deep convective regime, Meteor Atmos Phys 94:87–102
Li X, Sui CH, Lau KM, Chou MD (1999) Large-scale forcing and cloud-radiation interaction in the tropical deep convective regime. J Atmos Sci 56:3028–3042
Li X, Sui CH, Lau KM (2002a) Interactions between tropical convection and its environment: An energetics analysis of a 2-D cloud resolving simulation. J Atmos Sci 59:1712–1722
Li X, Sui CH, Lau KM (2002b) Dominant cloud microphysical processes in a tropical oceanic convective system: A 2-D cloud resolving modeling study. Mon Wea Rev 130:2481–2491
Li X, Sui CH, Lau KM, Tao WK (2005) Tropical convective responses to microphysical and radiative processes: A 2D cloud-resolving modeling study. Meteor Atmos Phys 90:245–259
Liu C, Moncrieff MW (1997) Dynamic influence of microphysics in tropical squall lines: A numerical study. Mon Wea Rev 125:2193–2210
Liu Y, Zhang DL, Yau MK (1997) A multiscale numerical study of Hurricane Andrew (1992). Part I: Explicit simulation and Verification. Mon Wea Rev 125:3073–3093
Lord SJ, Willoughby HE, Piotrowicz JM (1984) Role of a parameterized ice phase microphysics in an axisymmetric, nonhydrostatic tropical cyclone model. J Atmos Sci 41:2836–2848
Lorenz EN (1955) Available potential energy and the maintenance of the general circulation. Tellus 7:157–167
Manabe S, Strickler RF (1964) Thermal equilibrium of the atmosphere with a convective adjustment. J Atmos Sci 21:361–385
McCumber M, Tao WK, Simpson Penc JR, Soong ST (1991) Comparison of ice – phase microphysical parameterization schemes using numerical simulations of tropical convection. J Appl Meteor 30:985–1004
Nicholls ME (1987) A comparison of the results of a two-dimensional numerical simulation of a tropical squall line with observations. Mon Wea Rev 115:3055–3077

Orville HD, Kopp FJ (1977) Numerical simulation of the life history of a hailstorm. J Atmos Sci 34:1596–1618

Ping F, Luo Z, Li X (2007) Microphysical and radiative effects of ice clouds on tropical equilibrium states: A two-dimensional cloud-resolving modeling study. Mon Wea Rev 135:2794–2802

Ramanathan V, Pitcher EJ, Malone RC, Blackmon ML (1983) The response of a spectral general circulation model to refinements in radiative processes. J Atmos Sci 40:605–630

Randall DA, Pan DM (1993) Implementation of the Arakawa-Schubert cumulus parameterization with a prognostic closure. In: Emanuel KA, Raymond DJ (ed) The Representation of Cumulus Convection in Numerical Models of the Atmosphere, Meteor Monogr 46, Amer Meteor Soc, Boston, MA

Slingo JM (1987) The development and verification of a cloud prediction scheme for the ECMWF model. Quart J Roy Meteor Soc 113:899–927

Sui CH, Li X (2005) A tendency of cloud ratio associated with the development of tropical water and ice clouds. Terr Atmos Ocean Sci 16:419–434

Sui CH, Lau KM, Tao WK, Simpson J (1994) The tropical water and energy cycles in a cumulus ensemble model. Part I: Equilibrium climate. J Atmos Sci 51:711–728

Sui CH, Tsay CT, LI X (2007) Convective-stratiform rainfall separation by cloud content. J Geophys Res, doi:10.1029/2006JD008082

Tao WK, Simpson J (1989) Modeling study of a tropical squall-type convective line. J Atmos Sci 46:177–202

Tao WK, Simpson J, Soong ST (1991) Numerical simulation of a subtropical squall line over the Taiwan Strait. Mon Wea Rev 119:2699–2723

Tao WK, Simpson J, Sui CH, Ferrier B, Lang S, Scala J, Chou MD, Pickering K (1993) Heating, moisture, and water budgets of tropical and midlatitude squall lines: Comparisons and sensitivity to longwave radiation. J Atmos Sci 50:673–690

Thompson RM Jr, Payne SW, Recker EE, Reed RJ (1979) Structure and properties of synoptic-scale wave disturbances in the intertropical convergence zone of the eastern Atlantic. J Atmos Sci 36:53–72

Wang J, Randall DA (1994) The moist available energy of a conditionally unstable atmosphere. Part II: Further analysis of GATE data. J Atmos Sci 51:703–710

Willoughby HE, Jin HL, Lord SJ, Piotrowicz JM (1984) Hurricane structure and evolution as simulated by an axisymmetric, non-hydrostatic numerical model. J Atmos Sci 41:1169–1186

Wu X, Hall WD, Grabowski WW, Moncrieff MW, Collins WD, Kiehl JT (1999) Long-term evolution of cloud systems in TOGA COARE and their interactions with radiative and surface processes. Part II: Effects of ice microphysics on cloud-radiation interaction. J Atmos Sci 56:3177–3195

Xu KM (1995) Partitioning mass, heat, and moisture budgets of explicit simulated cumulus ensembles into convective and stratiform components. J Atmos Sci 52:1–23

Xu KM, Randall DA (1998) Influence of large-scale advective cooling and moistening effects on the quasi-equilibrium behavior of explicitly simulated cumulus ensembles. J Atmos Sci 55:896–909

Yoshizaki M (1986) Numerical simulations of tropical squall-line clusters: Two-dimensional model. J Meteor Soc Japan 64:469–491

Zhao Q, Carr FH (1997) A prognostic cloud scheme for operational NWP models. Mon Wea Rev 125:1931–1953

Chapter 7
Convective, Moist, and Dynamic Vorticity Vectors

As one of the most important dynamic/thermodynamic parameters, potential vorticity (PV) has been studied to enhance the understanding of the genesis and development of weather systems for more than six decades since it was first introduced by Ertel (1942). PV is conserved in a frictionless, adiabatic flow in a dry atmosphere. Later, moist PV was introduced by replacing potential temperature with the equivalent potential temperature. Moist PV is conserved in frictionless, moist adiabatic processes. Many studies have contributed to understanding the dry and moist PV associated with dynamic and thermodynamic processes in the genesis and development of weather systems (e.g., Bennetts and Hoskins 1979; Emanuel 1979; Danielsen and Hipskind 1980; Thorpe 1985; Hoskins and Berrisford 1988; Xu 1992; Montgomery and Farrell 1993; Cao and Cho 1995; Cho and Cao 1998; Gao et al. 2002). Helicity, as an important dynamic concept, has been applied to the study of convective storms in recent decades (e.g., Lilly 1986; Droegemeier et al. 1993; Tan and Wu 1994) since it was introduced by Betchov (1961). However, PV and helicity cannot be applied to the analysis in the 2D framework.

Convective (***CVV***), moist (***MVV***), and dynamic (***DVV***) vorticity vectors are introduced in the 2D framework by Gao et al. (2004, 2005) and are further studied in the 3D framework by Gao et al. (2007) and Gao (2007). How well do these vorticity vectors represent convective signals? What dominant physical processes determine the variations of these vorticity vectors? What are the differences between the 2D and 3D vorticity vectors? What are the differences between ***CVV*** and moist PV and between ***DVV*** and helicity in the study of 3D convection? These questions will be discussed in this chapter based on Gao et al. (2004, 2005, 2007) and Gao (2007).

7.1 Convective Vorticity Vector

The 3D ***CVV*** can be expressed by

$$\mathbf{CVV} = \frac{\xi \times \nabla \theta_e}{\bar{\rho}} = C_x\mathbf{i} + C_y\mathbf{j} + C_z\mathbf{k}, \tag{7.1a}$$

where $C_x = \zeta_y \partial\theta_e/\bar{\rho}\partial z - \zeta_z \partial\theta_e/\bar{\rho}\partial y$, $C_y = \zeta_z \partial\theta_e/\bar{\rho}\partial x - \zeta_x \partial\theta_e/\bar{\rho}\partial z$, $C_z = \zeta_x \partial\theta_e/\bar{\rho}\partial y - \zeta_y \partial\theta_e/\bar{\rho}\partial x$; $\zeta_x = \partial w/\partial y - \partial v/\partial z$, $\zeta_y = \partial u/\partial z - \partial w/\partial x$, $\zeta_z = \partial v/\partial x - \partial u/\partial y$; θ_e is the equivalent potential temperature; u, v, w are zonal, meridional, and vertical components of wind; planetary vorticity is excluded since it is much smaller than vertical component of relative vorticity.

The ***CVV*** in the 2D x–z frame can be written by

$$\mathbf{CVV} = P_x \mathbf{i} + P_z \mathbf{k}, \tag{7.1b}$$

where $P_x = \zeta_y \partial\theta_e/\bar{\rho}\partial z$ and $P_z = -\zeta_y \partial\theta_e/\bar{\rho}\partial x$. The ***CVV*** has zonal and vertical components in the 2D x–z frame.

Zonally averaged and mass-integrated P_x, P_z, and the total hydrometeor mixing ratio were calculated to examine their relationship. They are denoted by $[P_x]$, $[P_z]$, and $IWP + LWP$, respectively and are shown in Fig. 7.1. The time evolution of $[P_z]$ is in phase with that of $IWP + LWP$ as indicated by their correlation coefficient of 0.81, though more fluctuations occur in $[P_z]$ than in $IWP + LWP$. $[P_x]$, however, does not follow the time evolution of $IWP + LWP$, and their correlation coefficient is only 0.18. Thus, the tendency of the vertical component of ***CVV*** is closely associated with the variation of tropical convection and its tendency equation will be derived next.

The zonal and vertical momentum equations can be expressed by

$$\frac{\partial u}{\partial t} = -u\frac{\partial u}{\partial x} - w\frac{\partial u}{\partial z} - c_p \frac{\partial(\bar{\theta}\pi)}{\partial x}, \tag{7.2a}$$

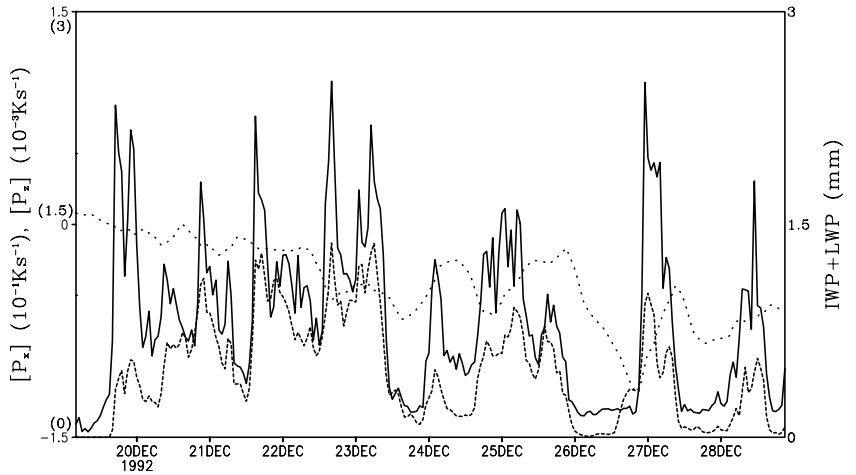

Fig. 7.1 Time series of zonally averaged, mass-integrated zonal $\left([P_x],\ 10^{-1}\,\mathrm{K\,s^{-1}},\ \text{dot line}\right)$ and vertical $\left([P_z],\ 10^{-3}\,\mathrm{K\,s^{-1}},\ \text{solid line}\right)$ components of the 2D ***CVV***, and $IWP + LWP$ (mm, dashed line) in the 10-day 2D cloud-resolving model simulation during TOGA COARE. The plotting scales of $[P_x]$ and $[P_z]$ and $IWP + LWP$ are $-0.15 - 0.15\,\mathrm{K\,s^{-1}}$, $0\text{–}3 \times 10^{-3}\,\mathrm{K\,s^{-1}}$, and 0–3 mm, respectively (Gao et al. 2004)

$$\frac{\partial w}{\partial t} = -u\frac{\partial w}{\partial x} - w\frac{\partial w}{\partial z} - c_p\frac{\partial(\bar{\theta}\pi)}{\partial z} + B, \tag{7.2b}$$

where $B = g(\theta'/\theta_b + 0.61q_v - q_l)$ is the buoyancy force.

Taking $\frac{\partial}{\partial z}(7.2a) - \frac{\partial}{\partial x}(7.2b)$ and applying mass continuity equation, the tendency equation for the vorticity in an elastic approximation is expressed by

$$\frac{\partial}{\partial t}\left(\frac{\zeta_y}{\bar{\rho}}\right) = -u\frac{\partial}{\partial x}\left(\frac{\zeta_y}{\bar{\rho}}\right) - w\frac{\partial}{\partial z}\left(\frac{\zeta_y}{\bar{\rho}}\right) - \frac{1}{\bar{\rho}}\frac{\partial B}{\partial x}. \tag{7.3}$$

The tendency equations for potential temperature and specific humidity are

$$\frac{\partial \theta}{\partial t} = -u\frac{\partial \theta}{\partial x} - w\frac{\partial \theta}{\partial z} + \frac{Q_{cn}}{\pi c_p} + \frac{Q_R}{\pi c_p}, \tag{7.4a}$$

$$\frac{\partial q_v}{\partial t} = -u\frac{\partial q_v}{\partial x} - w\frac{\partial q_v}{\partial z} - S_{qv}. \tag{7.4b}$$

Taking $\frac{1}{\theta} \times (7.4a) + \frac{L_v}{c_p T} \times (7.4b)$ and defining the equivalent potential temperature θ_e as $\theta \exp(L_v q_v / c_p T)$ yields a tendency equation for equivalent potential temperature,

$$\frac{\partial \theta_e}{\partial t} = -u\frac{\partial \theta_e}{\partial x} - w\frac{\partial \theta_e}{\partial z} + \frac{L_f}{c_p}\frac{P_{18}\theta_e}{T} + \frac{1}{c_p}\frac{Q_R\theta_e}{T}. \tag{7.5}$$

The term $\left(-\frac{L_v}{c_p}\frac{\theta_e q_v}{T^2}\left(\frac{\partial T}{\partial t} + \frac{\partial T}{\partial x} + w\frac{\partial T}{\partial z}\right)\right)$ is omitted in the derivation of (7.5) since it is much smaller than the other terms in (7.5). Based on Li et al. (2002), P_{18} (2.7a) in the tropical deep convective regime can be simplified as

$$\begin{aligned} P_{18} = {} & P_{DEP} - P_{MLTG}(T > T_o) + P_{SACW}(T < T_o) \\ & - P_{SMLT}(T > T_o) - P_{GMLT}(T > T_o). \end{aligned} \tag{7.5a}$$

Taking $-\frac{\partial \theta_e}{\partial x} \times (7.3) - \frac{\zeta_y}{\bar{\rho}}\frac{\partial(7.5)}{\partial x}$, the tendency equation for the vertical component of the 2D ***CVV*** ($P_z = -\zeta_y \partial\theta_e/\bar{\rho}\partial x$) can be expressed by

$$\frac{\partial P_z}{\partial t} = PZ1 + PZ2 + PZ3 + PZ4, \tag{7.6}$$

where

$$PZ1 = \left(-u\frac{\partial P_z}{\partial x} - w\frac{\partial P_z}{\partial z}\right) + \frac{\zeta_y}{\bar{\rho}}\left(\frac{\partial u}{\partial x}\frac{\partial \theta_e}{\partial x} + \frac{\partial w}{\partial x}\frac{\partial \theta_e}{\partial z}\right), \tag{7.6a}$$

$$PZ2 = \frac{1}{\bar{\rho}}\frac{\partial \theta_e}{\partial x}\frac{\partial B}{\partial x}, \tag{7.6b}$$

$$PZ3 = -\frac{L_f}{c_p}\frac{\zeta_y}{\bar{\rho}}\frac{\partial}{\partial x}\left(\frac{P_{18}\theta_e}{T}\right), \tag{7.6c}$$

$$PZ4 = -\frac{1}{c_p}\frac{\zeta_y}{\bar{\rho}}\frac{\partial}{\partial x}\left(\frac{Q_R\theta_e}{T}\right). \tag{7.6d}$$

Term $PZ1$ is related to dynamic and thermodynamic processes including the zonal and vertical advection of P_z and the interaction between vorticity and the gradients of wind and equivalent potential temperature. Term $PZ2$ is associated with the buoyancy force. Term $PZ3$ is associated with cloud microphysical processes. Term $PZ4$ includes the solar and IR radiative forcing.

The zonal mean and mass integration of (7.6) yields

$$\frac{\partial[P_z]}{\partial t} = [PZ1] + [PZ2] + [PZ3] + [PZ4]. \tag{7.7}$$

The zonal mean and mass integration of the first term in (7.6a) is much smaller than the other terms in (7.6) and is thus excluded in (7.7).

To examine the processes responsible for the variation of $[P_z]$, the four terms in (7.7) and tendency of $[P_z]$ are calculated. $[PZ3]$ follows the tendency of $[P_z]$ closely in both phase and amplitude with a correlation coefficient of 0.97 and an RMS difference of $1.2\times10^{-6}\,\mathrm{K\,s^{-2}}$, which is much smaller than the standard deviation of the tendency of $[P_z]$ $(3.7\times10^{-6}\,\mathrm{K\,s^{-2}})$. $[PZ2]$ is positive and has moderate amplitudes, whereas $[PZ1]$ is negative. Their correlation coefficients with the tendency of $[P_z]$ are smaller than 0.2, and their RMS differences with the tendency of $[P_z]$ are similar to the standard deviation of the tendency of $[P_z]$. $[PZ4]$ is negligible. Thus,

$$\frac{\partial[P_z]}{\partial t} \approx -\frac{L_f}{c_p}\left[\frac{\zeta_y}{\bar{\rho}}\frac{\partial}{\partial x}\left(\frac{P_{18}\theta_e}{T}\right)\right]. \tag{7.7a}$$

The dominance of $[PZ3]$ in the variation of $[P_z]$ indicates that the variation of the vertical component of the 2D ***CVV*** is controlled by the interaction between the vorticity and zonal gradient of cloud heating. Equation (7.5a) shows that the cloud heating comes from the ice microphysical processes including vapor deposition, evaporation of liquid water from the surface of graupel, accretion of cloud water by snow, and melting of snow and graupel. This implies that P_{18} could be zero in water clouds. Thus, the variation of the vertical component of the 2D ***CVV*** is associated with the variation of the ice hydrometeor mixing ratio through the interaction between the dynamics and ice microphysics.

Gao et al. (2007) used the data from a 3D cloud-resolving model simulation during the TRMM Kwajalein Experiment (KWAJEX) to analyze 3D ***CVV*** (7.1a) and their relations to tropical oceanic convection as well as moist PV. The model is forced by zonally uniform vertical velocity, zonal wind, and thermal and moisture advection based on 6-hourly KWAJEX observations. Kwajalein island is located at 8.44°N, 167.43°E, and has an area of $15\,\mathrm{km^2}$, which makes it the largest island in Kwajalein Atoll $(2{,}200\,\mathrm{km^2})$. The model is integrated from 0600 LST 7 August 1999 to 0600 LST 12 August 1999 (a total of 5 days). Shie et al. (2003) conducted

3D simulations and compared them with radar observations during three active periods in KWAJEX. The simulation and observation show reasonable agreement in rainfall, apparent heat, and moisture sources. Thus, hourly zonal-mean data are used in the following discussions.

To compare ***CVV*** with *PV*, the *PV* is calculated. The *PV* can be expressed by

$$PV = \frac{\xi \cdot \nabla \theta_e}{\bar{\rho}} = PV_1 + PV_2 + PV_3, \tag{7.8}$$

where $PV_1 = \zeta_x \partial \theta_e / \bar{\rho} \partial x$, $PV_2 = \zeta_y \partial \theta_e / \bar{\rho} \partial y$, and $PV_3 = \zeta_z \partial \theta_e / \bar{\rho} \partial z$.

Figure 7.2a shows the time series of $IWP + LWP$, $[C_x]$, $[C_y]$, $[C_z]$, and $[PV]$. $[C_z]$ closely follows evolution of $IWP + LWP$, whereas $[C_x]$ and $[C_y]$ do not. The linear correlation coefficient between $[C_z]$ and $IWP + LWP$ is 0.97, whereas those between $[C_x]$ and $IWP + LWP$, and $[C_y]$ and $IWP + LWP$ are 0.29 and 0.48, respectively. During the 5-day integration period, there are 7–8 convective events. A Student's t-test on the significance of the correlation coefficients is further conducted using five degrees of freedom and the critical correlation coefficient at the 5% significant level is 0.75. Thus, the relation between $IWP + LWP$ and $[C_z]$ is statically significant. $[PV]$ basically follows the evolution of $IWP + LWP$ with the linear correlation coefficient of 0.73, which is marginally statistically significant. From (7.8), $[PV]$ is determined by three components. $[PV_3]$ have a similar magnitude to $[PV]$ (Fig. 7.2b), whereas two other components (not shown) are about one order of magnitude smaller than $[PV_3]$. Thus, $[PV]$ is determined by the covariance between vertical component of vorticity (horizontal rotational circulations) and vertical gradient of moist potential gradient (stability parameter). Note that although the magnitude of $[PV_1]$ is small, the correlation coefficient between $[PV_1]$ and $IWP + LWP$ is 0.54, which is slightly smaller than that between $[PV_3]$ and $IWP + LWP$ (0.62). Since *PV* is a scalar, the role of horizontal component of vorticity in convective development cannot be analyzed. $[C_z]$ is determined by the covariance between horizontal components of vorticity (the secondary circulation in horizontal–vertical framework that is directly associated with the dynamic aspect of convection and is described by the zonal and meridional components of relative vorticity) and horizontal gradients of equivalent potential temperature (that is directly associated with the thermodynamic aspect of the convection). The larger correlation between convection and vertical component of ***CVV*** indicates that the secondary circulation more directly represents convection. The comparison between the *PV* and ***CVV*** shows that the vector analysis can be used to study the roles of horizontal and vertical components of vorticity in convective development separately.

$[C_z]$ can be broken down into $[C_{z1}]$ and $[C_{z2}]$, where $C_{z1} = \zeta_x \partial \theta_e / \bar{\rho} \partial y$, and $C_{z2} = -\zeta_y \partial \theta_e / \bar{\rho} \partial x$. Only $[C_{z2}]$ appears in the 2D framework. Gao et al. (2004) in their 2D study of ***CVV*** during TOGA COARE showed the high linear correlation coefficient between $[C_{z2}]$ and $IWP + LWP$. To examine the contribution of $[C_{z1}]$ and $[C_{z2}]$ to the lag correlation between $IWP + LWP$ and $[C_z]$, the weighted lag correlation coefficients between $IWP + LWP$ and $[C_{z1}]/[C_{z2}]$ are calculated. The two correlation coefficients at lag hour 0 show same values, which indicates that $[C_{z1}]$

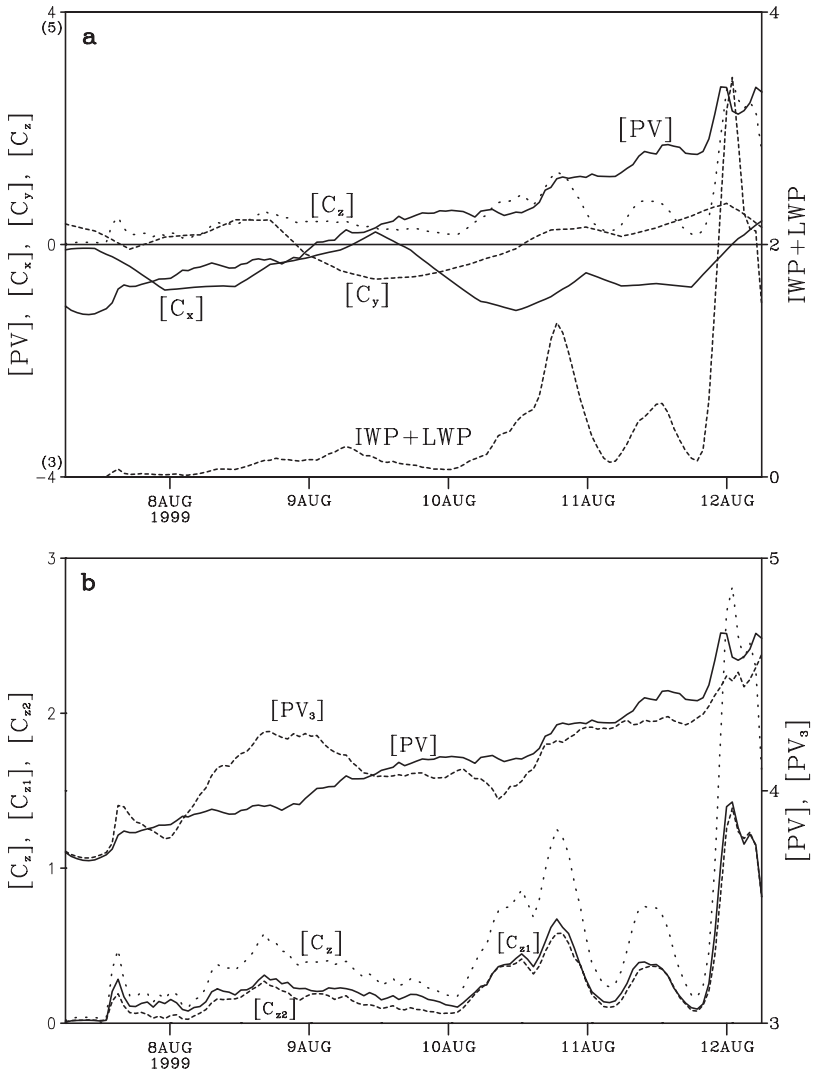

Fig. 7.2 Time series of **a** $IWP + LWP$ (light dashed), $[PV]$ (light solid), $[C_x]$ (dark solid), $[C_y]$ (dark dashed), and $[C_z]$ (dotted), and **b** $[C_z]$ (dotted), $[C_{z1}]$ (dark solid), $[C_{z2}]$ (dark dashed), $[PV]$ (light solid), and $[PV_3]$ (light dashed) in the 5-day 3D cloud-resolving model simulation during KWAJEX. Units are mm for $IWP + LWP$, 10^{-3} K s^{-1} for $[PV]$, $[PV_3]$, $[C_z]$, $[C_{z1}]$, and $[C_{z2}]$, and 10^{-1} K s^{-1} for $[C_x]$ and $[C_y]$. The plotting scales in **a** are 3 to 5×10^{-3} K s^{-1} for $[PV]$ and $[PV_3]$, -4 to 4×10^{-3} K s^{-1} for $[C_z]$, and -4 to 4×10^{-1} K s^{-1} for $[C_x]$ and $[C_y]$ (After Gao et al. 2007)

and $[C_{z2}]$ equally contribute to the correlation coefficient between cloud hydrometeors and vertical component of ***CVV***. Thus, vertical component of ***CVV*** can be a controlling parameter for studying tropical oceanic convection, regardless of the dimension of data (2D or 3D).

7.2 Moist Vorticity Vector

There is plenty of water vapor over the tropics. Thus, the vapor gradient may be much more important than the temperature gradient. P_z can be broken into the two parts:

$$P_z = P_{z1} + P_{z2}, \tag{7.9}$$

where

$$P_{z1} = -\frac{\zeta_y}{\bar{\rho}} \frac{\partial \theta}{\partial x} \exp\left(\frac{L_v q_v}{c_p T}\right), \tag{7.9a}$$

$$P_{z2} = -\frac{\zeta_y}{\bar{\rho}} \theta \frac{\partial}{\partial x} \exp\left(\frac{L_v q_v}{c_p T}\right). \tag{7.9b}$$

P_{z1} is associated with the horizontal gradient of the potential temperature, and P_{z2} is related to the horizontal gradient of the specific humidity. Figure 7.3 shows the time series of zonally averaged and mass-integrated P_z, P_{z1}, and P_{z2} ($[P_z]$, $[P_{z1}]$, and $[P_{z2}]$). $[P_z]$ is largely determined by $[P_{z2}]$, implying the important role of the moisture in equivalent potential temperature gradient in the tropical deep convective regime.

The moist vorticity vector (***MVV***) in the 2D x–z frame is defined as

$$\boldsymbol{MVV} = \frac{\xi \times \nabla q_v}{\bar{\rho}} = \frac{\zeta_y}{\bar{\rho}} \left(\frac{\partial q_v}{\partial z}\mathbf{i} - \frac{\partial q_v}{\partial x}\mathbf{k}\right). \tag{7.10}$$

MVV has zonal ($M_x = \zeta_y \partial q_v / \bar{\rho} \partial z$) and vertical ($M_z = -\zeta_y \partial q_v / \bar{\rho} \partial x$) components in the 2D x–z frame.

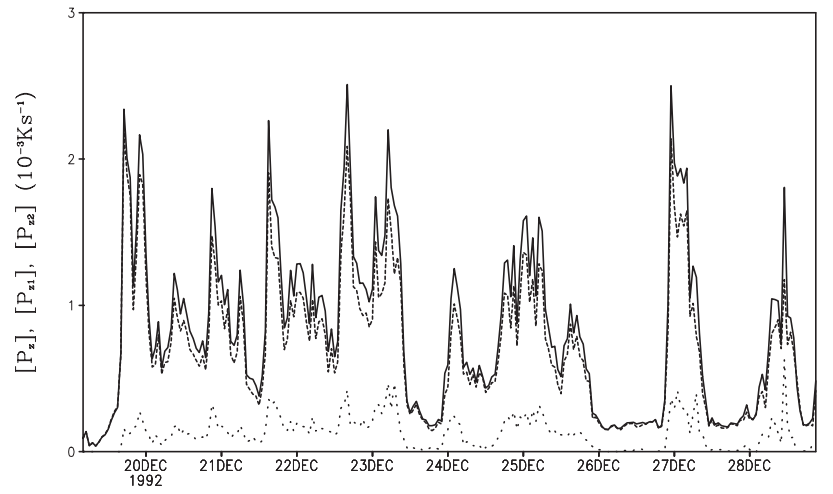

Fig. 7.3 Time series of $[P_z]$ (solid line), $[P_{z1}]$ (dotted line), and $[P_{z2}]$ (dashed line) in the 10-day 2D cloud-resolving model simulation during TOGA COARE. Units are 10^{-3} K s^{-1} (After Gao et al. 2005)

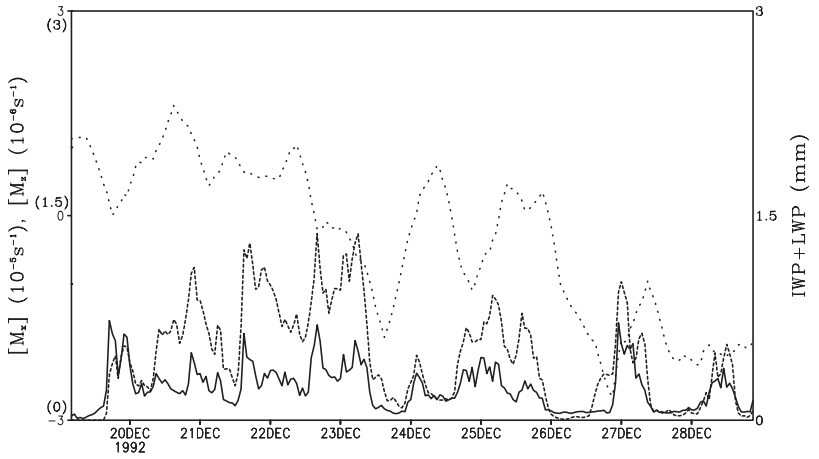

Fig. 7.4 Time series of $[M_x]$ $(10^{-5}\,\mathrm{s}^{-1}$, dotted line), $[M_z]$ $(10^{-6}\,\mathrm{s}^{-1}$, solid line) and $IWP+LWP$ (mm, dashed line) in the 10-day 2D cloud-resolving model simulation during TOGA COARE. The plotting scales of $[M_x]$, $[M_z]$, and $IWP+LWP$ are $-3-3\times10^{-5}\,\mathrm{s}^{-1}$, 0–$3\times10^{-6}\,\mathrm{s}^{-1}$, and 0–3 mm, respectively (After Gao et al. 2005)

Figure 7.4 shows the time series of $[M_x]$, $[M_z]$, and $IWP+LWP$, respectively. The time evolution of $[M_z]$ is in phase with that of $IWP+LWP$ as indicated by their correlation coefficient of 0.78. However, the correlation coefficient between $[M_x]$ and $IWP+LWP$ is only 0.32. Thus, the tendency of the vertical component of 2D ***MVV*** is closely associated with the variation of tropical convection and its tendency equation will be derived next.

Taking $-\frac{\partial q_v}{\partial x}\times(7.3)-\frac{\zeta_y}{\bar{\rho}}\frac{\partial(7.4\mathrm{b})}{\partial x}$, the tendency equation for the vertical component of the 2D ***MVV*** (M_z) can be expressed by

$$\frac{\partial M_z}{\partial t}=MZ1+MZ2+MZ3, \tag{7.11}$$

where

$$MZ1=\left(-u\frac{\partial M_z}{\partial x}-w\frac{\partial M_z}{\partial z}\right)+\frac{\zeta_y}{\bar{\rho}}\left(\frac{\partial u}{\partial x}\frac{\partial q_v}{\partial x}+\frac{\partial w}{\partial x}\frac{\partial q_v}{\partial z}\right), \tag{7.11a}$$

$$MZ2=\frac{1}{\bar{\rho}}\frac{\partial q_v}{\partial x}\frac{\partial B}{\partial x}, \tag{7.11b}$$

$$MZ3=\frac{\zeta_y}{\bar{\rho}}\frac{\partial}{\partial x}(S_{qv}). \tag{7.11c}$$

Term $MZ1$ is related to dynamic and thermodynamic processes including the zonal and vertical advection of M_z and the interaction between vorticity and the gradients of wind and specific humidity. Term $MZ2$ is associated with the buoyancy force. Term $MZ3$ is associated with cloud microphysical processes including condensation and deposition.

The zonal mean and mass integration of (7.11) yields

$$\frac{\partial [M_z]}{\partial t} = [MZ1] + [MZ2] + [MZ3]. \tag{7.12}$$

The zonal mean and mass integration of the first term in (7.11a) is much smaller than the other terms in (7.11) and is thus excluded in (7.12).

To examine the processes responsible for the variation of $[M_z]$, the three terms in (7.12) and the tendency of $[M_z]$ are calculated. $[MZ1]$ is always positive with the magnitudes of up to $3 \times 10^{-9}\,\mathrm{s}^{-2}$, whereas $[MZ3]$ varies between -5 and $5 \times 10^{-9}\,\mathrm{s}^{-2}$. $[MZ3]$ follows the tendency of $[M_z]$ roughly with a correlation coefficient of 0.8 and an RMS difference of $1.05 \times 10^{-9}\,\mathrm{s}^{-2}$, which is similar to than standard deviation of the tendency of $[M_z]$ $(1.06 \times 10^{-9}\,\mathrm{s}^{-2})$. A positive tendency for $[M_z]$ is initiated by positive $[MZ3]$; $[MZ1]$ contributes later. $[MZ2]$ has negligibly small magnitudes compared to $[MZ3]$ and $[MZ1]$. Thus, $[MZ3]$ has major contributions to the tendency of $[M_z]$, and $[MZ1]$ has the significant modifications. Since the vapor condensation and deposition rates are important parts of S_{qv}, the variation of the vertical component of the 2D ***MVV*** is associated with the total hydrometeor mixing ratio through the interaction between the dynamics and the water/ice microphysics.

The 3D ***MVV*** can be expressed by

$$\mathbf{MVV} = \frac{\xi \times \nabla q_v}{\bar{\rho}} = M_x \mathbf{i} + M_y \mathbf{j} + M_z \mathbf{k}, \tag{7.13}$$

where $M_x = \zeta_y \partial q_v/\bar{\rho}\partial z - \zeta_z \partial q_v/\bar{\rho}\partial y$, $M_y = \zeta_z \partial q_v/\bar{\rho}\partial x - \zeta_x \partial q_v/\bar{\rho}\partial z$, $M_z = \zeta_x \partial q_v/\bar{\rho}\partial y - \zeta_y \partial q_v/\bar{\rho}\partial x$.

Since moisture gradient is much important than temperature gradient in the tropical deep convective regime, it determines the variation of equivalent potential temperature gradient. Thus, $(\xi \cdot \nabla q_v)/\bar{\rho}$ is defined as the moist vorticity (MV). To compare ***MVV*** with MV, the MV is calculated. The MV can be expressed by

$$MV = \frac{\xi \cdot \nabla q_v}{\bar{\rho}} = MV_1 + MV_2 + MV_3, \tag{7.14}$$

where $MV_1 = \zeta_x \partial q_v/\bar{\rho}\partial x$, $MV_2 = \zeta_y \partial q_v/\bar{\rho}\partial y$, $MV_3 = \zeta_z \partial q_v/\bar{\rho}\partial z$.

Figure 7.5a shows the time series of $IWP + LWP$, $[M_x]$, $[M_y]$, $[M_z]$, and $[MV]$. Vertical component of ***MVV*** intimately follows the variation of $IWP + LWP$ with the correlation coefficient of 0.95. $[MV]$ and $IWP + LWP$ are correlated with the coefficient of 0.75. $[MV_3]$ have the similar magnitude to $[MV]$ (Fig. 7.5b), whereas two other components (not shown) are about one order of magnitude smaller than $[MV_3]$. Horizontal components of ***MVV*** ($[M_x]$ and $[M_y]$) are loosely correlated with cloud hydrometeors for only -0.26 and 0.17, respectively, which are not statistically significant. $[M_z]$ can be broken down into $[M_{z1}]$ and $[M_{z2}]$, where $M_{z1} = \zeta_x \partial q_v/\bar{\rho}\partial y$, and $M_{z2} = -\zeta_y \partial q_v/\bar{\rho}\partial x$. Only $[M_{z2}]$ appears in the 2D framework and has the high linear correlation coefficient with $IWP + LWP$. In the 3D framework, $[M_{z1}]$ is slightly larger than $[M_{z2}]$ when the convection is moderate or strong (e.g., from

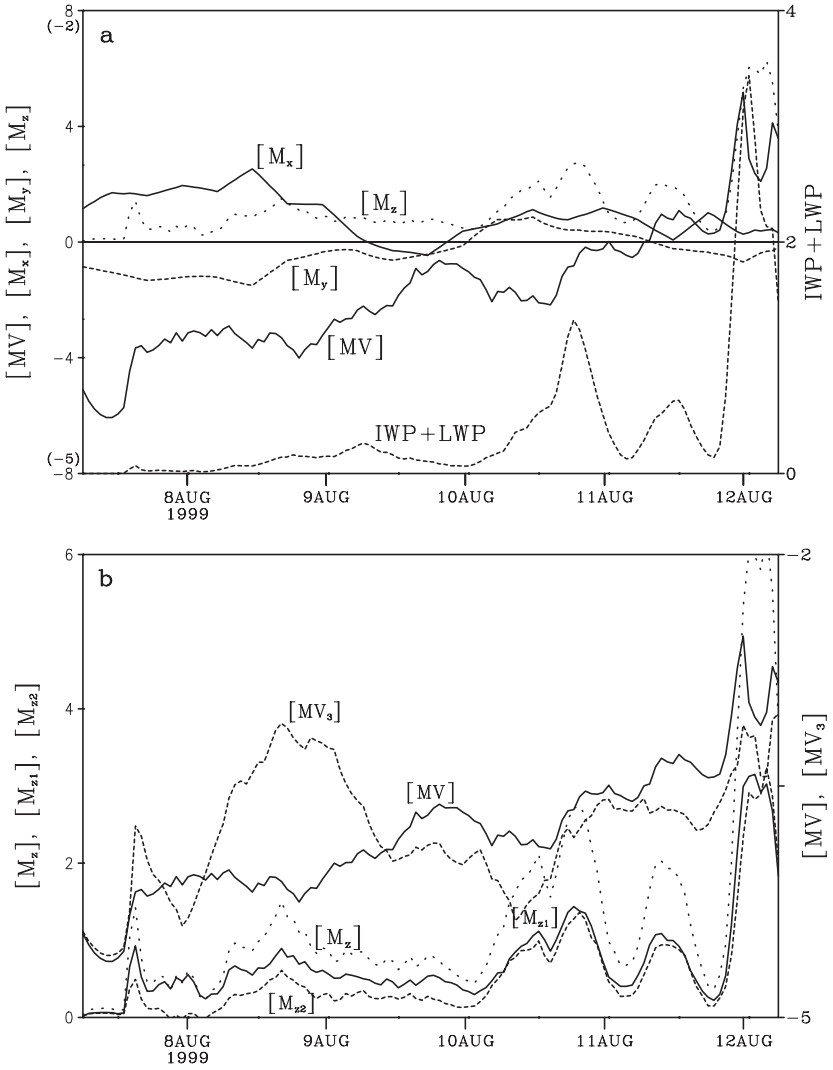

Fig. 7.5 Time series of **a** $IWP+LWP$, $[MV]$, $[M_x]$, $[M_y]$, $[M_z]$, and **b** $[M_z]$, $[M_{z1}]$, $[M_{z2}]$, $[MV]$, $[MV_3]$ in the 5-day 3D cloud-resolving model simulation during KWAJEX. Units are mm for $IWP+LWP$, $10^{-7}\,s^{-1}$ for $[MV]$, $[MV_3]$, $[M_z]$, $[M_{z1}]$, $[M_{z2}]$, and $10^{-5}\,s^{-1}$ for $[M_x]$, $[M_y]$. The plotting scales in (a) are -5 to $-2\times10^{-7}\,s^{-1}$ for $[MV]$, -8 to $8\times10^{-7}\,s^{-1}$ for $[M_z]$, and -8 to $8\times10^{-5}\,s^{-1}$ for $[M_x]$ and $[M_y]$ (After Gao et al. 2007)

0000 LST 10 August 1999 to 0600 LST 12 August 1999), whereas $[M_{z1}]$ is significantly larger when the convection is weak (e.g., from 1200 LST 7 August 1999 to 0000 LST 10 August 1999) (Fig. 7.5b). Thus, vertical component of ***MVV*** can be a controlling parameter for studying tropical oceanic convection, in particular strong convection, regardless of the dimension of data (2D or 3D).

7.3 Dynamic Vorticity Vector

The dynamic vorticity vector (***DVV***) in the 2D x–z frame is defined as:

$$\mathbf{DVV} = \frac{\xi \times \mathbf{V}}{\rho} = -\frac{w\zeta_y}{\rho}\mathbf{i} + \frac{u\zeta_y}{\rho}\mathbf{k}. \tag{7.15a}$$

DVV has zonal ($D_x = -w\zeta_y/\bar{\rho}$) and vertical ($D_z = u\zeta_y/\bar{\rho}$) components in the 2D x–z frame. Figure 7.6 shows that $[D_x]$ and $IWP + LWP$ are out of phase with a correlation coefficient of -0.62, whereas $[D_z]$ and $IWP + LWP$ are in phase with a correlation coefficient of 0.52. This indicates that both components are associated with tropical convection in the 2D framework.

The 3D ***DVV*** can be expressed by

$$\boldsymbol{DVV} = \frac{\xi \times \mathbf{V}}{\bar{\rho}} = D_x\mathbf{i} + D_y\mathbf{j} + D_z\mathbf{k}, \tag{7.15b}$$

where $D_x = D_{x1} + D_{x2}$, $D_y = D_{y1} + D_{y2}$, $D_z = D_{z1} + D_{z2}$; $D_{x1} = \zeta_y w/\bar{\rho}$, $D_{x2} = -\zeta_z v/\bar{\rho}$, $D_{y1} = \zeta_z u/\bar{\rho}$, $D_{y2} = -\zeta_x w/\bar{\rho}$; $D_{z1} = \zeta_x v/\bar{\rho}$; and $D_{z2} = -\zeta_y u/\bar{\rho}$.

To compare ***DVV*** with helicity (H), H is calculated. H can be expressed by

$$H = \frac{\xi \cdot \mathbf{V}}{\bar{\rho}} = H_1 + H_2 + H_3, \tag{7.16}$$

where $H_1 = \zeta_x u/\bar{\rho}$, $H_2 = \zeta_y v/\bar{\rho}$, $H_3 = \zeta_z w/\bar{\rho}$.

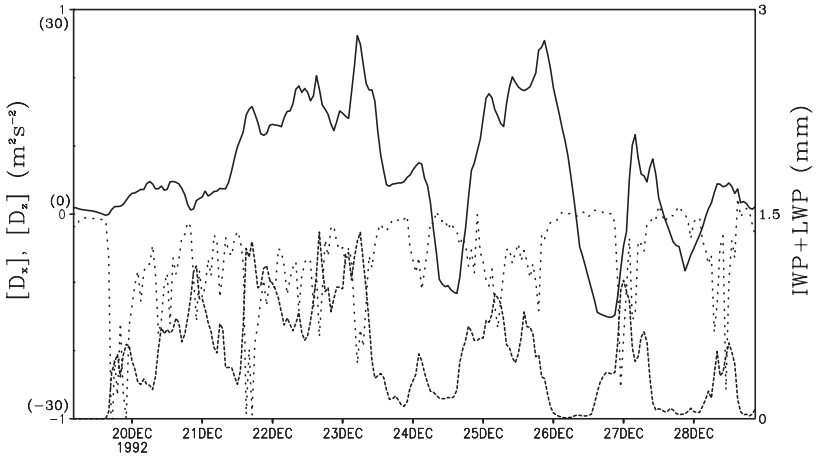

Fig. 7.6 Time series of $[D_x]$ ($\mathrm{m^2\,s^{-2}}$, dotted line), $[D_z]$ ($\mathrm{m^2\,s^{-2}}$, solid line) and $IWP + LWP$ (mm, dashed line) in the 10-day 2D cloud-resolving model simulation during TOGA COARE. The plotting scales of $[D_x]$, $[D_z]$, and $IWP + LWP$ are $-1 - 1\,\mathrm{m^2\,s^{-2}}$, $-30 - 30\,\mathrm{m^2\,s^{-2}}$, and 0–3 mm, respectively (After Gao et al. 2005)

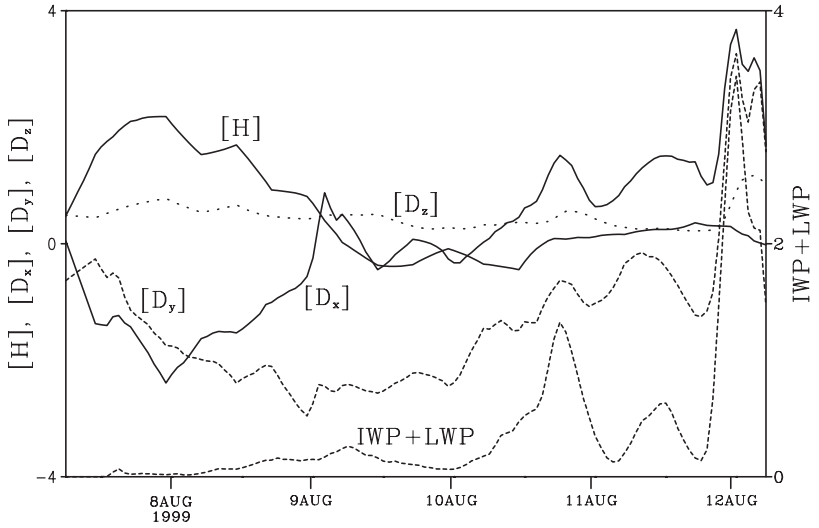

Fig. 7.7 Time series of $IWP+LWP$ (light dashed), $[H]$ (light solid), $[D_x]$ (dark solid), $[D_y]$ (dark dashed), and $[D_z]$ (dotted) in the 5-day 3D cloud-resolving model simulation during KWAJEX. Units are mm for $IWP+LWP$, $10^2\,\mathrm{m^2\,s^{-2}}$ for $[H]$, $\mathrm{m^2\,s^{-2}}$ for $[D_x]$ and $[D_y]$, and $10^2\,\mathrm{m^2\,s^{-2}}$ for $[D_z]$ (After Gao 2007)

Figure 7.7 shows that $[D_x]$ and $[D_y]$ follow evolution of $IWP+LWP$ more closely than $[D_z]$ does. The linear correlation coefficients between $[D_x]$ and IWP+LWP and $[D_y]$ and $IWP+LWP$ are 0.77 and 0.81, respectively, whereas the linear correlation coefficient between $[D_z]$ and $IWP+LWP$ is 0.45. The linear relations between $[D_x]$ and $IWP+LWP$, and $[D_y]$ and $IWP+LWP$ are statistically significant, whereas the linear relation between $[D_z]$ and $IWP+LWP$ is not. Further analysis shows that $[D_x]$ and $[D_y]$ are determined by $[D_{x2}]$ and $[D_{y1}]$, respectively (Fig. 7.8b and c), whereas $[D_z]$ is determined by both $[D_{z1}]$ and $[D_{z2}]$ after the 2-day integration (Fig. 7.8d).

The 3D ***DVV*** is different from the 2D ***DVV*** in two ways. Firstly, the zonal component of the 2D ***DVV*** is out of phase with the convection, whereas that of the 3D ***DVV*** is in phase with the convection. This is due to the fact that the zonal component of the 3D ***DVV*** is determined by $[D_{x2}]$, which is excluded from the zonal component of the 2D ***DVV***. Secondly, the linear correlation coefficient between the vertical component of the 3D ***DVV*** and the convection is significantly smaller than those between the horizontal components and the convection, whereas the linear correlation coefficients between the vertical component of the 2D ***DVV*** and the convection and the horizontal component of the 2D ***DVV*** and the convection have similar magnitudes.

$[H]$ and $IWP+LWP$ are loosely out of phase with the linear correlation coefficient of -0.28, which is not statistically significant. From (7.16), $[H]$ is determined by three components. $[H_1]$ and $[H_2]$ have similar magnitudes, which are much larger than that of $[H_3]$ (Fig. 7.8a). Thus, $[H]$ is determined by the covariance between

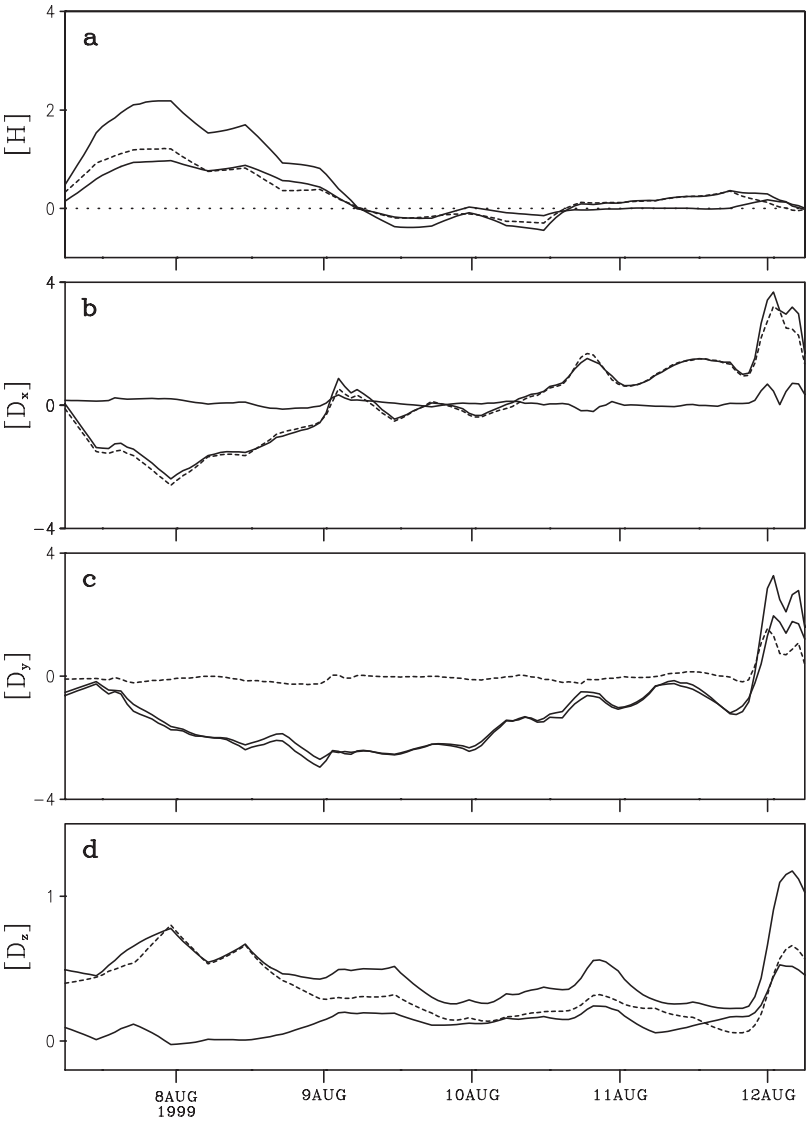

Fig. 7.8 Time series of **a** $[H]$ (dark solid), $[H_1]$ (light solid), $[H_2]$ (dashed), $[H_3]$ (dot), **b** $[D_x]$ (dark solid), $[D_{x1}]$ (light solid), $[D_{x2}]$ (dashed), **c** $[D_y]$ (dark solid), $[D_{y1}]$ (light solid), $[D_{y2}]$ (dashed), and **d** $[D_z]$ (dark solid), $[D_{z1}]$ (light solid), $[D_{z2}]$ (dashed) in the 5-day 3D cloud-resolving model simulation during KWAJEX. Units are $10^2\,\mathrm{m^2\,s^{-2}}$ for $[H]$, $\mathrm{m^2\,s^{-2}}$ for $[D_x]$ and $[D_y]$, and $10^2\,\mathrm{m^2\,s^{-2}}$ for $[D_z]$ (After Gao 2007)

horizontal components of vorticity and horizontal wind. The results indicate that the linear correlations between the 3D ***DVV*** and tropical oceanic convection are better than those between the helicity and tropical oceanic convection.

Figure 7.7 shows that during the strong upward motion at midnight of 11 August 1999, ***DVV*** has a large fluctuation correspondingly, whereas $[H]$ does not. Due to the conservation property of equivalent potential temperature, the particles are restricted to move on the isentropic surface during an adiabatic process. During the development of convective systems, all particles move vertically on the isentropic surface that is nearly perpendicular to the earth surface, whereas 3D vorticity vector develops horizontally, which directly leads to a small $[H]$ and a large ***DVV***. Thus, ***DVV*** better captures strong convective signals than $[H]$ does.

When the wind is separated into rotational and divergent components, ***DVV*** contains both interactions between divergence wind and vorticity and rotational wind and vorticity, whereas $[H]$ only includes the interaction between divergence wind and vorticity. The large signals of ***DVV*** with strong upward motions during the convective development suggest the importance of the interaction between rotational wind and vorticity in the strong convective events.

References

Bennetts DA, Hoskins BJ (1979) Conditional symmetric instability - a possible explanation for frontal rainbands. Quart J Roy Meteor Soc 105:945–962

Betchov R (1961) Semi-isotropic turbulence and helicoidal flows. Phys Fuilds 4:925–926

Cao Z, Cho H (1995) Generation of moist vorticity in extratropical cyclones. J Atmos Sci 52: 3263–3281

Cho H, Cao Z (1998) Generation of moist vorticity in extratropical cyclones. Part II: Sensitivity to moisture distribution. J Atmos Sci 55:595–610

Danielsen EF, Hipskind RS (1980) Stratospheric-tropospheric exchange at polar latitudes in summer. J Geophys Res 85:393–400

Droegemeier KK, Lazarus SM (1993) The influence of helicity on numerically simulated convective storms. Mon Wea Rev 121:2005–2029

Emanuel KA (1979) Inertial instability and mesoscale convective systems. Part I: Linear theory of inertial instability in rotating viscous fluids. J Atmos Sci 36:2425–2449

Ertel H (1942) Ein neuer hydrodynamischer wirbelsatz. Meteorology Zeitschr Braunschweigs 6:277–281

Gao S (2007) A three-dimensional dynamic vorticity vector associated with tropical oceanic convection. J Geophys Res, doi:10.1029/2007JD008247

Gao S, Lei T, Zhou Y (2002) Moist potential vorticity anomaly with heat and mass forcings in torrential rain system. Chin Phys Lett 19:878–880

Gao S, Ping F, Li X, Tao WK (2004) A convective vorticity vector associated with tropical convection: A 2D cloud-resolving modeling study. J Geophys Res, doi:10.1029/2004JD004807

Gao S, Cui X, Zhou Y, Li X, Tao WK (2005) A modeling study of moist and dynamic vorticity vectors associated with 2D tropical convection. J Geophys Res, doi:10.1029/2004JD005675

Gao S, Li X, Tao WK, Shie CL, Lang S (2007) Convective and moist vorticity vectors associated with three-dimensional tropical oceanic convection during KWAJEX, J Geophys Res, doi:10.1029/2006JD007179

Hoskins BJ, Berrisford P (1988) A potential vorticity perspective of the storm of 15–16 October 1987. Weather 43:122–129

Li X, Sui CH, Lau KM (2002) Dominant cloud microphysical processes in a tropical oceanic convective system: A 2-D cloud resolving modeling study. Mon Wea Rev 130:2481–2491

Lilly DK (1986) The structure, energetics and propagation of rotating convective storms. Part II: Helicity and storm stabilization. J Atmos Sci 43:126–140

Montgomery MT, Farrell BF (1993) Tropical cyclone formation. J Atmos Sci 50:285–310

Shie CL, Tao WK, Simpson J (2003) Simulated KWAJEX convective systems using a 2D and 3D cloud resolving model and their comparisons with radar observations. 31st Conference on Radar Meteorology, Seattle, Washington, 6–12 August 2003

Tan Z, Wu R (1994) Helicity dynamics of atmospheric flow. Adv Atmos Sci 11:175–188

Thorpe AJ (1985) Diagnosis of balanced vortex structure using potential vorticity. J Atmos Sci 42:397–406

Xu Q (1992) Formation and evolution of frontal rainbands and geostrophic potential vorticity anomalies. J Atmos Sci 49:629–648

Chapter 8
Diurnal Variations of Tropical Oceanic Convection

The diurnal variation of tropical oceanic convection is one of the most important components in tropical variability and plays a crucial role in regulating tropical hydrological and energy cycles. The dominant diurnal signal is the nocturnal peak in precipitation that occurs in the early morning. The second rainfall peak appears in the early afternoon. The nocturnal rainfall maximum may be primarily caused by the IR cooling or radiational difference between cloudy regions and clear-sky regions. The afternoon rainfall maximum may result from the increase of *SST*. The cloud-resolving model simulations could provide a powerful tool in enhancing the understanding of physical mechanisms associated with the formation of two rainfall peaks through the sensitivity experiments and associated budget analysis of heat, water vapor, and surface rainfall. In this chapter, a four-decade history of observational and numerical studies of diurnal rainfall variations is briefly reviewed. The nocturnal rainfall peak is discussed by analyzing domain mean cloud-resolving model simulation data during TOGA COARE. The nocturnal and afternoon rainfall peaks are examined by analyzing grid data from a coupled ocean-cloud-resolving atmosphere model simulation. The diurnal variations of convective and stratiform rainfall are analyzed using the equilibrium data from cloud-resolving model simulations.

8.1 Introduction

Kraus (1963) analyzed precipitation data collected from nine weatherships, showed nocturnal rainfall peaks, and suggested that solar heating and IR cooling tend to suppress convection during daytime and enhance convection during nighttime, respectively. The solar radiative heating reduces rainfall by evaporating cloud drops and lowering vapor condensation rate. Gray and Jacobson (1977) found that heavy rainfall is 2–3 times greater in the morning than in the late afternoon and evening, and argued that the nocturnal rainfall peaks are enhanced by the secondary circulation forced by the radiational differences between cloudy regions and clear-sky regions. The cloud radiative forcing causes upward motion and convection during

nighttime through the low-level convergence. Randall et al. (1991) carried out sensitivity experiments using a general circulation model and showed that with the absence of the radiative effects of clouds, the phase of simulated diurnal rainfall cycle is not changed but the amplitude is much weakened. Xu and Randall (1995) conducted the experiments with the cloud-resolving model and showed the diurnal variation regardless of whether radiation is interactive or noninteractive, indicating the mechanism proposed by Gray and Jacobson plays a secondary role in the diurnal processes. Tao et al. (1996) carried out a series of cloud-resolving model simulations to study cloud–radiation interaction mechanisms and emphasized that the increase of surface precipitation by IR cooling is due to the increased relative humidity. The surface rainfall is not sensitive to the cloud-top cooling and cloud-base warming, and differential cooling between clear-sky and cloudy regions. Liu and Moncrieff (1998) from their cloud-resolving model simulations found that the simulated diurnal variation is primarily due to the direct interaction between radiation and convection, and the mechanism proposed by Gray and Jacobson (1977) is a secondary factor.

Sui et al. (1997) conducted the diurnal analysis using the observational data from TOGA COARE. The data are first categorized into the disturbed and undisturbed periods by calculating the standard deviation of brightness temperature measured by the GMS operated by the Japanese Meteorological Agency. Over the disturbed periods, total surface rain rates as well as convective and stratiform rain rates reach the maxima at 0300 LST. Fractional coverage for stratiform clouds shows a maximum at 0300 LST, whereas fractional coverage for convective clouds does not show a significant diurnal variation. Diurnal variation of the rain rate histogram shows the evolution of nocturnal rainfall has a growing phase from 2200 to 0300 LST, when a wide range of convection (rain rate is higher than $0.5\,\mathrm{mm\,h^{-1}}$) becomes enhanced with most occurrences within $0.5–5\,\mathrm{mm\,h^{-1}}$. The nocturnal rainfall is associated with anomalous ascending motion in the layer between 500 and 200 mb at 0400 LST. Over the undisturbed periods, the surface rain rate is very small, but shows a maximum from 1200 to 1800 LST. The diurnal variation of rain rate histogram shows that the evolution of afternoon rainfall has a growing phase from 1200 to 1800 LST, when most occurrences of rain rates are within $0.2–0.4\,\mathrm{mm\,h^{-1}}$. The afternoon rainfall peak is associated with the maximum *SST* after the solar radiation flux reaches the maximum. Based on the observational analysis, Sui et al. suggested that the nocturnal rainfall peak is related to the destabilization by radiative cooling during nighttime and the falling temperature increases the available precipitable water that could be easier for the surface precipitation.

Sui et al. (1998) conducted the cloud-resolving model simulations to test their nocturnal rainfall mechanism. An experiment with the imposed large-scale ascending motion and a time-invariant *SST* generates a positive rainfall anomaly in the night and a negative rainfall anomaly in the day. The maximum simulated rain rate occurs around 0200 LST. Two additional experiments are carried out: one with a zero-imposed vertical velocity and a time-invariant *SST*, and the other with the cloud–radiation interaction suppressed. All three experiments show a dominant nocturnal rainfall maximum. The results imply cloud–radiation interaction does not

play a crucial role in the formation of the nocturnal rainfall peak. The common feature in all the experiments is the falling temperature induced by the nocturnal IR cooling. Thus, the numerical experiments support the suggestion by Sui et al. (1997) that the nocturnal rainfall peak is related to more (less) available precipitable water in the night (day) due to the diurnal cooling/heating cycle. They also conducted the experiment with zero-imposed vertical velocity and a zonally uniform diurnally varied *SST* and found that the simulated diurnal variations still have a nocturnal rainfall maximum, but with a weaker magnitude and a secondary rainfall peak in the afternoon. This indicates that the maximum *SST* in the afternoon induces the unstable atmosphere that eventually leads to the rainfall peak.

8.2 Diurnal Variation of Zonal-Mean Surface Rainfall

Diurnal variations of tropical oceanic precipitation are analyzed with the surface rainfall (2.5) using hourly zonal-mean simulation data in COARE. Figure 8.1 shows diurnal composites of P_s and four contributing components (Q_{WVT}, Q_{WVF}, Q_{WVE}, and Q_{CM}). The maximum surface rain rates ($\sim$0.4 mm h^{-1}) occur in the early morning and afternoon. Q_{WVE} has a constant of roughly 0.2 mm h^{-1}. Q_{CM} has fluctuations around 0 with amplitudes of 0.1 mm h^{-1} or less. Q_{WVT} and Q_{WVF} show

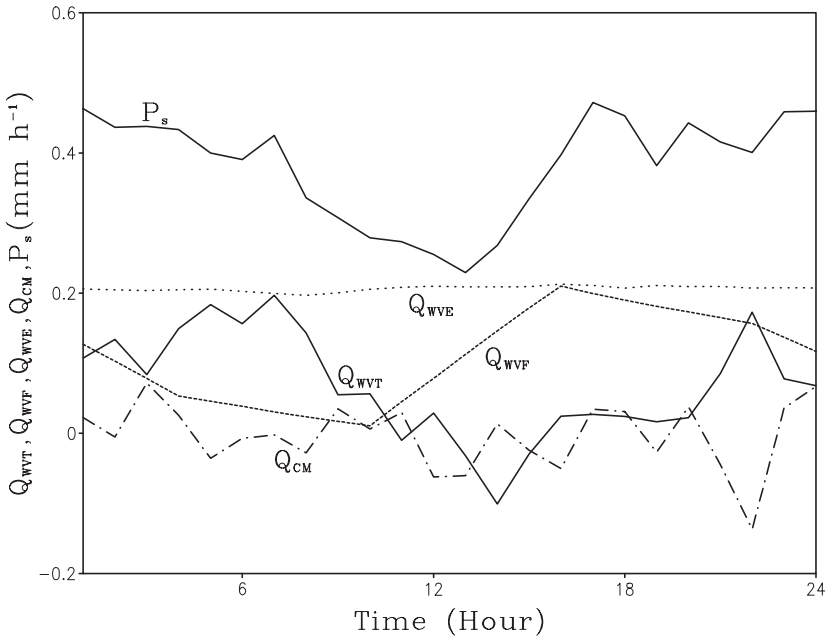

Fig. 8.1 Diurnal composites of zonal-mean Q_{WVT} (light solid), Q_{WVF} (dashed), Q_{WVE} (dot), Q_{CM} (dashed dot), and P_s (dark solid) simulated in COARE. Unit is mm h^{-1}

significant diurnal cycles. Q_{WVF} has its maximum ($\sim$0.2 mm h^{-1}) at hour 16 and decreases during nighttime and reaches its minimum ($\sim$0 mm h^{-1}) at hour 10. Since the *SST* does not show any strong diurnal signals (Fig. 4.1c), a forced rainfall peak in the afternoon is associated with the imposed large-scale vertical velocity. Q_{WVT} has its maximum ($\sim$0.2 mm h^{-1}) at hours 5–7 and decreases to its minimum (~ -0.1 mm h^{-1}) at hour 14. Maximum Q_{WVT} occurs at hours 5–7 when Q_{WVF} reaches its minimum. Positive Q_{WVT} signifies a local atmospheric drying. Thus, the rainfall maximum in the early morning is in phase with the local atmospheric drying.

While the vapor and cloud budgets basically represent the redistributions of the vapor and cloud hydrometeors, the thermal forcing may act to trigger the variations of vapor, clouds, and surface rainfall. Thus, diurnal composite of zonal-mean mass-weighted mean thermal budget is analyzed to explain the nocturnal rainfall peak. The diurnal composite of zonal-mean mass-weighted mean thermal budget (3.3) is shown in Fig. 8.2 and the diurnal composite of *CAPE* for the reversible moist adiabatic process (2.11 and 2.12b) is also calculated and shown in Fig. 8.3. After reaching its maximum at noon, the solar heating starts to decrease its magnitude. The net radiation becomes cool around hour 15 when IR cooling becomes dominant. The net radiative cooling reaches its maximum after hour 18 when solar radiation vanishes. The advective cooling (Q_{HF}) associated with the ascending motion in the afternoon also acts to lower local temperature. The similar cooling rates from Q_{HF} and Q_{RAD} occur from hour 18 to 8. Thus, the radiative and advective cooling lowers

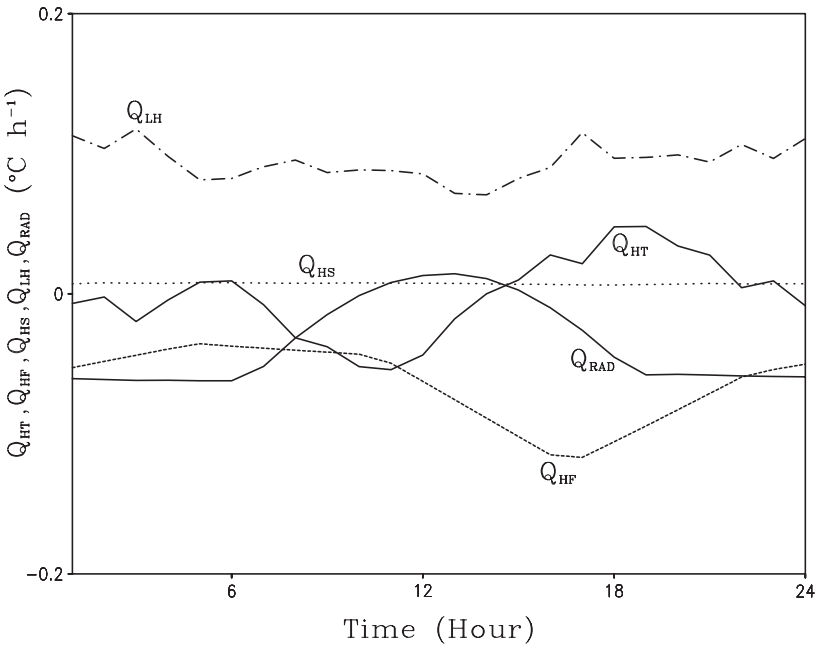

Fig. 8.2 Diurnal composites of zonal-mean Q_{HT} (light solid), Q_{HF} (dashed), Q_{HS} (dot), Q_{LH} (dashed dot), and Q_{RAD} (dark solid) simulated in COARE. Unit is °C h^{-1}

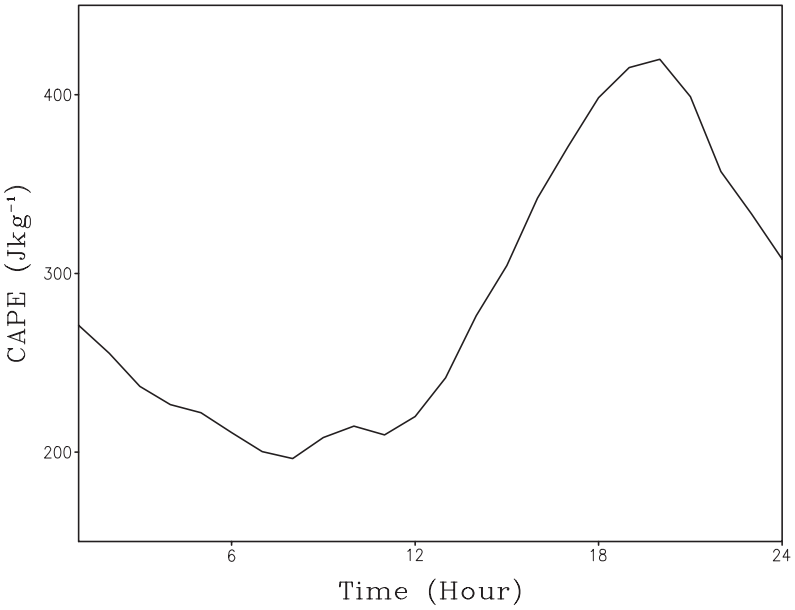

Fig. 8.3 Diurnal composite of zonal-mean *CAPE* simulated in COARE. Unit is J kg^{-1}

local temperature (positive Q_{HT}) from noon to midnight. The temperature decrease eventually halts the increase of *CAPE* around hour 20 (Fig. 8.3) after sunset. Continuous radiative and advective cooling causes a significant release of *CAPE*, a clear signal for destabilizing the atmosphere. The *CAPE* is transferred to energize nocturnal convective development. The *CAPE* reaches minimum around hour 8.

To understand the peaks of Q_{WVT} and Q_{WVF}, zonal-mean *PW* budget (3.1a) can be also written as

$$Q_{WVT} + Q_{WVF} + Q_{WVE} = Q_{WVOUT} - Q_{WVIN}. \tag{8.1}$$

Here, $Q_{WVOUT}(= [P_{CND} + \Sigma P_{DEP}])$ is a vapor sink, whereas $Q_{WVIN}(= [P_{REVP} + P_{MLTS} + P_{MLTG}])$ is a vapor source.

Diurnal composites of Q_{WVOUT} and Q_{WVIN} (Fig. 8.4) display that the diurnal amplitude of $Q_{WVOUT}(0.4\,\text{mm h}^{-1})$ is more than twice as large as that of $Q_{WVIN}(<0.2\,\text{mm h}^{-1})$, although both show similar diurnal signals to P_s. Thus, the diurnal variation of Q_{WVOUT} is consistent with the diurnal variation of $Q_{WVT} + Q_{WVF} + Q_{WVE}$, which is largely contributed by Q_{WVT} and Q_{WVF} as indicated in Fig. 8.1. The afternoon peak of Q_{WVOUT} occurs at hour 17, 1 h after Q_{WVF} reaches its maximum at hour 16 (Fig. 8.1). This suggests that the afternoon Q_{WVF} maximum associated with the imposed large-scale upward motion whose maximum $(3\,\text{cm s}^{-1})$ appears around 340 mb (not shown) is responsible for the afternoon Q_{WVOUT} peak through large vapor condensation and deposition rates. The large magnitudes of Q_{WVOUT} at hours 5–7 account for the early morning Q_{WVT} peak. Thus, a favorable

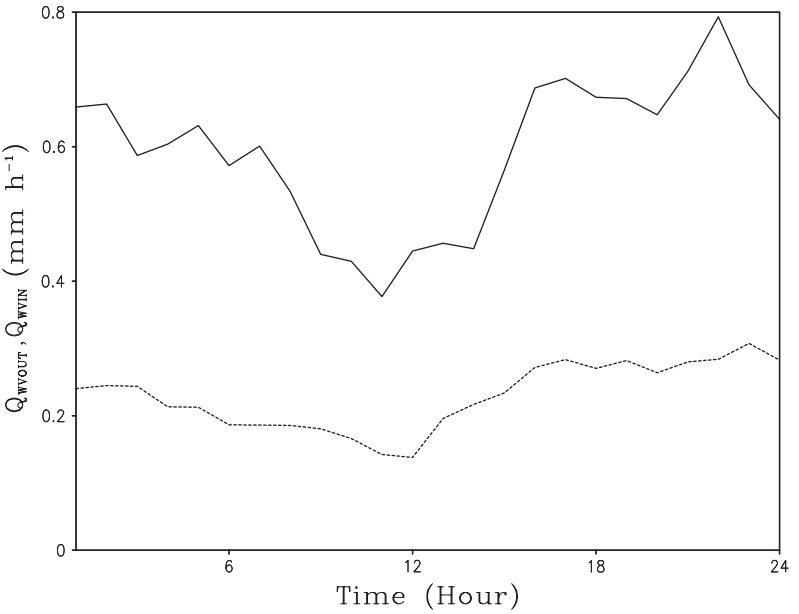

Fig. 8.4 Diurnal composites of zonal-mean Q_{WVOUT} (solid) and Q_{WVIN} (dashed) simulated in COARE. Unit is mm h^{-1}

coupling vapor-temperature (moist and cool) condition has induced a large rainfall, which results in a large local atmospheric drying when the large-scale forcing does not have any significant contributions to the surface rainfall processes.

Li (2004) conducted a scale analysis of the vapor condensation (P_{CND}) and deposition (P_{DEP}) rates to explain the maxima in the condensation and deposition rates in the morning. Following Tao et al. (1989), the sum of P_{CND} and (P_{DEP}) from (1.16) and (1.26) can be expressed by

$$P_{CND} + P_{DEP} = \frac{q_v - (q_{ws} + q_{is})}{\Delta t}, \tag{8.2}$$

since

$$\frac{A_1 q_c q_{ws} + A_2 q_i q_{is}}{q_c + q_i} \frac{L_v(T - T_{oo}) + L_s(T_o - T)}{c_p(T_o - T_{oo})} \ll 1.$$

Each variable can be decomposed into a daily mean (m) and a diurnal anomaly (d). $T = T_m + T_d$, and $q_v = q_{vm} + q_{vd}$. The diurnal anomaly of $P_{CND} + P_{DEP}$ then becomes

$$(P_{CND} + P_{DEP})_d = \frac{q_{vd} - q_{wisd}}{\Delta t}, \tag{8.3}$$

where

$$q_{wisd} = -\frac{E_1 T_d}{(T_m - F_1)^2} q_{wsm} - \frac{E_2 T_d}{(T_m - F_2)^2} q_{ism}. \tag{8.3a}$$

Note that the relations $1/(1+x) = 1-x$ and $e^x = 1+x$ for $x \ll 1$ are used in the derivation of (8.3). Equation (8.3) indicates that the diurnal variation of vapor condensation and deposition is determined by the diurnal variation of temperature and specific humidity. The diurnal variation of temperature and specific humidity is therefore further analyzed.

The linear correlation coefficients between the diurnal anomalies of vapor condensation and deposition rates and mass-weighted mean temperature and between the diurnal anomalies of vapor condensation and deposition rates and PW are -0.68 and 0.52, respectively. The correlation coefficient for 24 samples at the 99% confidence level is 0.5. Thus, the temperature correlation is well above, but the moisture correlation is only marginally above the 99% confidence level. Furthermore, taking into account that $<T_m>= 261.5\,\mathrm{K}$, $<T_d>= 0.5\,\mathrm{K}$, $[q_{vm}] = 54.7\,\mathrm{mm}$, and $[q_{vd}] = 1\,\mathrm{mm}$, $[q_{vd}]$ is about 1.8% of $[q_{vm}]$, and $[q_{wisd}]$ is about 4.5% of $[q_{wsm}]+[q_{ism}]$. These suggest that the diurnal variation of temperature is the primary factor in the diurnal variation of the vapor condensation and deposition rates and the surface rain rate. The diurnal variation of moisture is a secondary factor. The negative correlation between the diurnal vapor condensation and deposition anomalies and the mass-weighted mean temperature indicates that colder temperatures cause lower saturated mixing ratios, making it easier for water vapor to be condensed and deposited into precipitation. Therefore, nocturnal radiative cooling leads to colder air temperatures that make it easier for clouds to develop and hence induce rainfall.

8.3 Diurnal Analysis with Grid Simulation Data from a Coupled Model

Gao et al. (2006) analyzed the grid data from the 2D coupled ocean-cloud-resolving atmosphere model simulation with the imposed COARE forcing by categorizing the data into two groups: the amplitude of diurnal *SST* variation is smaller than 0.6°C in case W, whereas it is larger than 0.6°C in case S; and the amplitudes of diurnal *SST* composites are 0.8°C in case S and 0.3°C in case W (Fig. 8.5b in left panel), respectively. The *SST* peaks occur at hour 16 in both cases. The diurnal variations of surface rain rates in the two cases are virtually out of phase (Fig. 8.5a in left panel). In case W, the large rain rate occurs in the first half of the day, with the maximum of $0.67\,\mathrm{mm\,h^{-1}}$ at hours 6–10. The rain rate reaches the minimum of $0.31\,\mathrm{mm\,h^{-1}}$ at hour 16. In case S, the surface rain rate decreases in the early morning and reaches the minimum of $0.17\,\mathrm{mm\,h^{-1}}$ at hours 10–11. It increases to its peak of $0.54\,\mathrm{mm\,h^{-1}}$ at hour 16. The rainfall peaks around hours 6–10 in case W are virtually different from nocturnal rainfall peaks around hours 2–3 in the previous studies (also see section 8.1). However, the rainfall peaks appear at hours 2–3 when the diurnal variations of rainfall in case S are included in zonal-mean variations, which is consistent with nocturnal rainfall peaks in the observed area-mean surface rain rates.

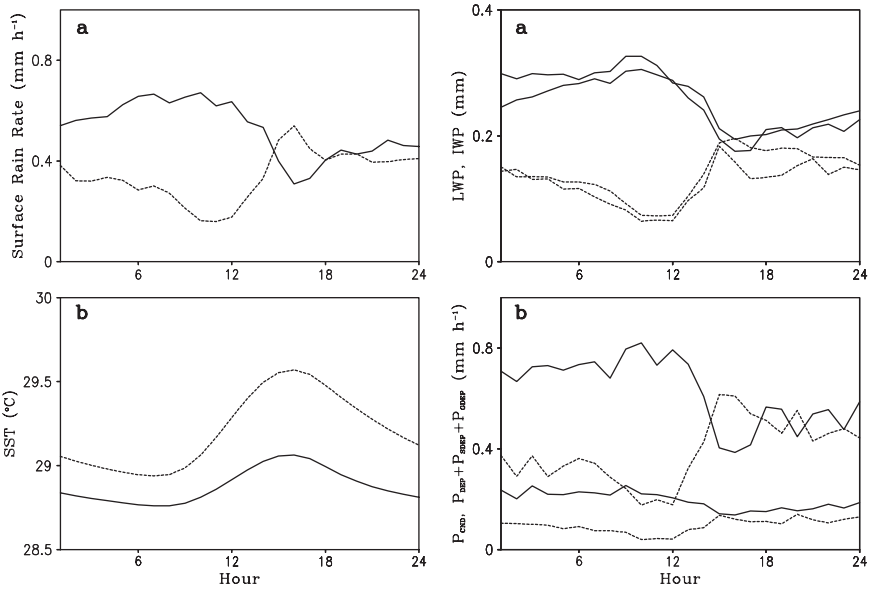

Fig. 8.5 Left panel: diurnal composites of **a** P_s (mm h^{-1}) and **b** *SST* (°C). Right panel: diurnal composites of **a** *LWP* (dark) and *IWP* (light) (mm) and **b** P_{CND} (dark) and sum of P_{DEP}, P_{SDEP}, and P_{GDEP} (light) (mm h^{-1}). Solid and dashed lines denote cases W and S in the coupled model simulation, respectively (After Gao et al. 2006)

To examine the diurnal variations of clouds, *LWP* and *IWP* are analyzed. Like the surface rain rates in case W versus those in case S, the diurnal variations of both *LWP* and *IWP* in the two cases are out of phase (Fig. 8.5a in right panel). The *LWP* and *IWP* have similar magnitudes. The *IWP* is slightly larger than the *LWP* in case W, whereas it is slightly smaller than the *LWP* in case S. The differences between the *IWP* and *LWP* become larger when the surface rain rates hit the maximum in both cases. To examine the cloud source, the diurnal composites of the P_{CND} and ΣP_{DEP} are plotted (Fig. 8.5b in right panel). Like the *LWP* and *IWP* in case W versus those incase S, the diurnal variations of vapor condensation and deposition rates in the two cases are out of phase. The vapor condensation rates are much larger than the vapor deposition rates in both cases, but particularly in case W because the vapor deposition rates are almost constant. Thus, the major cloud sources come from the vapor condensation process. In case W, the P_{CND} varies from 0.4 to 0.8 mm h^{-1}, whereas the ΣP_{DEP} is about 0.2 mm h^{-1}. The P_{CND} has a dramatic decrease from hour 12 to hour 15 when the *LWP* has a significant decrease. In case S, the P_{CND} varies from 0.2 to 0.65 mm h^{-1}, whereas the ΣP_{DEP} is about 0.1 mm h^{-1}. The P_{CND} has a dramatic increase from hour 12 to hour 15 when the *LWP* increases its values twice. The maximum of the P_{CND} is 0.62 mm h^{-1}. Large differences in magnitudes between the vapor condensation and deposition rates and similarities of magnitudes between the *LWP* and *IWP* imply the important exchange processes between the water and ice clouds.

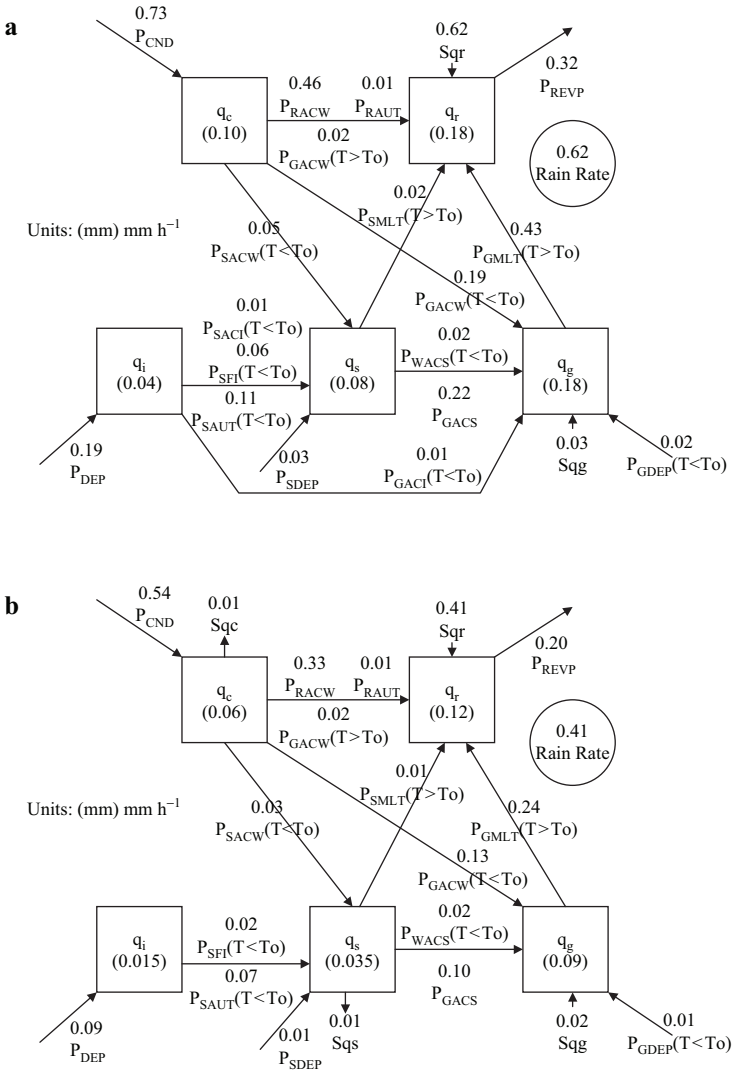

Fig. 8.6 Cloud microphysics budgets in **a** case W (averaged within hours 1–10) and **b** case S (averaged within hours 16–20) simulated in coupled model experiment. Units for cloud hydrometeors and conversions are mm and mm h^{-1}, respectively (After Gao et al. 2006)

Cloud microphysics budgets in case W are calculated by averaging within hours 1–10 (Fig. 8.6a), whereas the budgets in case S are calculated by averaging within hours 16–20 (Fig. 8.6b) when the surface rain rates reach their peaks and the differences between the *IWP* and *LWP* are the largest. The *IWP* (0.3 mm) is 7% larger than the *LWP* (0.28 mm) in case W, whereas the *IWP* (0.14 mm) is 32% smaller than the *LWP* (0.18 mm) in case S. In case W, vapor condensation rate

($[P_{CND}]$) is 0.73 mm h^{-1} and vapor deposition rates ($[\Sigma P_{DEP}]$) are 0.25 mm h^{-1}. Vapor deposition rates contribute to the cloud growth by 26%. In case S, vapor condensation rate is 0.54 mm h^{-1} and vapor deposition rates are 0.12 mm h^{-1}. Vapor deposition rates contribute to the cloud growth by 18%. Although rates are different in the two cases, 67% of $[P_{CND}]$ goes to growth of rain mainly through $[P_{RACW}]$ and 30–33% contributes to growth of precipitation ice mainly through $[P_{GACW}]$. The major sources responsible for rainfall are $[P_{RACW}]$ and $[P_{GMLT}]$. Rainfall source comes from $[P_{GMLT}]$ by 48% in case W and 41% in case S, respectively. Thus, smaller *IWP* in case S results from smaller vapor deposition rates, which is in turn due to warmer air temperature by solar heating, in comparison with those in case W. Thus, vapor deposition rates are directly responsible for the growth of ice clouds.

8.4 Diurnal Variations of Convective and Stratiform Rainfall

Cui (2008) analyzed diurnal variations of convective and stratiform rainfall using hourly equilibrium simulation data from experiment SST29, in which the zero vertical velocity and constant *SST* of 29°C are imposed in the model during the integration (also see section 11.2). The convective rain rate is higher than the stratiform rain rate in the early morning and evening. The diurnal variation of convective rain rate is mainly determined by that of vapor convergence over convective regions, whereas diurnal variation of stratiform rainfall is determined by that of local vapor and hydrometeor loss over raining stratiform regions.

The effects of diurnal variation of *SST* on diurnal variations of convective and stratiform rainfall can be further examined by comparing SST29 with SST29D1. A diurnally varied *SST* with the time-mean of 29°C and diurnal amplitude of 1°C is imposed in SST29D1 (also see section 11.3). Hourly equilibrium simulation data are used to make a diurnal composite of surface rainfall. The differences in diurnal variation of model domain mean surface rain rates between SST29D1 and SST29 are mainly caused by those of convective surface rain rates (Fig. 8.7) since the stratiform rain rates in both experiments show similar diurnal variations. The differences in diurnal variation of vapor convergences (Q_{WVF}) between SST29D1 and SST29 mainly account for the differences in diurnal variation of convective rain rates (Fig. 8.7c) because the local vapor changes (Q_{WVT}) and surface evaporation rates (Q_{WVE}) have at least one order of magnitude smaller than vapor convergences, and hydrometeor sources in both experiments display similar variations (Fig. 8.7).

Since higher *SST* induced by solar radiative heating significantly enhances convective rain rate for hours 15–20, the surface rainfall budgets averaged in this period in both SST29 and SST29D1 are analyzed. The model domain mean calculations of surface rainfall equation in the late afternoon (Table 8.1) show that the surface rain rate is larger in SST29D1 (0.1322 mm h^{-1}) than in SST29 (0.1023 mm h^{-1}) largely because the local atmospheric moistening rate is smaller in SST29D1 (-0.0131 mm h^{-1}) than in SST29 (-0.0369 mm h^{-1}) and partly because the surface evaporation rate is larger in SST29D1 (0.1456 mm h^{-1}) than

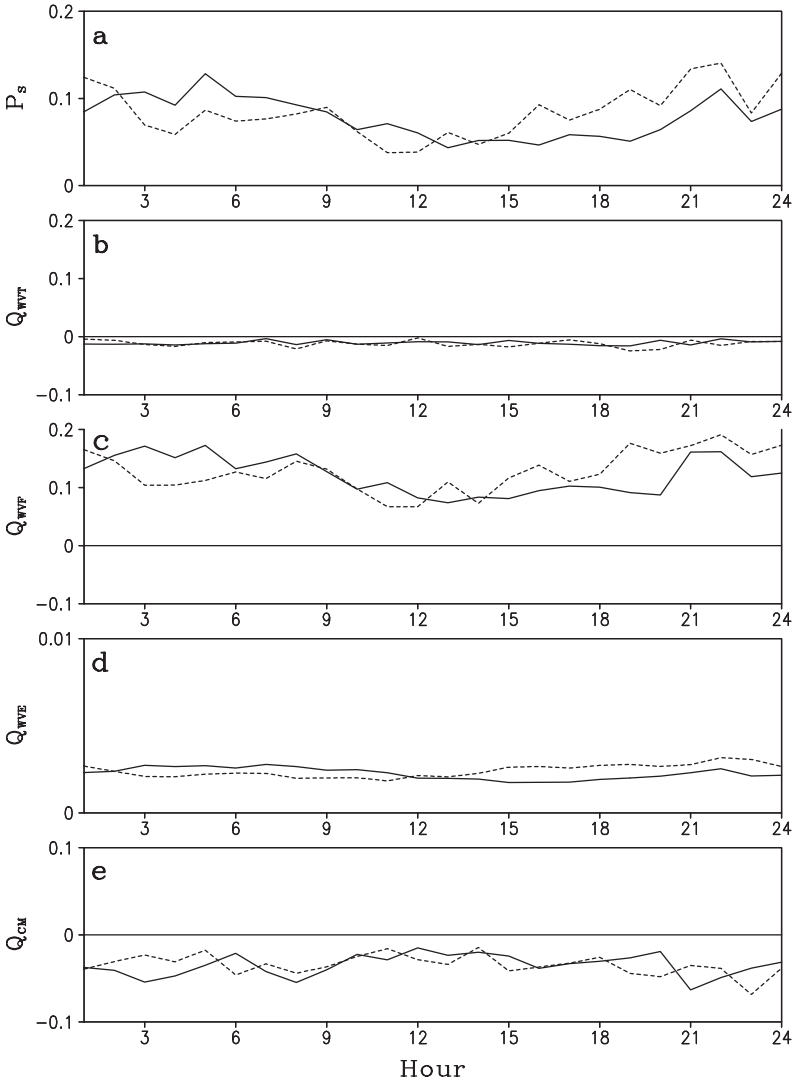

Fig. 8.7 Diurnal composites of **a** P_s, **b** Q_{WVT}, **c** Q_{WVF}, **d** Q_{WVE}, and **e**Q_{CM} over convective regions simulated in SST29 (solid) and SST29D1 (dashed). Unit is mm h^{-1}

in SST29 $(0.1341\,\text{mm}\,h^{-1})$. The partition calculations of surface rain rate in the late afternoon reveal that model domain mean surface rain rate is larger in SST29D1 than in SST29 mainly because the convective surface rain rate is larger in SST29D1 $(0.0862\,\text{mm}\,h^{-1})$ than in SST29 $(0.0547\,\text{mm}\,h^{-1})$, which is mainly due to the fact that the vapor convergence rate over convective regions is larger in SST29D1 $(0.1374\,\text{mm}\,h^{-1})$ than in SST29 $(0.0929\,\text{mm}\,h^{-1})$. Due to cyclic boundary condition in the model, the vapor convergence in convective regions is largely

Table 8.1 Time means of fractional coverage, P_s, Q_{WVT}, Q_{WVF}, Q_{WVE}, and Q_{CM} over clear-sky regions, raining stratiform regions, convective regions, and nonraining stratiform regions and their sums (model domain means) averaged using diurnal composite data from hour 15 to hour 20 in (a) SST29 and (b) SST29D1. Unit is mm h^{-1}

(a) SST29					
	Clear-sky regions	Raining stratiform regions	Convective regions	Nonraining stratiform regions	Model domain mean
P_s	0.00	0.0476	0.0547	0.0	0.1023
Q_{WVT}	−0.0056	0.0178	−0.0115	−0.0375	−0.0369
Q_{WVF}	−0.0690	−0.0001	0.0929	−0.0235	0.0
Q_{WVE}	0.0744	0.0040	0.0019	0.0538	0.1341
Q_{CM}	0.0002	0.0258	−0.0286	0.0072	0.0046
(b) SST29D1					
	Clear-sky regions	Raining stratiform regions	Convective regions	Nonraining stratiform regions	Model domain mean
P_s	0.0	0.0459	0.0862	0.0	0.1322
Q_{WVT}	0.0059	0.0164	−0.0157	−0.0197	−0.0131
Q_{WVF}	−0.0845	−0.0062	0.1374	−0.0467	0.0
Q_{WVE}	0.0770	0.0048	0.0027	0.0611	0.1456
Q_{CM}	0.0016	0.0309	−0.0382	0.0054	−0.0003

balanced by vapor divergence in rainfall-free regions. In SST29D1, the surface evaporation $(0.1381\,\text{mm h}^{-1})$ is used to offset vapor divergence $(-0.1312\,\text{mm h}^{-1})$ in rainfall-free regions. In SST29, the surface evaporation $(0.1282\,\text{mm h}^{-1})$ offsets vapor divergence $(-0.0925\,\text{mm h}^{-1})$ and enhances water vapor $(-0.0431\,\text{mm h}^{-1})$ in rainfall-free regions. SST29D1 transports more water vapor from rainfall-free regions to convective regions and thus produces larger convective rainfall and model domain mean surface rainfall than SST29 does.

To examine cloud radiative effects on diurnal variations of tropical convective and stratiform rainfall, additional experiment SST29NCR (without cloud radiative effects) is carried out (also see section 11.4). The magnitude of diurnal variation of convective rain rate is larger in SST29NCR than in SST29, whereas the diurnal phases in the two experiments are similar (Fig. 8.8a). The diurnal variations of stratiform rain rate in the two experiments are similar in both magnitude and phase (Fig. 8.9a). This indicates that the magnitude of diurnal variation of convective rain rate is sensitive to the cloud radiative effects, whereas the phase of diurnal variation of convective rain rate and both magnitude and phase of diurnal variation of stratiform rain rate are not.

Over convective regions, the positive difference in rain rate for SST29NCR–SST29 is mainly contributed to by the positive difference in vapor convergence since the differences in local vapor and hydrometeor changes are negative and the difference in surface evaporation is small (Fig. 8.8). Over stratiform regions, the similar rain rates in the two experiments are due to the fact that the negative

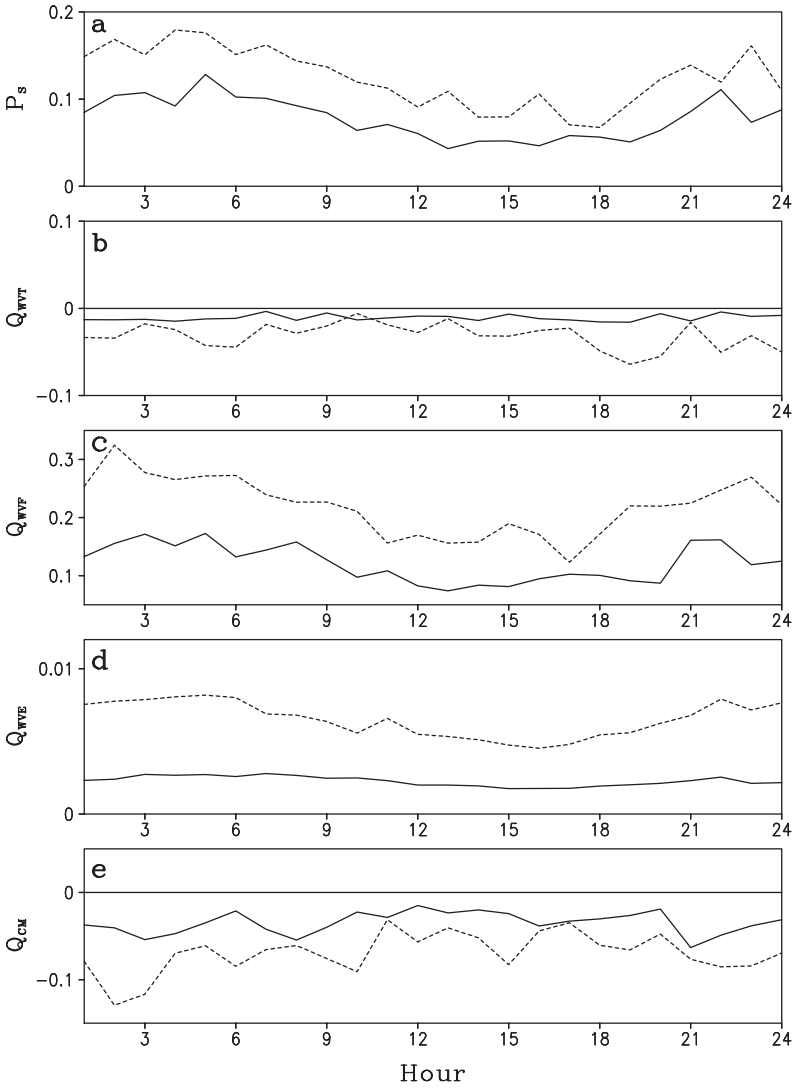

Fig. 8.8 Diurnal composites of **a** P_s **b** Q_{WVT}, **c** Q_{WVF}, **d** Q_{WVE}, and **e** Q_{CM} over convective regions simulated in SST29 (solid) and SST29NCR (dashed). Unit is mm h^{-1}

difference in vapor convergence for SST29NCR–SST29 is nearly balanced by the positive differences in local vapor and hydrometeor changes and surface evaporation (Fig. 8.9).

The positive difference in vapor convergence over convective regions (Fig. 8.8c) for SST29NCR–SST29 is balanced by the negative difference in vapor divergence over stratiform regions (Fig. 8.9c) and rainfall-free regions (Fig. 8.10b) since the lateral boundary in the model is cyclic. Over rainfall-free regions, the negative dif-

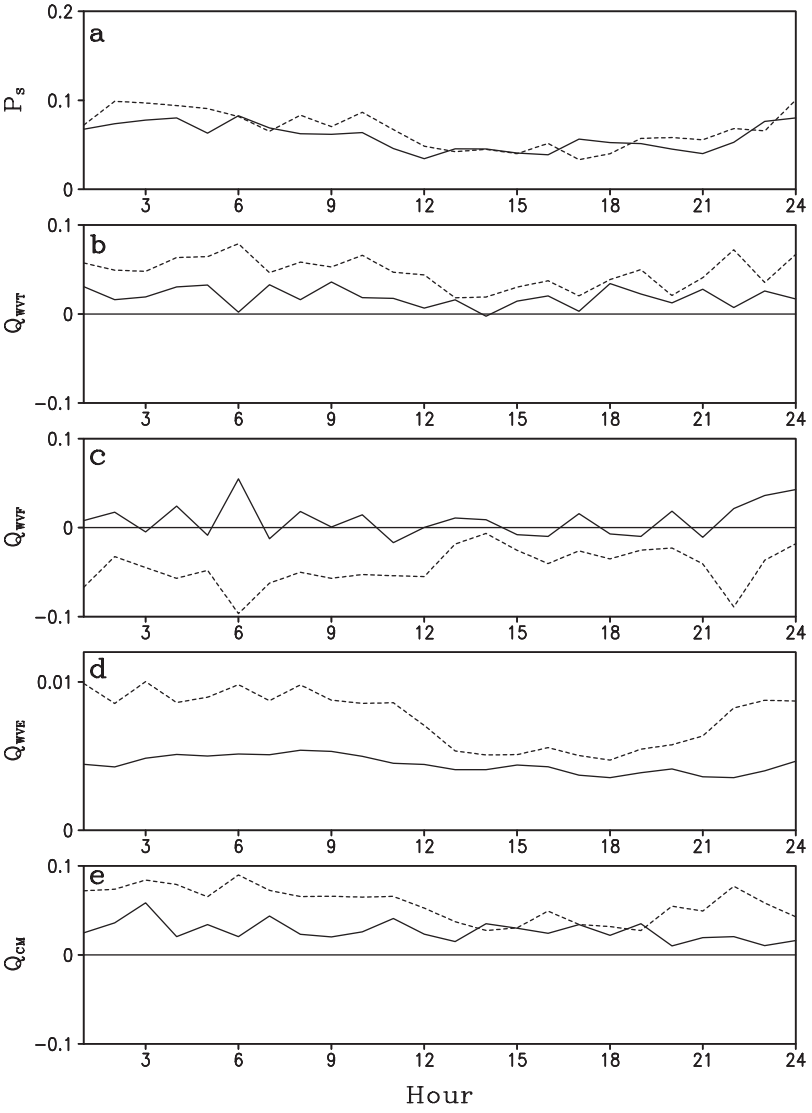

Fig. 8.9 As in Fig. 8.8 except over raining stratiform regions

ference in vapor divergence is mainly compensated by the positive difference in surface evaporation (Fig. 8.10c). The exclusion of cloud radiative effects in the model produces colder and drier equilibrium atmosphere (see section 11.4) than the inclusion does. The drier atmosphere in SST29NCR leads to larger surface evaporation and vapor divergence than the warmer atmosphere in SST29 does while the two experiments are imposed in the same constant *SST* of 29°C. Thus, the larger vapor divergence over rainfall-free regions as well as over stratiform regions leads to the larger vapor convergence over convective regions in SST29NCR than in SST29.

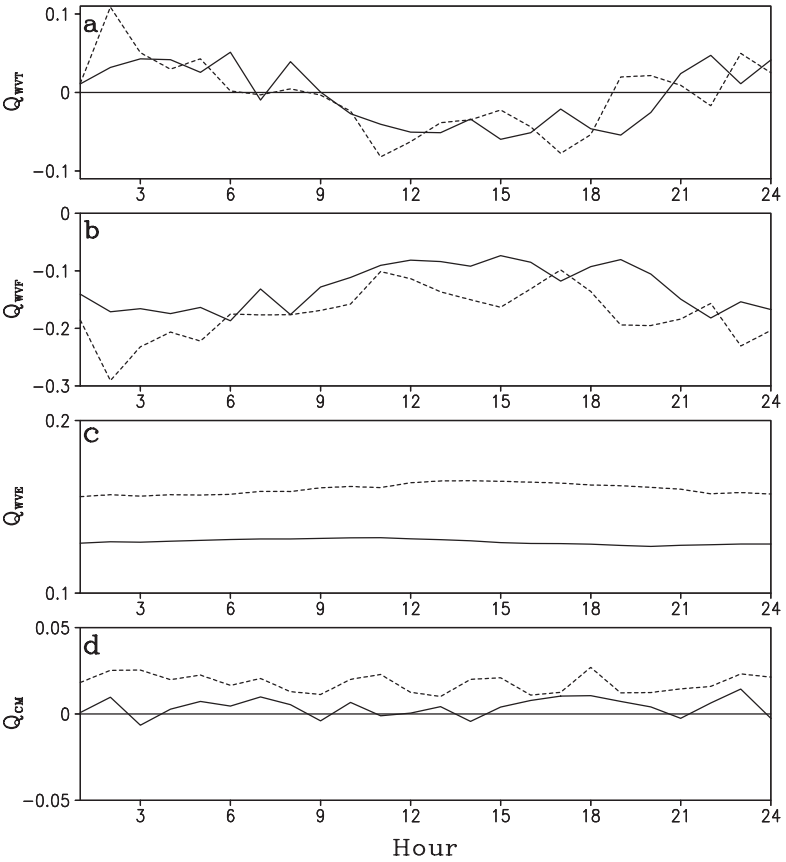

Fig. 8.10 Diurnal composites of **a** Q_{WVT}, **b** Q_{WVF}, **c** Q_{WVE}, and **d** Q_{CM} over rainfall-free regions simulated in SST29 (solid) and SST29NCR (dashed). Unit is mm h^{-1}

References

Cui X (2008) A cloud-resolving modeling study of diurnal variations of tropical convective and stratiform rainfall. J Geophys Res, doi:10.1029/2007JD008990

Gao S, Ping F, Li X (2006) Cloud microphysical processes associated with the diurnal variations of tropical convection: A 2D cloud resolving modeling study. Meteor Atmos Phys 91:9–16

Gray WM, Jacobson RW (1977) Diurnal variation of deep cumulus convection. Mon Wea Rev 105:1171–1188

Kraus EB (1963) The diurnal precipitation change over the sea. J Atmos Sci 20:546–551

Li X (2004) Cloud modeling in the tropical deep convective regime. In: Zhu X (ed) Observation, Theory, and Modeling of Atmospheric Variability. World Scientific, New Jersey

Liu C, Moncrieff MW (1998) A numerical study of the diurnal cycle of tropical oceanic convection. J Atmos Sci 55:2329–2344

Randall DA, Harshvardhan, Dazlich DA (1991) Diurnal variability of the hydrologic cycle in a general circulation model. J Atmos Sci 48:40–62

Sui CH, Lau KM, Takayabu Y, Short D (1997) Diurnal variations in tropical oceanic cumulus ensemble during TOGA COARE. J Atmos Sci 54:639–655

Sui CH, Li X, Lau KM (1998) Radiative-convective processes in simulated diurnal variations of tropical oceanic convection. J Atmos Sci 55:2345–2359

Tao WK, Simpson J, McCumber M (1989) An ice-water saturation adjustment. Mon Wea Rev 117:231–235

Tao WK, Lang S, Simpson J, Sui CH, Ferrier BS, Chou MD (1996) Mechanisms of cloud-radiation interaction in the Tropics and midlatitude. J Atmos Sci 53:2624–2651

Xu KM, Randall DA (1995) Impact of interactive radiative transfer on the macroscopic behavior of cumulus ensembles. Part II: Mechanisms for cloud-radiation interactions. J Atmos Sci 52: 800–817

Chapter 9
Precipitation Efficiency

Precipitation efficiency is an important physical parameter in vapor, cloud, and surface rainfall budgets. Although it has been intensively studied for more than five decades (e.g., Braham 1952), it remains a difficult and complex quantity for definition and estimation. Generally, precipitation efficiency is precipitation divided by sources associated with the precipitation in convective systems. There are two ways to define precipitation efficiency. It can be defined in the point view of large-scale water vapor budgets, in which the water vapor convergence and surface evaporation are traditionally considered as major indirect precipitation sources. It also can be defined in the point view of cloud microphysical budget, in which vapor condensation and deposition are considered as the direct rainfall sources. Calculations of precipitation efficiency show that they could be more than 100%. This indicates that some precipitation sources may not be included in the definitions. To fix it, new definitions of precipitation efficiency are introduced by Sui et al. (2007), in which the precipitation efficiency is less than or equal to 100%. In this chapter, the definition of precipitation efficiency will be intensively discussed and the relation between precipitation efficiency and other physical parameters are also addressed based on Li et al. (2002) and Sui et al. (2005, 2007).

For large-scale applications involving cumulus parameterization (e.g., Kuo 1965, 1974), precipitation efficiency is defined as the ratio of the surface rain rate to the sum of the surface evaporation and the vertically integrated horizontal and vertical vapor advection (vapor convergence), which is referred to as large-scale precipitation efficiency (*LSPE*). *LSPE* can be written as

$$LSPE = \frac{P_s}{Q_{WVF} + Q_{WVE}}. \tag{9.1}$$

Braham (1952) proposed a vapor cycle in which the water vapor is transported into the air column by dynamic convergence and the vapor is condensed to liquid or frozen water. The condensational hydrometeors partially fall down to form the precipitation and partially stay in the atmosphere to form the clouds. Braham defined the precipitation efficiency as the ratio of the surface rain rate to the total moisture

influx of the thunderstorm. For a thunderstorm with a typical life span of 25 min, Braham estimated that only 10% of the water vapor transported into the thunderstorm is eventually measured as surface rainfall. With the data from surface to 700 mb, Newton (1963, 1966) suggested that the precipitation efficiency is about 50%. Foote and Fankhauser (1973) used the radar-determined rain rate and vapor convergence derived by aircraft data at 800 mb and showed that the precipitation efficiency is about 60%. Auer and Marwitz (1968) defined the precipitation as the ratio of surface rain rate to the moisture flux through the cloud base and calculated the precipitation efficiency with the radar data averaged within 1 h and found that the precipitation efficiency associated with the thunderstorms that produce hail is about 55%, whereas the efficiency of the thunderstorms that do not produce any hail is nearly 100% or more. Heymsfield and Schotz (1985) calculated the efficiency associated with a severe squall line over Oklahoma using the moisture budget in which rainfall is balanced by moisture influx, anvil outflow, and entrainment-induced vapor loss and found that the precipitation efficiency is only 25–40%, and argued that the low precipitation efficiency may be due to large moisture losses in the upper troposphere. Ferrier et al. (1996) calculated precipitation efficiency with the cloud-resolving model simulation data and found that the precipitation efficiency is sensitive to the inflow depths and is 26–66%. Doswell et al. (1996) showed that the precipitation efficiency of individual cells could vary considerably across a large convective system and suggested that the precipitation efficiency should be understood as a time average over the history of a precipitation-producing weather system. Doswell et al.'s estimate of precipitation efficiency is 44%.

For smaller-scale cloud-resolving models (e.g., Li et al. 1999), the precipitation efficiency is defined as the ratio of the surface rain rate to the sum of the vertically integrated condensation and deposition rates. This is referred to as cloud-microphysics precipitation efficiency (*CMPE*). The *CMPE* is similar to the precipitation efficiency defined by Weisman and Klemp (1982), Lipps and Hemler (1986), Chong and Hauser (1989), and Tao et al. (2004). *CMPE* can be written as

$$CMPE = \frac{P_s}{Q_{WVOUT}}. \tag{9.2}$$

Lipps and Hemler (1986) defined cloud efficiency as the total rain reaching the ground divided by the total positive cloud condensation occurring over a specific time interval, and analyzed mass continuity of water substance in which the total cloud condensation is balanced by total cloud water evaporation, rain water evaporation, total rain at the ground, and residual amounts of cloud water and rain water with the cloud-resolving model simulation data during the GATE period and found that the precipitation efficiency is 42%. Chong and Hauser (1989) analyzed water budgets over convective and stratiform regions for a tropical squall line in West Africa using Doppler radar data. In the water budgets, surface precipitation is contributed by the mass of water condensed, the mass of water lost due to evaporation in cloud region, the mass of water lost due to evaporation into environment, and the mass of water transported by horizontal flow between convective and stratiform region. Chong and Hauser found that the precipitation efficiency is 47–57%

for the convective region and 45–57% for the stratiform region, respectively. Ferrier et al. (1996) used the simulation data averaged over the last 3 h of each experiment and displayed the precipitation efficiency of 24–45%. Tao et al. (2004) examined the relationship of precipitation efficiency with moisture and wind with cloud-resolving model simulation data during TOGA COARE, GATE, SCSMEX, and Atmospheric Radiation Measurement (ARM), and showed that the precipitation efficiency is 30–45%, individual precipitation efficiency is insensitive to environmental moisture, and it decreases with increasing mid-tropospheric wind shear.

Li et al. (2002) calculated the simulation data in COARE and found that the *LSPE* can exceed 100% for strong convection. This suggests that the surface rain rate could be larger than the total moisture convergence, which is contrary to the assumption in Kuo's scheme (1965, 1974) that a small portion of the surface evaporation and moisture convergence (say 5%) is used to moisten the atmosphere.

To examine the *LSPE* and local vapor and cloud change, the surface rainfall (2.5) is divided by the vapor source $(Q_{WVF} + Q_{WVE})$ to yield

$$LSPE - \frac{Q_{WVT}}{Q_{WVF} + Q_{WVE}} - \frac{Q_{CM}}{Q_{WVF} + Q_{WVE}} = 1. \tag{9.3}$$

The role of cloud hydrometeors can be ignored in the surface rainfall processes by assuming that $[\bar{S}_{qv}] \cong P_s$. Thus, (9.3) becomes

$$LSPE - \frac{Q_{WVT}}{Q_{WVF} + Q_{WVE}} = 1. \tag{9.4}$$

The ratio of the local *PW* change $(-Q_{WVT})$ to the moisture sources $(Q_{WVF} + Q_{WVE})$ and *LSPE* is shown in Fig. 9.1, and $-Q_{WVT}$ and P_s is shown in Fig. 9.2. The upper left square in Figs. 9.1 and 9.2 indicates that the light rain regime exists where the atmosphere is always moistened by the moisture convergence and surface evaporation. Figures 9.1 and 9.2 show that in the heavy rain regime (outside the upper left square) up to 60% of the moisture source for precipitation came from the drying processes of the environmental atmosphere. Newton (1963, 1966), Foote and Fankhauser (1973), Gamache and Houze (1983), and Ferrier et al. (1996) also showed that the precipitation efficiency defined by Braham (1952) could be larger than 100%. The cumulus parameterization schemes (e.g., Kuo 1965, 1974) moisten the atmosphere by consuming 5% of the moisture source, which eliminates the drying processes. Figure 9.2 shows that the drying processes in the rainfall production are important. Thus, the cumulus parameterization scheme should allow the precipitation rate to be larger than the rate of the sum of the moisture convergence and surface evaporation in some circumstances in order to avoid moisture bias.

The regression relation between Q_{WVOUT} and $Q_{WVF} + Q_{WVE}$ can be expressed by

$$Q_{WVOUT} = 0.17 + 0.84(Q_{WVF} + Q_{WVE}). \tag{9.5}$$

Thus, *CMPE* and *LSPE* have the following statistic relation:

$$CMPE = 1.19\ LSPE. \tag{9.6}$$

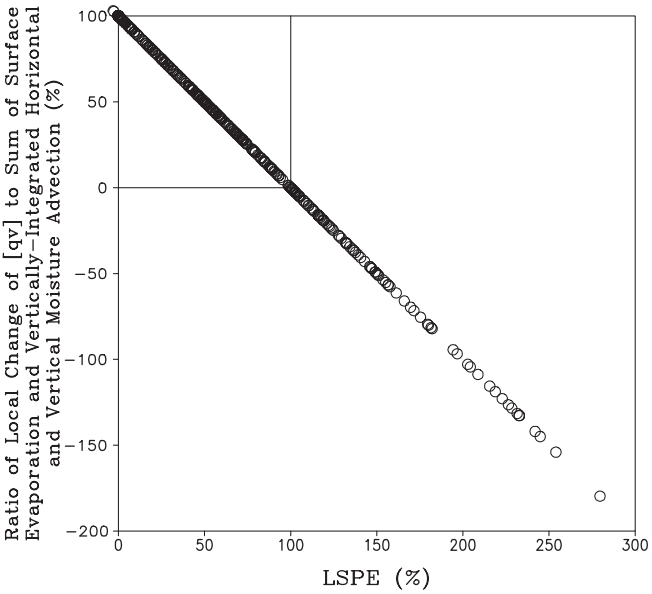

Fig. 9.1 Ratio of local *PW* change to the sum of moisture convergence and surface evaporation versus *LSPE* calculated using hourly zonal-mean simulation data from COARE. Unit is % (After Li et al. 2002)

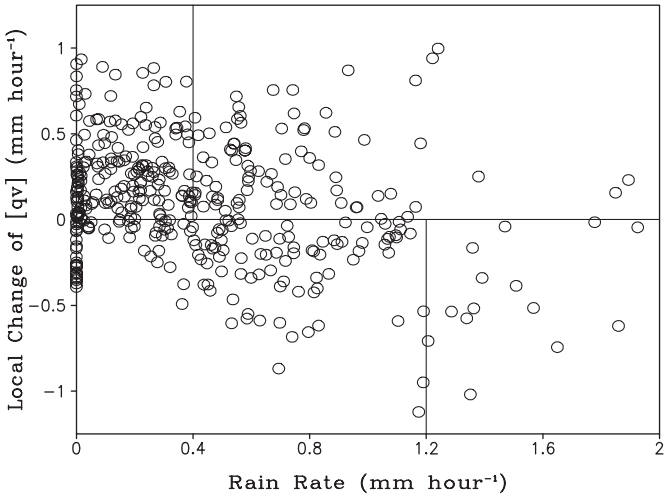

Fig. 9.2 Local *PW* change versus surface rain rate calculated using hourly zonal-mean simulation data from COARE. Unit is mm h^{-1} (After Li et al. 2002)

Equation (9.6) indicates that *CMPE* is larger than *LSPE*. Figure 9.3 shows that *LSPE* is about 80% of *CMPE* when *LSPE* is smaller than 60%, and the *CMPE* is a constant of about 70% when *LSPE* is larger than 60%. Figure 9.3 also indicates that (9.6) is valid only when both *CMPE* and *LSPE* are smaller than 100%.

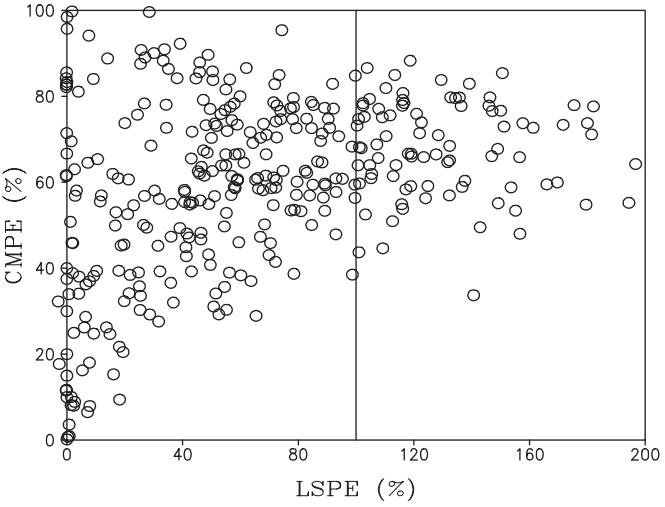

Fig. 9.3 *CMPE* versus *LSPE* calculated using hourly zonal-mean simulation data from COARE. Unit is % (After Li et al. 2002)

Since large-scale forcing is imposed in vapor budget, whereas lateral boundary condition causes zero zonal-mean hydrometeor convergence, the zonal-mean calculations show that *CMPE* is smaller than 100% whereas *LSPE* could be larger than 100% (Fig. 9.3). Sui et al. (2005) calculated *CMPE* and *LSPE* using data averaged over 96, 48, and 24 km from the grid data in COARE and found that the statistical relation

$$Q_{WVOUT} = Q_{WVF} + Q_{WVE} \tag{9.7}$$

is a valid approximation, in particular, for the 24-km averages. Thus, *CMPE* and *LSPE* are statistically equivalent as indicated by Fig. 9.4.

The *CMPE* provides a basis for identifying the relevant processes determining precipitation efficiency.

$$CMPE = 1 - \frac{[Q_{WVIN}]}{[Q_{WVOUT}]} + \frac{[CONV_C]}{[Q_{WVOUT}]}. \tag{9.8}$$

Here $[CONV_c] = CONV_{IWP} + CONV_{LWP}$ [see (6.3a and b)]. Equation (9.8) indicates that the positive values of $[CONV_c]$ make *CMPE* larger through the advection of clouds into the region of interest, while the negative values of $[CONV_c]$ make *CMPE* smaller. Figure 9.5 shows that the larger *CMPE* is associated with hydrometeor convergence, whereas smaller *CMPE* is associated with hydrometeor divergence. *CMPE* could be even larger than 1 if $[CONV_c] > [Q_{WVIN}]$. Figure 9.5 displays many cases of $CMPE > 100\%$. The above results indicate a significant effect of hydrometeor convergence on surface precipitation processes.

Since the hydrometeor convergence is expected to be a function of the strength of convection, the dependence of *CMPE* on rainfall rate is examined using the data

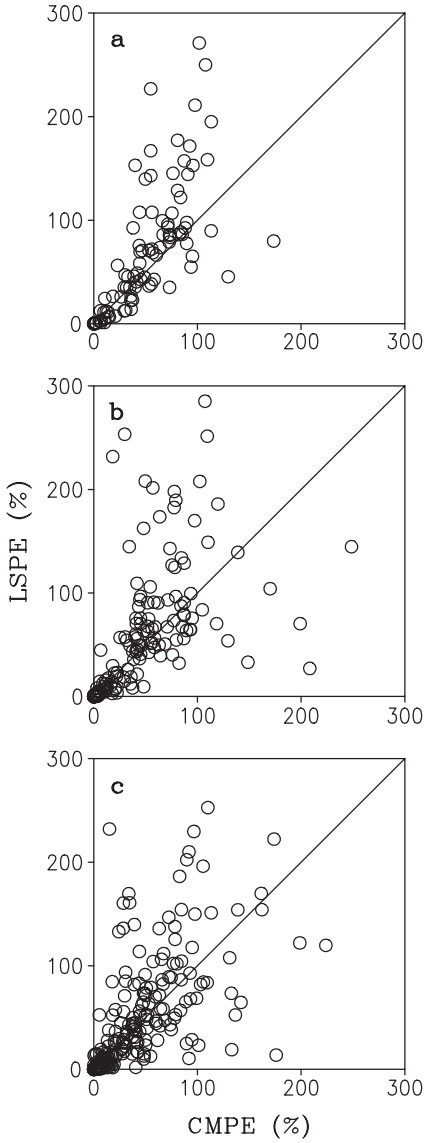

Fig. 9.4 *LSPE* versus *CMPE* averaged within **a** 96 km, **b** 48 km, and **c** 24 km in COARE. Unit is %. The diagonal lines denote *CMPE* = *LSPE* (After Sui et al. 2005)

averaged in three grid area sizes of 96, 48, and 24 km in COARE. Figure 9.6 shows that *CMPE* values spread over a wide range and become even larger than 100% in light-rain conditions (surface rainfall rates are smaller than 5 mm h^{-1} for 96- and 48-km averages and smaller than 10 mm h^{-1} for 24-km average). But the *CMPE* tends to converge to a threshold value with increasing surface rainfall rate.

From the above discussions, both *LSPE* and *CMPE* could be greater than 100% and *LSPE* could be negative, which is not physically meaningful. This could be due

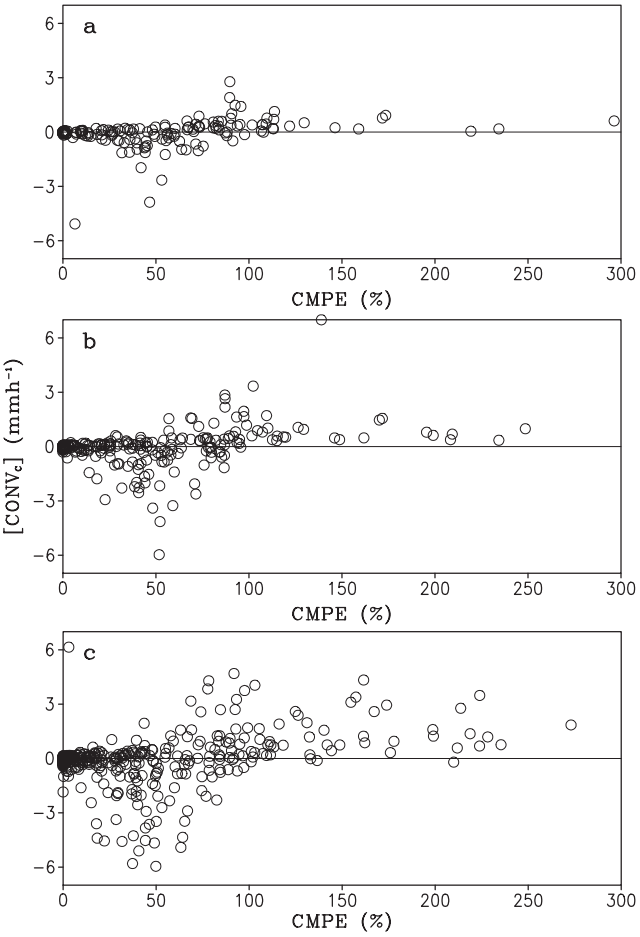

Fig. 9.5 $[CONV_C]$ (mm h^{-1}) versus *CMPE* (%) averaged within **a** 96 km, **b** 48 km, and **c** 24 km in COARE (After Sui et al. 2005)

to exclusion of some sources associated with precipitation or inclusion of precipitation sink in the definition of precipitation efficiency. For example, local atmospheric drying and local hydrometeor loss could be major contributors to surface rain rate during the weakening and dissipating stages of tropical oceanic convection while vapor divergence occurs (see Table 5.1). Local atmospheric drying and local hydrometeor loss could make *LSPE* larger than 100% since they are not included as the rainfall sources in the definition of *LSPE* [see (9.1)]. Vapor divergence could make *LSPE* negative since it is included in the definition of *LSPE* as the precipitation source. Thus, Sui et al. (2007) introduced new definitions for *LSPE* and *CMPE*. The new *LSPE* is defined as

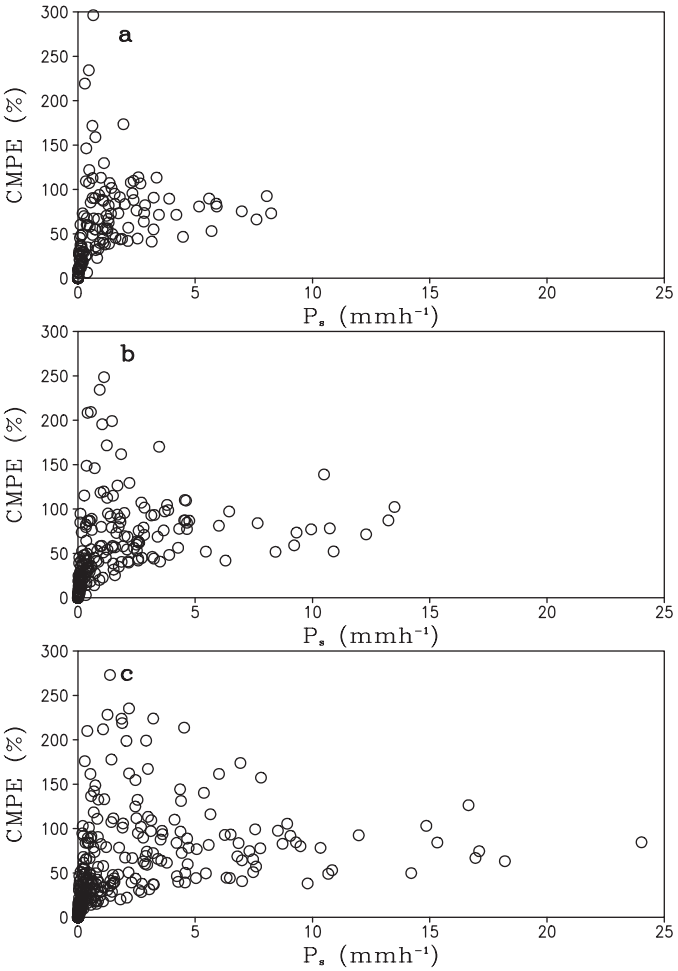

Fig. 9.6 *CMPE* (%) versus P_s (mm h^{-1}) averaged within **a** 96 km, **b** 48 km, and **c** 24 km in COARE (After Sui et al. 2005)

$$LSPE = \frac{P_s}{\sum_{i=1}^{4} sgn(Q_i)Q_i}, \tag{9.9}$$

where

$$Q_i = (Q_{WVT}, Q_{WVF}, Q_{WVE}, Q_{CM}), \tag{9.9a}$$

$sgn(F) = 1$ when $F > 0$,

$$sgn(F) = 0 \text{ when } F \leq 0. \tag{9.9b}$$

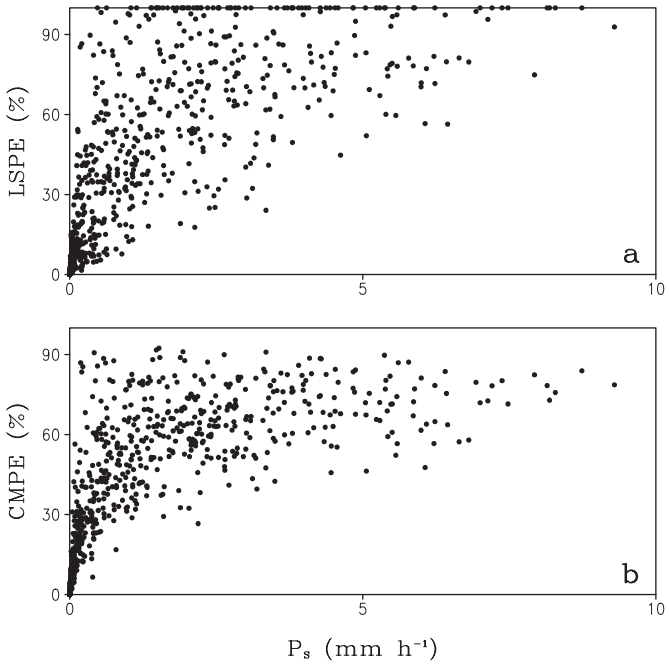

Fig. 9.7 **a** *LSPE* (%) vs P_s $(\mathrm{mm\,h^{-1}})$ and **b** *CMPE* vs P_s using hourly 96-km averaged data from COARE. *LSPE* and *CMPE* are defined in (9.9) and (9.10), respectively (After Sui et al. 2007)

The new *CMPE* is defined as

$$CMPE = \frac{P_s}{W_{WVOUT} + sgn(Q_{CM})Q_{CM}}. \tag{9.10}$$

The new *LSPE* and *CMPE* as a function of surface rain rate are calculated using 96-km averaged simulation data from COARE and are shown in Fig. 9.7. With new definitions, both *LSPE* and *CMPE* range from 0% to 100% and increase as surface rain rate increases. From definitions of *LSPE* and *CMPE*, *CMPE* is only associated with cloud microphysical processes, whereas *LSPE* is related to water cycling processes including both water vapor and cloud hydrometeors. Thus, *CMPE* is a physically more straightforward definition of precipitation efficiency than *LSPE*. *CMPE* can only be estimated using model simulation data with explicit cloud microphysical parameterization, whereas *LSPE* can be estimated using observational data including available assimilation data of satellite and sounding measurements.

References

Auer AH Jr, Marwitz JD (1968) Estimates of air and moisture flux into hailstorms on the High Plains. J Appl Meteor 7:196–198

Braham RR Jr (1952) The water and energy budgets of the thunderstorm and their relation to thunderstorm development. J Meteor 9:227–242

Chong M, Hauser D (1989) A tropical squall line observed during the CORT 81 experiment in West Africa. Part II: Water budget. Mon Wea Rev 117:728–744

Doswell CA III, Brooks HE, Maddox RA (1996) Flash flood forecasting: An ingredients-based methodology. Wea Forecast 11:560–581

Ferrier BS, Simpson J, Tao WK (1996) Factors responsible for different precipitation efficiencies between midlatitude and tropical squall simulations. Mon Wea Rev 124:2100–2125

Foote GB, Fankhauser JC (1973) Airflow and moisture budget beneath an Northeast Colorado hailstorm. J Appl Meteor 12:1330–1353

Gamache JF, Houze RA Jr (1983) Water budget of a mesoscale convective system in the tropics. J Atmos Sci 40:1835–1850

Heymsfield GM, Schotz S (1985) Structure and evolution of a severe squall line over Oklahoma. Mon Wea Rev 113:1563–1589

Kuo HL (1965) On formation and intensification of tropical cyclones through latent heat release by cumulus convection. J Atmos Sci 22:40–63

Kuo HL (1974) Further studies of the parameterization of the influence of cumulus convection on large-scale flow. J Atmos Sci 31:1232–1240

Li X, Sui CH, Lau KM, Chou MD (1999) Large-scale forcing and cloud-radiation interaction in the tropical deep convective regime. J Atmos Sci 56:3028–3042

Li X, Sui CH, Lau KM (2002) Precipitation efficiency in the tropical deep convective regime: A 2-D cloud resolving modeling study. J Meteor Soc Japan 80:205–212

Lipps FB, Hemler RS (1986) Numerical simulation of deep tropical convection associated with large-scale convergence. J Atmos Sci 43:1796–1816

Newton CW (1963) Dynamics of severe convective storms. Severe Local Storms Meteor Monogr, No. 27, Amer Meteor Soc, Boston, MA

Newton CW (1966) Circulations in large sheared cumulonimbus. Tellus 18:699–712

Sui CH, Li X, Yang MJ, Huang HL (2005) Estimation of oceanic precipitation efficiency in cloud models. J Atmos Sci 62:4358–4370

Sui CH, Li X, Yang MJ (2007) On the definition of precipitation efficiency. J Atmos Sci 64: 4506–4513

Tao WK, Johnson D, Shie CL, Simpson J (2004) The atmospheric energy budget and large-scale precipitation efficiency of convective systems during TOGA COARE, GATE, SCSMEX, and ARM: Cloud-resolving model simulations. J Atmos Sci 61:2405–2423

Weisman ML, Klemp JB (1982) The dependence of numerically simulated convective storms on vertical wind shear and buoyancy. Mon Wea Rev 110:504–520

Chapter 10
Air–Sea Coupling

Air–sea interaction is one of the important processes that affect both atmospheric and oceanic variability. The atmosphere may affect *SST* and upper temperature stratification through changing ocean surface heat fluxes. The ocean may affect the atmospheric convection and associated thermodynamic distributions through changing the boundary layer stability. In this chapter, the brief history of coupled modeling studies of air–sea interaction processes is reviewed. The 2D coupled ocean-cloud-resolving atmosphere model and its applications to study effects of small-scale fluctuations associated with atmospheric convection and precipitation on spatial distribution of ocean mixed-layer temperature and salinity and role of air–sea coupling in the surface rainfall process are discussed in this chapter based on Li et al. (2000) and Gao et al. (2006).

10.1 Introduction

Precipitation and the associated stratification of salinity affect *SST* by changing the mixed-layer depth (e.g., Miller 1976; Li et al. 1998) and the upper-ocean thermal structure by forming a barrier layer between the halocline and the thermocline (e.g., Godfrey and Lindstrom 1989; Lukas and Lindstrom 1991; Vialard and Delecluse 1998a, b). Miller (1976) found that precipitation could induce shallow mixed layers in numerical simulations. Since the effect of heating/cooling is inversely related to the mixed-layer depth, shallow mixed layers cause larger temperature changes than do deep mixed layers with the same thermal forcing. Cooper (1988) found that salinity effects could account for as much as a 0.5°C temperature bias and a $0.1\,\mathrm{m\,s^{-1}}$ velocity bias near the surface after 110 days of integration over the Indian Ocean. Murtugudde and Busalacchi (1998) found that the differences in annual mean *SST* between simulations with and without salinity and climatological precipitation could be as much as 0.5°C, indicating the inclusion of salinity effects is necessary to simulate realistic climatic systems. Yang et al. (1999) also found that in the western Pacific warm pool, *SST* would be 0.6°C lower if there were no salinity effect associated with precipitation.

Sui et al. (1997) employed a mixed-layer model to study the role of vertical solar absorption profile in the diurnal ocean temperature simulations and their impacts in the intraseasonal variability. Due to the asymmetric diurnal variation for shoaling and deepening of the mixed layer, the cumulative effects of diurnal mixing cycles are essential to maintain a stable upper-ocean thermal stratification and to simulate a realistic evolution of mixed layer and temperature at the intraseasonal time. Further sensitivity tests of mixed layer to diurnal cycles indicate that the inclusion of diurnal convective–radiative processes in the atmosphere–ocean systems in the coupled models affect the capability of simulating intraseasonal variability.

Li et al. (1998) further included the salinity in the ocean mixed-layer model to examine the impacts of the precipitation and associated upper-ocean salinity stratification in the ocean mixed layer. The inclusion of salinity and precipitation-induced freshwater flux in the simulation shows much deep mixing occurs when rainfall occurs during nighttime since the freshwater flux induces a much shallower mixed layer with a large deepening rate. The salinity contributes more to the density stratification than does the temperature, which takes care of upper-ocean stability. The inclusion of the salinity stratification could cause the entrainment of warmer water into the ocean mixed layer since the salinity stratification takes care of the upper-ocean stability, whereas the exclusion of salinity in the simulation only shows entrainment of cold water into the ocean mixed layer since the thermal stratification accounts for the upper-ocean stability. Since the Kraus-Tuner mixing parameterization scheme (Niiler and Kraus 1977) requires both thermal and saline stratifications to determine the mixed-layer depth, decoupled salinity experiments are further conducted to examine the effect of thermal stratification on saline structure. The experiments reveal that a large freshwater input could cause a large difference (0.2 PSU) in the salinity between the experiments with and without the thermal stratification. The simulations indicate that the inclusion of precipitation-induced freshwater flux and salinity stratification improve the simulation of thermal evolution in the ocean mixed layer.

The simulation of the mixed-layer temperature relies largely on the vertical solar absorption profile. The simulated amplitudes of the mixed-layer temperature ($<1^{\circ}$C) are significantly smaller than the observed amplitudes (1–3°C), implying that the mixed layer in the simulation does not absorb enough solar heat. Sui et al. (1998) calculated mixed-layer heat budget with the observed *SST* data to retrieve the amount of heat absorbed in the observed mixed layer to maintain the observed amplitudes of the *SST* and found that more than 39% of the net surface solar irradiance is absorbed within the first 0.45 m, which is higher than previous estimates. The vertical solar absorption profile is then modified and the simulation with the modified solar profile yields more realistic amplitudes of the *SST* at both diurnal and intraseasonal timescales.

10.2 Development of a Cloud-Resolving Air–Sea Coupling System

Li et al. (2000) developed a 2D coupled ocean-cloud-resolving atmosphere model to study small-scale air–sea coupling processes (see section 1.1). The simulation from 0400 LST 18 December to 0400 LST 25 December 1992 during TOGA COARE

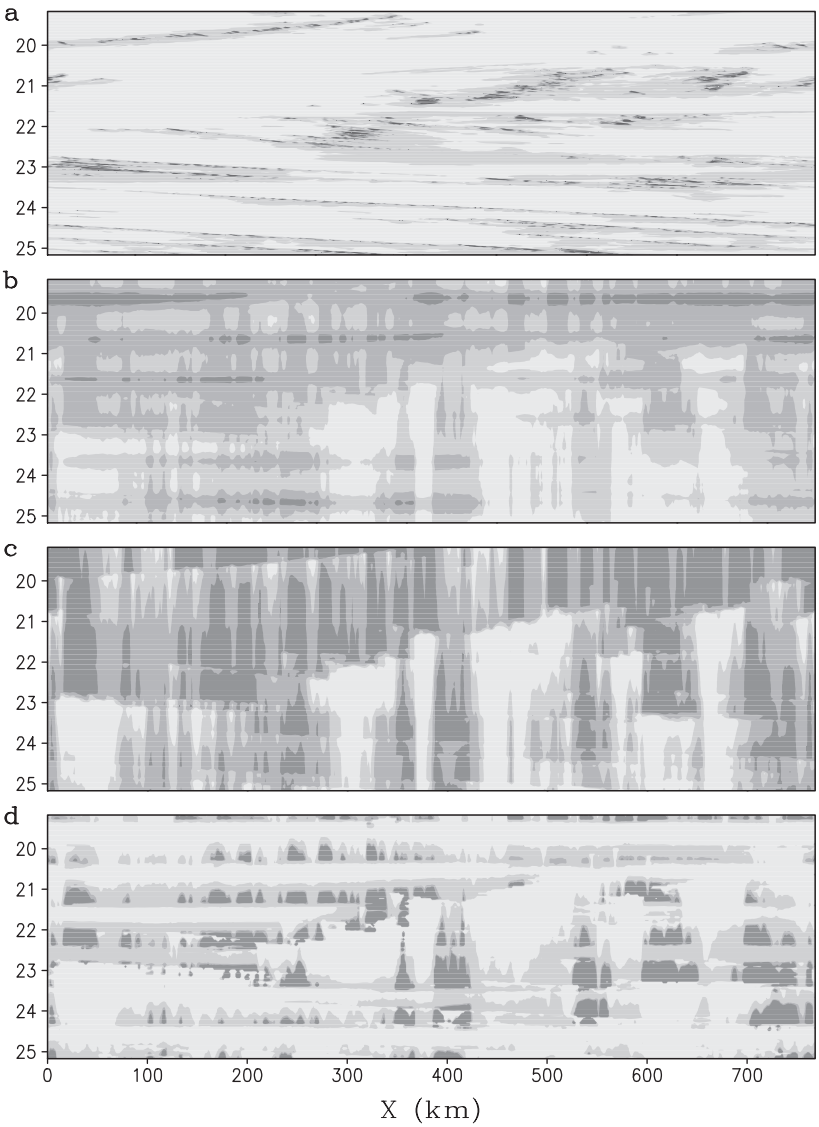

Fig. 10.1 Temporal and zonal distribution of **a** P_s, **b** T_m, **c** S_m, and **d** h_m. Light shadings denote 0–10 mm h^{-1} for P_s, 28.75–29.25°C for T_m, 33.75–34 PSU for S_m, and 2–10 m for h_m, respectively; medium shadings denote 5–10 mm h^{-1} for P_s, 29.25–29.75°C for T_m, 34–34.25 PSU for S_m, and 10–20 m for h_m, respectively; dark shadings denote >10 mm h^{-1} for P_s, >29.75°C for T_m, >34.25 PSU for S_m, and >20 m for h_m, respectively (After Li et al. 2000)

shows the small-scale structures in the mixed layer associated with surface rainfall (Fig. 10.1). When the effects of freshwater flux and salinity were included in the coupled model, differences in the zonal-mean mixed-layer temperature and salinity

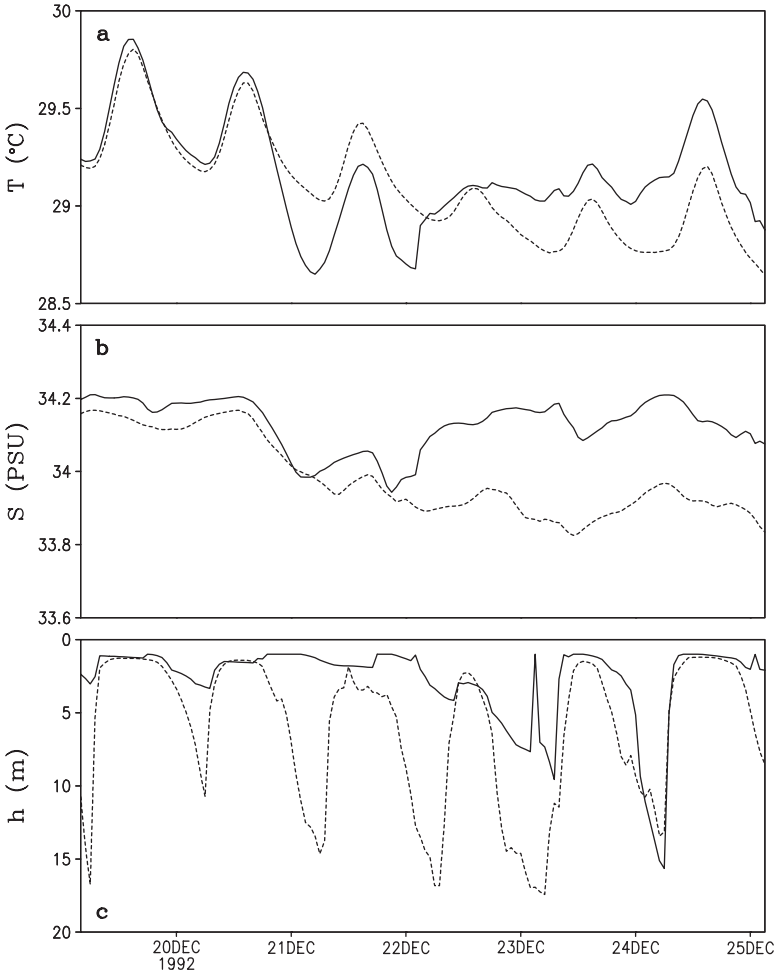

Fig. 10.2 Temporal evolution of **a** zonal-mean mixed-layer temperature (°C), **b** salinity (PSU), and **c** depth (m) simulated in coupled model experiments with 1D (solid) and 2D (dashed) ocean mixed-layer models, respectively (After Li et al. 2000)

between one-dimensional (1D) and 2D experiments were about 0.4°C and 0.3 PSU, respectively (Fig. 10.2). The mean salinity difference was larger than the mean temperature difference in terms of their contributions to the mean density difference. In the 2D experiment, the surface heat flux showed a significant diurnal signal with the dominance of downward solar radiation during daytime and upward flux (IR radiative, sensible, and latent heat fluxes) during nighttime at each grid, although the amplitude was affected by precipitation. Thus, there was a strong thermal correlation between grids (Fig. 10.3). Narrow cloudy areas were surrounded by broad cloud-free areas. Zonal-mean precipitation could occur, whereas the precipitation might not occur during most of the integration period. Thus, there is very low correlation between zonal-mean and grid value of the freshwater fluxes (Fig. 10.3). Since

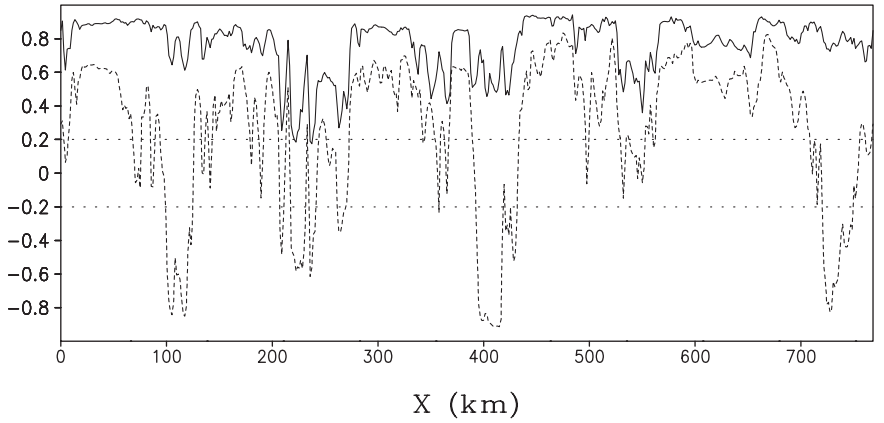

Fig. 10.3 Zonal distribution of linear correlation coefficients between grid-point value and zonal-mean for mixed-layer temperature (dot), salinity (dashed), and depth (solid) in the 2D coupled model simulation. The linear correlation coefficient curves above upper dotted straight line or below lower dotted straight line exceed 95% confidence level (After Li et al. 2000)

the rain rates have significant spatial variations, the freshwater flux has much larger spatial fluctuations than the saline entrainment does. Therefore, the freshwater flux determines large spatial salinity fluctuations, which contributes to large mean salinity difference between the 1D ocean model experiment and the 2D ocean model experiment.

The zonal-mean mixed-layer temperature in both experiments shows a similarity in the first 2 days of model integrations (Fig. 10.2a). The mixed-layer temperature simulated by the 1D ocean model experiment becomes 1°C lower than that simulated by the 2D ocean model experiment from later part of the night of 20 December and it is higher after the afternoon of 22 December 1992. The zonal-mean heat budgets averaged from 2000 LST 20 December to 0400 LST 21 December show that the thermal forcing in the 1D ocean model experiment (-2.38°C day^{-1}) is larger than that in the 2D ocean model experiment (-1.14°C day^{-1}) due to the fact that the mixed-layer depth in the 1D ocean model experiment (1.1 m) is much smaller than that in the 2D ocean model experiment (7.8 m). As a result, the mixed-layer temperature in the 1D ocean model experiment (-2.07°C day^{-1}) decreases at a higher rate than that in the 2D ocean model experiment (-0.89°C day^{-1}) does. The zonal-mean heat budgets averaged from 1400 LST to midnight of 22 December reveal that the thermal entrainment (0.61°C day^{-1}) is nearly balanced by the thermal forcing (-0.54°C day^{-1}) in the 1D ocean model experiment, whereas the thermal forcing (-0.92°C day^{-1}) cannot be compensated by the thermal entrainment (0.38°C day^{-1}) in the 2D ocean model experiment. Thus, the mixed-layer shows a slight warming in the 1D ocean model experiment, whereas the mixed-layer has a cooling in the 2D ocean model experiment.

The zonal-mean mixed-layer salinity in both experiments shows a similarity in the first 3 days of model integrations (Fig. 10.2b). After 22 December, the salinity

in the 2D ocean model experiment becomes 0.3 PSU lower than that in the 1D ocean model experiment. To explain this salinity difference, the zonal-mean salinity budgets averaged from 0100 LST to 1100 LST 22 December are analyzed. In the 1D ocean model experiment, the saline entrainment (0.33 PSU day^{-1}) overcomes freshwater forcing (-0.16 PSU day^{-1}) to enhance the ocean mixed-layer salinity at the rate of 0.17 PSU day^{-1}. In the 2D ocean model experiment, the saline entrainment (0.17 PSU day^{-1}) and salinity advection (0.16 PSU day^{-1}) are nearly balanced by freshwater forcing (-0.34 PSU day^{-1}) so that the zonal-mean salinity is a constant during this period.

10.3 Role of Air–Sea Coupling in Surface Rainfall Process

The ocean may affect the formation and development of clouds by *SST* through changing ocean surface fluxes, including surface evaporation flux. One of the most important air–sea interaction processes is intensification of convection with increasing *SST* from 26.5°C to 29.5°C over the tropical deep convective regime as shown in various analyses of monthly mean data (e.g., Gadgil et al. 1984; Graham and Barnett 1987; Gutzler and Wood 1990; Zhang 1993; Waliser and Graham 1993; Webster 1994; Waliser 1996; Lau et al. 1997). Gao et al. (2006) analyzed hourly 50-day 2D coupled model simulation during TOGA COARE and calculated cloud-weighted P_s and cloud-weighted *SST* by averaging P_s and *SST* over cloudy area. P_s increases with *SST* from 28°C to 30°C (Fig. 10.4), which is qualitatively consistent with the results

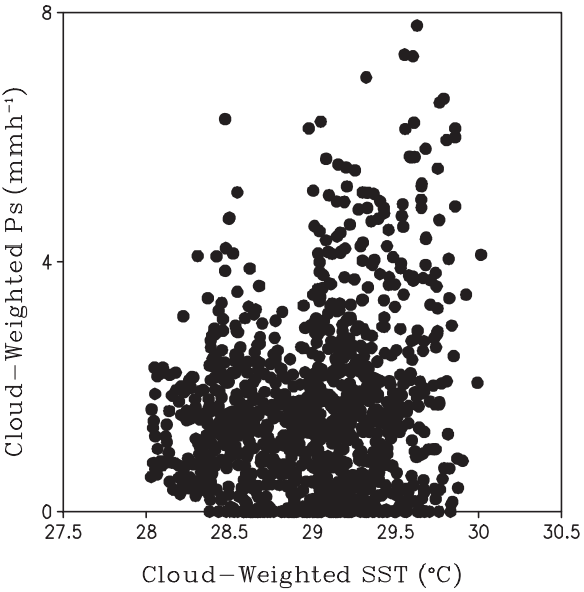

Fig. 10.4 Cloud-weighted P_s (mm h^{-1}) versus cloud-weighted *SST* (°C) (After Gao et al. 2006)

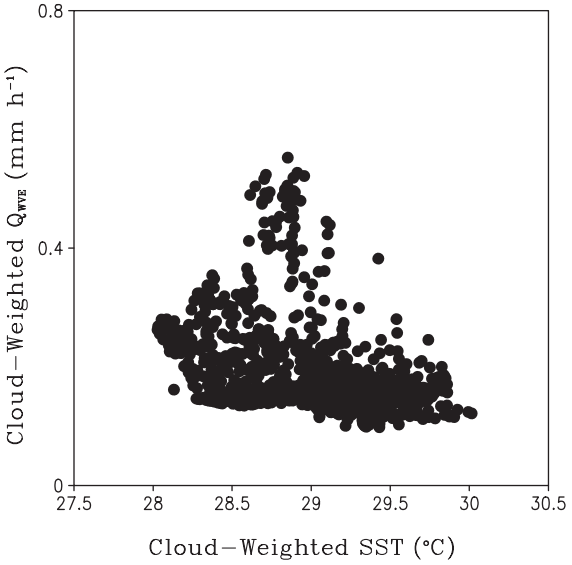

Fig. 10.5 Cloud-weighted Q_{WVE} versus cloud-weighted *SST* (°C) (After Gao et al. 2006)

from previous studies. The linear correlation coefficient calculated with 1,161 samples is 0.18, which is above the 1% significance level (0.081). However, the variance between cloud-weighted P_s and cloud-weighted *SST* only is 3.2%, which implies that the other 96.8% of the variation in rainfall is explained by variations in other physical processes. Surface rainfall equation (2.4) shows contribution of surface evaporation to surface rain rate. Thus, *SST* affects atmospheric precipitation through changing surface evaporation (Q_{WVE}). Cloud-weighted Q_{WVE} decreases with increasing *SST* (Fig. 10.5) as indicated by their linear correlation coefficient of -0.35. Only 12.3% of the variation in surface evaporation flux is explained by the variation in *SST*, whereas most (87.7%) of the variation in surface evaporation flux is accounted for by variations in the other processes in the hourly data analysis. Thus, surface evaporation flux associated with *SST* has negligible impacts in the variation of atmospheric water vapor and surface rainfall over tropical cloudy regions. The negative correlation coefficient also indicates that the warm *SST* cannot produce a large surface evaporation flux to moisten the atmosphere over cloudy regions at a short timescale.

To examine the time-dependent importance of surface evaporation flux in atmospheric *PW* budget and ocean mixed-layer thermal budget over cloudy regions, magnitudes of surface evaporation flux and sum of condensation and atmospheric moisture convergence in *PW* budget and magnitudes of surface thermal forcing and the sum of ocean thermal entrainment rate and thermal advections are calculated using the data averaged over various time frames shown in Fig. 10.6. For the *PW* budget averaged over the time frames that are less than 2 days, maximum magnitudes of the sum of condensation and atmospheric moisture convergence are much

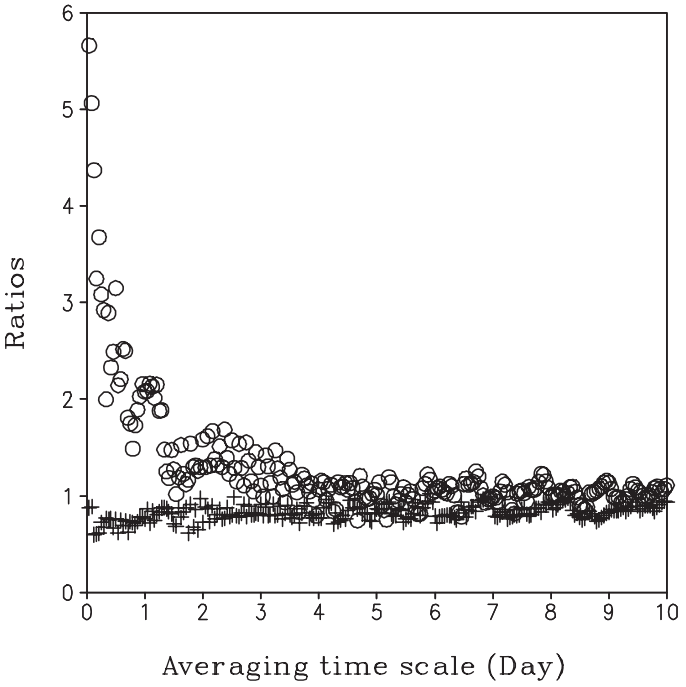

Fig. 10.6 Ratio of maximum magnitude of sum of condensation and atmospheric moisture convergence to maximum magnitude of surface evaporation flux (open circle) and ratio of maximum magnitude of sum of ocean thermal entrainment rate and thermal advections to surface thermal forcing (cross) versus the time frame in which the analyzed data are averaged (day) (After Gao et al. 2006)

larger (2–6 times) than maximum magnitudes of surface evaporation flux. For the *PW* budget averaged over the time frames that are more than 2 days, they are about the same. In the ocean mixed-layer thermal budget, surface thermal forcing and the sum of ocean thermal entrainment rate and thermal advections have similar maximum magnitudes regardless of the time frames in which the analyzed data are averaged. This indicates that the impacts of the upper ocean in atmospheric moisture through surface evaporation flux associated with *SST* over cloudy regions may be time-dependent.

References

Cooper NS (1988) The effect of salinity on tropical ocean models. J Phys Oceanogr 18:697–707

Gadgil S, Joseph PV, Joshi NV (1984) Ocean-atmospheric coupling over monsoon regions. Nature 312:141–143

Gao S, Ping F, Cui X, Li X (2006) Short timescale air-sea coupling in the tropical deep convective regime. Meteor Atmos Phys 93:37–44

Godfrey JS, Lindstrom EJ (1989) The heat budget of the equatorial western Pacific surface mixed layer. J Geophys Res 94:8007–8017
Graham N, Barnett TP (1987) Sea surface temperature, surface wind divergence, and convection over tropical oceans. Science 238:657–659
Gutzler DS, Wood TM (1990) Structure of large-scale convective anomalies over the tropical oceans. J. Climate 6:2049–2062
Lau KM, Wu HT, Bony S (1997) The role of large-scale atmospheric circulation in the relationship between tropical convection and sea surface temperature. J. Climate 10:381–392
Li X, Sui CH, Adamec D, Lau KM (1998) Impacts of precipitation in the upper ocean in the western Pacific warm pool during TOGA COARE. J Geophys Res 103:5347–5359
Li X, Sui CH, Lau KM, Adamec D (2000) Effects of precipitation on ocean mixed-layer temperature and salinity as simulated in a 2-D coupled ocean-cloud resolving atmosphere model. J Meteor Soc Japan 78:647–659
Lukas R, Lindstrom E (1991) The mixed layer of the western equatorial Pacific Ocean. J Geophys Res 96:3343–3457
Miller JR (1976) The salinity effect in a mixed-layer ocean model. J Phys Oceanogr 6:29–35
Murtugudde R, Busalacchi AJ (1998) Salinity effects in a tropical ocean model. J Geophys Res 103:3283–3300
Niiler PP, Kraus EB (1977) One-dimensional models. In: Kraus EB (ed) Modeling and Prediction of the Upper Layers of the Ocean. Pergamon, New York
Sui CH, Li X, Lau KM, Adamec D (1997) Multi-scale air-sea interactions during TOGA COARE. Mon Wea Rev 125:448–462
Sui CH, Li X, Lau KM (1998) Selective absorption of solar radiation and upper ocean temperature in the equatorial western Pacific. J Geophys Res 103:10313–10321
Vialard J, Delecluse P (1998a) An OGCM study for the TOGA decade. Part I: Role of salinity in the physics of the western Pacific fresh pool. J Phys Oceanogr 28:1071–1088
Vialard J, Delecluse P (1998b) An OGCM study for the TOGA decade. Part II: Barrier layer formation and variability. J Phys Oceanogr 28:1089–1106
Waliser DE (1996) Formation and limiting mechanisms for very high sea surface temperature: Linking the dynamics and thermodynamics. J. Climate 9:161–188
Waliser DE, Graham NE (1993) Convective cloud systems and warm pool sea surface temperatures: Coupled interactions and self-regulation. J Geophys Res 98:12881–12893
Webster PJ (1994) Role of hydrological processes in ocean-atmosphere interactions. Rev Geophys 32:427–476
Yang S, Lau KM, Schopf PS (1999) Sensitivity of the tropical Pacific Ocean to precipitation induced freshwater flux. Clim Dyn 15:737–750
Zhang C (1993) Large-scale variability of atmospheric deep convection in relation to sea surface temperature in the Tropics. J. Climate 6:1898–1912

Chapter 11
Climate Equilibrium States

Tropical climate equilibrium states are essentially determined by the nonlinear interactions of multiscale physical processes including the large-scale and cloud dynamics, cloud microphysics, radiative and surface processes, turbulence, and ocean mixing processes. The cloud-resolving modeling of convective–radiative equilibrium states provides ways to enhance the understanding of these controlling processes. The equilibrium studies with cloud-resolving models have been conducted for two decades since Nakajima and Matsuno first ran an equilibrium simulation with a 2D cloud-resolving model in 1988. In this chapter, a brief history of equilibrium studies with cloud-resolving modeling is reviewed. Effects of *SST*, diurnal variations, and cloud microphysical and radiative processes on tropical equilibrium states are discussed based on Gao et al. (2007), Ping et al. (2007), Cui and Gao (2008), and Gao (2008).

11.1 Introduction

Nakajima and Matsuno (1988) used a 2D cloud-resolving model with a constant radiative cooling profile and water microphysical schemes to study tropical cloud clusters. Their experiment with the 50-h integrations simulates tropical quasi-equilibrium states, which was the first successful experiment for equilibrium cloud-resolving model simulation. Nakajima and Matsuno found that individual clouds with a horizontal scale of 1 km and timescale of 1 h are embedded in cloud clusters with a horizontal scale of 100 km and timescale of 10 h, which is due to the fact that the formation of cold air at the foot of an individual cloud limits a small horizontal scale and a short life cycle for the individual cloud, whereas the density current associated with the cloud air pool triggers the formation of a new cloud along the edge of the pool extending a long horizontal scale and a long life cycle for cloud clusters. Their results also showed that the model cloud can be terminated by evaporative cooling. Islam et al. (1993) employed a 3D model to study the predictability of tropical mesoscale rainfall. The balance between the surface fluxes and constant

radiative cooling is imposed in the model that leads to an equilibrium state after 50 h of the integration. Held and Hemler (1993) used a 2D model with interactive cloud-radiative forcing and water and ice microphysical schemes to study radiative–convective equilibrium in tropical moist convection and found that a quasi-biennial oscillation (QBO)-like variability with a period of 60 days is associated with the evolution of model domain mean zonal wind and the localization of tropical convection is a result of zero model domain mean zonal wind.

Lau et al. (1993) and Sui et al. (1994) studied the tropical water and energy cycles and their roles in the tropical system by integrating the 2D cloud-resolving model to the climate equilibrium states. The model uses initial conditions from 1956 Marshall Islands Experiment in the central Pacific and is imposed with a time-invariant horizontally uniform large-scale vertical velocity and a constant *SST* of 28°C, in which the simulated atmosphere is conditionally unstable below the freezing level and close to neutral above the freezing level. After the adjustment in about 20 days, the simulations reach the quasi-equilibrium states with the temperature of 258°C and *PW* of 51 mm. In the convective–radiative equilibrium conditions, two thirds of surface rainfall comes from the convective clouds while one third comes from the stratiform clouds. The *PW* budget shows that three fourths and one fourth of the total moisture supply are from the moisture advection associated with the imposed large-scale vertical velocity and the surface evaporation flux, respectively. The total moisture supply is completely converted into surface rainfall. The heat budget reveals that the cooling from the radiation and advection associated with the imposed large-scale vertical velocity are mainly balanced by the latent heat release associated with the precipitation processes. Grabowski et al. (1996) integrated the 2D cloud-resolving model for 24 days with similar initial conditions and found a quasi-equilibrium state with a temperature of 263°C and *PW* of 70 mm. Thus, tropical equilibrium states are warmer and more humid in Grabowski et al. (1996) than in Sui et al. (1994).

Robe and Emanuel (1996) used a 3D cloud-resolving model with a constant radiative cooling profile and water microphysical schemes to simulate statistical equilibrium. The simulations reach equilibrium states due to the balance between the net upward mass flux by moist convection and the net radiative cooling. The cloud mass flux increases with increasing radiative cooling. The mean updraft velocity is independent of the strength of the radiative forcing. Tompkins and Craig (1998) used a 3D cloud-resolving model with interactive cloud-radiative forcing and water and ice microphysical schemes and also simulated a statistical equilibrium state. After 30 days of integration, they found that the adjustment timescale could be different, for instance, vertical mass flux adjusts to the equilibrium state much more quickly than thermodynamic variables do. The simulated convection is organized due to interaction between radiation, convection, and surface fluxes. Xu and Randall (1998) carried out the sensitive tests of quasi-equilibrium states to large-scale advective cooling and moistening and found that the time-varying large-scale forcing has no significant impact on the long-term behaviors while they affect short-term variations. Xu and Randall (1999) showed that simulated statistical equilibrium state is between the cold and dry regime in Sui et al. (1994) and the warm and humid regime

in Grabowski et al. (1996) and found that the statistical equilibrium states are more sensitive to the transient large-scale forcing than to the magnitude of the forcing. Xu and Randall compared the model differences between Sui et al. and Grabowski et al. and found that Sui et al.'s model may be unable to maintain the initial wind profile reducing the surface wind speed and weakening surface evaporation. Tao et al. (1999) further compared the models by Sui et al. and Grabowski et al. and found that the mass-weighted relative humidity is 10% higher in Grabowski et al. than in Sui et al., the *CAPE* in Grabowski et al. is also larger than that of Sui et al., and the microphysical parameterization schemes, grid sizes, and domains between their models are quite different. To explain the differences of equilibrium states between Sui et al. and Grabowski et al.'s experiments, sensitivity tests with the 2D cloud-resolving model were conducted by Tao et al. (1999). The equilibrium states are not sensitive to the initial conditions whereas they are sensitive to the minimum surface speed prescribed in the calculation of surface fluxes. Equilibrium thermodynamic states depend on the surface evaporation, where the surface wind plays a central role. The small surface evaporation associated with weak surface winds produces a cold and dry equilibrium state whereas the large evaporation associated with strong surface winds causes a warm and humid equilibrium state.

Randall et al. (1994) studied the deviations from the statistical equilibrium state in cloud-resolving model simulations, which could be due to an imbalance between a transient large-scale dynamic process such as waves and transient radiative processes associated with multi timescale variations. Gao et al. (2006) analyzed the simulation data in COARE to study tropical heat and water vapor quasi-equilibrium and cycle. The data in the quasi-equilibrium states are averaged for two groups: surface rain rate is larger than mean value ($0.29\,\mathrm{mm\,h^{-1}}$) in group A and it is smaller in group B. As group-mean local atmospheric drying in group A ($-0.09\,\mathrm{mm\,h^{-1}}$) changes to local atmospheric moistening in group B ($0.17\,\mathrm{mm\,h^{-1}}$), group-mean local atmospheric warming ($0.05^{\circ}\mathrm{C\,h^{-1}}$) changes to local atmospheric cooling ($-0.03^{\circ}\mathrm{C\,h^{-1}}$), the surface rain rate decreases from 0.63 to $0.07\,\mathrm{mm\,h^{-1}}$, the *CAPE* increases from 234 to $407\,\mathrm{J\,kg^{-1}}$, and the sum of surface evaporation and moisture convergence decreases from 0.48 to $0.21\,\mathrm{mm\,h^{-1}}$. This implies that enhanced surface rainfall associated with the development of convection is a result of the release of more unstable energy and consumption of more water vapor. The energy and water vapor sources set a constraint for the tropical heat/water cycling. Convection develops with the enhanced rainfall as a result of the consumption of water vapor, and the release of *CAPE*, which causes the local atmospheric drying and warming. The convection and rainfall are suppressed until the atmosphere becomes more stable with small *CAPE* and low amount of water vapor. *CAPE* is generated and moisture is accumulated to rebuild a favorable environmental condition for the development of convection. Such cloud–environment interaction limits the deviation of thermodynamic state from its mean state and the life cycle of the clouds. Thus, clouds and associated precipitation serve as a regulator that ensures the approximate thermal and moisture balance and small variations of local water vapor and temperature.

Ramanathan and Collins (1991) conducted the observational study using NASA's Earth Radiation Budget Experiment (ERBE) and proposed that the thermostat effect

is necessary to counteract the super-greenhouse warming, and accounts for limiting *SST* over the western Pacific warm pool to a rather uniform distribution between 29°C and 30°C. Lau et al. (1994) further used the cloud-resolving model to investigate the cirrus-cloud thermostat effect for tropical *SST* by analyzing the net radiation flux at the top of the atmosphere and the net heat at the ocean–atmosphere interface. The model is integrated with the constant *SST*s of 28°C and 30°C, and with and without the large-scale forcing, respectively. The net radiation flux at the top of the atmosphere is comprised of the net absorbed solar radiation averaged over clear-sky regions, the IR radiation emitted by the ocean surface, atmospheric greenhouse effect, as well as IR and shortwave cloud forcing, whereas the net heat flux at the ocean–atmosphere interface consists of solar and IR radiative, and sensible and latent heat fluxes. The comparison of the experiments with the same large-scale forcing but different *SST*s shows that the largest changes in the components contributing to the net radiation flux at the top of the atmosphere are due to the emission of the surface IR radiation and greenhouse warming by the increase in water vapor, which offset each other in a large part. The magnitude of the emission of the surface IR radiation is smaller than the greenhouse warming, suggesting no apparent "super-greenhouse" effect. The changes in IR and shortwave cloud forcing are small, and are insensitive to the changes in the *SST*s, because the change in the *SST* induces the change in low and mid-tropospheric clouds but does not have any impact on upper tropospheric clouds. The change in the net heat flux at ocean–atmosphere interface is mainly due to the change in the surface latent heat flux. The increase in the *SST* induces surface cooling by increasing surface evaporation. The increase in the *SST* produces 13% increase in surface precipitation. The comparison of the experiments with the same *SST*s but different large-scale forcing (with and without the forcing) displays that the largest changes in the budget at the top of the atmosphere occur in the shortwave and IR cloud forcing, which cancel each other out in a large part. The experiment without the forcing undergoes a large reduction of greenhouse effect by decreasing the moisture. At the ocean–atmosphere interface, the largest change appears in the surface radiative flux due to largest difference of clouds between the experiments with and without large-scale forcing.

11.2 Effects of *SST* on Equilibrium Climate

Surface boundary has an important impact on convective development as well as equilibrium climate. Chao (1961) investigated effects of surface heating on convective development by introducing a surface heat balance condition in which the surface solar heat flux is transported upward by turbulence. His analytical model solution showed intensification of a vertical circulation associated with the surface forcing under an unstable stratification. Li et al. (1964) found that a cloud with a size of 3 km in horizontal length and 2 km in depth corresponds to a surface heating perturbation of 0.4°C and 2 km in horizontal length. In an oceanic coupled system, *SST* is affected by surface radiative and heat flux. *SST* in turn impacts the atmosphere

through surface sensible heat and evaporation fluxes. In an atmospheric system alone, *SST* becomes an important forcing. Gao et al. (2007) studied effects of *SST* on tropical equilibrium states by conducting three experiments in a model framework of zero imposed vertical velocity and vertically invariant zonal wind. Experiments SST27, SST29, and SST31 are imposed by time-invariant *SST*s of 27°C, 29°C, and 31°C, respectively. A vertical wind shear has important impacts on convective development and configuration. For example, Chao and Chen (1964) in their linear analytical analysis showed that the vertical wind shear intensifies convective development when it is larger than $10^{-2}\,s^{-1}$. The model produced unicell-type convection in a unidirectional wind shear (e.g., Dudhia et al. 1987; Tao et al. 1995) whereas the model generated multicell-type convection in a reversing wind shear (Tao et al. 2003). To emphasize the effects of *SST*, imposed zonal wind is vertically invariant.

Figure 11.1 shows time series of zonal- and mass-weighted mean temperatures and zonal-mean *PW*. Temperature and *PW* reach equilibrium states in three experiments during the 40-day integrations. Zonal- and mass-weighted mean temperatures averaged from 31 to 40 days are −6.2°C in SST27, −3.0°C in SST29, and 0.1°C in SST31, respectively. Amounts of zonal-mean *PW* averaged from day 31 to day 40 are 37.1 mm in SST27, 44.9 mm in SST29, and 52.5 mm in SST31, respectively. This indicates that cold *SST* produces cold and dry equilibrium states whereas warm *SST* generates warm and moist equilibrium states.

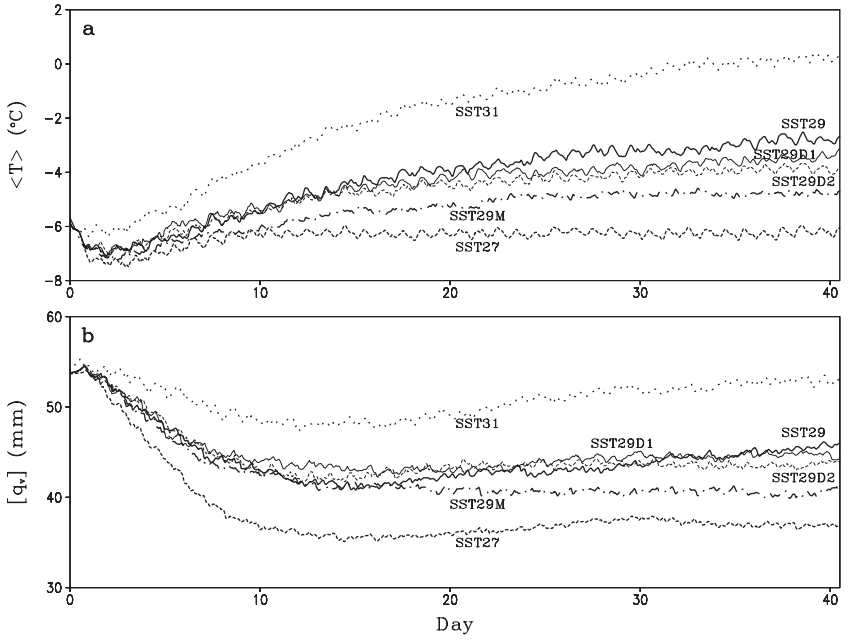

Fig. 11.1 Time series of **a** zonal- and mass-weighted mean temperature (°C) and **b** zonal-mean *PW* (mm) in SST27 (dark dashed), SST29 (dark solid), SST31 (dot), SST29M (dark dot dashed), SST29D1 (light solid), and SST29D2 (light dashed) (After Gao et al. 2007)

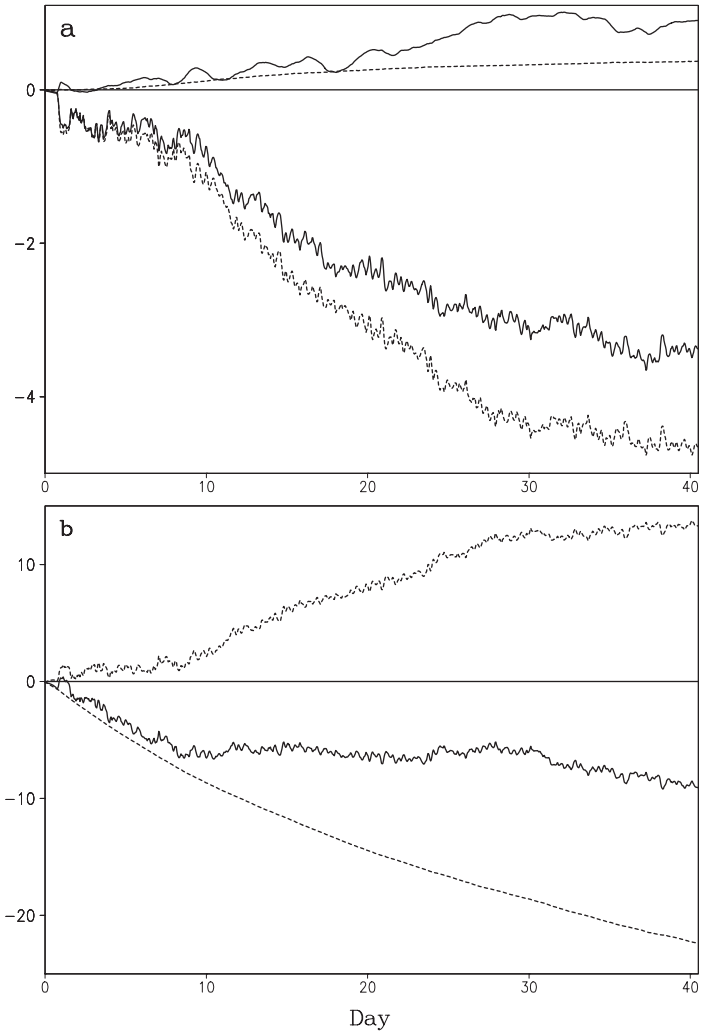

Fig. 11.2 Time series of **a** mass-weighted mean temperature (°C) difference (dark solid) for SST27–SST29 and differences caused by condensational heating (dark dashed), radiative heating (light solid), and surface sensible heat flux (light dashed), and **b** *PW* (mm) difference (dark solid) and the differences caused by condensation (dark dashed) and surface evaporation flux (light dashed) (After Gao et al. 2007)

The temperature difference in condensational heating for SST27–SST29 is negative whereas the temperature differences in radiation and surface sensible heat flux are positive (Fig. 11.2a). Thus, the negative difference in condensational heating accounts for the negative temperature difference. The *PW* difference in condensation for SST27–SST29 is positive whereas the difference in surface evaporation flux is negative (Fig. 11.2b). Thus, the negative evaporation-induced difference is

responsible for the negative *PW* difference. The analysis of heat and *PW* budgets reveals that the colder *SST* in SST27 pumps a smaller amount of water vapor from the ocean to the atmosphere than warmer *SST* in SST29 does, which leads to an atmospheric drying in SST27. Less water vapor in SST27 causes less condensation and associated heating than in SST29, which causes an atmospheric cooling in SST27.

Equilibrium cloud and rainfall properties in SST29 are calculated using simulation data from day 31 to 40 (Table 11.1a). Time- and zonal-mean surface rain rate ($P_s = 0.130\,\mathrm{mm\,h^{-1}}$) is mainly from zonal-mean surface evaporation rate ($Q_{WVE} = 0.134\,\mathrm{mm\,h^{-1}}$). Time- and zonal-mean *LWP* (0.086 mm) is larger than time- and zonal-mean *IWP* (0.60 mm). Fractional coverage is 50.1% for non-raining stratiform regions, 3.2% for convective regions, and 5.8% for raining stratiform regions. Raining clouds (0.081 mm) have a larger *LWP* than non-raining clouds (0.005 mm) do whereas non-raining clouds (0.036 mm) have a larger *IWP* than raining clouds (0.023 mm) do. Over clear-sky regions, the surface evaporation flux ($Q_{WVE} = 0.074\,\mathrm{mm\,h^{-1}}$) has a smaller magnitude than the vapor divergence ($Q_{WVF} = -0.088\,\mathrm{mm\,h^{-1}}$) has, which yields an atmospheric drying ($Q_{WVT} = 0.013\,\mathrm{mm\,h^{-1}}$). Over raining stratiform regions, all four processes contribute to surface rainfall. Among them, the cloud source ($Q_{CM} = 0.025\,\mathrm{mm\,h^{-1}}$) is the largest while the evaporation ($Q_{WVE} = 0.004\,\mathrm{mm\,h^{-1}}$) is the smallest. Over convective regions, the vapor convergence ($Q_{WVF} = 0.116\,\mathrm{mm\,h^{-1}}$) is a main source for surface rainfall as well as a hydrometeor gain/convergence ($Q_{CM} = -0.033\,\mathrm{mm\,h^{-1}}$). Over non-raining stratiform regions, the vapor divergence ($Q_{WVF} = -0.034\,\mathrm{mm\,h^{-1}}$) has a smaller magnitude than does the surface evaporation flux ($Q_{WVE} = 0.053\,\mathrm{mm\,h^{-1}}$), which leads to an atmospheric moistening ($Q_{WVT} = -0.021\,\mathrm{mm\,h^{-1}}$).

Equilibrium cloud and rainfall properties in SST27 (Table 11.1b) are compared with those in SST29 to examine the effects of *SST* on equilibrium cloud and rainfall processes. Time- and zonal-mean surface rain rates are similar in SST27 and SST29 ($0.130\,\mathrm{mm\,h^{-1}}$) although time- and zonal-mean surface evaporation rate is smaller in SST27 ($0.119\,\mathrm{mm\,h^{-1}}$) than in SST29 ($0.134\,\mathrm{mm\,h^{-1}}$). Similar rain rates in both experiments are due to the local atmospheric drying in SST27 ($0.012\,\mathrm{mm\,h^{-1}}$). While time- and zonal-mean *IWP* is insensitive to the change of *SST*, the decrease in the imposed *SST* from 29°C to 27°C causes a decrease in the time- and zonal-mean *LWP* from 0.084 to 0.074 mm. The decrease in the imposed *SST* from 29°C to 27°C leads to a decrease in the fractional coverage for convective regions from 3.2% to 2.9%, in raining stratiform regions from 5.8% to 5.6%, and in non-raining stratiform clouds from 50.1% to 45.8%.

Although the time- and zonal-mean Q_{WVT}, Q_{WVF}, and Q_{CM} are negligibly small, they may contribute to surface rainfall processes over specific regions. Area-weighted values (that are calculated by dividing the values in Tables 11.1a and b with corresponding fractional cloud coverage in each region) are used for discussion in this paragraph. Over clear-sky regions, Q_{WVE} is $0.152\,\mathrm{mm\,h^{-1}}$ in SST27 and $0.182\,\mathrm{mm\,h^{-1}}$ in SST29. Q_{WVF} is $-0.196\,\mathrm{mm\,h^{-1}}$ in SST27 and $-0.213\,\mathrm{mm\,h^{-1}}$

Table 11.1 Fractional cloud coverage (%), *IWP, LWP* (mm), P_s, Q_{WVT}, Q_{WVF}, Q_{WVE}, and Q_{CM} $(\mathrm{mm\,h^{-1}})$ over clear-sky regions, raining stratiform regions, convective regions, and non-raining stratiform regions averaged from days 31 to 40 in (a) SST29, (b) SST27, (c) SST29M, and (d) SST29D2

(a)	Clear-sky regions	Raining stratiform regions	Convective regions	Non-raining stratiform regions	Zonal mean
Fractional coverage	40.7	5.8	3.2	50.1	100
IWP	0.000	0.018	0.005	0.036	0.060
LWP	0.000	0.041	0.040	0.005	0.086
P_s	0.000	0.056	0.074	0.000	0.130
Q_{WVT}	0.013	0.019	−0.011	−0.021	0.000
Q_{WVF}	−0.088	0.007	0.116	−0.034	0.000
Q_{WVE}	0.074	0.004	0.002	0.053	0.134
Q_{CM}	0.000	0.025	−0.033	0.002	−0.005

(b)	Clear-sky regions	Raining stratiform regions	Convective regions	Non-raining stratiform regions	Zonal mean
Fractional coverage	45.5	5.6	2.9	45.8	100
IWP	0.000	0.022	0.005	0.033	0.061
LWP	0.000	0.036	0.035	0.004	0.074
P_s	0.000	0.059	0.071	0.000	0.130
Q_{WVT}	0.019	0.019	−0.009	−0.017	0.012
Q_{WVF}	−0.089	0.007	0.111	−0.029	0.000
Q_{WVE}	0.069	0.004	0.002	0.044	0.119
Q_{CM}	0.000	0.029	−0.034	0.002	−0.002

(c)	Clear-sky regions	Raining stratiform regions	Convective regions	Non-raining stratiform regions	Zonal mean
Fractional coverage	47.8	4.7	3.1	44.2	100
IWP	0.000	0.021	0.007	0.031	0.059
LWP	0.000	0.036	0.043	0.005	0.084
P_s	0.000	0.065	0.103	0.000	0.168
Q_{WVT}	0.022	0.024	−0.013	−0.024	0.010
Q_{WVF}	−0.113	0.004	0.149	−0.039	0.000
Q_{WVE}	0.091	0.005	0.003	0.056	0.155
Q_{CM}	0.000	0.032	−0.037	0.007	0.003

(d)	Clear-sky regions	Raining stratiform regions	Convective regions	Non-raining stratiform regions	Zonal mean
Fractional coverage	49.5	4.6	3.0	42.7	100
IWP	0.000	0.018	0.006	0.032	0.056
LWP	0.000	0.035	0.040	0.005	0.080
P_s	0.000	0.058	0.091	0.000	0.150
Q_{WVT}	0.020	0.021	−0.010	−0.020	0.011
Q_{WVF}	−0.103	0.001	0.134	−0.032	0.000
Q_{WVE}	0.082	0.004	0.003	0.048	0.137
Q_{CM}	0.000	0.032	−0.035	0.004	0.002

in SST29. Q_{WVT} is 0.041 mm h^{-1} in SST27 and 0.032 mm h^{-1} in SST29. Both surface evaporation flux and the vapor divergence increase their magnitudes with increasing *SST*, whereas the local atmospheric drying rate decreases with increasing *SST*. Over raining stratiform regions, P_s is 1.054 mm h^{-1} in SST27 and 1.073 mm h^{-1} in SST29. The stratiform rain rate is insensitive to the variation of *SST*. Over convective regions, convective rain rate is larger in SST27 (2.448 mm h^{-1}) than in SST29 (2.313 mm h^{-1}) because the vapor convergence rate is larger in SST27 (3.828 mm h^{-1}) than in SST29 (3.625 mm h^{-1}). The vapor convergence is a dominant factor in convective rainfall. The vapor convergence rate and the surface rain rate increase as the *SST* decreases. Over non-raining stratiform regions, Q_{WVE} is 0.096 mm h^{-1} in SST27 and 0.106 mm h^{-1} in SST29. Q_{WVF} is -0.063 mm h^{-1} in SST27 and -0.068 mm h^{-1} in SST29. Q_{WVT} is -0.037 mm h^{-1} in SST27 and -0.042 mm h^{-1} in SST29. Q_{WVF}, Q_{WVE}, and Q_{WVT} increase their magnitudes with increasing *SST*. Thus, the *SST*-induced decrease in the surface evaporation flux suppresses the atmospheric moistening and vapor divergence.

11.3 Effects of Diurnal Variation on Equilibrium Climate

To examine effects of diurnal variation of solar radiative heating on tropical equilibrium states, the experiment SST29M with a fixed daily-mean cosine of solar zenith angle is conducted and compared with SST29 (Gao et al. 2007). Two experiments with diurnally varying *SST*s are also conducted to study effects of diurnal variations of *SST* on tropical equilibrium states (Gao et al. 2007). Experiments SST29D1 and SST29D2 have diurnally varying *SST*s with the mean of 29°C and diurnal differences of 1°C and 2°C, respectively. The maximum and minimum *SST*s occur at 1600 LST and 0700 LST, respectively.

Zonal- and mass-weighted mean temperatures in SST29M and SST29 have similar magnitudes and evolution in the first 2 days and their differences become larger later on (Fig. 11.1a). The zonal-mean equilibrium temperature averaged in the last 10 days of the integration in SST29M is -4.8°C, which is 1.8°C colder than the equilibrium temperature in SST29. Amounts of zonal-mean *PW* in SST29M and SST29 have similar magnitudes and evolution in the first 18 days. Later on, the *PW* in SST29M becomes smaller than it does in SST29 (Fig. 11.1b). Zonal-mean equilibrium *PW* averaged in the last 10 days of the integration in SST29M is 40.6 mm, which is 4.3 mm smaller than the equilibrium *PW* in SST29. These indicate that the simulation with a daily-mean solar zenith angle produces a colder and drier equilibrium state than does the simulation with a diurnally varied solar zenith angle.

The difference in heat budgets between SST29M and SST29 shows that the temperature difference in condensational heating is positive whereas the temperature differences in radiation and surface sensible heat flux are negative (Fig. 11.3a). The negative difference in radiation has a much larger magnitude than the negative difference in surface sensible heat flux does. Thus, the negative radiation-induced difference leads to the negative temperature difference for SST29M–SST29.

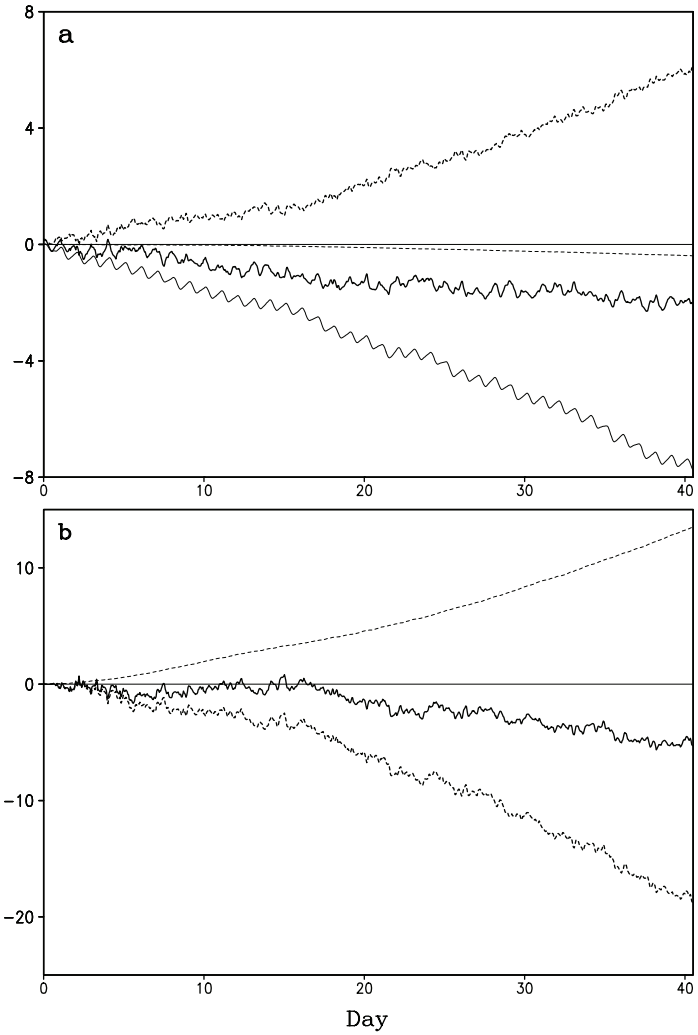

Fig. 11.3 As in Fig. 11.2, except for the difference for SST29M–SST29 (After Gao et al. 2007)

A separation analysis between solar heating and IR cooling reveals that the negative difference in solar heating accounts for the negative temperature difference since the difference in solar heating is negative whereas the difference in IR cooling is positive (Fig. 11.4a). The negative difference in solar heating for SST29M–SST29 is mainly contributed to by the negative difference in clear-sky regions in the first few days (Fig. 11.4c) and in cloudy regions later on (Fig. 11.5b). This indicates that the clouds enhance the negative difference in solar heating.

The difference in *PW* budgets for SST29M–SST29 shows that the negative *PW* difference is mainly determined by the negative difference in condensation since

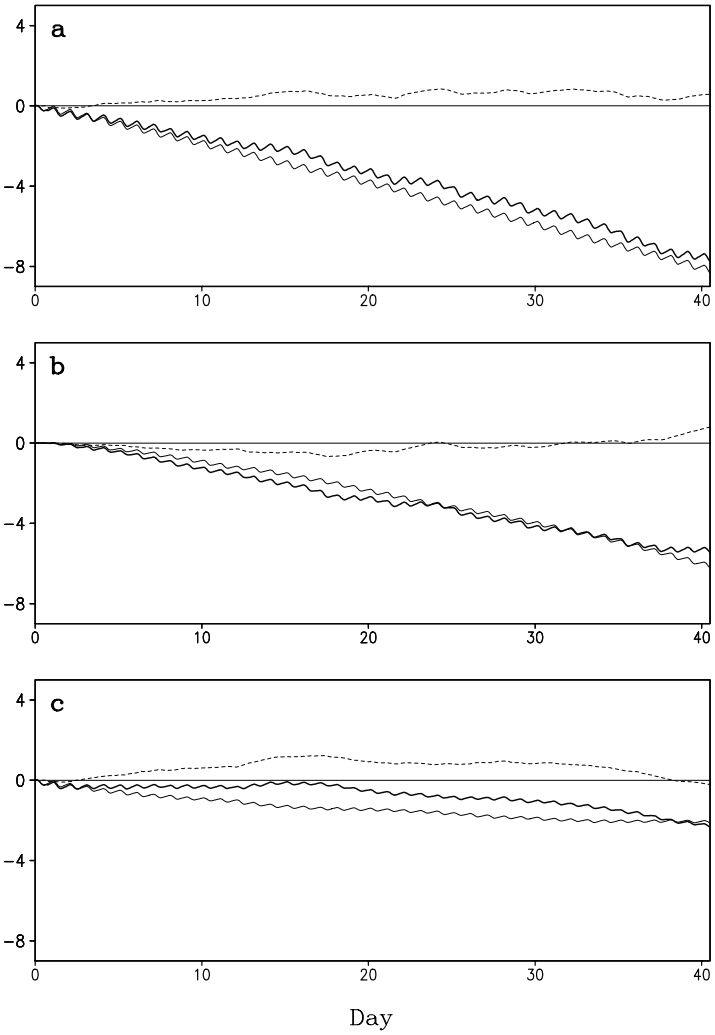

Fig. 11.4 Time series of mass-weighted mean temperature (°C) differences for SST29M–SST29 caused by radiation (dark solid), solar heating (light solid), and IR cooling (light dashed) in **a** horizontal domain mean, **b** cloudy regions, and **c** clear-sky regions (After Gao et al. 2007)

the difference in surface evaporation flux is positive whereas the difference in condensation is negative (Fig. 11.3b). This indicates that SST29M produces more condensation and consumes more water vapor than SST29 does.

Initially, SST29M produces smaller solar heating and colder temperature than SST29 does. The colder atmosphere in SST29M causes more condensation than the warm atmosphere in SST29 does. More condensates in SST29M consume more water vapor and cause smaller solar heating than in SST29, maintaining colder and drier equilibrium states in SST29M.

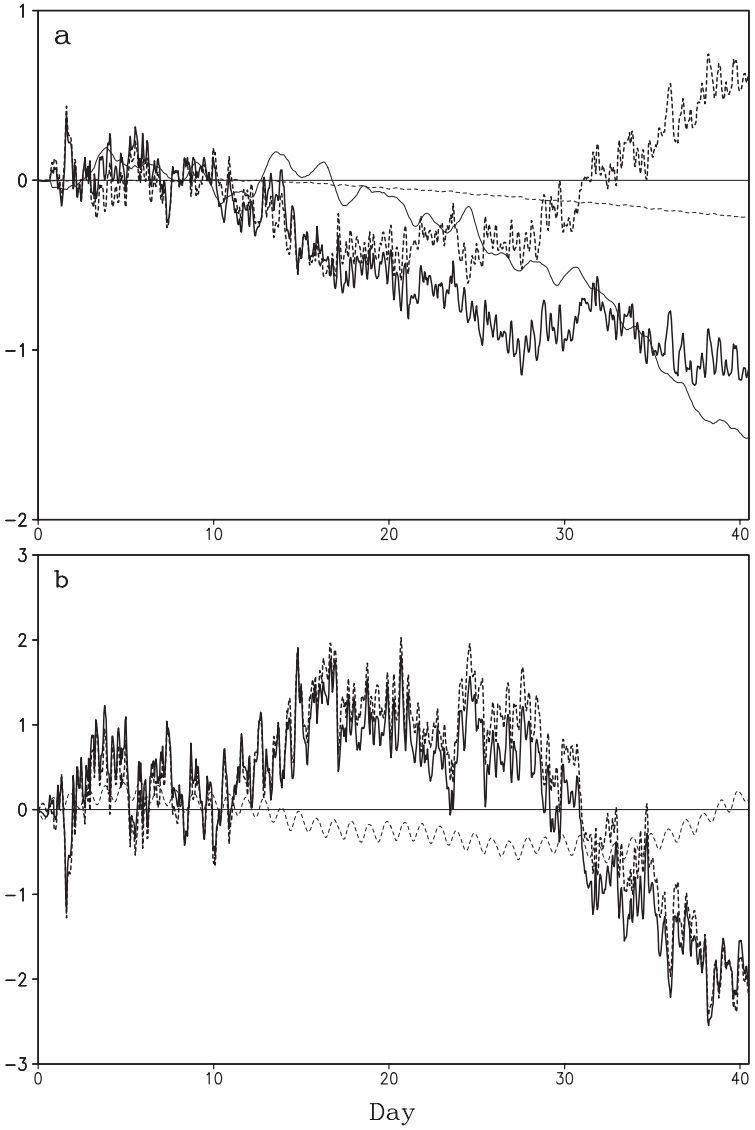

Fig. 11.5 As in Fig. 11.2, except for the difference for SST29D2–SST29 (After Gao et al. 2007)

Equilibrium cloud and rainfall properties in SST29M (Table 11.1c) are compared with those in SST29 to examine the effects of diurnal variation of solar zenith angle on equilibrium cloud and rainfall processes. Time- and zonal-mean surface rain rate is larger in SST29M ($0.168\,\mathrm{mm\,h^{-1}}$) than in SST29 ($0.130\,\mathrm{mm\,h^{-1}}$) due to the fact that time- and zonal-mean surface evaporation rate is larger in SST29M ($0.155\,\mathrm{mm\,h^{-1}}$) than in SST29 ($0.134\,\mathrm{mm\,h^{-1}}$) and that time- and zonal-mean local

atmospheric drying also contributes to surface rain rate in SST29M ($0.010\,\mathrm{mm\,h^{-1}}$). Thus, the exclusion of diurnal variation of solar zenith angle in the simulation enhances surface rain rate through enhanced surface evaporation fluxes and atmospheric drying process. Both time- and zonal-mean *IWP* and *LWP* are not very sensitive to diurnal variation of solar zenith angle. While fractional coverage of convective regions is insensitive to the diurnal variation of solar zenith angle, SST29M produces a smaller fractional coverage of both raining and non-raining stratiform regions and larger fractional coverage of clear-sky regions than SST29 does. In convective regions, SST29M generates larger *IWP* and *LWP* than SST29 does. In raining stratiform regions, SST29M produces a larger *IWP* and a smaller *LWP* than SST29 does. In non-raining stratiform regions, *IWP* is 14% smaller in SST29M than in SST29 although both experiments have same *LWP*.

SST29M produces larger time- and zonal-mean surface rain rate than SST29 does mainly because SST29M ($0.103\,\mathrm{mm\,h^{-1}}$) has larger time-mean convective rain rate than SST29 ($0.074\,\mathrm{mm\,h^{-1}}$) does. The difference in time-mean stratiform rain rate for SST29M–SST29 also contributes to the difference in time- and zonal mean surface rain rate. The vapor convergence largely determines convective rain rate in both experiments. Thus, the exclusion of diurnal variation of solar zenith angle in the simulation enhances water vapor convergence in convective regions, convective rain rate, and thus zonal-mean surface rain rate. SST29M generates larger surface evaporation rate than SST29 does over clear-sky regions, while the surface evaporation rates in both experiments are similar over non-raining stratiform regions. Thus, SST29M has larger water vapor divergence than SST29 does over clear-sky regions. Therefore, the exclusion of diurnal variation of solar zenith angle in the simulation enhances surface evaporation over clear-sky regions and water vapor transport from clear-sky regions to convective regions, and increases convective rainfall.

To examine the effects of diurnally varied *SST* on tropical equilibrium states, two additional experiments SST29D1 and SST29D2 are carried out. SST29D1 and SST29D2 show slightly warmer horizontal domain and mass-weighted mean temperatures in the first 10 days and colder temperatures after day 10 than SST29 does (Fig. 11.1a). Zonal-mean equilibrium temperatures averaged from day 31 to day 40 are -3.6°C in SST29D1 and -3.9°C in SST29D2, which are 0.6°C and 0.9°C colder than the equilibrium temperature in SST29, respectively. Amounts of zonal-mean *PW* in SST29D1 and SST29D2 show larger magnitudes than are shown in SST29 between day 10 and day 30 and they become smaller in the last 10 days of the integrations (Fig. 11.1b). Zonal-mean equilibrium *PW* amounts averaged in the last 10 days are 44.6 mm in SST29D1 and 43.6 mm in SST29D2, which are 0.3 mm and 1.3 mm smaller than the equilibrium *PW* in SST29, respectively.

The differences in *PW* budgets for SST29D2–SST29 reveal that SST29D2 enhances surface evaporation flux and condensation through a warm afternoon *SST* anomaly than SST29 does initially (Fig. 11.5b). The positive difference in condensation for SST29D2–SST29 induces a positive difference in IR cooling in the first 10 days (Fig. 11.6). The positive temperature difference is mainly caused by the positive differences in IR cooling and condensational heating (Fig. 11.5a). The positive difference in IR cooling comes from the positive difference in IR cooling in

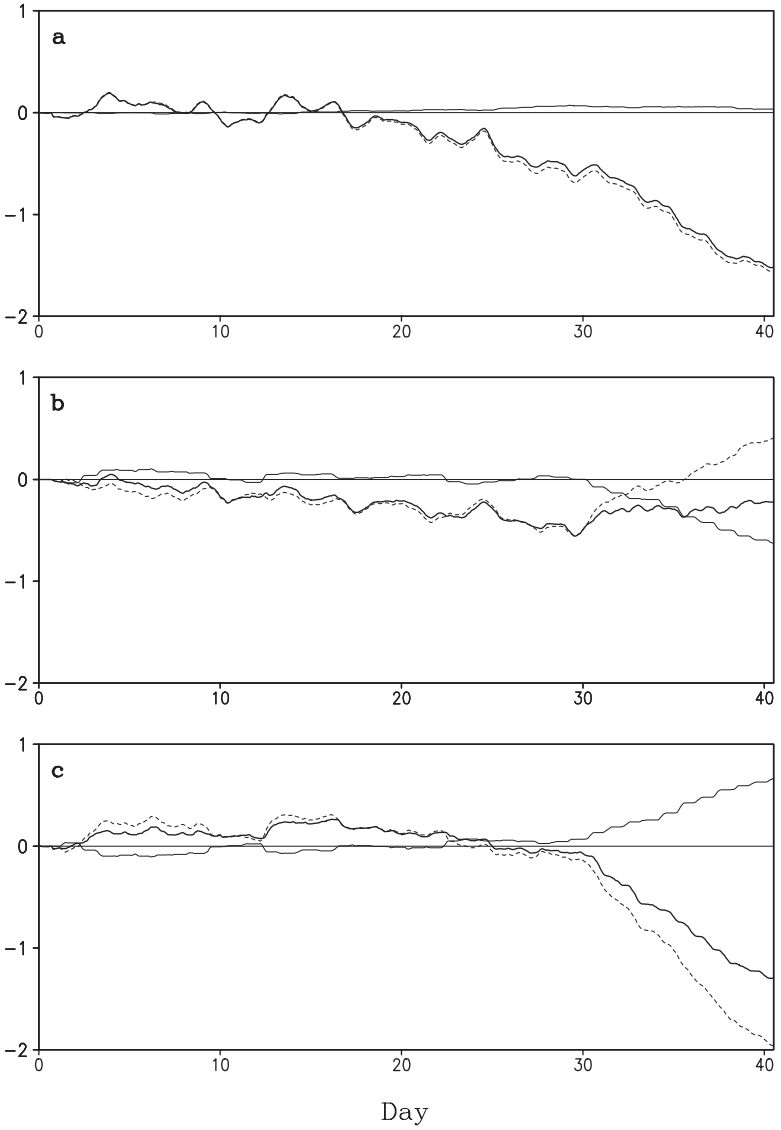

Fig. 11.6 As in Fig. 11.4, except for the difference for SST29D2–SST29 (After Gao et al. 2007)

clear-sky regions (Fig. 11.6). From day 10 to day 20, the negative difference in condensational heating mainly accounts for the negative temperature difference. From day 20 to day 30, the negative differences in condensational heating and radiation are responsible for the negative temperature difference. The negative difference in radiation results from the negative difference in IR cooling in cloudy regions (Fig. 11.6b). In the last 10 days, the negative differences in IR cooling in clear-sky

regions (Fig. 11.6c) as well as in solar heating in cloudy regions (Fig. 11.6b) keep the negative temperature difference since the difference in radiation remains negative whereas the difference in condensational heating becomes positive (Fig. 11.5a).

The differences in *PW* budgets for SST29D2–SST29 show that the difference in condensation determines the *PW* difference because the positive difference in surface evaporation flux is small (Fig. 11.5b). The positive differences in condensation as well as in surface evaporation contribute to the positive *PW* difference in the first 10 days. The positive difference in condensation accounts for the positive *PW* difference from day 10 to day 30 since the difference in condensation is positive whereas the difference in surface evaporation is negative. The negative difference in condensation is mainly responsible for the negative *PW* difference in the last 10 days.

Initially, a warm afternoon *SST* anomaly in SST29D2 enhances surface evaporation and condensation, compared to SST29. More condensation induces less IR cooling in SST29D2 than in SST29. The warmer atmosphere in SST29D2 produces a smaller surface evaporation flux than is found in SST29 around day 10. Compared to SST29, the smaller surface evaporation flux in SST29D2 pumps less moisture into the atmosphere and causes less condensation and less moisture consumption from day 10 to day 30. Meanwhile, the smaller condensation in SST29D2 releases less latent heat and more IR cooling than in SST29, which leads to a colder temperature in SST29D2. In the last 10 days, a colder atmosphere in SST29D2 yields more condensation and more moisture consumption than in SST29, which results in a small amount of *PW* in SST29D2. More condensation in SST29D2 leads to more latent heat and larger IR cooling than in SST29. The larger IR cooling in SST29D2 maintains a colder atmosphere than in SST29.

Equilibrium cloud and rainfall properties in SST29D2 (Table 11.1d) are compared with those in SST29 to examine the effects of diurnal variation of *SST* on equilibrium cloud and rainfall processes. Time- and zonal-mean surface rain rate is smaller in SST29D2 ($0.150\,\mathrm{mm\,h^{-1}}$) than in SST29 ($0.130\,\mathrm{mm\,h^{-1}}$) due to the fact that local atmospheric drying contributes to surface rain rate in SST29D2 ($0.011\,\mathrm{mm\,h^{-1}}$) and that the local hydrometeor loss occurs in SST29D2 ($0.002\,\mathrm{mm\,h^{-1}}$) whereas the local hydrometeor gain appears in SST29 ($-0.005\,\mathrm{mm\,h^{-1}}$). Thus, the inclusion of diurnal *SST* variation in the simulation enhances surface rain rate through the atmospheric drying and hydrometeor loss. Both time- and zonal-mean *IWP* and *LWP* are 9% smaller in SST29D2 than in SST29. While fractional coverage of convective regions is not very sensitive to the diurnal *SST* variation, SST29D2 produces smaller fractional coverage of stratiform regions and larger clear-sky regions than SST29 does. In convective regions, time-mean *IWP* and *LWP* are insensitive to the diurnal *SST* variation. Time-mean stratiform *LWP* contributes less to time- and zonal-mean *LWP* in SST29D2 than in SST29 although time-mean stratiform *IWP* has same contributions to time- and zonal-mean *IWP* in both experiments. SST29D2 produces larger time- and zonal-mean surface rain rate than SST29 does mainly because SST29D2 ($0.091\,\mathrm{mm\,h^{-1}}$) has larger time-mean convective rain rate than SST29 ($0.074\,\mathrm{mm\,h^{-1}}$) does, which

is due to the fact that the vapor convergence is larger in SST29D2 $(0.134\,\mathrm{mm\,h^{-1}})$ than in SST29 $(0.116\,\mathrm{mm\,h^{-1}})$. Thus, the inclusion of diurnal *SST* variation in the simulation enhances water vapor convergence in convective regions that intensifies convective rain rate, and thus zonal-mean surface rain rate. SST29D2 generates larger surface evaporation rate and local atmospheric drying rate than SST29 does over clear-sky regions, which leads to larger water vapor divergence in SST29D2 than in SST29 over clear-sky regions. Therefore, the inclusion of diurnal *SST* variation in the simulation enhances surface evaporation over clear-sky regions and water vapor transport from clear-sky regions to convective regions, which increases convective rainfall.

11.4 Cloud Microphysical and Radiative Effects on Equilibrium Climate

To study microphysical and radiative effects of tropical equilibrium states, two sensitivity experiments (SST29NIR and SST29NIM) are conducted by Ping et al. (2007). The control experiment SST29 includes ice microphysics that fully interacts with radiation. Experiment SST29NIR is identical to SST29 except that SST29NIR excludes ice cloud-radiative effects by setting ice hydrometeor mixing ratio to zero in the calculation of radiation. The comparison between SST29NIR and SST29 shows the radiative effects of ice clouds on tropical equilibrium states. Experiment SST29NIM excludes ice-cloud variables and associated ice microphysical processes by setting ice hydrometeor mixing ratio to zero during the model integration. The comparison between SST29NIM with SST29NIR shows the microphysical effects of ice clouds on the tropical equilibrium states. The comparison between SST29NIM and SST29 reveals both microphysical and radiative effects of ice clouds on tropical equilibrium states.

Mean temperature and *PW* reach equilibrium states in three experiments during the 40-day integrations (Fig. 11.7). Zonal- and mass-weighted mean temperatures averaged from 31 to 40 days are -7.4°C in SST29NIR and -5.9°C in SST29NIM, which are 4.4°C and 2.9°C colder than the equilibrium temperature in SST29, respectively. Amounts of zonal-mean *PW* averaged from day 31 to day 40 are 35.7 mm in SST29NIR and 41.4 mm in SST29NIM, which are 9.2 mm and 3.5 mm smaller than the equilibrium *PW* in SST29, respectively. The comparison between SST29NIR and SST29 shows that the exclusion of radiative effects of ice clouds in the simulation causes cold and dry equilibrium states. The comparison between SST29NIM and SST29NIR indicates that the exclusion of microphysical effects of ice clouds in the simulation induces warm and moist equilibrium states. The comparison between SST29NIM and SST29 reveals that the exclusion of ice microphysics produces a cold and dry tropical equilibrium state.

To understand the physical processes that are responsible for these similarities and differences, zonal-mean heat and *PW* budgets are calculated by averaging the simulation data in the first 30 days and are shown in Table 11.2. The negative dif-

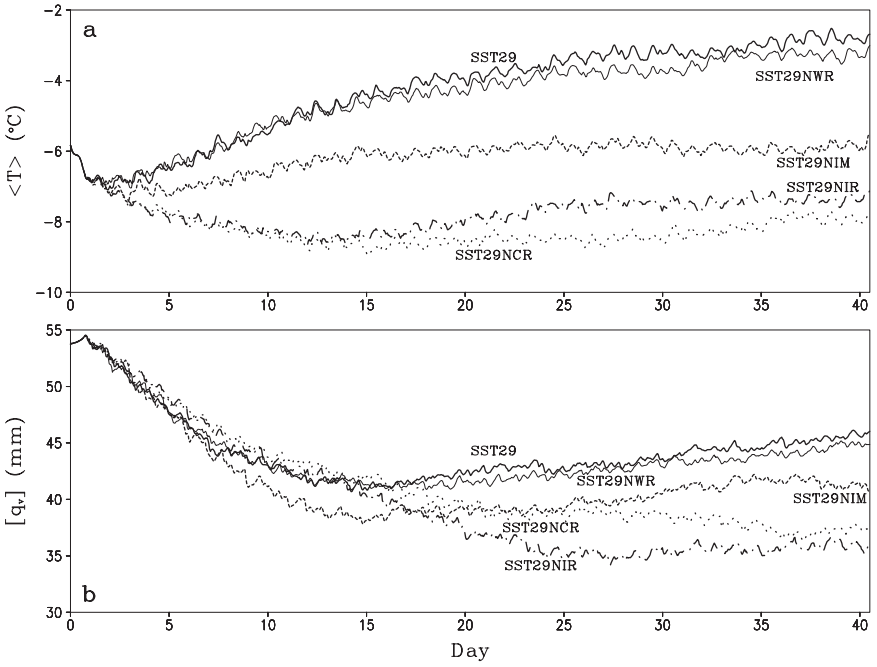

Fig. 11.7 Time series of **a** zonal- and mass-weighted mean temperature (°C) and **b** zonal-mean *PW* (mm) in SST29 (dark solid), SST29NIM (dark dashed), SST29NIR (dark dot dashed), SST29NWR (light solid), and SST29NCR (dot) (After Ping et al. 2007 and Gao 2008)

ference in radiative heating is responsible for the negative difference in temperature tendency for SST29NIR–SST29 whereas the negative condensation difference accounts for the negative difference in *PW* tendency. The negative radiation difference for SST29NIR–SST29 is mainly determined by the negative difference in zonal-mean IR cooling (Table 11.2c). This indicates that the simulation that excludes the ice radiative effects yields a larger IR cooling rate through allowing more outgoing IR radiation from the atmosphere than the simulation that includes the ice radiative effects does.

To examine microphysical effects of ice clouds on equilibrium states, SST29NIM is compared with SST29NIR since the radiative effects of ice clouds are excluded in both experiments. The positive difference in radiative heating is responsible for the positive difference in temperature tendency for SST29NIM–SST29NIR whereas the positive condensation difference accounts for the positive difference in *PW* tendency (Table 11.2). The positive difference in IR cooling explains the positive temperature tendency difference (Table 11.2c). The differences in temperature and *PW* budgets for SST29NIM–SST29 are similar to those for SST29NIR–SST29. Thus, the radiative effects of ice clouds on thermodynamic equilibrium states are dominant and the microphysical effects of ice clouds are secondary.

Table 11.2 Differences in (a) zonal and mass-weighted mean temperature budget ($^{\circ}$C d^{-1}), (b) zonal-mean *PW* budget (mm d^{-1}), and (c) zonal-mean temperature tendency differences caused by solar heating and IR cooling for SST29NIM–SST29, SST29NIR–SST29, and SST29NIM–SST29NIR averaged from the first 30-day simulation data (After Ping et al. 2007)

(a)	SST29NIM–SST29	SST29NIR–SST29	SST29NIM–SST29NIR
Temperature tendency	−0.091	−0.146	0.055
Condensational heating	0.032	0.223	−0.191
Radiative heating	−0.113	−0.382	0.269
Surface sensible heat flux	−0.009	0.013	−0.022
(b)	SST29NIM–SST29	SST29NIR–SST29	SST29NIM–SST29NIR
PW tendency	−0.098	−0.212	0.114
Condensation	−0.283	−0.709	0.426
Surface evaporation flux	0.186	0.437	−0.251
(c)	SST29NIM–SST29	SST29NIR–SST29	SST29NIM–SST29NIR
Zonal-mean solar heating	−0.011	0.002	−0.013
Zonal-mean IR cooling	−0.103	−0.384	0.281

The exclusion of ice radiative effects in SST29NIR increases *IWP* in raining stratiform and convective regions and thus zonal-mean *IWP* while it does not change zonal-mean *LWP* (Tables 11.1a and 11.3a). The exclusion of ice microphysical effects in SST29NIM mainly enhances *LWP* in non-raining stratiform regions and thus zonal-mean *LWP* (Tables 11.3a and b). The exclusion of ice microphysical and radiative effects enhances *LWP* in non-raining stratiform and convective regions and thus zonal-mean *LWP* (Tables 11.1a and 11.3b). The exclusion of ice radiative effects leads to a larger zonal-mean surface rain rate in SST29NIR than in SST29 (Tables 11.1a and 11.3a). SST29NIR produces a larger convective rain rate than SST29 does because SST29NIR has a larger vapor convergence than SST29 does. Due to the cyclic lateral boundary condition, the larger vapor convergence in convective regions is caused by the larger vapor divergence in clear-sky regions in SST29NIR that is balanced by the larger surface evaporation in SST29NIR, compared to that in SST29. The larger surface evaporation in clear-sky regions is caused by drier air and larger clear-sky coverage in SST29NIR because of the same constant *SST* imposed in both experiments.

The exclusion of ice microphysical effects yields a smaller zonal-mean surface rain rate in SST29NIM than in SST29NIR (Tables 11.3a and b). SST29NIM produces both smaller convective and stratiform rain rates than SST29NIR does because it has a smaller vapor convergence in convective regions and smaller local atmospheric drying and hydrometeor loss rates in raining stratiform regions. In clear-sky regions, vapor divergences in the two experiments are similar. In non-raining stratiform regions, the vapor divergence in SST29NIM is one order of

Table 11.3 As in Table 11.1 except for (a) SST29NIR and (b) SST29NIM (After Ping et al. 2007)

(a)	Clear-sky regions	Raining stratiform regions	Convective regions	Non-raining stratiform regions	Zonal mean
Fractional coverage	64.3	4.5	3.2	28.0	100
IWP	0.000	0.028	0.011	0.029	0.069
LWP	0.000	0.032	0.048	0.005	0.085
P_s	0.000	0.065	0.121	0.000	0.186
Q_{WVT}	0.001	0.030	−0.024	0.003	0.010
Q_{WVF}	−0.125	−0.018	0.197	−0.053	0.000
Q_{WVE}	0.122	0.007	0.005	0.044	0.178
Q_{CM}	0.002	0.046	−0.056	0.006	−0.003
(b)	Clear-sky regions	Raining stratiform regions	Convective regions	Non-raining stratiform regions	Zonal mean
Fractional coverage	72.6	2.3	3.4	21.5	100
IWP	0.000	0.000	0.000	0.000	0.000
LWP	0.000	0.039	0.052	0.026	0.117
P_s	0.000	0.038	0.086	0.000	0.124
Q_{WVT}	0.007	0.009	−0.008	−0.006	0.002
Q_{WVF}	−0.126	0.018	0.111	−0.005	0.000
Q_{WVE}	0.117	0.003	0.003	0.024	0.147
Q_{CM}	0.002	0.008	−0.021	−0.012	−0.023

magnitude smaller than that in SST29NIR because the surface evaporation rate is smaller in SST29NIM. Compared to SST29NIR, the smaller surface evaporation rate in SST29NIM is caused by more humid air and smaller coverage of non-raining stratiform regions. The exclusion of ice microphysical and radiative effects in simulation produces a slightly smaller zonal-mean surface rain rate in SST29NIM than in SST29 (Tables 11.1a and 11.3b), indicating that the ice microphysical effects and ice radiative effects on surface rainfall processes are cancelled out.

To examine radiative effects of water and ice clouds on tropical equilibrium states, two additional sensitivity experiments (SST29NWR and SST29NCR) are carried out by Gao (2008). SST29NWR and SST29NCR are identical to SST29 except that the radiative effects of water clouds and clouds (both water and ice clouds) are excluded by setting water and total hydrometeor mixing ratios to zero, respectively, in the cloud optical thickness and radiation calculations. Mean temperature and *PW* reach equilibrium states in SST29NWR and SST29NCR during the 40-day integrations (Fig. 11.7). Zonal- and mass-weighted mean equilibrium temperatures averaged from 31 to 40 days are −8.1°C in SST29NCR and −3.4°C in SST29NWR. Zonal-mean amounts of equilibrium *PW* averaged from day 31 to day 40 are 37.5 mm in SST29NCR and 44.0 mm in SST29NWR. The magnitudes of temperature differences for SST29NWR–SST29 (−0.4°C) and SST29NCR–SST29NIR (−0.7°C) are much smaller than those for SST29NIR–SST29 (−4.4°C) and SST29NCR–SST29NWR (−4.7°C). The magnitudes of the *PW* differences for

SST29NWR–SST29 (−0.9 mm) and SST29NCR–SST29NIR (1.8 mm) are also significantly smaller than those for SST29NIR–SST29 (−9.0 mm) and SST29NCR–SST29NWR (−6.5 mm). Thus, SST29 and SST29NWR have similar warm and humid equilibrium states whereas SST29NCR and SST29NIR have similar cold and dry equilibrium states. The similarities in zonal-mean temperature and *PW* between SST29 and SST29NWR and between SST29NCR and SST29NIR suggest that the water clouds may have minor radiative effects on tropical equilibrium states. The significant differences in zonal-mean temperature and *PW* between SST29NCR and SST29NWR and between SST29NIR and SST29 indicate that the ice clouds have major radiative effects on tropical equilibrium states.

The negative radiation-induced temperature difference for SST29NCR–SST29 mainly accounts for the negative temperature difference whereas the negative condensation-induced *PW* difference for SST29NCR–SST29 is mainly responsible for the negative *PW* difference (Fig. 11.8). The temporal-vertical distributions of zonal-mean solar radiation-induced temperature differences for SST29NCR–SST29 (Fig. 11.9a) show that the temperature difference is negative in the upper troposphere due to the fact that SST29NCR absorbs less solar radiation and allows more solar radiation penetrating into the mid and lower troposphere than SST29 does. Thus, SST29NCR could have more solar radiation to absorb in the mid and lower troposphere than SST29 does. The negative solar radiation-induced temperature difference in the upper troposphere and the positive difference in the mid and lower troposphere nearly cancel each other out in mass-weighted mean temperature calculations. Since ice clouds trap IR radiation, SST29NCR emits more IR radiation into space than SST29 does. Thus, the IR-induced temperature difference is negative in most of the troposphere (Fig. 11.9b), which causes the negative mass-weighted mean IR-induced temperature difference. SST29NCR produces a colder atmosphere than SST29 does through more IR cooling. The zonal-mean surface rain rates averaged from day 31 to 40 show that SST29NCR ($0.198\,\mathrm{mm\,h^{-1}}$) produces 52% more rainfall than SST29 ($0.130\,\mathrm{mm\,h^{-1}}$) does. While both experiments have similar zonal-mean *LWP* (0.086 mm), SST29NCR (0.070 mm) generates more zonal-mean *IWP* than SST29 (0.060 mm) does (Tables 11.1a and 11.4a). Thus, SST29NCR generates colder and drier atmosphere, larger condensates, and higher surface rainfall than SST29 does.

The comparison in cloud and precipitation properties between SST29NIR and SSTNCR (Tables 11.3a and 11.4a) shows vapor convergence in both experiments determines convective rain rate, which contributes two thirds of time- and zonal-mean surface rain rate. Cloud and rainfall properties in SST29NCR differ from those in SST29NIR in four ways. First, time- and zonal-mean surface rain rate is larger in SST9NCR than in SST29NIR because the local hydrometeor loss occurs in SST29NCR whereas the local hydrometeor gain appears in ST29NIR. Second, fractional coverage of convective and non-raining stratiform regions is larger in SST29NCR than in SST29NIR whereas that of clear-sky and raining stratiform regions is smaller. Third, surface evaporation rate over non-raining stratiform regions is larger in SST29NCR than in SST29NIR whereas it is smaller over clear-sky regions. Fourth, over raining stratiform regions, vapor divergence rate in

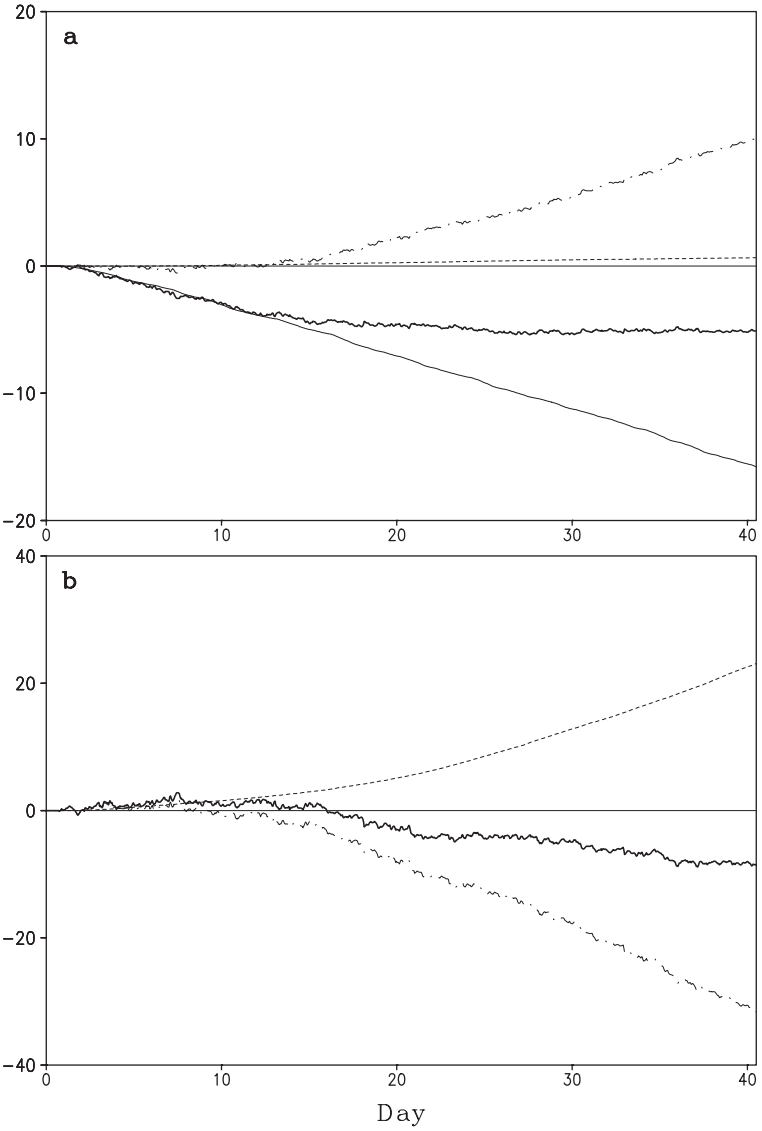

Fig. 11.8 As in Fig. 11.2, except for the difference for SST29NCR–SST29 (After Gao 2008)

SST29NCR is twice as large as that in SST29NIR, which leads to a larger vapor convergence rate over convective regions in SST29NCR.

The comparison in cloud and rainfall properties between SST29NWR and SST29 (Tables 11.1a and 11.4b) shows that the time- and zonal-mean surface rain rate is larger in SST29NWR than in SST29 due to the local vapor and hydrometeor loss in SST29NWR and the local hydrometeor gain in SST29. The difference in time- and

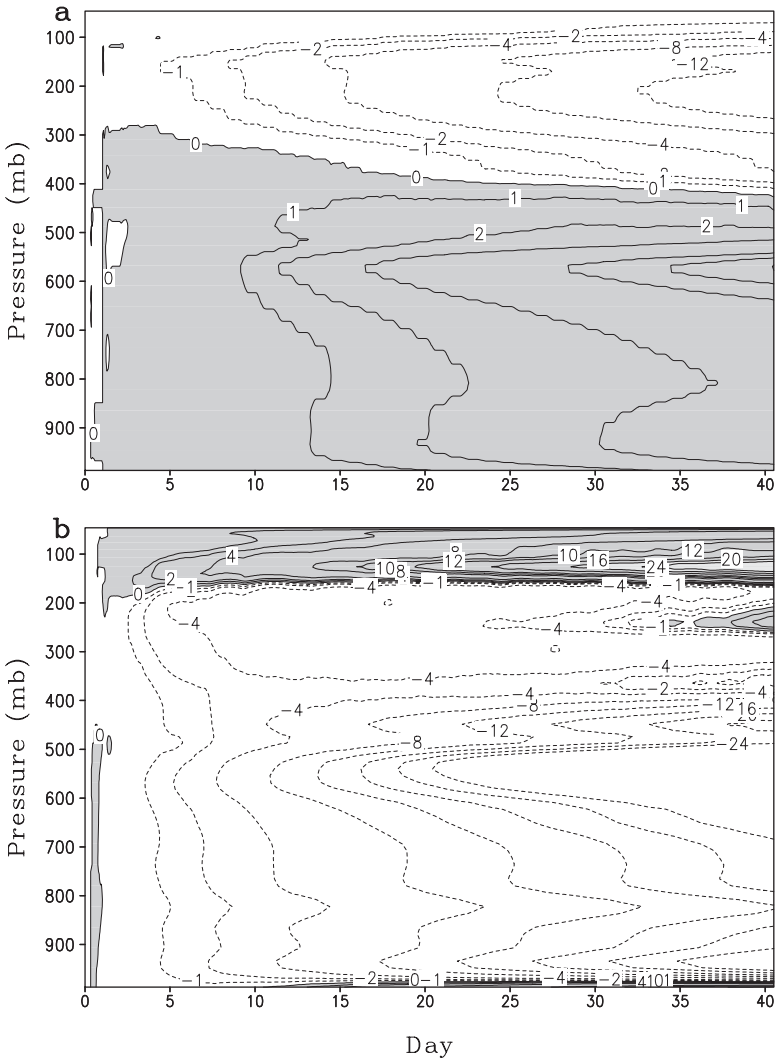

Fig. 11.9 Temporal and vertical distribution of zonal-mean temperature differences for SST29NCR–SST29 due to (a) solar and (b) IR radiation. Unit is °C. Positive differences are shaded (After Gao 2008)

zonal-mean surface rain rate is from the difference in convective rain rate between the two experiments, which results from the difference in vapor convergence over convective regions. Compared to SST29, the larger vapor convergence over convective regions is caused by the larger vapor divergence over clear sky regions in SST29NWR, which is balanced by the larger surface evaporation rate due to the larger fractional coverage of clear-sky regions in SST29NWR.

Table 11.4 As in Table 11.1, except for (a) SST29NCR and (b) SST29NWR

(a)	Clear-sky regions	Raining stratiform regions	Convective regions	Non-raining stratiform regions	Zonal mean
Fractional coverage	61.3	4.3	3.8	30.5	100
IWP	0.000	0.032	0.013	0.025	0.070
LWP	0.000	0.032	0.051	0.003	0.086
P_s	0.000	0.069	0.129	0.000	0.198
Q_{WVT}	0.016	0.043	−0.027	−0.020	0.013
Q_{WVF}	−0.134	−0.035	0.211	−0.041	0.000
Q_{WVE}	0.113	0.008	0.006	0.050	0.176
Q_{CM}	0.005	0.053	−0.061	0.011	0.008
(b)	Clear-sky regions	Raining stratiform regions	Convective regions	Non-raining stratiform regions	Zonal mean
Fractional coverage	44.6	5.7	3.2	46.4	100
IWP	0.000	0.018	0.006	0.038	0.062
LWP	0.000	0.041	0.041	0.006	0.088
P_s	0.000	0.057	0.089	0.000	0.146
Q_{WVT}	0.020	0.020	−0.009	−0.026	0.005
Q_{WVF}	−0.099	0.004	0.125	−0.029	0.000
Q_{WVE}	0.079	0.005	0.002	0.050	0.137
Q_{CM}	0.000	0.028	−0.030	0.004	0.003

11.5 Effects of Zonal Perturbations of *SST* on Equilibrium States

The horizontal distribution of *SST* may be affected by clouds and precipitation. Since clouds and precipitation have small spatial scale, *SST* may have large spatial perturbations in the presence of convective development. Cui and Gao (2008) conducted a series of sensitivity experiments of tropical equilibrium states to zonally perturbed *SST*. In their study, the zonal wave-like perturbations of *SST* with zonal wave number 1, 2, 4, and 8 (the zonal scale of 768, 384, 192, and 96 km) are superimposed in zonal-mean *SST* of 29°C in experiments SST29Z1, SST29Z2, SST29Z4, and SST29Z8, respectively. The amplitudes of zonal *SST* perturbations are 1°C. Note that the zonal-mean *SST* is 29°C in five experiments. The four perturbation experiments are compared to SST29.

During 40-day integrations, temperatures in all five experiments show quasi-equilibrium states with distinct differences (Fig. 11.10) whereas *PW* does not display distinct equilibrium differences in the five experiments (not shown). Compared to SST29 (−3.0°C), SST29Z4 (−4.4°C) and SST29Z8 (−3.7°C) produce colder equilibrium states whereas SST29Z1 (−2.6°C mm) and SST29Z2 (−2.3°C) generate warmer equilibrium states. SST29Z8 and SST29Z4 stop their warming trends on days 4 and 8, respectively, causing cold equilibrium states while the other experiments continue their warming courses. To explain physical processes that are responsible for thermal equilibrium states, the differences in temperature budgets

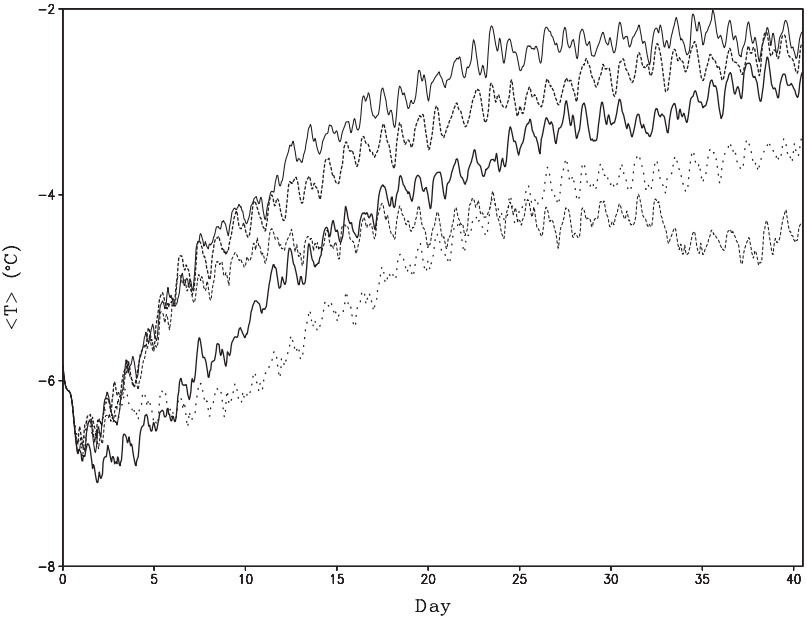

Fig. 11.10 Time series of zonal- and mass-weighted mean temperature (°C) and (b) zonal-mean *PW* (mm) in SST29 (dark solid), SST29Z1 (dark dashed), SST29Z2 (solid), SST29Z4 (dashed), and SST29Z8 (dot) (After Cui and Gao 2008)

Table 11.5 Zonal- and mass-weighted mean temperature budget differences ($^\circ$C d^{-1}) for SST29Z1–SST29, SST29Z2–SST29, SST29Z4–SST29, and SST29Z8–SST29 based on the data averaged from days 4–7 (After Cui and Gao 2008)

	SST29Z1–SST29	SST29Z2–SST29	SST29Z4–SST29	SST29Z8–SST29
Temperature tendency	0.136	0.204	0.143	−0.154
Condensational heating	0.013	0.137	0.123	−0.121
Radative heating	0.124	0.067	0.023	−0.030
Surface sensible heat flux	−0.002	0.000	−0.002	−0.002

for SST29Z1–SST29, SST29Z2–SST29, SST29Z4–SST29, and SST29Z4–SST29 are calculated (Table 11.5). The analysis on days 4–7 shows that the positive difference in temperature tendency is mainly determined by the positive difference in radiative heating for SST29Z1–SST29. Fractional coverage for clear-sky regions is 56.9% in SST29 with a uniform *SST* of 29°C over the model domain. Fractional coverage for clear-sky regions in SST29Z1 is 49.3% since half of the model domain in SST29Z1 has *SST* of colder than 29°C. The positive difference in radiative heating for SST29Z1–SST29 is determined by the positive difference in IR cooling over clear-sky regions (Table 11.6) since SST29Z1 has a smaller fractional coverage of clear-sky regions than SST29 does.

Table 11.6 Temperature tendency differences in zonal-mean solar heating and IR cooling and corresponding contributions from clear-sky regions and cloudy regions for SST29Z1–SST29, SST29Z2–SST29, SST29Z4–SST29, and SST29Z8–SST29 based on the data averaged from days 4–7. Unit is in $^{\circ}$C d^{-1} (After Cui and Gao 2008)

	SST29Z1–SST29	SST29Z2–SST29	SST29Z4–SST29	SST29Z8–SST29
Zonal-mean solar heating	−0.015	−0.011	−0.011	0.000
Zonal-mean IR cooling	0.139	0.077	0.034	−0.030
Solar heating in clear-sky regions	−0.063	−0.029	−0.013	0.000
IR cooling in clear-sky regions	0.134	0.045	0.000	0.004
Solar heating in cloudy regions	0.048	0.018	0.002	0.000
IR cooling in cloudy regions	0.005	0.032	0.034	−0.034

Table 11.5 reveals that the positive differences in temperature tendencies for SST29Z2–SST29 and SST29Z4–SST29 are caused by the positive differences in condensational heating during days 4–7. Although convection occupies similar sizes of areas in SST29 (43.1%), SST29Z2 (45.8%), and SST29Z4 (42.8%), the convection in SST29Z2 and SST29Z4 is more organized than in SST29, explaining that more condensational heating occurs in SST29Z2 and SST29Z4 than in SST29. Meanwhile, the similar fractional coverage of clear-sky regions in SST29 (56.9%), SST29Z2 (54.2%), and SST29Z4 (57.2%) significantly reduces the difference in IR cooling over clear-sky regions for SST29Z2–SST29 and SST29Z4–SST29 (Table 11.6), which causes smaller contributions to the positive differences in temperature tendencies for SST29Z2–SST29 and SST29Z4–SST29 than that for SST29Z1–SST29.

The negative difference in temperature tendency is mainly caused by the negative difference in condensational heating for SST29Z8–SST29 (Table 11.5). Since the distance between maximum *SST*s is only 96 km in SST29Z8, convective systems interact with each other so that some convective systems are suppressed whereas other convective systems cannot grow freely due to the small areas of warm *SST*. As a result, the contribution from condensational heating to temperature tendency in SST29Z8 is smaller than in SST29 (Table 11.5). Again, similar fractional coverage of clear-sky regions in SST29 (56.9%) and SST29Z8 (58.1) as well as cloudy regions in SST29 (43.1%) and SST29Z8 (41.9%) causes small differences in IR cooling over clear-sky regions and cloudy regions (Table 11.6), which account for small contributions from IR cooling to the positive difference in temperature tendency for SST29Z8–SST29.

The heat budgets averaged on days 4–7 are compared with those averaged on days 8–11 in SST29, SST29Z1, SST29Z2, and SST29Z4 (Table 11.7) to explain why SST29Z4 stops a warming course around day 8, which eventually leads to a cold equilibrium state (see Fig. 11.10). While SST29 has a positive difference in temperature tendency between averages on days 8–11 and days 4–7, SST29Z1, SST29Z2, and SST29Z4 show negative differences and SST29Z4 has the largest negative difference (Table 11.7). This shows that SST29Z4 turns out to have a colder equilibrium state than SST29 does. The positive difference in temperature

Table 11.7 Zonal- and mass-weighted mean temperature budget difference ($^\circ$C d^{-1}) between averages in days 8–11 and days 4–7 in SST29, SST29Z1, SST29Z2, SST29Z4 (After Cui and Gao 2008)

	SST29	SST29Z1	SST29Z2	SST29Z4
Temperature tendency	0.067	−0.170	−0.174	−0.206
Condensational heating	−0.049	−0.170	−0.224	−0.194
Radiative heating	0.124	−0.002	0.048	−0.011
Surface sensible heat flux	−0.007	0.002	0.001	−0.002

Table 11.8 Temperature tendency differences in zonal-mean solar heating and IR cooling and corresponding contributions from clear-sky regions and cloudy regions for SST29, SST29Z1, SST29Z2, and SST29Z4 between averages in days 8–11 and days 4–7. Unit is in $^\circ$C d^{-1} (After Cui and Gao 2008)

	SST29	SST29Z1	SST29Z2	SST29Z4
Zonal-mean solar heating	−0.017	0.001	−0.009	−0.006
Zonal-mean IR cooling	0.141	−0.002	0.058	−0.006
Solar heating in clear-sky regions	−0.080	−0.041	−0.076	−0.052
IR cooling in clear-sky regions	0.200	0.161	0.230	0.135
Solar heating in cloudy regions	0.063	0.042	0.067	0.046
IR cooling in cloudy regions	−0.059	−0.163	−0.172	−0.141

tendency in SST29 is mainly determined by the positive difference in radiative heating. The negative differences in temperature tendency in SST29Z1, SST29Z2, and SST29Z4 are determined by the negative differences in condensational heating and SST29Z2 has the largest negative difference. The positive difference in radiative heating offsets the negative difference in condensational heating in SST29Z2, thereby decreasing the magnitude of the negative difference in temperature tendency. The negative difference in radiative heating along with the negative difference in condensational heating in SST29Z4 serve to increase the magnitude of the negative difference in temperature tendency. The shrinking of zonal areas of tropical water clouds in SST29Z1, SST29Z2, and SST29Z4 reduce the vapor condensation and associated condensational heating on days 8–11, compared to those on days 4–7. Further analysis (Table 11.8) reveals that the positive differences in radiative heating in SST29 and SST29Z2 are caused by the positive difference in IR cooling over clear-sky regions. The small differences in radiative heating in SST29Z1 and SST29Z4 are from the cancellation in solar heating and IR cooling over clear-sky regions and cloudy regions, respectively. The positive differences in radiative heating in SST29 and SST29Z2 may be the results of significant reductions of clear-sky regions from days 4–7 (56.9% in SST29 and 54.2% in SST29Z2) to days 8–11 (48.3% in SST29 and 44.8% in SST29Z2).

References

Chao J (1961) A nonlinear analysis of development of thermal convection in a stratified atmosphere. Acta Meteor Sinica 31:191–204

Chao J, Chen L (1964) Effects of vertical wind shear on convective development. Acta Meteor Sinica 34:94–102

Cui X, Gao S (2008) Effects of zonal perturbations of sea surface temperature on tropical equilibrium states: A 2D cloud-resolving modeling study. Prog Nat Sci 18:179–182

Dudhia J, Moncrieff MW, So DWK (1987) The two-dimensional dynamics of West African squall lines. Quart J Roy Meteor Soc 113:121–146

Gao S (2008) A cloud-resolving modeling study of cloud radiative effects on tropical equilibrium states. J Geophys Res, doi:10.1029/2007JD009177

Gao S, Ping F, Li X (2006) Tropical heat/water vapor quasi-equilibrium and cycle as simulated in a 2D cloud resolving model. Atmos Res 79:15–29

Gao S, Zhou Y, Li X (2007) Effects of diurnal variations on tropical equilibrium states: A two-dimensional cloud-resolving modeling study. J Atmos Sci 64:656–664

Grabowski WW, Moncrieff MW, Kiehl JT (1996) Long-term behaviour of precipitating tropical cloud systems: A numerical study. Quart J Roy Meteor Soc 122:1019–1042

Held IM, Hemler RS (1993) Radiative-convective equilibrium with explicit two-dimensional moist convection. J Atmos Sci 50:3909–3927

Islam S, Bras RL, Emanuel KA (1993) Predictability of mesoscale rainfall in the tropics. J Appl Meteor 32:297–310

Lau KM, Sui CH, Tao WK (1993) A preliminary study of the tropical water cycle using the Goddard Cumulus Ensemble model. Bull Am Meteor Soc 74:1313–1321

Lau KM, Sui CH, Chou MD, Tao WK (1994) An inquiry into the cirrus cloud thermostat effect for tropical sea surface temperature. Geophys Res Lett 21:1157–1160

Li X, Chao J, Hu Y (1964) A dynamic analysis of development of an anvil cumulonimbus cloud. Acta Meteor Sinica 34:225–232

Nakajima K, Matsuno T (1988) Numerical experiments concerning the origin of cloud clusters in the tropical atmosphere. J Meteor Soc Japan 66:309–329

Ping F, Luo Z, Li X (2007) Microphysical and radiative effects of ice clouds on tropical equilibrium states: A two-dimensional cloud-resolving modeling study. Mon Wea Rev 135:2794–2802

Ramanathan V, Collins W (1991) Thermodynamic regulation of ocean warming by cirrus clouds deduced from observations of the 1987 El Nino. Nature 351:27–32

Randall DA, Hu Q, Xu KM, Krueger SK (1994) Radiative-convective disequilibrium. Atmos Res 31:315–327

Robe FR, Emanuel KA (1996) Moist convective scaling: Some inferences from three-dimensional cloud ensemble simulations. J Atmos Sci 53:3265–3275

Sui CH, Lau KM, Tao WK, Simpson J (1994) The tropical water and energy cycles in a cumulus ensemble model. Part I: Equilibrium climate. J Atmos Sci 51:711–728

Tao WK, Scala J, Ferrier B, Simpson J (1995) The effects of melting processes on the development of a tropical and a midlatitude squall line. J Atmos Sci 52:1934–1948

Tao WK, Simpson J, Sui CH, Shie CL, Zhou B, Lau KM, Moncrieff MW (1999) Equilibrium states simulated by cloud-resolving models. J Atmos Sci 56:3128–3139

Tao WK, Shie CL, Simpson J, Braun S, Johnson RH, Ciesielski PE (2003) Convective systems over the South China Sea: Cloud-resolving model simulations. J Atmos Sci 60:2929–2956

Tompkins AM, Craig GC (1998) Radiative-convective equilibrium in a three-dimensional cloud-ensemble model. Quart J Roy Meteor Soc 124:2073–2097

Xu KM, Randall DA (1998) Influence of large-scale advective cooling and moistening effects on the quasi-equilibrium behavior of explicitly simulated cumulus ensembles. J Atmos Sci 55:896–909

Xu KM, Randall DA (1999) A sensitivity study of radiative-convective equilibrium in the tropics with a convection-resolving model. J Atmos Sci 56:3385–3399

Chapter 12
Remote Sensing Applications

Microwave radiances are sensitive to vertical profiles of temperature, water vapor, and cloud hydrometeors. Thus, satellite microwave measurements are important sources that provide atmospheric thermodynamic profiles, cloud properties, and surface parameters, in particular over vast ocean, where conventional observations are not available. Cloud-resolving model simulations can provide vertical profiles of temperature, water vapor, and cloud hydrometeors to radiative transfer models, which can simulate radiances. The comparison between the simulated radiances and satellite-measured radiances can evaluate how well numerical models produce cloud properties. The sensitivity tests of radiances to cloud hydrometeors can be used to eliminate cloud contamination from cloudy radiances. Thus, responses of radiance to cloud hydrometeors, correction of cloud contamination on cloudy radiances, and comparison between observed and simulated radiances are discussed in this chapter.

12.1 Introduction

The microwave instruments were first flown aboard U.S. satellites in 1972. In 1978, the NOAA launched the Microwave Sounding Unit (MSU) aboard the polar orbiting satellites. Recently, NOAA launched the Advance MSU (AMSU), which contains 12 channels within the 50–60 GHz oxygen bands (AMSU-A channels 3–14), 3 channels around the 183 GHz water vapor line (AMSU-B channels 18–20), and 5 window channels (AMSU-A channels 1–2, 15, and AMSU-B channels 16–17). The satellite microwave measurements are used to retrieve temperature (Spencer et al. 1990), water vapor (Grody 1980), ocean wind (Wentz et al. 1986), cloud liquid water (Weng and Grody 1994), ice cloud parameters (Weng and Grody 2000), precipitation (Ferraro 1997), snow cover (Grody 1991), and sea ice concentration (Grody et al. 2000). The retrieval of temperature and moisture is largely contaminated by the clouds. The cloud contamination on the AMSU measurements is dependent on the vertical profiles of cloud hydrometeors that are usually not available from observations. Thus, the correction of cloud contamination on AMSU measurements

resorts to the radiative transfer simulation with reasonable vertical cloud structures from the cloud-resolving model.

The sensitivity of the microwave radiances to clouds has been investigated by many researchers in the remote sensing community. In particular, the relation between the microwave radiances and surface rain rate has been intensively studied in the past two decades. Wu and Weinman (1984) computed microwave radiances as a function of rain rate and cloud hydrometeors and found that the lower-frequency radiances are sensitive to liquid precipitation at low altitudes whereas the high-frequency radiances are more sensitive to the ice hydrometeor at the cloud top. Mugnai and Smith (1988) used a microwave radiative transfer model with cloud inputs from the cloud model of Hall (1980) to investigate the impact of time-dependent cloud microphysical structure on the transfer to space of passive microwave radiation at frequencies from 19.35 to 231 GHz. They demonstrated that cloud water can have a major impact on the upwelling microwave radiation originating from both the surface and a rain layer placed below cloud base. They showed the different roles of absorption, emission, and scattering in determining the radiances at the top of the atmosphere in different stages of cloud development. Smith and Mugnai (1988) further showed that the relation between the microwave brightness temperature and surface rain rate is a function of cloud water processes and microwave frequencies. Smith and Mugnai (1989) found the important impacts of large ice particles on the microwave radiances. Yeh et al. (1990) used a microwave radiative transfer model to simulate the upwelling brightness temperatures at frequencies from 18 to 183 GHz based on the input hydrometeor profile derived from the ground-based radar reflectivities, and found that the upwelling brightness temperatures at both 92 and 181 GHz are most sensitive to the cloud structures in the upper portion of storms. Adler et al. (1991) employed a 3D cloud-microwave radiative transfer model to study the relation between upwelling radiances and cloud properties including rain rate of a tropical oceanic squall line and showed that the relation between microwave brightness temperature and rain rate is a function of cloud structure and content as well as development stages of convection. Smith et al. (1992) investigated precipitation retrieval from the responses of microwave radiances at the top of the atmosphere to clouds based on the microwave radiative transfer simulations and found that the relation between the microwave radiance and surface rain rate is largely affected by the ice clouds. Mugnai et al. (1993) developed a hybrid statistical-physical rainfall algorithm to produce liquid-ice profile information and surface rain rate. Muller et al. (1994) simulated the effects of water vapor and cloud properties on AMSU moisture channel measurements and found that the water vapor, cloud water, and ice have impacts on microwave radiances near 183 GHz.

Schaerer and Wilheit (1979) demonstrated theoretically a concept for obtaining water vapor profiles by using stronger resonance at 183 GHz and derived a weighting function at 183 GHz. The retrievals of water vapor profiles have been intensively studied by Rosenkranz et al. (1982), Kakar (1983), and Kakar and Lambrightsen (1984). Wang et al. (1983) and Lambrightsen and Kakar (1985) retrieved the water vapor profiles from 183 GHz measurements made from the NASA WRB-57 aircraft

using a nonlinear physical relaxation and a linear statistical retrieval algorithm, respectively. The above mentioned retrievals of water vapor profiles were limited to clear conditions. Isaacs and Deblonde (1987) derived a linear statistical retrieval algorithm that included clouds, and found some shortcomings related to the inclusion of clouds. Wilheit (1990) developed an algorithm for retrieving water vapor profiles in clear and cloudy atmospheres from 183 GHz radiometric measurements based on numerical simulations.

12.2 AMSU Responses to Cloud Hydrometeors

Li and Weng (2001) use a new, fast, and accurate microwave radiative transfer model (Liu and Weng 2002) including scattering and polarization to conduct the radiance simulations with the cloud-resolving model outputs from experiment COARE (see Section 3.1) to study the AMSU-B responses to various cloud parameters. The model is applied to compute the radiances at AMSU-B frequencies and bandwidths (see Table 12.1) based on thermodynamic profiles and cloud information derived from the cloud-resolving model simulation at 1400 LST on 21 December 1992, when strong convection occurred. Figure 12.1 shows horizontal distributions of brightness temperatures and total transmittance for AMSU-B frequencies at nadir, cloud contents, surface rain rate, *PW*, and surface wind. Strong convection occurs within 500–570 km, where surface rain rate has a maximum of 70 mm h^{-1}. The convection is associated with large *PW*, large horizontal wind shear, and large magnitudes of cloud hydrometeors, in particular raindrop and graupel. The convection causes a large drop of brightness temperatures for all AMSU-B frequencies, which are as low as 100 K. The convection also causes zero total transmittance at channels 16 and 17, whereas total transmittance is zero at channels 18–20 because of strong water vapor absorption.

Simulated radiances at AMSU frequencies with both ice and water hydrometeors are compared with those simulated with ice hydrometeors or with water hydrometeors to examine the AMSU responses to cloud hydrometeors (Fig. 12.2). Simulated radiances at 23.8, 31.4, and 50.3 GHz are only sensitive to water hydrometeors. Both ice and water hydrometeors have impacts on the variations of radiances simulated at 52.8, 53.596, 54.4, 54.94, and 55.5 GHz. Only ice hydrometeors are responsible

Table 12.1 AMSU-B channel characteristics

Channel number	Center frequency (GHz)	No. of pass-bands	Bandwidth per pass-band (MHz)	NEΔT (K)
16	89 (0.9)	2	1,000	0.37
17	150 (0.9)	2	1,000	0.84
18	183.31(1)	2	500	1.06
19	183.31(3)	2	1,000	0.70
20	183.31(7)	2	2,000	0.60

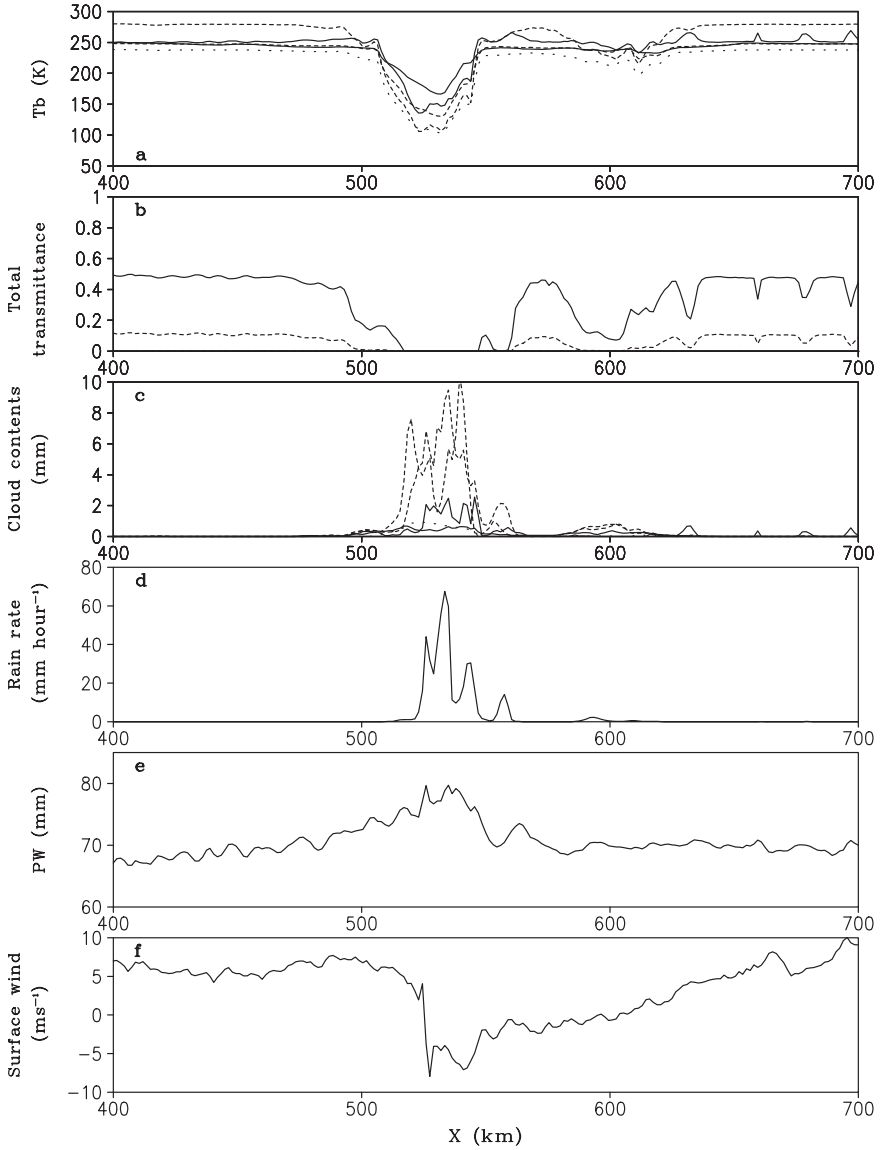

Fig. 12.1 Horizontal distributions of **a** brightness temperatures and **b** total transmittance for AMSU-B frequencies (dark solid: channel 16, dark dashed: channel 17, dot: channel 18, light solid: channel 19, light dashed: channel 20), **c** cloud hydrometeors (dark solid: cloud water, dark dashed: raindrop, dot: cloud ice, light solid: snow, light dashed: graupel), **d** surface rain rate, **e** *PW*, and **f** surface zonal wind simulated in experiment COARE on 1400 LST 21 December 1992 (After Li and Weng 2001)

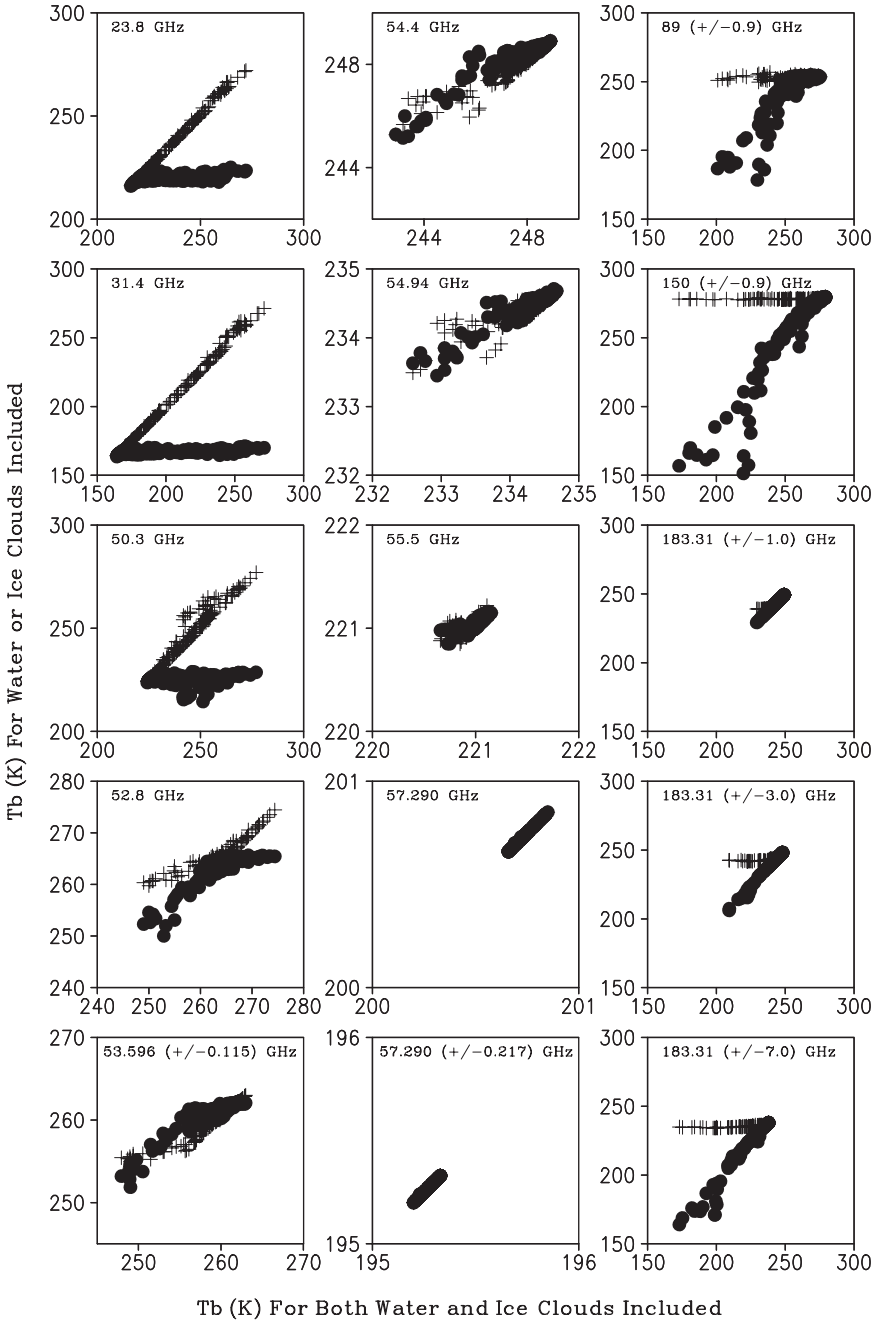

Fig. 12.2 Brightness temperatures (K) simulated with water hydrometeor (cross) or with ice hydrometeors (close circle) versus those simulated with both water and ice hydrometeors. The cloud data are from experiment COARE

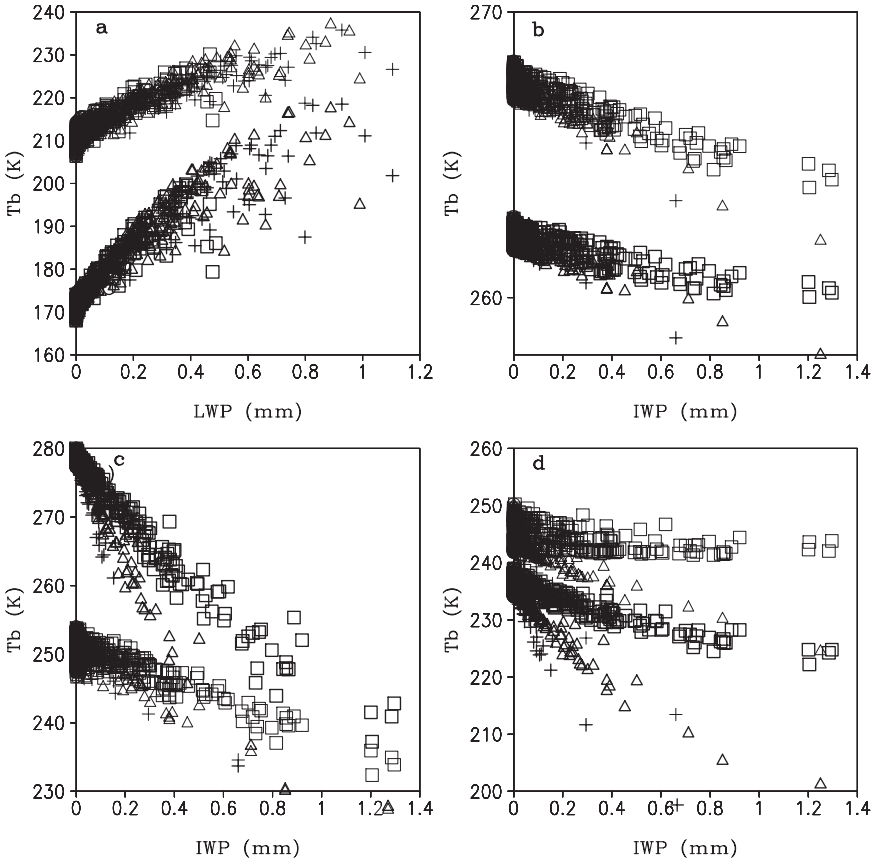

Fig. 12.3 **a** Tb at 23.8 GHz versus *LWP* (upper light) and T_b at 31.4 GHz versus *LWP* (lower dark) from simulations with raindrop only, **b** T_b at 52.8 GHz versus *IWP* (upper light) and T_b at 53.596 ± 0.115 GHz versus *IWP* (lower dark), **c** T_b at 89 ± 0.9 GHz versus *IWP* (upper light) and T_b at 150 ± 0.9 GHz versus *IWP* (lower dark), and **d** T_b at 183 ± 3 GHz versus *IWP* (upper light) and T_b at 183 ± 7 GHz versus *IWP* (lower dark) from simulations with graupel only. In Fig. 12.3a, the crosses, triangles, and squares represent raindrop within 570–696, 739–866, and 907–1007 mb, respectively. In Figs. 12.3b–d, the crosses, triangles, and squares represent graupel within 175–253, 282–380, and 416–530 mb, respectively. The cloud data are from experiment COARE

for the variations of radiances simulated at AMSU-B frequencies. The simulated radiances at 23.8 and 31.4 GHz increase with increasing *LWP* (Fig. 12.3a) whereas the simulated radiances at 52.8, 53.596 ± 0.115, 89 ± 0.9, 150 ± 0.9, 183.31 ± 3, and ± 7 GHz decrease with increasing *IWP* (Fig. 12.3b–d). The simulated radiances at 52.8, 53.596 ± 0.115, 89 ± 0.9, 150 ± 0.9, 183.31 ± 3, and ± 7 GHz are sensitive to the height whereas the simulated radiances at 23.8 and 31.4 GHz are insensitive to the height.

12.3 Correction of Cloud Contamination on AMSU Measurements

Radiances in cloudy and rainy conditions are affected by the clouds. The retrieval of atmospheric thermodynamic profiles requires correction of cloud contamination on radiances. Figure 12.4 shows the differences of brightness temperatures simulated with clouds minus those simulated without clouds at 52.8 and 53.596 GHz versus *LWP* and *IWP*. The comparison between the two figures clearly shows that the relation between the T_b difference and *IWP* is much better than that between the T_b difference and *LWP*. This suggests that the cloud contamination on 52.8 and 53.596 GHz should be corrected by *IWP* information. This is a typical case where the modeling information can serve as a guide for remote sensing.

Large differences between the simulated radiances with and without clouds exist at most of AMSU channels as shown in Fig. 12.5 (left panel). After corrections, the RMS differences between clear-sky and predicted clear-sky brightness temperatures over cloudy regions are smaller than 1 K and the linear correlation coefficients are larger than 0.7 that exceed the 1% confidence level (Fig. 12.5 in right panel). The contamination corrected AMSU radiances are used to retrieve temperature and moisture profiles over cloudy regions. Figure 12.6 shows the retrieved

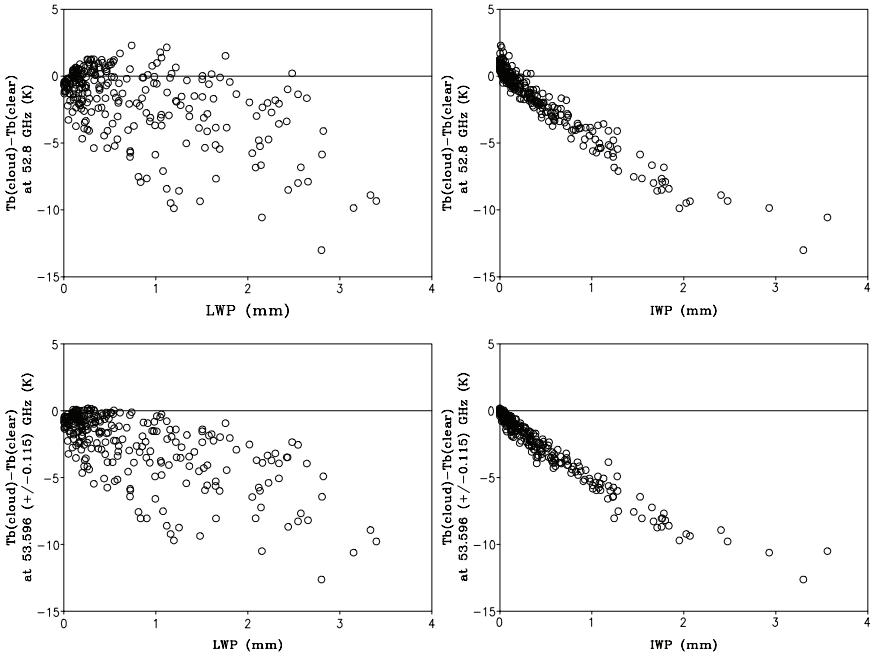

Fig. 12.4 Difference of brightness temperatures (K) simulated with clouds minus those without clouds at 52.8 (upper panel) and 53.596 GHz (lower panel) versus *LWP* (mm) in the left panels and *IWP* (mm) in the right panels. The cloud data are from experiment COARE

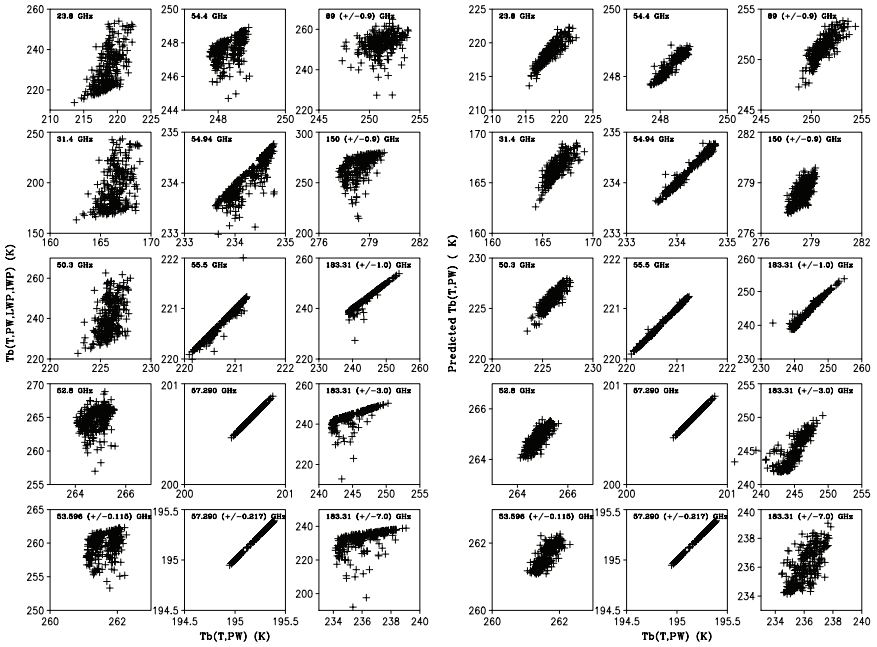

Fig. 12.5 Brightness temperatures (K) simulated with clouds versus those simulated without clouds at AMSU channel over cloudy regions before the correction of cloud contamination in the left panels and clear-sky brightness temperatures versus predicted clear-sky brightness temperatures over cloudy regions after the correction in the right panels. The cloud data are from experiment COARE

specific humidity versus true specific humidity at selected vertical levels, where the RMS differences are smaller than $0.5\,\mathrm{g\,kg^{-1}}$, and the correlation coefficients are larger than 0.7.

12.4 Comparison Studies Between Simulated and Observed Radiances

The comparison between simulated and observed radiances can be used to evaluate cloud simulations. Water and ice hydrometeor-sensitive radiances are used to assess the water and ice cloud simulations. As an example, Fig. 12.7 shows the good agreement between simulations and observations, indicating the capability of simulating cloud structures by the cloud-resolving model (Li and Weng 2003).

The cloud microphysics budget averaged from 2200 LST 19 December to 1000 LST 21 December 1992 using the data from experiment COARE (Fig. 12.8a) reveals that the accretion of snow by graupel ($[P_{GACS}] = 0.19\,\mathrm{mm\,h^{-1}}$) is as important as the riming of cloud water by graupel ($[P_{GACW}] = 0.19\,\mathrm{mm\,h^{-1}}$). The P_{GACS} is a strong

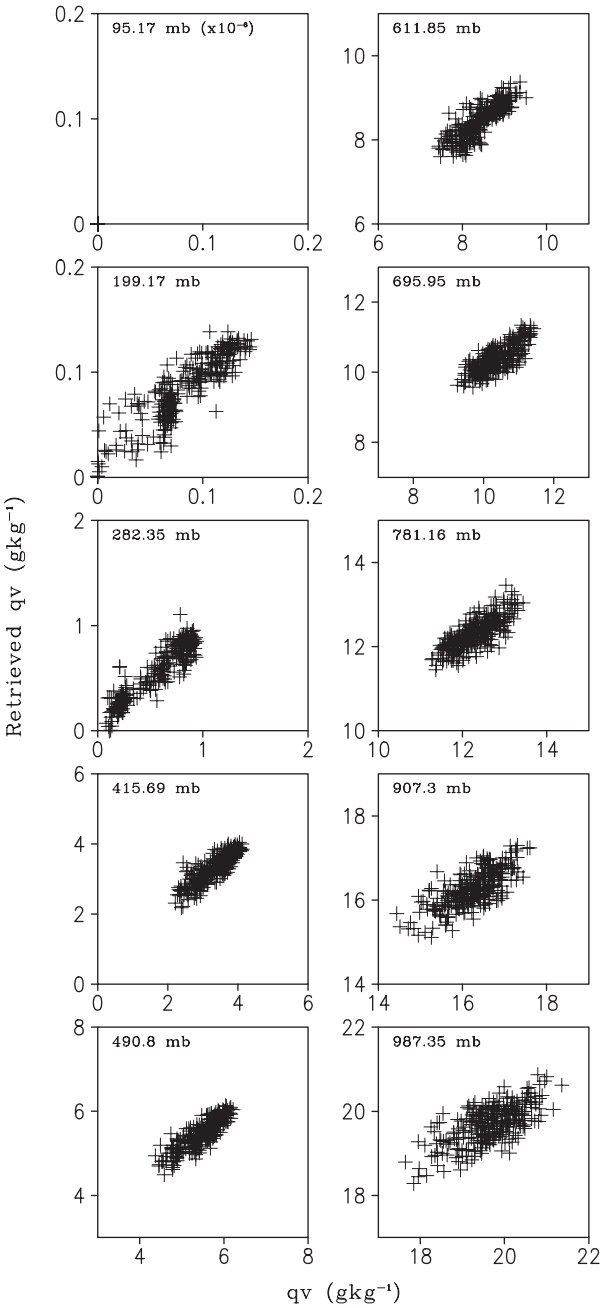

Fig. 12.6 Specific humidity versus retrieved specific humidity at selected vertical levels. Unit is g kg^{-1}. The cloud data are from experiment COARE

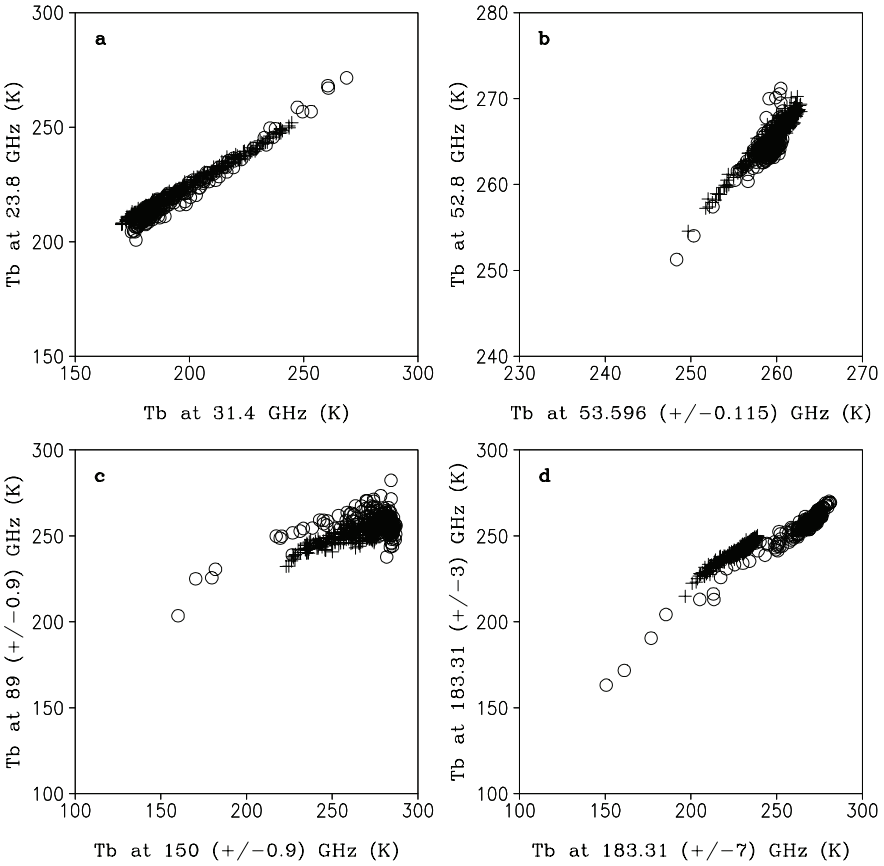

Fig. 12.7 **a** Brightness temperature T_b at AMSU-A channel 1 (23.8 GHz) versus channel 2 (31.4 GHz), **b** T_b at AMSU-A channel 4 (52.8 GHz) versus channel 5 [53.596 $(+/-0.115)$ GHz), **c** T_b at AMSU-B channel 16 [89 $(+/-0.9)$ GHz] versus channel 17 [150 $(+/-0.9)$ GHz], and **d** T_b at AMSU-B channel 19 [183.31 $(+/-3)$ GHz] versus channel 20 [183.31 $(+/-7)$ GHz]. The dots represent the observations over $(10^\circ\text{S}-10^\circ\text{N},\ 140^\circ\text{E}-180^\circ)$ from NOAA-15 and 16 satellites in selected days of year 2001, whereas the crosses denote the simulations from microwave radiative transfer model developed by Liu and Weng (2002). The simulations use cloud information in COARE from 2200 LST 19 December to 1000 LST 21 December 1992. The simulation data are averaged in 32 grid points (48 km mean), which is similar to the horizontal resolution of AMSU observation at nadir. All data are obtained in cloudy condition in which vertically integrated cloud water is larger than 0.1 mm (After Li and Weng 2003). The cloud data are from experiment COARE

function of the assumed accretion efficiency of snow by graupel, which is not well known. Thus, this term is set to be zero or very small (e.g., Ziegler 1985; Ferrier et al. 1995), because it is hard to argue that a snowflake colliding with a graupel particle will stick to the graupel. Therefore, an additional experiment with P_{GACS} excluded is carried out (Fig. 12.8b). The vapor condensation and deposition rates (P_{CND} and P_{DEP}) in the two experiments are similar. The *LWP* in the two experiments are about the same, whereas the *LWP* in the experiment without P_{GACS} (0.39 mm) is

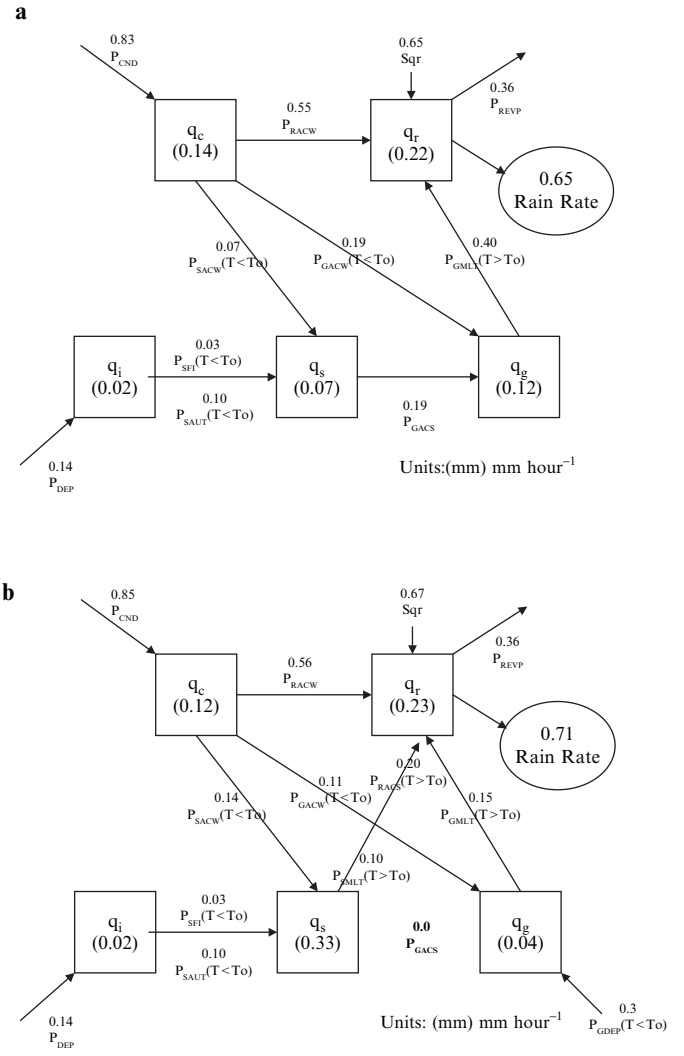

Fig. 12.8 36-h and model domain mean cloud microphysics budgets averaged from 2200 LST 19 December to 1000 LST 21 December 1992 using the data from experiments **a** with P_{GACS} and **b** without P_{GACS} during TOGA COARE (After Li and Weng 2003)

much larger than that in the experiment with P_{GACS} (0.21 mm). Compared to the experiment with P_{GACS}, the mixing ratio of graupel decreases significantly, whereas the mixing ratio of snow increases significantly and becomes the major component of ice hydrometeors in the experiment without P_{GACS}. In the experiment without P_{GACS}, the conversion rate from snow to rain through the accretion of snow by rain ($[P_{RACS}] = 0.2\,\mathrm{mm\,h^{-1}}$) and the melting of snow ($[P_{SMLT}] = 0.1\,\mathrm{mm\,h^{-1}}$)

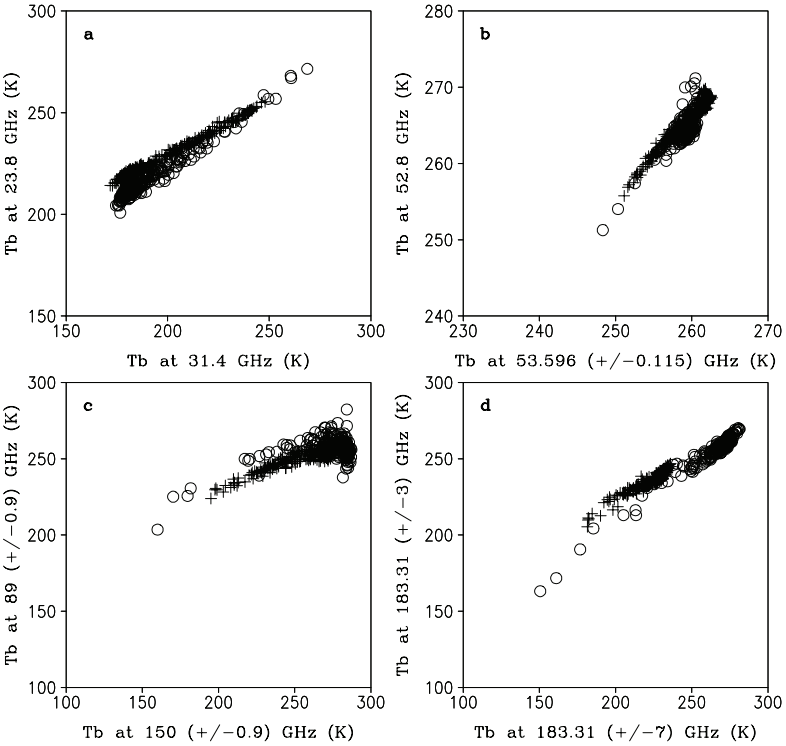

Fig. 12.9 Same as in Fig. 12.7 except for the experiment without P_{GACS} (After Li and Weng 2003)

is larger than the conversion from graupel to rain through the melting of graupel ($[P_{GMLT}] = 0.15\,\mathrm{mm\,h^{-1}}$) in the rain budget.

Figure 12.9 shows the pairs of brightness temperatures in observations and simulations without P_{GACS}. The variations of radiances in the experiment without P_{GACS} are closer to the observations than those in the experiment with P_{GACS} (Fig. 12.7). The signals are very significant in AMSU channels 16 and 17 because of significant changes of ice clouds. The comparison between simulations and observations suggests that the P_{GACS} suppress the development of precipitation ice unrealistically.

References

Adler RF, Yeh HYM, Prasad N, Tao WK, Simpson J (1991) Microwave simulations of a tropical rainfall system with a three-dimensional cloud model. J Appl Meteor 30:924–953

Ferraro R (1997) Special sensor microwave imager derived global rainfall estimates for climatological applications. J Geophys Res 102:16715–16735

Ferrier BS, Tao WK, Simpson J (1995) A double-moment multiple-phase four-class bulk ice scheme. Part II: Simulations of convective storms in different large-scale environments and comparisons with other bulk parameterizations. J Atmos Sci 52:1001–1033

Grody N (1980) Atmospheric water content over the tropical Pacific derived from the Nimbus-6 Scanning Microwave Spectrometer. J Appl Meteor 19:986–996

Grody N (1991) Classification of snow cover and precipitation using the special sensor microwave imager. J Geophys Res 96:7423–7435

Grody N, Weng F, Ferraro R (2000) Application of AMSU for obtaining hydrological parameters. In: Pampaloni P, Paloscia S (ed) Microwave Radiometery and Remote Sensing of Earth's Surface and Atmosphere. VSP, Zeist, Netherlands, pp. 339–351

Hall WD (1980) A detailed microphysical model within a two-dimensional dynamic framework: Model description and preliminary results. J Atmos Sci 37:2486–2507

Isaacs RG, Deblonde G (1987) Millimeter wave moisture sounding: The effect of clouds. Radio Sci 14:793–802

Kakar RK (1983) Retrieval of clear sky moisture profiles using the 183 GHz water vapor line. J Climate Appl Meteor 22:1282–1289

Kakar RK, Lambrightsen BH (1984) A statistical correlation method for the retrieval of atmospheric moisture profiles by microwave radiometry. J Climate Appl Meteor 23:1110–1114

Lambrightsen BH, Kakar RK (1985) Estimation of atmospheric moisture content from microwave radiometric measurements during CCOPE. J Climate Appl Meteor 24:266–274

Li X, Weng F (2001) Effects of cloud and precipitation microphysics on AMSU measurements as simulated using cloud resolving model outputs. 11th Conference on Satellite Meteorology and Oceanography, Madison, WI, October 15–18, 2001

Li X, Weng F (2003) Toward direct uses of satellite cloudy radiances in NWP models. Part II: Radiance simulations at microwave frequencies. 12th Conference on Satellite Meteorology and Oceanography, Long Beach, CA, February 9–13, 2003

Liu Q, Weng F (2002) A microwave polarimetric two-stream radiative transfer model. J Atmos Sci 59:2396–2402

Mugnai A, Smith EA (1988) Radiative transfer to space through a precipitation cloud at multiple microwave frequencies. Part I: Model description. J Appl Meteor 27:1055–1073

Mugnai A, Smith EA, Tropoli GJ (1993) Foundation for statistical-physical precipitation retrieval from passive microwave satellite measurements. Part II: Emission-source and generalized weighting-function properties of a time-dependent cloud-radiation model. J Appl Meteor 32:17–39

Muller BM, Fuelberg HE, Xiang X (1994) Simulations of the effects of water vapor, cloud liquid water, and ice on AMSU moisture channel brightness temperatures. J Appl Meteor 33:1133–1154

Rosenkranz PW, Komichak MJ, Staelin DH (1982) A method for estimation of atmospheric water vapor profiles by microwave radiometry. J Climate Appl Meteor 21:1364–1370

Schaerer G, Wilheit TT (1979) A passive technique for profiling atmospheric water vapor. Radio Sci 14:371–375

Smith EA, Mugnai A (1988) Radiative transfer to space through a precipitation cloud at multiple microwave frequencies. Part II: Results and analysis. J Appl Meteor 27:1074–1091

Smith EA, Mugnai A (1989) Radiative transfer to space through a precipitation cloud at multiple microwave frequencies. Part III: Influence of large ice particles. J Meteor Soc Japan 67:739–755

Smith EA, Mugnai A, Cooper HJ, Tropoli GJ, Xiang X (1992) Foundation for statistical-physical precipitation retrieval from passive microwave satellite measurements. Part I: Brightness-temperature properties of a time-dependent cloud-radiation model. J Appl Meteor 31:506–531

Spencer R, Christy J, Grody N (1990) Global atmospheric temperature monitoring with satellite microwave measurements: Method and results 1979–1984. J Climate 3:1111–1128

Wang JR, King JL, Wilheit TT, Szejwach G, Gesell LH, Nieman RA, Niver DS, Krupp BM, Gagliano JA (1983) Profiling atmospheric water vapor by microwave radiometry. J Climate Appl Meteor 22:779–788

Weng F, Grody N (1994) Retrieval of cloud liquid water using the Special Sensor Microwave Imager (SSM/I). J Geophys Res 99:25535–25551

Weng F, Grody N (2000) Retrieval of ice cloud parameters using a microwave imaging radiometer. J Atmos Sci 57:1069–1081

Wentz F, Mattox L, Peteherych S (1986) New algorithms for microwave measurements of ocean winds application to SEASAT and the Special Sensor Microwave Imager. J Geophys Res 91:2289–2307

Wilheit TT (1990) An algorithm for retrieving water vapor profiles in clear and cloudy atmospheres from 183 GHz radiometric measurements: Simulation studies. J Appl Meteor 29:508–515

Wu R, Weinman JA (1984) Microwave radiances from precipitating clouds containing aspherical ice, combined phase, and liquid hydrometeors. J Geophys Res 89:7170–7178

Yeh HYM, Prasad N, Mack RA, Adler RF (1990) Aircraft microwave observations and simulations of deep convection from 18 to 183 GHz. Part II: Model results. J Atmos Oceanic Technol 7:377–391

Ziegler CL (1985) Retrieval of thermal and microphysical variables in observed convective storms. Part 1: Model development and preliminary testing. J Atmos Sci 42:1487–1509

Chapter 13
Future Perspective of Cloud-Resolving Modeling

The simulations show that the performance of prognostic cloud microphysical parameterization schemes has direct, crucial impacts on the simulations of cloud clusters in the genesis, evolution, propagation, and amplitudes. However, the computation of the full set of prognostic cloud microphysical equations is time-consuming. Thus, simplified prognostic cloud microphysical parameterization schemes are discussed in this chapter. Possible replacement of cumulus parameterization in general circulation models (GCMs) with cloud-resolving model (CRM) package and recent progress in global cloud-resolving modeling are addressed.

13.1 Simplification of Cloud Microphysical Parameterization Schemes

Li et al. (2002) found from their analysis of cloud microphysical budgets in COARE1 that in the deep tropical convective regime, the magnitudes of 12 terms out of a total of 29 cloud microphysical processes are negligibly small. Thus, they proposed a simplified set of cloud microphysical equations (13.1), which saves 30–40% of CPU time.

$$S_{q_c} = -P_{SACW}(T < T_o) - P_{RAUT} - P_{RACW} - P_{GACW} + P_{CND}, \tag{13.1a}$$

$$\begin{aligned} S_{q_r} = {} & P_{RAUT} + P_{RACW} + P_{GACW}(T > T_o) - P_{REVP} \\ & + P_{SMLT}(T > T_o) + P_{GMLT}(T > T_o), \end{aligned} \tag{13.1b}$$

$$\begin{aligned} S_{q_i} = {} & -P_{SAUT}(T < T_o) - P_{SACI}(T < T_o) - P_{SFI}(T < T_o) \\ & - P_{GACI}(T < T_o) + P_{DEP}, \end{aligned} \tag{13.1c}$$

$$\begin{aligned} S_{q_s} = {} & P_{SAUT}(T < T_o) + P_{SACI}(T < T_o) + P_{SFI}(T < T_o) \\ & - P_{GACS} + P_{SMLT}(T > T_o) - (1 - \delta_4) P_{WACS}(T < T_o) \\ & + P_{SACW}(T < T_o) + (1 - \delta_1) P_{SDEP}(T < T_o), \end{aligned} \tag{13.1d}$$

$$S_{q_g} = P_{GACS} + (1-\delta_4)P_{WACS}(T < T_o) - P_{GMLT}(T > T_o) - P_{MLTG}(T > T_o) + P_{GACI}(T < T_o) + P_{GACW}(T < T_o) - (1-\delta_1)P_{GDEP}(T < T_o). \quad (13.1e)$$

The neglected terms in the simplified set include the accretion of cloud ice and snow by raindrops, the evaporation of melting snow, the accretion of cloud water and raindrops by snow, the accretion of raindrops and the homogeneous freezing of cloud water by cloud ice, the accretion and freezing of raindrops by graupel, the growth of cloud water by the melting of cloud ice, and the growth of cloud ice and snow by the deposition of cloud water. An experiment with the simplified set of cloud microphysical equations was conducted and compared to an experiment with the full set of cloud microphysical equations (COARE1) (see section 3.1). Both experiments show similar time evolution and magnitudes of temperature and moisture profiles, surface rain rates including stratiform percentage and fractional coverage of convective, raining and nonraining stratiform clouds (Fig. 13.1). This suggests that the original set of cloud microphysical equations could be replaced by the simplified set in simulations of tropical oceanic convection.

Li et al. (2005) proposed a prognostic cloud scheme that includes 18 cloud microphysical terms from a total of 29 included in the CRM (Tao and Simpson 1993) based on the prognostic cloud scheme from Zhao and Carr (1997), which

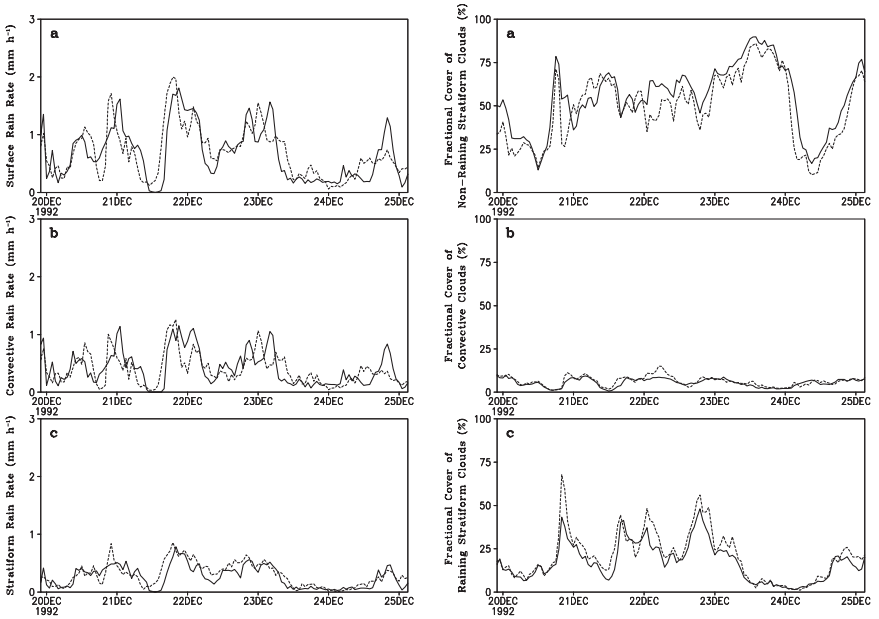

Fig. 13.1 Left panel: time series of **a** surface rain rate $(\mathrm{mm\,h^{-1}})$, **b** convective rain rate, and **c** stratiform rain rate simulated with the simplified set of cloud microphysics equations (solid) and simulated in COARE1 (with the full set) (dashed); right panel: time series of fractional coverage (%) of **a** nonraining stratiform regions, **b** convective regions, and **c** raining stratiform regions (After Li et al. 2002)

shows reasonable thermodynamic simulations. Combined with Li et al. (2002, 2005), Li and Weng (2004) proposed a new simplified prognostic cloud scheme.

$$S_{q_c} = -P_{RAUT} - P_{RACW} + P_{CND}, \tag{13.2a}$$

$$S_{q_r} = P_{RAUT} + P_{RACW} - P_{REVP} + P_{SMLT}(T > T_o) + P_{GMLT}(T > T_o), \tag{13.2b}$$

$$S_{q_i} = -P_{SAUT}(T < T_o) - P_{SACI}(T < T_o) - P_{SFI}(T < T_o) + P_{DEP}, \tag{13.2c}$$

$$\begin{aligned} S_{q_s} = {} & P_{SAUT}(T < T_o) + P_{SACI}(T < T_o) + P_{SFI}(T < T_o) \\ & - P_{GACS} - P_{SMLT}(T > T_o) - (1 - \delta_4) P_{WACS}(T < T_o), \end{aligned} \tag{13.2d}$$

$$S_{q_g} = P_{GACS} + (1 - \delta_4) P_{WACS}(T < T_o) - P_{GMLT}(T > T_o) - P_{MLTG}(T > T_o). \tag{13.2e}$$

The experiments with both the full set of cloud microphysical equations and the simplified set of cloud equations (13.2) are carried out with the forcing calculated from NCEP/GDAS data averaged over the area of 150–160°E and 0.5°S–0.5°N. The model is integrated from 0500 LST 18 April to 1100 LST 26 April 2003. The simulations are evaluated with the MSPPS *IWP* and *LWP* to examine the simplification of the cloud scheme. Note that roughly 6-hourly data from three satellites (NOAA-15, 16, 17) are used in the MSPPS data, whereas hourly simulation data are analyzed. The *IWP* (0.2 mm) is generally smaller than the *LWP* (0.3 mm) in the MSPPS data (Fig. 13.2a), whereas the *IWP* and *LWP* simulated with the full set of microphysical equations (Fig. 13.2b) have the same values of up to 0.4 mm. Thus, the magnitudes of *IWP* and *LWP* simulated with the full set of microphysical equations are 50% and 25% larger than those observed in the MSPPS data, respectively, indicating that the full set of cloud microphysical equations produces relatively large cloud condensates. The *IWP* simulated with the simplified set of microphysical equations (0.3 mm Fig. 13.2c) becomes smaller than that simulated with the full set of microphysical equations (0.4 mm Fig. 13.2b) so that the *IWP* is smaller than the *LWP* in the simulation with the simplified set of microphysical equations and the ratio of the *IWP* to *LWP* is similar to that observed in the MSPPS data (Fig. 13.2a). This comparison shows that the simplified prognostic cloud scheme may produce better cloud simulations than the original one.

13.2 Cloud-Resolving Convection Parameterization

Grabowski and Smolarkiewicz (1999) and Grabowski (2001) applied a 2D CRM into each column of a 3D large-scale model based on the assumption of scale separation between small-scale convection and large-scale circulation. The approach allows interaction between columns through the large-scale dynamics only, and is referred to as cloud-resolving convection parameterization (CRCP). The comparison between the CRCP and CRM simulation in a 2D nonrotating atmosphere with the presence of *SST* gradients shows that large-scale thermodynamic states and circulations are reasonably simulated in the CRCP, whereas the interaction between

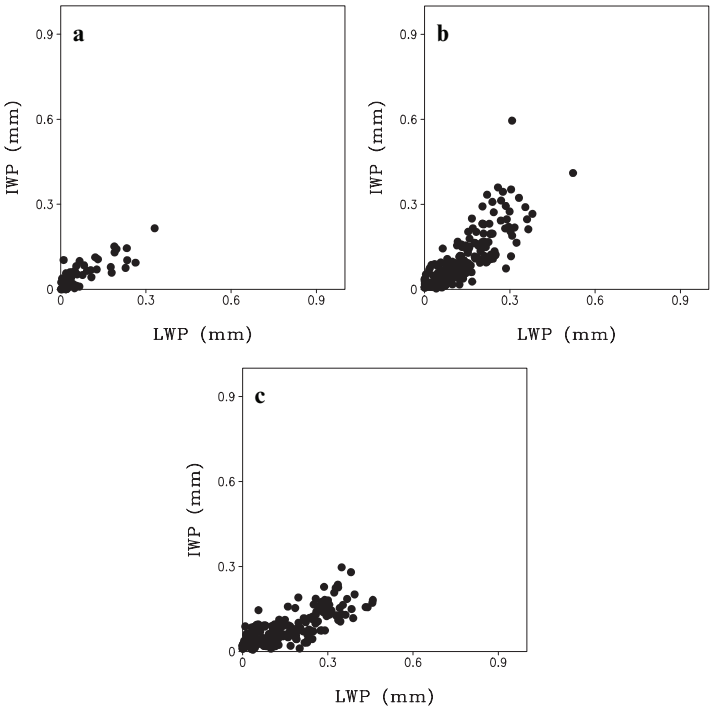

Fig. 13.2 **a** MSPPS *IWP* (mm) versus *LWP* (mm), **b** *IWP* versus *LWP* simulated by the full set of cloud equations, and **c** *IWP* versus *LWP* simulated by the simplified set of cloud equations. The imposed forcing calculated from NCEP/GDAS data averaged over the area of 150–160°E and 0.5°S–0.5°N from 0500 LST 18 April to 1100 LST 26 April 2003 (After Li and Weng 2004)

ascending and descending branches through the gravity wave mechanism and the organization of small-scale convection into mesoscale convective systems are poorly captured. The studies further show that the CRCP simulation produces the large-scale organization of convection within the equatorial waveguide. Khairoutdinov and Randall (2001) carried out a 2-month simulation with a 2D CRM installed in a realistic GCM, analyzed the results in January, and found that the CRM domain used in the combined GCM/CRM model produces good cloud statistics and that the model generates reasonable simulations, including January precipitation patterns in both extratropical storm tracks and the tropics, the Inter-Tropical Convergence Zone, the South Pacific Convergence Zone, as well as the South Atlantic Convergence Zone. Randall et al. (2003) performed an annual cycle simulation to simulate a vigorous Madden-Julian Oscillation including a slow propagation over the warm water over the Indian Ocean and western Pacific and a fast movement east of the date line. Khairoutdinov et al. (2005) conducted a 500-day simulation using the NCAR Community Atmosphere Model (CAM) with superparameterization and compared it with the simulation using the standard CAM and found that the CAM with superparameterization simulated between mean states in terms of precipitation, *PW*,

top-of-atmosphere radiative fluxes, cloud radiative forcing, and fractional cover for high clouds in both winter and summer seasons, and that the model also produced more realistic intraseasonal variability. However, the disadvantages of CRCP are arbitrary dimension configuration for CRMs and artificial scale separation between the CRM and the GCM.

13.3 Global Cloud-Resolving Model

Grabowski (1998) conducted a 2D CRM simulation with a zonally varied *SST* over the large domain of 4,000 km. The maximum *SST* at the center of the domain is 28°C and the amplitude of the *SST* is 4°C. Grabowski integrated the model into quasi-equilibrium states in 60 days. The clouds occur around the center of the domain where the *SST* is relatively high, which resembles an ascending branch of the Walker circulation. The subsidence over the cold water causes dry air, which forms a descending branch of the Walker circulation. The explicitly resolved convection shows quasi-2-day oscillations that are similar to those observed by Takayabu et al. (1996).

Satoh et al. (2005) and Tomita et al. (2005) applied the CRM into global domain to conduct a global CRM simulation by developing an icosahedral grid technique. The new model is referred to as Nonhydrostatic Icosahedral Atmospheric Model (NICAM). The model includes a simple two-category cloud microphysics scheme with the ice effects proposed by Grabowski (1998), a radiation parameterization scheme developed by Nakajima et al. (2000), and the Meller-Yamada level-2 subgrid-scale turbulence closure and surface flux scheme by Louis et al. (1982). Satoh et al. started a 60-day integration with a horizontal resolution of 14 km, then integrated the model for another 30 days with a grid mesh of 7 km, and finally used the data on the 20th day of 7-km run as the initial conditions to integrate another 10 days with a horizontal resolution of 3.5 km. The analysis of 10-day simulation data in 3.5-km run shows realistic cloud simulations including mutiscale cloud structures, Intertropical Convergence Zone (ITCZ), Madden and Julian Oscillation (MJO)-like wave propagation, and diurnal rainfall variations. Miura et al. (2005) conducted an additional experiment with the increase of 2K for *SST* in the experiment by Tomita et al. (2005). Comparison between the two experiments shows that the temperature and relative humidity is 4°C warmer but 15% smaller in the experiment with +2K than in Tomita et al.'s experiment in the tropics. Cloud amount and albedo are larger in the experiment with +2K than in Tomita et al.'s experiment near the equator and in high latitudes. The results are encouraging. As the computational power increases, the global cloud-resolving modeling will bring realistic cloud simulations, and be beneficial to a better understanding of cloud–radiation interaction and associated impacts on climate variability.

References

Grabowski WW (1998) Toward cloud resolving modeling of large-scale tropical circulations: A simple cloud microphysics parameterization. J Atmos Sci 55:3283–3298

Grabowski WW (2001) Coupling cloud processes with the large-scale dynamics using the cloud-resolving convection parameterization (CRCP). J Atmos Sci 58:978–997

Grabowski WW, Smolarkiewicz PK (1999) CRCP: A cloud resolving convection parameterization for modeling the tropical convecting atmosphere. Physica D 133:171–178

Khairoutdinov M, Randall DA (2001) A cloud resolving model as a cloud parameterization in the NCAR Community Climate Model: Preliminary results. Geophys Res Lett 28:3617–3620

Khairoutdinov M, Randall DA, DeMott C (2005) Simulations of the atmospheric general circulations using a cloud-resolving model as a superparameterization of physical processes. J Atmos Sci 62:2136–2154

Li X, Weng F (2004) An operational cloud verification system and its application to validate cloud simulations in the operational models, 13th Conference on Satellite Meteorology and Oceanography, Norfolk, Virginia, 20–24 September 2004

Li X, Sui CH, Lau KM (2002) Dominant cloud microphysical processes in a tropical oceanic convective system: A 2-D cloud resolving modeling study. Mon Wea Rev 130:2481–2491

Li X, Sui CH, Lau KM, Tao WK (2005) Tropical convective responses to microphysical and radiative processes: A 2D cloud-resolving modeling study. Meteor Atmos Phys 90:245–259

Louis JF, Tiedke FM, Geleyn JF (1982) A short history of the PBL paramterization at ECMWF. Workshop on Planetary Boundary Layer Parameterization. ECMWF, Reading, UK

Miura H, Tomita H, Nasuno T, Iga S, Satoh M (2005) A climate sensitivity test using a global cloud resolving model under an aqua planet condition. Geophys Res Lett, doi:10.1029/2005GL023672

Nakajima T, Tsukamoto M, Tsushima Y, Numaguti A, Kimura T (2000) Modeling of the radiative process in an atmospheric general circulation model. Appl Opt 39:4869–4878

Randall DA, Khairoutdinov M, Arakawa A, Grabowski WW (2003) Breaking the cloud parameterization deadlock. Bull Am Meteor Soc 84:1547–1564

Satoh M, Tomita H, Miura H, Iga S, Nasumo T (2005) Development of a global resolving model – a multi-scale structure of tropical convections. J Earth Sim 3:1–9

Takayabu YN, Lau KM, Sui CH (1996) Observation of a quasi-2-day wave during TOGA COARE. Mon Wea Rev 124:1892–1913

Tao WK, Simpson J (1993) The Goddard Cumulus Ensemble model. Part I: Model description. Terr Atmos Oceanic Sci 4:35–72

Tomita H, Miura H, Iga S, Nasuno T, Satoh M (2005) A global cloud-resolving simulation: Preliminary results from an aqua planetary experiment. Geophys Res Lett, doi:-10.1029/2005 GL022459

Zhao Q, Carr FH (1997) A prognostic cloud scheme for operational NWP models. Mon Wea Rev 125:1931–1953

Abbreviations and Acronyms

1D	One-dimensional
2D	Two-dimensional
3D	Three-dimensional
AMSU	Advanced MSU
ARM	Atmospheric radiation measurement
CAM	Community Atmosphere Model
CAPE	Convective available potential energy
CCM2	Community Climate Model 2
CEM	Cumulus Ensemble Model
CFAD	Contoured frequency with altitude diagram
COARE	Coupled Ocean-Atmosphere Response Experiment
COR	Correlation
CMPE	Cloud-microphysics precipitation efficiency
CR	Cloud ratio
CRCP	Cloud-resolving convection parameterization
CRM	Cloud-Resolving Model
CVV	Convective vorticity vector
DVV	Dynamic vorticity vector
EQ	Equator
ERBE	Earth Radiation Budget Experiment
GARP	Global Atmospheric Research Program
GATE	GARP Atlantic Tropical Experiment
GCE	Goddard cumulus ensemble
GCM	General Circulation model
GDAS	Global Data Assimilation System
GMS	Geostationary meteorological satellite
GSFC	Goddard Space Flight Center
H	Helicity
IFA	Intensive Flux Array
IOP	Intensive Observing Period
IR	Infrared

ITCZ	Intertropical Convergence Zone
IWP	Ice water path
KWAJEX	Kwajalein Experiment
LFC	Level of free convection
LSPE	Large-scale precipitation efficiency
LST	Local standard time
LWP	Liquid water path
MJO	Madden-Julian Oscillation
MSPPS	Microwave Surface and Precipitation Products System
MSU	Microwave Sounding Unit
MV	Moist vorticity
MVV	Moist vorticity vector
NASA	National Aeronautics and Space Administration
NCAR	National Center for Atmospheric Research
NCEP	National Centers for Environmental Prediction
NESDIS	National Environmental Satellite, Data, and Information Service
NICAM	Nonhydrostatic Icosahedral Atmospheric Model
NOAA	National Oceanic and Atmospheric Administration
PSU	Practical salinity units
PV	Potential vorticity
PW	Precipitable water
RMS	Root-mean-square
SCS	South China Sea
SCSMEX	SCS Monsoon Experiment
SST	Sea surface temperature
TOGA	Tropical Ocean Global Atmosphere
TMI	TRMM Microwave Imager
TRMM	Tropical Rainfall Measuring Mission
UV	Ultraviolet
VIS	Visible

Index